



Calhoun: The NPS Institutional Archive DSpace Repository

Theses and Dissertations

1. Thesis and Dissertation Collection, all items

1998-03-01

Discrete-mode source development and testing for new seismo-acoustic sonar

Gaghan, Frederick E.

Monterey, California. Naval Postgraduate School

<http://hdl.handle.net/10945/8272>

This publication is a work of the U.S. Government as defined in Title 17, United States Code, Section 101. Copyright protection is not available for this work in the United States.

Downloaded from NPS Archive: Calhoun



<http://www.nps.edu/library>

Calhoun is the Naval Postgraduate School's public access digital repository for research materials and institutional publications created by the NPS community.

Calhoun is named for Professor of Mathematics Guy K. Calhoun, NPS's first appointed -- and published -- scholarly author.

Dudley Knox Library / Naval Postgraduate School
411 Dyer Road / 1 University Circle
Monterey, California USA 93943

NPS ARCHIVE
1998.03
GAGHAN, F.

DUDLEY K. ROX LIBRARY
NAVAL POSTGRADUATE SCHOOL
MONTEREY, CA 93943-5101

NAVAL POSTGRADUATE SCHOOL

MONTEREY, CALIFORNIA



THESIS

**DISCRETE-MODE SOURCE DEVELOPMENT AND
TESTING FOR NEW SEISMO-ACOUSTIC SONAR**

by

Frederick E. Gaghan, Jr.

March 1998

Thesis Advisor:
Co-Advisor:

Steven R. Baker
Thomas G. Muir

Approved for public release; distribution is unlimited.

DUDLEY KNOX LIBRARY
NAVAL POSTGRADUATE SCHOOL
MONTEREY CA 93943-5101

REPORT DOCUMENTATION PAGE

Form Approved OMB No. 0704-0188

Public reporting burden for this collection of information is estimated to average 1 hour per response, including the time for reviewing instruction, searching existing data sources, gathering and maintaining the data needed, and completing and reviewing the collection of information. Send comments regarding this burden estimate or any other aspect of this collection of information, including suggestions for reducing this burden, to Washington Headquarters Services, Directorate for Information Operations and Reports, 1215 Jefferson Davis Highway, Suite 1204, Arlington, VA 22202-4302, and to the Office of Management and Budget, Paperwork Reduction Project (0704-0188) Washington DC 20503.

1. AGENCY USE ONLY (<i>Leave blank</i>)	2. REPORT DATE March 1998	3. REPORT TYPE AND DATES COVERED Master's Thesis	
4. TITLE AND SUBTITLE OF THESIS DISCRETE-MODE SOURCE DEVELOPMENT AND TESTING FOR NEW SEISMO-ACOUSTIC SONAR			5. FUNDING NUMBERS
6. AUTHOR(S) Frederick E. Gaghan, Jr.			
7. PERFORMING ORGANIZATION NAME(S) AND ADDRESS(ES) Naval Postgraduate School Monterey CA 93943-5000			8. PERFORMING ORGANIZATION REPORT NUMBER
9. SPONSORING/MONITORING AGENCY NAME(S) AND ADDRESS(ES)			10. SPONSORING/MONITORING AGENCY REPORT NUMBER
11. SUPPLEMENTARY NOTES The views expressed in this thesis are those of the author and do not reflect the official policy or position of the Department of Defense or the U.S. Government.			
12a. DISTRIBUTION/AVAILABILITY STATEMENT Approved for public release; distribution is unlimited.			12b. DISTRIBUTION CODE
13. ABSTRACT (<i>maximum 200 words</i>) A seismo-acoustic sonar concept that uses guided interface waves (Rayleigh or Scholte) is being developed to detect buried ordnance in the sea floor and beach sediments. This thesis describes the initial research conducted into the design, construction, and field testing of possible seismic sources that excite preferentially the interface waves desired for use in such a system. The theory of elasticity shows that seismic interface waves have elliptical particle velocity orbits in the vertical plane along the path of propagation. It was therefore decided that to selectively excite the desired interface waves, a harmonic source employed at the interface must induce elliptical particle motion in this plane. Several exploratory sources were developed to produce this type of excitation. Field tests of the discrete-mode sources developed were conducted to evaluate this hypothesis, but due to the non-optimum nature of the experimental sources, perfect discrete source excitation was not obtained. However, it was found that the medium itself acted as a selective filter for the interface waves after a few tens of meters of propagation. The experimental results obtained here suggest that the basic concept of discrete-mode excitation looks promising.			
14. SUBJECT TERMS Seismo-acoustic sonar, seismic surface waves, Rayleigh waves, Scholte waves, buried ordnance detection, mine detection			15. NUMBER OF PAGES 195
16. PRICE CODE			
17. SECURITY CLASSIFICATION OF REPORT Unclassified	18. SECURITY CLASSIFICATION OF THIS PAGE Unclassified	19. SECURITY CLASSIFICATION OF ABSTRACT Unclassified	20. LIMITATION OF ABSTRACT UL

DUDLEY KNOX LIBRARY
NAVAL POSTGRADUATE SCHOOL
MONTEREY, CA 93943-5101

Approved for public release; distribution is unlimited.

**DISCRETE-MODE SOURCE DEVELOPMENT AND
TESTING FOR NEW SEISMO-ACOUSTIC SONAR**

Frederick E. Gaghan, Jr.
Lieutenant, United States Navy
B.S., Hartwick College, 1987

Submitted in partial fulfillment
of the requirements for the degree of

**MASTER OF SCIENCE IN PHYSICS
MASTER OF SCIENCE IN ENGINEERING ACOUSTICS**

from the

**NAVAL POSTGRADUATE SCHOOL
March 1998**

ABSTRACT

A seismo-acoustic sonar concept that uses guided interface waves (Rayleigh or Scholte) is being developed to detect buried ordnance in the sea floor and beach sediments. This thesis describes the initial research conducted into the design, construction, and field testing of possible seismic sources that excite preferentially the interface waves desired for use in such a system. The theory of elasticity shows that seismic interface waves have elliptical particle velocity orbits in the vertical plane along the path of propagation. It was therefore decided that to selectively excite the desired interface waves, a harmonic source employed at the interface must induce elliptical particle motion in this plane. Several exploratory sources were developed to produce this type of excitation. Field tests of the discrete-mode sources developed were conducted to evaluate this hypothesis, but due to the non-optimum nature of the experimental sources, perfect discrete source excitation was not obtained. However, it was found that the medium itself acted as a selective filter for the interface waves after a few tens of meters of propagation. The experimental results obtained here suggest that the basic concept of discrete-mode excitation looks promising.

TABLE OF CONTENTS

I.	INTRODUCTION	1
A.	RESEARCH OBJECTIVE	1
B.	RESEARCH MOTIVATION	2
C.	CURRENT AND EMERGING MINE WARFARE TECHNOLOGY	3
1.	Current Mine Warfare Technology	4
a.	<i>Shallow Water Mine Warfare Technology</i>	4
b.	<i>Land Warfare Technology</i>	4
2.	Emerging Mine Warfare Technology	6
D.	PROPAGATION MEDIUM CHARACTERISTICS	6
1.	Soil Characteristics	6
2.	Surf Zone Characteristics	7
E.	SEISMIC WAVE RESEARCH	7
II.	SEISMIC WAVE THEORY	9
A.	GENERAL SEISMOLOGY	9
1.	Body Waves	9
2.	Surface Waves	10
B.	RAYLEIGH WAVES	11
C.	SEISMIC WAVES	16
III.	PREVIOUS RESEARCH EFFORTS	21
A.	NAVAL POSTGRADUATE SCHOOL (NPS)	21
B.	ARL:UT	22
C.	COASTAL SYSTEMS STATION	23
D.	EXPERIMENTAL LIMITATIONS	24
IV.	DISCRETE-MODE SOURCE DEVELOPMENT AND TESTING (GROUND PHASE)	25
A.	DESIGN CRITERIA	25

B. CONCEPT SOURCE	26
1. Vibration Source	26
2. Ground Coupling Mechanism	27
3. Experimental Results	28
C. FIELD TEST SOURCE – MOD I	30
1. Vibration Source	30
2. Ground Coupling Mechanism	31
3. Experimental Results	32
D. FIELD TEST SOURCE – MOD II	34
1. Vibration Source	34
2. Ground Coupling Mechanism	37
3. Experimental Results	39
E. FIELD TEST SOURCE – MOD III	39
1. Ground Coupling Mechanism	40
2. Experimental Results	41
V. DISCRETE-MODE SOURCE DEVELOPMENT AND TESTING (BEACH PHASE)	45
A. FIELD TEST SOURCE – MOD IV	46
B. BACKGROUND NOISE AND GROUND TRUTHING EXPERIMENTS ..	47
1. Background Noise Analysis	48
2. Ground Truthing	48
C. DISCRETE-MODE EXCITATION	58
1. Propagation Characteristics	59
2. Selective Excitation	67
VI. CONCLUSIONS AND RECOMMENDATIONS	71
APPENDIX A. THEORETICAL PROPERTIES OF RAYLEIGH WAVES IN A HOMOGENEOUS, ISOTROPIC, ELASTIC HALF-SPACE	75
APPENDIX B. MANUFACTURER SPECIFICATIONS SHEETS	95
APPENDIX C. DISCRETE MODE SOURCE TECHNICAL DRAWINGS	105

APPENDIX D. TEST EQUIPMENT WIRING DIAGRAMS AND EXPERIMENTAL SETUPS	117
APPENDIX E. CONCEPT SOURCE EXPERIMENTAL RESULTS	139
APPENDIX F. AMBIENT BACKGROUND NOISE ANALYSIS	143
APPENDIX G. GROUND TRUTHING	147
APPENDIX H. DISCRETE-MODE ANALYSIS	159
LIST OF REFERENCES	179
INITIAL DISTRIBUTION LIST	181

ACKNOWLEDGMENT

The author would like to acknowledge the financial support of Dr. Jeffrey Simmen, Office of Naval Research, Code 321OA. This work was performed under Research Project No. 03201.

The author would also like to thank Professors Baker and Muir for their guidance and personal sacrifice during the course of performing this investigation. Last but not least I would like to thank my wife and children for persevering with the long hours and lost weekends, which allowed this thesis to come to fruition.

I. INTRODUCTION

The research described in this thesis is a continuation of work started at the Applied Research Laboratories of the University of Texas at Austin, sponsored by the Office of Naval Research, into the development of a seismo-acoustic sonar for the detection of buried ordnance using guided, seismic interface waves. Their research identified certain key issues requiring resolution prior to further concept development. The primary focus of the present research is to address and resolve some of these issues, specifically; the design, construction, and field testing of a discrete-mode excitation source for seismic interface waves.

This thesis contains six chapters dedicated to this purpose. The introduction describes the necessity and motivation for this research. It also includes a brief exposition on current and emerging mine warfare technology as it relates to buried ordnance detection. The second chapter provides an introduction into general seismology with a detailed description of interface waves and the characteristics that make them ideally suited for such an application. The third chapter describes the previous research efforts conducted in this and similar areas. The following two chapters contain the major portion of the information on the discrete-mode source development and the experimental results, through the ground and surf zone testing phases. The final chapter provides concluding remarks and recommendations for continuing research efforts, which should serve to further future project development.

A. RESEARCH OBJECTIVE

In November of 1996, during the Mine Warfare Symposium held at the Naval Postgraduate School in Monterey, California, the concept of a seismo-acoustic sonar for the detection of buried ordnance was introduced to the mine warfare community, and was based on the work conducted by the Applied Research Laboratories of the University of Texas at Austin (ARL:UT). [Ref. 1]

The main objective of the ARL:UT study was to demonstrate that an electro-mechanical transducer could be employed to excite seismic surface waves, of which there

are many types, but especially Rayleigh waves, which could be used to ensonify a buried mine-like target, and which in turn would produce seismic echoes that could be received, processed, and displayed. Due to the generally large contrast in density and elasticity between buried ordnance and the surrounding soil, the target produces seismo-acoustic echoes that travel in all directions, in all of the possible propagating modes allowed by the theory of elasticity [Ref. 1]. The experimental results of the study showed that the concept of a seismo-acoustic sonar for the detection of buried ordnance was scientifically feasible.

During the course of this first investigation into the use of a seismo-acoustic sonar for buried ordnance detection, certain key issues requiring resolution were identified. These issues need to be solved before the overall concept will have sufficient credibility to progress onto naval system development. These issues included [Ref. 1]:

- Development of sources for selective, or discrete-mode, excitation of seismic interface waves.
- Development of techniques for selective reception of seismic target echoes.
- Adaptive methods for excitation and reception of optimal modes.
- Measurement, analysis, and utilization of real mine target strengths.
- Incorporation of new discovered cetacean sonar protocols and signal physics.
- Re-examination of vector signal processing technology.

The purpose of the present research is to address and attempt to resolve some of these key issues, specifically, to initiate development of a discrete-mode source and to further refine the vector signal processing techniques. The results of this research should bring the concept of a seismo-acoustic sonar closer to field implementation.

B. RESEARCH MOTIVATION

Because of the series of events that transpired during the Persian Gulf War, a great deal of attention has been directed towards “main-streaming” mine warfare in the US military. The use of mines in the battlefield poses a serious threat to many different

military operations, and thus significantly impacts the United States' ability to execute its national security objectives. The tactical use of mine warfare directly influences the shape of the battlespace and may exclude our military forces from areas in which they are called upon to serve. In order to accomplish its military objectives, US forces need effective methods to detect and counter enemy mines. As Admiral Boorda stated in his 1995, white paper on mine warfare, "This warfare area must take its proper place among, as well as influence, future research and development, acquisition, and modernization plans and programs"[Ref. 2].

In terms of cost-effectiveness and operational and psychological impact, mines are perhaps the single most attractive weapons available for disrupting the battlespace. For the foreseeable future, we must expect increases in both the lethality and number of mines available. Therefore, more advanced technologies must be pursued to make the detection, classification, and removal of mines and other buried ordnance items quicker, safer, and more cost-effective.

C. CURRENT AND EMERGING MINE WARFARE TECHNOLOGY

At the present time (1998) there is no single method currently available that can detect buried mines in shallow water sediments, through the surf zone, onto the beach and beyond. All the varying buried mine amphibious countermeasure operations can be effectively grouped into either breaching for amphibious assaults or post conflict clearance operations. Breaching operations involve the construction of safe paths through a minefield during combat, while clearance operations deal with eliminating unexploded ordnance from large areas for occupation and use. Accurate detection and identification are essential for both types of operations. For combat breaching it is important to quickly know where the minefields are located and what their density is, while ordnance clearance operations need to deal with each and every mine, on a non-real-time basis.

1. Current Mine Warfare Technology

a) Shallow Water Mine Warfare Technology

From the high-water mark seaward Explosive Ordnance Disposal (EOD) divers, Naval Special Warfare (NSW) combat swimmers, Marine Corps reconnaissance swimmers, and the U.S. Navy marine mammals, plus a variety of towed sweep gear provide the bulk of the available shallow water mine countermeasure systems.

EOD and NSW personnel serve as an extremely effective neutralization component, but provide only minimal detection capability. Sonar and laser detection systems such as the Coastal Battlefield Reconnaissance and Analysis system (COBRA), the Remote Minehunting System (RMS), and the Airborne Laser Mine Detection System (ALMDS) are limited to detection of floating mines, shallow water moored mines, and exposed bottom mines. Of all the sonar and laser technologies currently employed for shallow water detection only one system is truly effective in the detection of buried mines, namely the marine mammals. Even though great strides have been made in increasing the effectiveness of marine mammal systems, search rates are low and the mammals have difficulty working in the surf zone or in warm water.

b) Land Warfare Technology

From the high-water mark landward, the currently employed breaching and clearance technologies revolve around hand-held probes, metal detectors, ground penetrating radar, trained dogs, and mechanical breaching equipment. Each of these methods has its unique advantages and disadvantages, but they are in general slow, costly, labor intensive, and not optimal for combat operations.

Manual mine countermeasures provide the most reliable and consistent method of ordnance location, classification, and identification. But manual mine clearance is slow and dangerous, with an injury rate of nearly one technician every 1,000 mines cleared [Ref. 3].

“Metal detectors” are only capable of detecting ordnance containing ferrous components. They are generally difficult to successfully operate because they have high false alarm rates. The accuracy of these systems to detect, locate, and analyze target returns is based on operator judgment and experience. The high false alarm rates associated with these systems is usually due to the high ferromagnetic soil content in battlefield areas, as well as by the presence of man made ferromagnetic false targets such as hubcaps, tea pots, etc. [Ref. 4]

Ground penetrating radar incorporates the same general technology as conventional radar, but on a much smaller scale. Ground penetrating radar systems fall into four main categories: common short pulse systems, video pulse systems, synthetic aperture pulse radar, and frequency modulated-continuous wave radar [Ref. 4]. They all use the propagation of electromagnetic energy into the soil for target detection and localization. Subsurface sensing radars rely on the strength of the electromagnetic signal reflected from the target. The strength of the reflected signal is highly dependent on target distance, composition, and orientation, in addition to soil characteristics such as layering, presence of boulders, etc. High resolution ground penetrating radar systems usually operate in the frequency range of 30 MHz to 2 GHz , which implies short operating ranges due to the high attenuation of electromagnetic energy in the ground at these frequencies. They also suffer from high false alarm rates.

Trained dogs provide a high degree of detection capability without the requirement for prior visual location. Most explosive sniffing dogs are trained to identify only one or two types of explosives; thus a whole squad of dogs would be needed to detect all the possible explosives types used in just landmines alone. Additionally, the amount of time required to train a dog for buried ordnance detection is extremely high, while search rates are low because the dogs get tired and detection capability is reliable only over very short ranges.

Lastly, breaching equipment is the brute force method of land mine countermeasures. The use of breaching equipment is the most expedient, but of the low-end types of available breaching equipment, rollers rarely achieve more than 70% clearance effectiveness and rotary flails or blades less than 80%. Explosive net breaching

whereby a “fish net” containing shaped charges is rocket fired over an area is more effective, but much more expensive.

Although these current methods offer the greatest assurance that an area is safe for use, they are also quite dangerous because they put the operator in close proximity to the ordnance.

2. Emerging Mine Warfare Technology

Emerging technologies with application to detection and clearance can be grouped into the following categories: infrared, microwave, photon (laser linescan) backscatter, nuclear or thermal neutron analysis, passive optical imaging, and “new” acoustic and seismic technologies. Many of these approaches suffer from large power and high data processing requirements, and their effectiveness is highly dependent on the propagation characteristics of the medium.

D. PROPAGATION MEDIUM CHARACTERISTICS

To realistically address the issue of buried mine detection in the surf zone and on land, much emphasis must be placed on understanding the characteristics of the media in which the mine detection system must operate. Depth of signal penetration, resolution characteristics, detection capability, and other system parameters are all highly dependent upon the medium of propagation. These conditions will usually vary from location to location and from season to season.

1. Soil Characteristics

In general, the earth’s boundary layers consist of a variety of minerals, rocks, organic and inorganic compounds, water, and air. The amount of organic materials present is specific to particular areas and geographical regions, but most organic materials significant to mine warfare are only present in the first few meters of the upper sediment layer, and decrease with increasing depth. Changes in the water content result

in changes of the dielectric and conduction characteristics of the medium. All these varying conditions have significant effects on the propagation of electromagnetic and acoustic waves. [Ref. 4]

Nominally, low frequency electromagnetic waves are less attenuated and result in increased depths of penetration. Higher frequency electromagnetic signals are attenuated more, but provide better resolution characteristics. Acoustic energy is less attenuated than electromagnetic energy in high moisture and densely compacted soil environments.

2. Surf Zone Characteristics

In offshore sediments and in the surf zone, the affect of the water and sediment interfaces on energy propagation are quite pronounced. Optical techniques have been developed to penetrate the water interface, but cannot penetrate the underlying sediment, so are essentially useless in buried ordnance detection. Magnetic techniques are also limited because of their low resolution qualities, short operating ranges, and the increased use of non-magnetic mines. Radar systems are ineffective in the surf zone because of the extremely high attenuation suffered by electromagnetic energy in seawater, penetrating no more than the first meter into the water. Acoustic sonar systems are capable of penetrating both the water and sediment boundaries, but in the surf zone extensive clouds of micro bubbles generated by wave action scatter and attenuate most of the acoustic energy. The energy which is left can penetrate the sediments, but is limited by Snell's Law, which establishes a "critical grazing angle", below which sound is totally reflected within the water column and does not penetrate the sediments. [Ref. 5]

E. SEISMIC WAVE RESEARCH

With the limitations imposed by the operating environment to current buried ordnance detection systems, it was obvious that another method of energy propagation must be identified that could more effectively utilize the soil and sediments as a propagating medium. With this in mind, it became necessary to extend research efforts to incorporate seismic wave techniques. Seismic surface waves also propagate along both

water/sediment and air/sediment interfaces and can be easily excited in the environments of primary interest for buried mine detection systems. Because of their propagating characteristics, the use of seismic interface waves can provide a safe minimum standoff distance between the operator and the ordnance.

There are no systems currently available today that can detect buried mines on land and in the surf zone. It is clear that development of such a system would help to provide the military with the kind of system needed to make the transitions to the shore, implied in such documents like "...From the Sea", physically realizable. The benefits to other operations, such as, humanitarian demining could also be significant.

The most common types of seismic waves are those generated by earthquakes, which travel both through the body of the earth and along its surface. Seismic waves have also been used extensively in geological prospecting for oil and mineral deposits. The next chapter contains an overview of seismic wave theory and specific information on interface waves and their application to buried ordnance detection.

II. SEISMIC WAVE THEORY

This chapter contains a description of the types of seismic waves that propagate through an elastic medium and along its surface. Within this cornucopia of wave types exist a category of boundary waves known as Rayleigh and Scholte waves. The general characteristics exhibited by these waves that make them of practical use in buried ordnance detection systems will be explored as well as their relation to the other seismic waves.

A. GENERAL SEISMOLOGY

When one studies the general theory of elasticity, two types of mechanical waves can be found to propagate in an unbounded, infinite, homogeneous, elastic medium. These waves, one compressional and one shear, are called body waves since they travel within the body of the propagating medium. In 1885, the English scientist, Lord Rayleigh (J.W. Strutt) [Ref. 6] demonstrated theoretically that there exist waves that can propagate over the planar interface between a semi-infinite elastic half-space and a rarefied gas. These waves later came to be known as Rayleigh waves. Further research lead to the discovery of many other boundary waves. Seismic waves can be grouped into one of the following two categories: body waves and surface waves.

1. Body Waves

There are two types of body waves. The first and fastest propagating wave is called the Primary wave or P-wave. A P-wave is a compressional wave, in which the wave motion alternately compresses and dilates the medium. The particles of the medium undergo displacements in a direction co-linear with the direction of propagation; hence the P-wave is also called the longitudinal wave. P-waves can travel through both solid rock and liquid materials with a (longitudinal) propagation speed given by

$$c_p^2 = \frac{B + \frac{4}{3}\mu}{\rho}, \quad (2.1)$$

where B is the adiabatic bulk modulus, μ the shear modulus, and ρ the density of the medium.

The second, and slower, body wave is called the Secondary wave or S-wave. S-waves are shear waves, in that, as an S-wave propagates it shears the medium at right angles to the direction of propagation. Due to the fact that liquids do not support finite shear stresses, S-waves cannot propagate in liquids. S-waves travel with a speed given by

$$c_s^2 = \frac{\mu}{\rho}. \quad (2.2)$$

In general, when an external force deforms a solid, both P-waves and S-waves will normally be produced. When a wave of either type interacts with an interface boundary, reflected waves of both types can be produced.

2. Surface Waves

When a solid has a fluid surface (air or water), or when there is an interface boundary between two media or between layers of a single medium, surface waves are normally present. Surface waves are somewhat similar to gravitational ocean waves for which most of the wave motion is located near the surface and decays exponentially with increasing distance into both the elastic substrate and the overlying fluid, although the mechanisms are different.

Surface waves can also be divided into many types. One type of surface wave, which propagates in the duct between two sedimentary boundaries, is called a Love wave. Love waves induce side-to-side particle motion in a horizontal plane, but at right angles to the direction of propagation. A second type and more prevalent surface wave is the Rayleigh wave. Rayleigh waves, which occur at the planar interface between a semi-infinite elastic half-space and a gas, have both vertical and horizontal particle motion in a vertical plane oriented along the direction of propagation. Rayleigh waves propagate with a phase velocity slightly less than the bulk shear wave velocity in the elastic medium. Another type of boundary wave, analogous to the Rayleigh wave, is the Scholte wave, which occurs at the interface between a liquid and an elastic half-space such as the seafloor. Scholte waves are characterized by a phase velocity that is also slightly slower

than the shear wave speed in the solid. Essentially, Rayleigh and Scholte waves are very similar, the only difference being that the liquid media component of Scholte waves is more pronounced than the gas media component of Rayleigh waves. The interface wave that propagates along the boundary created by two elastic half-spaces is called a Stoneley wave. Stoneley waves travel with a velocity that is slower than the shear wave velocity in either media.

B. RAYLEIGH WAVES

In an isotropic solid the stress-strain relations have the following form

$$\begin{aligned}\sigma_{xx} &= \lambda\theta + 2\mu\varepsilon_{xx}, & \sigma_{yy} &= \lambda\theta + 2\mu\varepsilon_{yy}, & \sigma_{zz} &= \lambda\theta + 2\mu\varepsilon_{zz} \\ \sigma_{xy} &= \mu\varepsilon_{xy}, & \sigma_{yz} &= \mu\varepsilon_{yz}, & \sigma_{zx} &= \mu\varepsilon_{zx}\end{aligned}\quad (2.3)$$

where λ and μ are the Lame constants, θ the dilatation, or volume strain, and σ_{ij} and ε_{ij} are the stress and strain, respectively, where i denotes the direction of the stress or strain and j defines the plane over which it is applied. Using the elastic relations from (2.3), the equations of motion for an isotropic solid (neglecting body forces) can be written as

$$\rho \frac{\partial^2 \vec{u}}{\partial t^2} = (\lambda + \mu) \nabla \theta + \mu \nabla^2 \vec{u}, \quad (2.4)$$

where \vec{u} represents the particle displacement and ρ the density of the medium [Ref. 7]. These equations of motion can be shown to lead to the propagation of the two types of body waves with phase velocities given by (2.1) and (2.2).

If we consider the propagation of a plane wave through an elastic medium with a free boundary, such that the boundary is free from stress, we are lead to the wave equations

$$\frac{\partial^2 \phi}{\partial t^2} = c_l^2 \nabla^2 \phi, \quad \frac{\partial^2 \psi}{\partial t^2} = c_s^2 \nabla^2 \psi, \quad (2.5)$$

where the potentials ϕ and ψ were introduced to separate the effects of compression and rotation in the medium [Ref. 7]. The simultaneous solution of (2.5) for a disturbance that is localized at the boundary and decays with increasing depth requires that the following relation be satisfied

$$\kappa^6 - 8\kappa^4 + (24 - 16\gamma^2)\kappa^2 + (16\gamma^2 - 16) = 0. \quad (2.6)$$

This relation is known as the Rayleigh equation, where κ is the ratio of the Rayleigh wave speed to the shear wave speed, normally 0.9, and γ^2 is the ratio of the shear wave speed to the longitudinal wave speed. γ^2 can also be expressed solely in terms of the Poisson's ratio, namely

$$\gamma^2 = \frac{c_s}{c_l} = \frac{\mu}{\lambda + 2\mu} = \frac{1 - 2\nu}{2 - 2\nu}, \quad (2.7)$$

where ν is the Poisson's ratio. Thus, to solve the Rayleigh equation, which is cubic in κ^2 , requires that only the Poisson's ratio for the propagating medium be known. Therefore the Rayleigh wave speed in an infinite isotropic solid is independent of frequency and depends only on the elastic constants of the medium. The Rayleigh wave corresponds to the root of the Rayleigh equation that lies in the (real) interval (0,1). It can be shown that for values of the Poisson's ratio in the range 0 - 0.5 the Rayleigh equation has one and only one such root. Hence Rayleigh waves (R-waves) traveling at the boundary of an isotropic, homogeneous medium are dispersionless. [Ref. 7,8]

Figure 2.1 shows the variation in the wave speed ratios as a function of the Poisson's ratio for an isotropic, homogeneous solid substrate. From the figure we can see that Rayleigh waves propagate at almost the same speed as shear waves, varying from

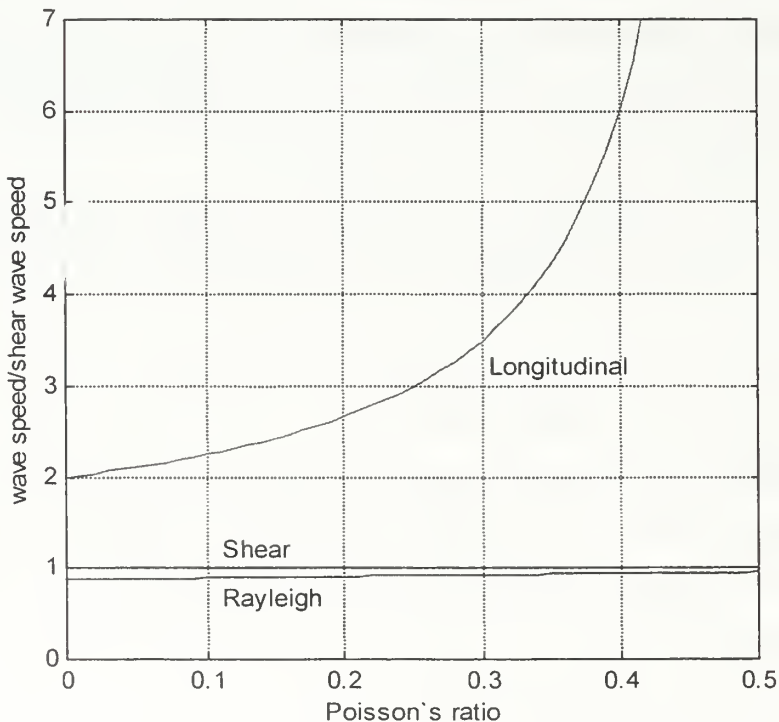


Figure 2.1. Variation in Wave Speed Ratios as a Function of Poisson's Ratio

approximately 0.87 to 0.96 of the shear wave speed. Appendix A1 contains the MATLAB code used to generate Figure 2.1 and Appendix A2, the code used to evaluate just the Rayleigh wave speed ratio as a function of the Poisson's ratio.

Rayleigh waves can be visualized as the superposition of two waves, one longitudinal and one transverse, which propagate along the boundary of an elastic half-space. The particle motion associated with a Rayleigh wave is normally elliptical in nature, with the semi-major axis of the ellipse perpendicular to the boundary and the semi-minor axis parallel to the direction of propagation, depending on the boundary conditions. As Figure 2.2 illustrates the particle motion at the surface is retrograde elliptical, but shifts to prograde at a finite depth. The shift in particle rotation occurs at a depth of approximately $0.2\lambda_r$, for solids, and approximately $0.1\lambda_r$, for real sediments, where λ_r is the Rayleigh wavelength [Ref. 8,9].

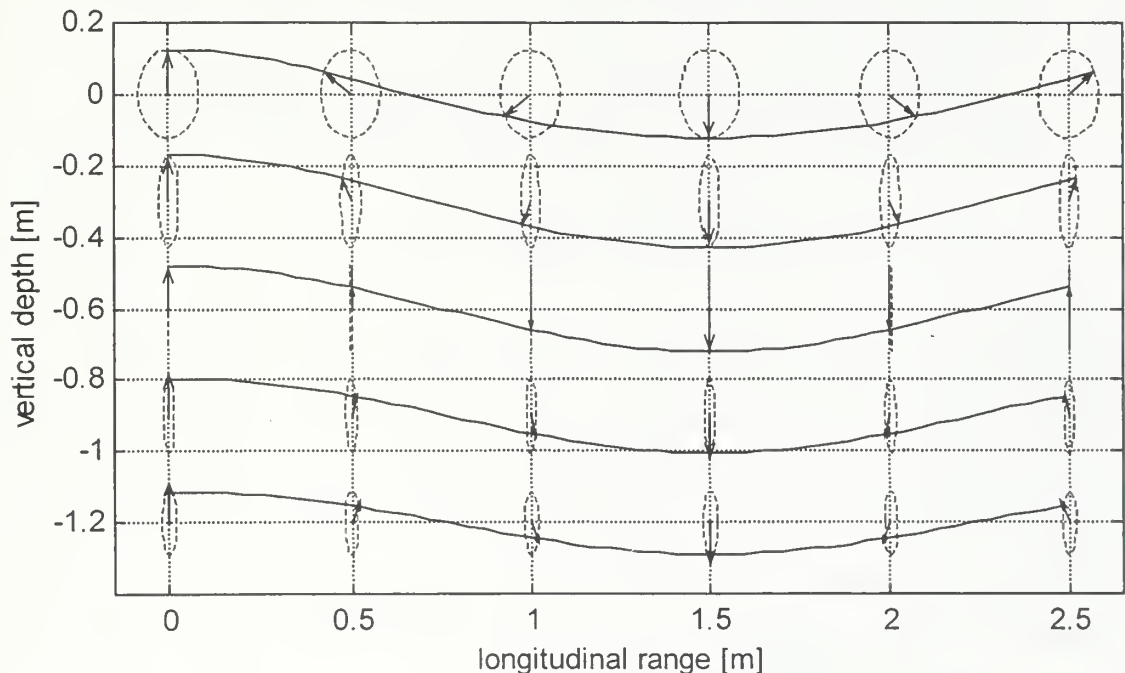


Figure 2.2. Elliptical Particle Motion Induced by Rayleigh Wave

Figure 2.3 displays the variation in the ratio of the longitudinal to vertical particle displacements for Rayleigh waves at the surface of an homogeneous, isotropic solid, as a

function of the Poisson's ratio, while Figure 2.4 depicts how the particle displacements vary with depth.

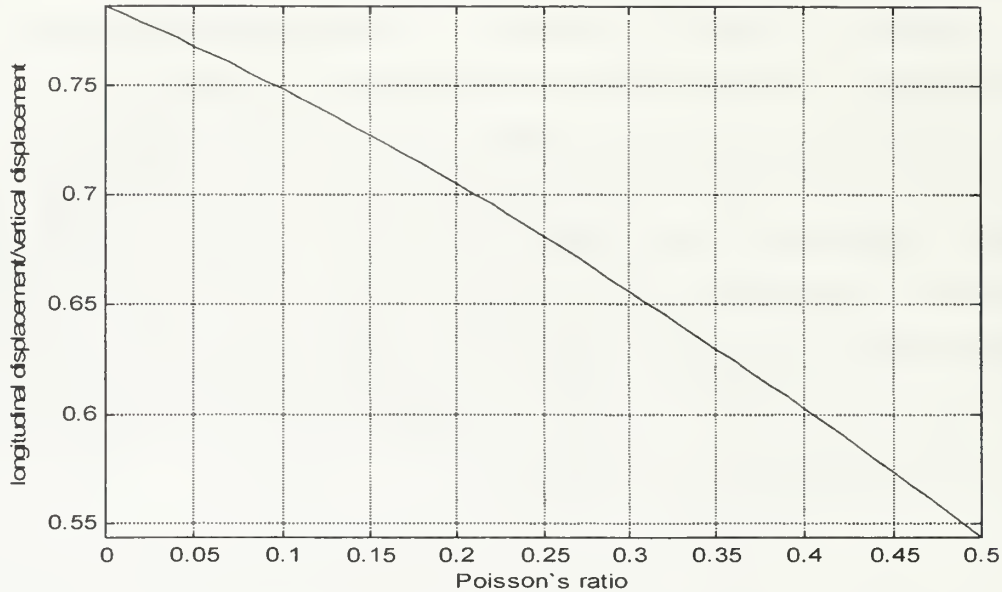


Figure 2.3. Ratio of Longitudinal to Vertical Particle Displacements

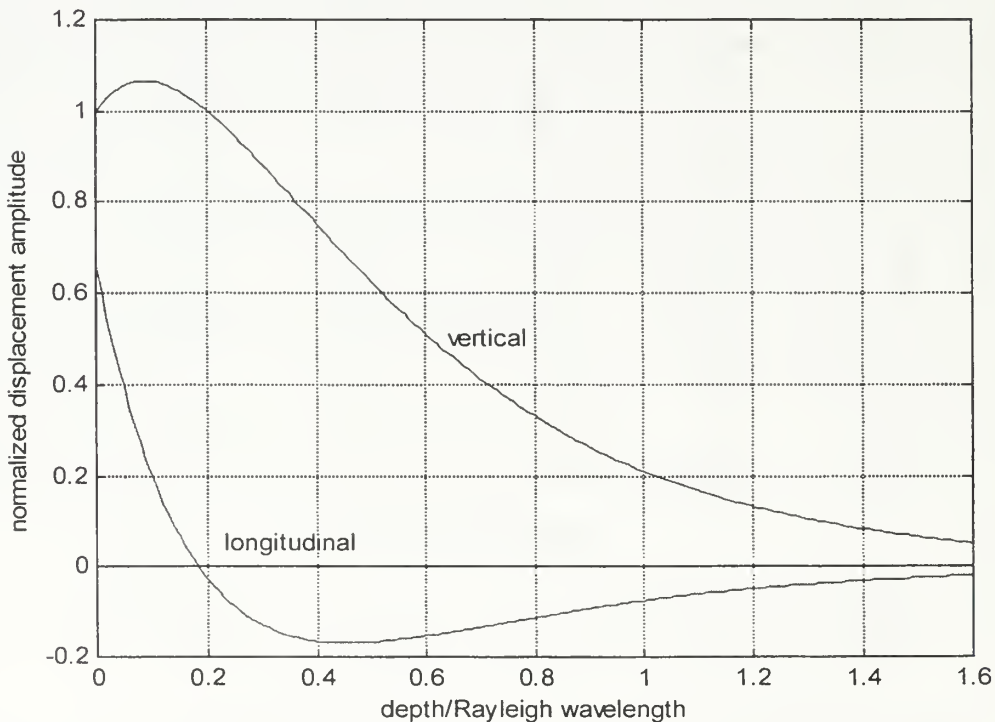


Figure 2.4. Variation of Longitudinal and Vertical Particle Displacements
(normalized by the surface vertical particle displacement)

Figure 2.5 shows the variation in the stress components that occur with depth for the same isotropic conditions.

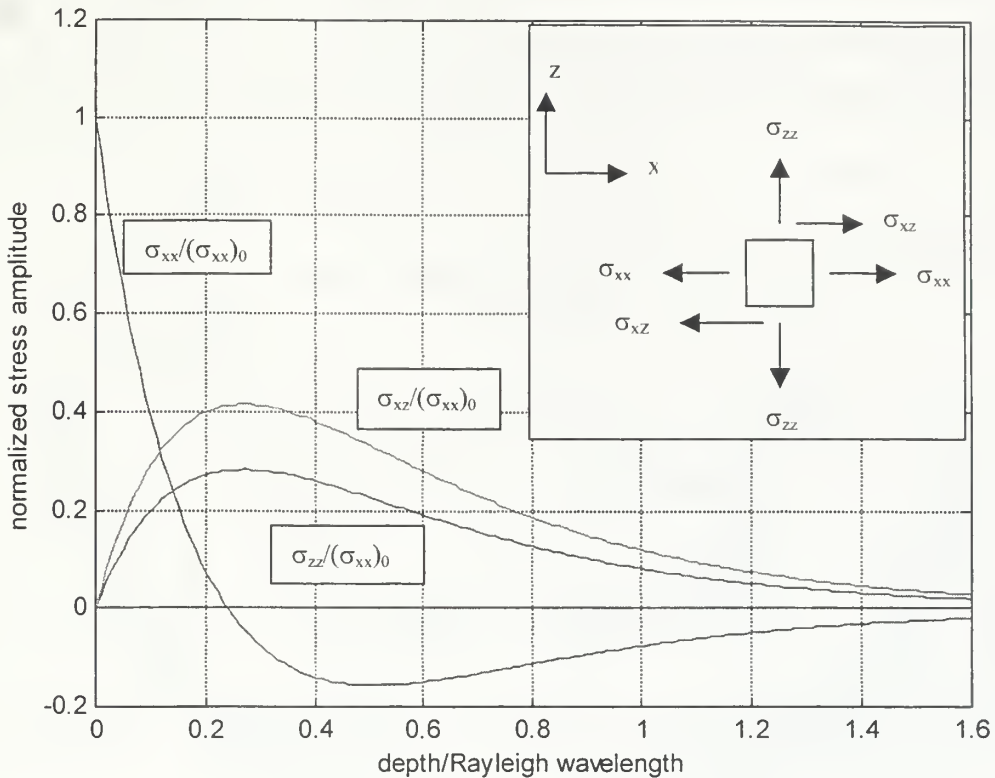


Figure 2.5. Tensile and Shear Stresses

From Figure 2.4 we can see that the vertical displacement first increases and reaches its maximum at approximately $0.1\lambda_r$, then exponentially decreases with depth. The longitudinal displacement decreases with depth from the outset and changes direction at approximately $0.2\lambda_r$, reaching a secondary maximum at $0.5\lambda_r$. From Figure 2.5 one can see that the tensile stress along the direction of propagation also changes direction at approximately $0.25\lambda_r$, and the other stress components reach their maximums at $0.3\lambda_r$, then all exponentially decay with depth. These sets of curves serve to show the localization of the Rayleigh wave to a layer approximately two wavelengths thick under isotropic conditions.

Appendices A3-A6 contains the MATLAB code used to generate Figures 2.2-2.5, respectively. Additional insight into Rayleigh wave behavior is contained in the computer codes and figures making up the rest of Appendix A.

C. SEISMIC WAVES

From the literature [Ref. 6,7,10], where solutions to the elastic wave equations have been obtained, we can form an idealized picture, as shown in Figure 2.6, of the wave system created by a vertical point impulse at the surface of an ideal, isotropic,

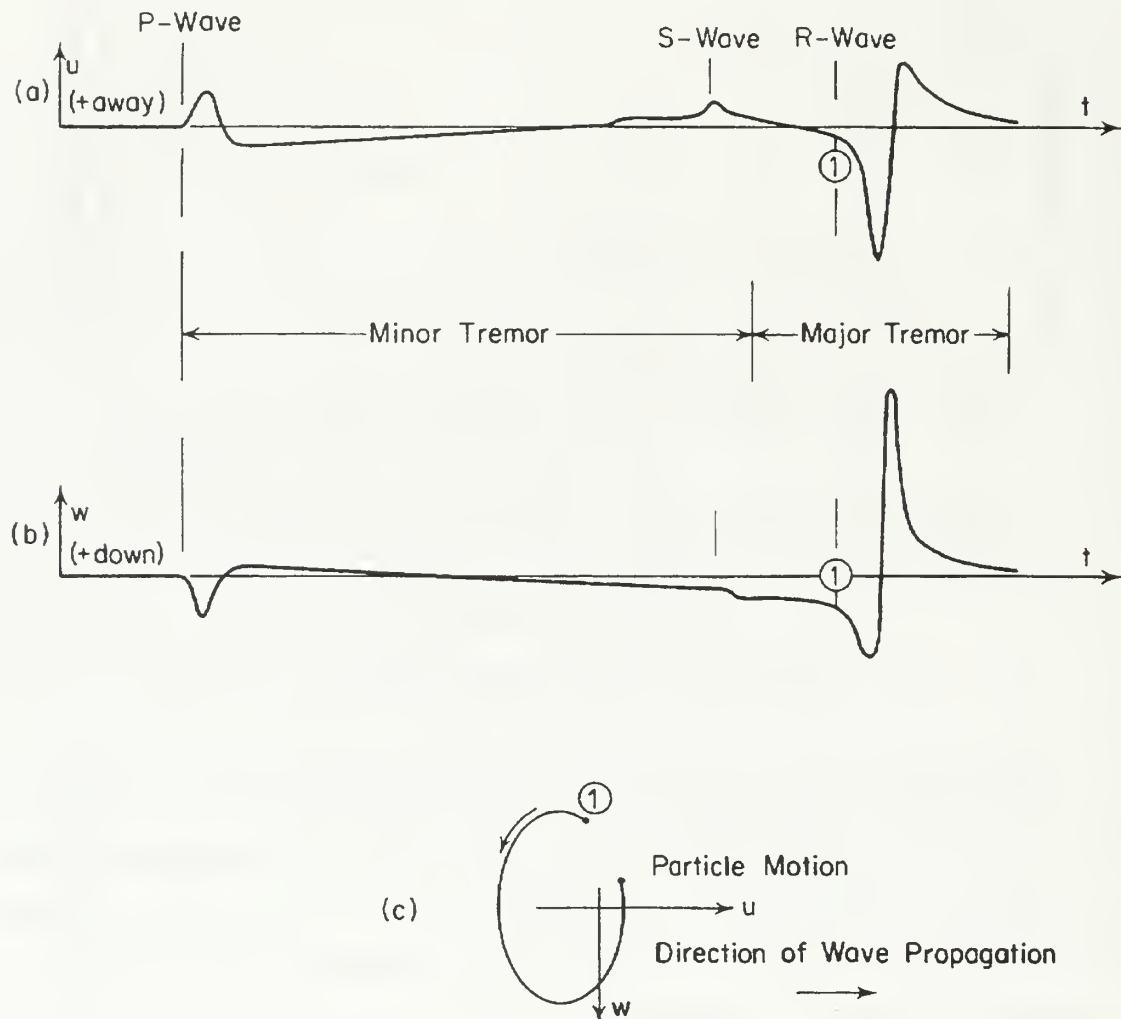
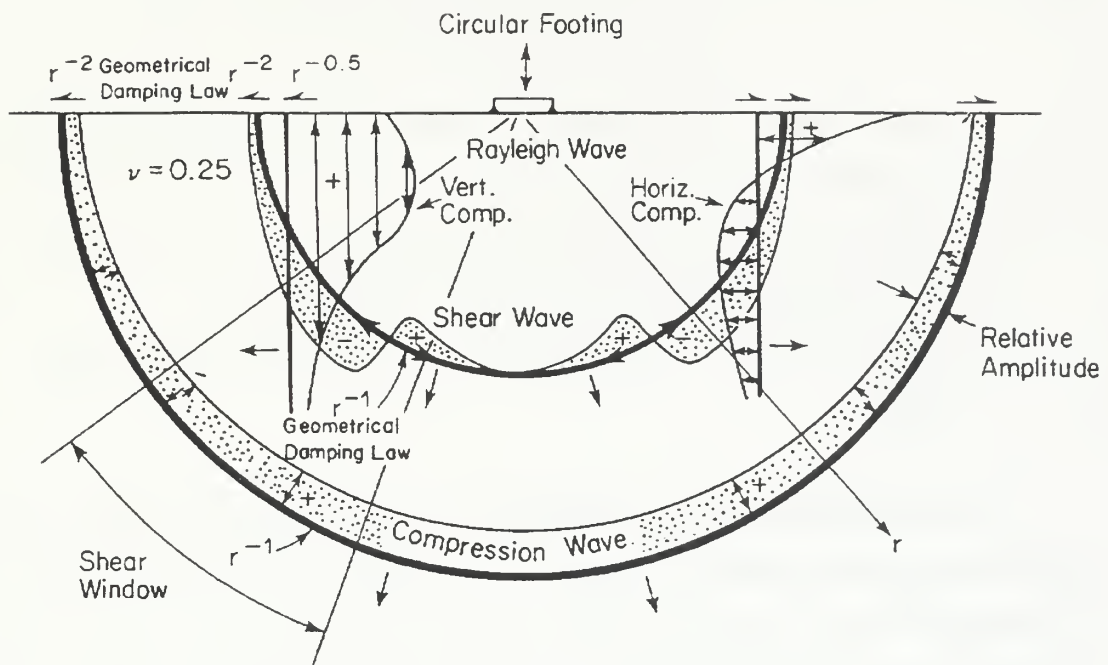


Figure 2.6. Wave System from Vertical Point Impulse [Ref. 10]

substrate medium. From the figure we can see that the wave system is composed of three major events corresponding chronologically to the arrivals of the P-wave, bulk S-wave, and R-wave. Thus a particle at the surface will first be displaced by the P-wave, then by the bulk S-wave, followed by a much larger oscillation due to the passing

Rayleigh wave. This illustrates that the Rayleigh wave is the most significant disturbance along the surface of an isotropic half-space, and at large distances from the source may be the only clearly distinguishable wave. [Ref. 10]

For a disturbance in the form of a circular footing undergoing vertical oscillations at the surface of an isotropic, elastic half-space the basic features of the wave field far away from the source are shown in Figure 2.7 [Ref. 10].



Wave Type	Per Cent of Total Energy
Rayleigh	67
Shear	26
Compression	7

Figure 2.7. Wave Field from a Circular Footing

The two body waves propagate radially outward from the source along a hemispherical wavefront. The decrease in the amplitudes of the body waves within the medium is proportional to $1/r$, where r is the radial distance from the source, while along the surface

of the half-space the far-field amplitudes decrease as $1/r^2$. Rayleigh waves, on the other hand, propagate radially outward with a cylindrical wavefront and experience a far-field amplitude decrease that is proportional to $1/\sqrt{r}$. For a vertically oscillating point source at the surface of an isotropic, elastic half-space, it was determined that the distribution of input energy among the three wave types is 67% Rayleigh wave, 26% shear wave, and 7% compressional wave. [Ref. 10]

From this brief exposition on seismic wave fundamentals, the features that make Rayleigh waves unique (in an isotropic half-space) are that they are:

- Dispersionless, thus propagate with a phase velocity that is independent of frequency.
- Localized within a layer that is approximately two wavelengths deep.
- The most significant disturbance along a surface boundary.
- Easy to excite, with a particle motion that is retrograde elliptical at the surface.

It is these features that make Rayleigh waves ideal for buried ordnance detection in the earth and along the beach. Scholte waves exhibit the same general characteristics as Rayleigh waves, the major difference being that Scholte waves occur along the interface between a liquid and an elastic half-space, thus making them ideally suited for surf zone applications.

It should be remarked that in natural soil, beach, or seafloor sediments, the overburden weight of the surface sediments causes the shear modulus to increase with increasing depth. This means that the shear velocity increases with depth and that, in turn, means we have a condition requiring dispersion. This occurs because the lower frequency, long wavelength waves naturally propagate at deeper depths in the sediment, where the shear velocity is greater. Thus, low frequency, long wavelength signals propagate faster than high frequency, short wavelength signals.

If an electromechanical source could be built that could selectively excite Rayleigh waves, more of the energy used in signal generation could be put on target, and less of the projected energy would exist to create unwanted reverberation carried in non-

Rayleigh wave modes. However, at the target, even pure Rayleigh waves get distributed into other non-Rayleigh modes. With the addition of special signal processing techniques that exploit the known features of Rayleigh waves from target echoes, we could capitalize on discrete-mode sonar methods. The next chapter discusses the previous research efforts made in buried ordnance detection using seismic waves and the experimental limitations imposed by the systems used.

III. PREVIOUS RESEARCH EFFORTS

This chapter briefly reviews two previous research projects that explored the propagation of energy along an air/sediment interface to detect buried objects. The first project was an experiment conducted at the Naval Postgraduate School, investigating the applicability of array theory to target localization. The second project, done at the Applied Research Laboratories of the University of Texas at Austin (ARL:UT), for which this thesis is a direct continuation, developed the theory and signal processing techniques for the first phase of the seismo-acoustic sonar system. Other significant prior research consists of the dry-land experimental work done at the firm of Bolt, Beranek, and Newman (BBN) and theoretical work done at the Coastal Systems Station. These works will be cited subsequently.

A. NAVAL POSTGRADUATE SCHOOL (NPS)

In 1995, NPS student LT William Stewart conducted research into the feasibility of using a phased array to generate surface waves to detect buried ordnance [Ref.11]. His research was the continuation of a study conducted by BBN Systems and Technology from 1987 to 1992 [Ref. 12]. The source utilized in the NPS study was a four-inch, large cone excursion, electrodynamic speaker, whose frequency response for the radiation of sound was relatively constant over the range 50 – 7000 Hz. The speaker cone was modified by bonding to it a 25-gram mass, cone-tipped plunger, which was used to improve ground coupling. See Figure 3.1.

Three single-axis seismometers were used as ground vibration receivers. Testing was conducted in a twelve-foot diameter, four-foot deep redwood tank filled with approximately 17 tons of medium grain sand. With a single source and the three receivers, LT Stewart was able to successfully demonstrate target localization using surface waves. Though no data was reported on the results for target localization using a phased array, his study did show that beamforming with a three element linear array of surface sources was possible. [Ref. 11]

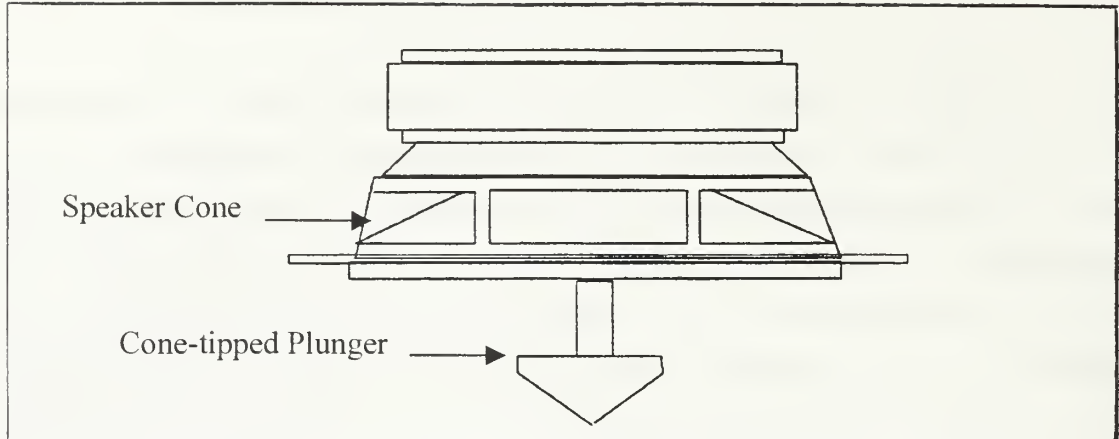


Figure 3.1. NPS Source Design

B. ARL:UT

An investigation into the use of Rayleigh waves for buried ordnance detection was conducted by ARL:UT on the beach of Mustang Island, near Corpus Christi, Texas, in 1996 [Ref. 1]. Their experimental setup consisted of a source which employed a six-inch by eight-inch exciter foot, from which protruded 43, $\frac{3}{4}$ -inch nails and a receiving array composed of three seismometers, as shown in Figure 3.2.

Their raw, field recorded data did not show the target. But with the use some sophisticated vector signal processing techniques and some coherent subtraction methods, operating on the reverberation, the target was detected at its appropriate range and bearing. A seismo-acoustic detection model for elastic targets buried in elastic sediments was also developed to support the measurements [Ref. 13].

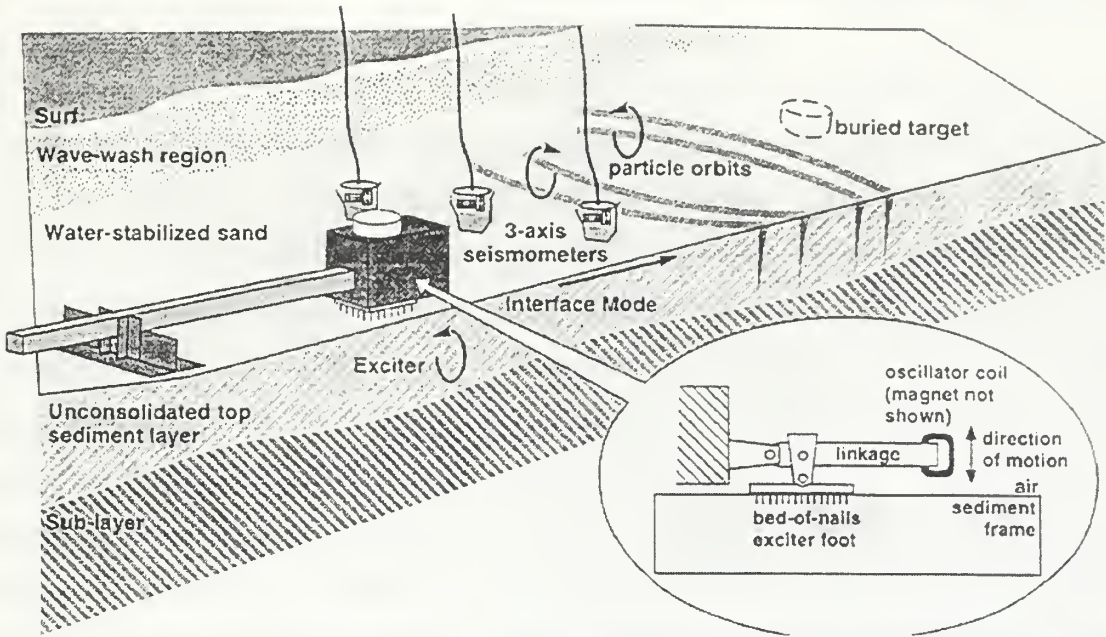


Figure 3.2. ARL:UT Seismic Sonar Experiment

C. COASTAL SYSTEMS STATION

Some of the benchmark research efforts recently produced by the laboratories of the Coastal Systems Station concern the theoretical solutions and numerical modeling of acoustic wave scattering from elastic objects buried in underwater sediments and plane-stratified poroelastic media [Ref. 14,15]. Objects located in fluid mediums produce resonant scattering behaviors. These same objects when buried in ocean sediments display a resonant scattering behavior which is modified by the proximity to interfaces, sediment attenuation, and sediment loading, thus information obtained from the scattering field can be used for identification as well as detection. Further experimental verification of these solutions could have significant impact on the capabilities of seismo-acoustic sonar systems.

D. EXPERIMENTAL LIMITATIONS

What is common to the aforementioned experiments is the use of vertical source excitation, which generates not only Rayleigh waves, but also undesired P- and S-waves. Thus, the Rayleigh wave signals of interest were contaminated by body wave signals. To satisfactorily localize the target, in the ARL:UT experiments, this unwanted reverberation had to be removed during the signal processing by coherent subtraction of the reverberant background field in the absence of the target from the field with the target present. Vector signal processing was also used for the first time, in the ARL:UT experiments, to bring the target echoes above the reverberation. This technique capitalizes on the known, 90-degree phase difference between vertical and horizontal components in propagating Rayleigh waves. But since coherent subtraction is not a feasible signal processing option in a operationally fielded system, another solution must be identified. The research team at ARL:UT theorized that considerable reverberation suppression could be achieved by utilizing an excitation source that could selectively excite Rayleigh waves [Ref. 1]. They also experimented with a two-degree of freedom source, which preferentially excited Rayleigh waves that propagated to tens of meters in range. Unfortunately, this source produced a signal too long in time duration for sonar application.

The use of ultrasonic Rayleigh waves in non-destructive testing is a well-documented science, but selective excitation of low frequency Rayleigh waves in terrestrial media has not been previously attempted. The remainder of this thesis describes the development and testing of a discrete-mode, electromechanical, Rayleigh wave source for a seismo-acoustic sonar.

IV. DISCRETE-MODE SOURCE DEVELOPMENT AND TESTING (GROUND PHASE)

This chapter documents the initial design, construction, and testing of the first four generations of the discrete-mode, Rayleigh wave source. The associated experimentation involved testing in both a laboratory environment and various field environments. This portion of the research, known as the Ground Phase, was used for proof-of-concept testing and qualitative determination of the relations between input signal parameters and the resulting surface wave field.

A. DESIGN CRITERIA

The first step in constructing a discrete-mode, electromechanical, Rayleigh wave source for a seismo-acoustic sonar system was to establish a set of guiding design criteria. Based on the known features of Rayleigh waves and the previous research work completed, it was decided that minimum requirements that a source needed to meet were that it:

- Have sufficient degrees of freedom (2) to drive the ground in elliptical orbits.
- Have good ground coupling in both the horizontal and vertical directions.
- Generate Rayleigh waves with sufficient amplitudes to allow detection at a range of at least 10 m.
- Provide a repeatable waveform capable of high repetition rates over long periods of time.
- Be able to operate over a range of low frequencies in the 20 – 200 Hz band.

The most important of these requirements is that the transducer oscillate the ground in elliptical orbits, so that as much as possible of the input energy be converted to discretely excite Rayleigh waves.

All seismic transducers consist of two basic components: a vibration source and a source-to-ground coupling mechanism. The vibration source transfers the input electrical

energy into output mechanical energy. The source-to-ground coupling mechanism provides the means by which the output mechanical energy is transmitted into the propagating medium. A constraint on the source design was that the ground coupling mechanism be as light weight as possible, while at the same time being as stiff as possible. This was desired so most of the mechanical force generated by the source would be used to move the ground and not just the source.

B. CONCEPT SOURCE

With the design criteria established for a suitable source, the next step was to design and construct laboratory prototypes that could be tested to examine the effects of varying source parameters such as frequency and driving voltage, on the resulting surface wave field. This was deemed a necessary first step because the results obtained would help in selecting an appropriate vibration source and designing the ground coupling mechanism for a field test source. It was decided to construct the concept source out of on-hand laboratory equipment and to conduct the required testing in the twelve-foot diameter, four-foot deep redwood, sand filled tank used in the previous NPS experiment.

1. Vibration Source

The Model F5B Electromagnetic Shaker (or Mini-Shaker for short) produced by Wilcoxon Research was chosen as the vibration source for proof-of-concept testing. The Mini-Shaker is an electrically driven force generator, with a constant (blocked) force output of 0.2 lbs (0.89 N) over the frequency range of 100 – 1000 Hz (See Appendix B1 for manufacturer specifications). The design configuration of the Mini-Shaker allows it to be stud-mounted in any position without external support or shaft alignment considerations.

2. Ground Coupling Mechanism

The source-to-ground coupling mechanism, as shown in Figure 4.1, was constructed from two pieces of aluminum. Aluminum was chosen because of its high tensile strength and low mass. Appendix C1 contains the actual design drawings.

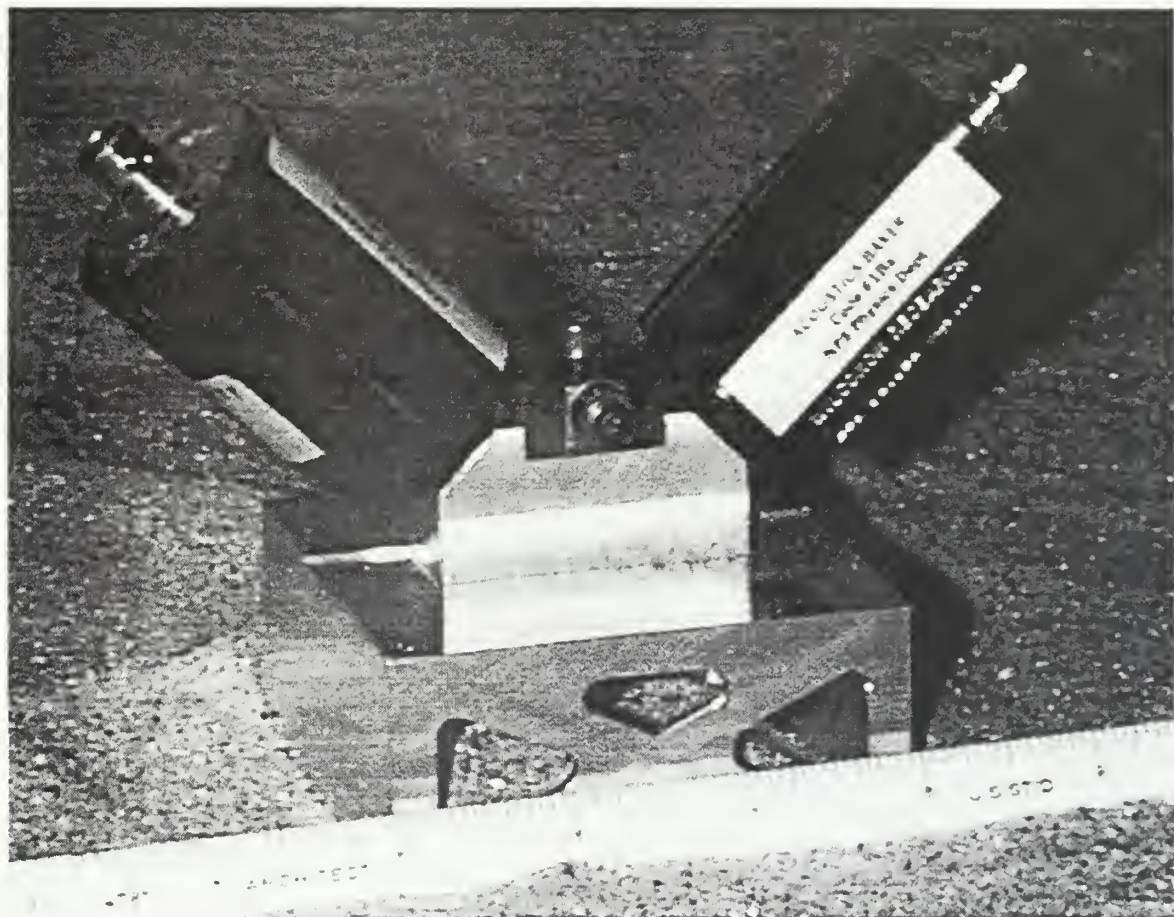


Figure 4.1. Picture of Concept Rayleigh Wave Source (scale in inches)

The bottom piece was constructed from a hollowed out aluminum block. When buried in the sand, the inside surfaces of the block provide the required vertical and horizontal coupling to the medium. The top piece was manufactured to hold two Mini-Shakers and a tri-axial accelerometer (Accelerometer specifications contained in Appendix B2). Mounting studs were placed in the top piece so as to align the Mini-Shakers at a 45 degree angle with the horizontal surface plane of the sand. This specific

placement of the Mini-Shakers was chosen so that any two-dimensional oscillatory motion could be excited by individually controlling the phase and amplitude of each shaker.

3. Experimental Results

The test equipment setup as described in Appendix D1 was used for the concept source testing. The source and seismometer receivers were positioned in the test tank as shown in Figure 4.2 and Appendix D1. This setup allowed for the greatest separation between the source and the tank wall and the farthest receiver and the tank wall. The seismometers were tri-axial, moving coil geophones, which measure the velocity of ground movement.

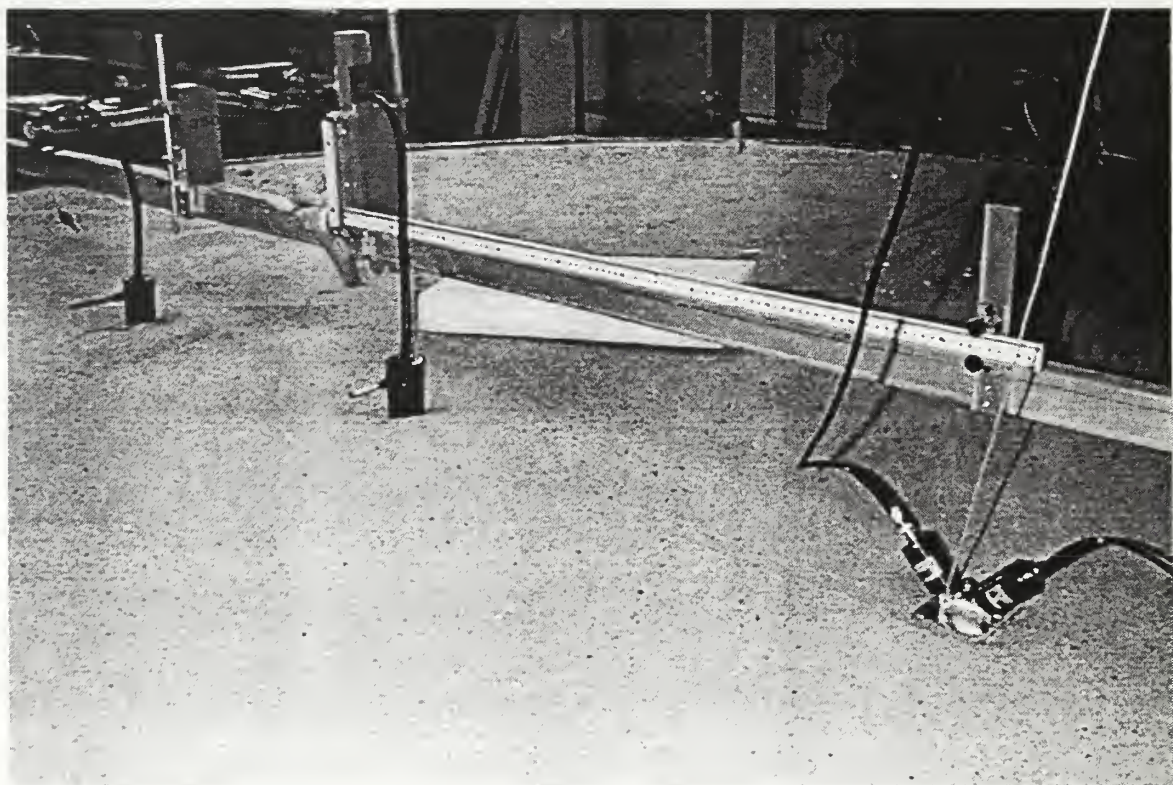


Figure 4.2 Concept Source Testing Experimental Setup

The first experiment was intended to qualitatively determine the effects of phase differences between the Mini-Shakers on the axial surface wave field, as a function of frequency. These results were characterized by the difference in the seismometer outputs for the axial and vertical directions. The transverse direction was not evaluated because the Rayleigh wave motion of interest exists in the vertical plane along the direction of propagation. Continuous sinusoids of frequencies 100, 150, 200, 250, 300, and 500 Hz were chosen as the test values. Since the left most Mini-Shaker in Figure 4.2 was used as the reference shaker, phase differences were chosen to correspond to the following six cases:

- Case 1 - Right shaker lagging by 25 degrees.
- Case 2 - Both shakers in phase.
- Case 3 - Right shaker leading by 25 degrees.
- Case 4 - Right shaker leading by 45 degrees.
- Case 5 - Right shaker leading by 90 degrees.
- Case 6 - Right shaker leading by 135 degrees.

In all test cases except the second, which produced exclusively vertical motion, the motion of the source was elliptical as was seen by the lissajous pattern of the radial and vertical components of the accelerometer. Appendix E contains the qualitative experimental results for all phases and frequencies evaluated. The results of this first experiment showed that there was a great deal of variation in the axial surface wave field with both source frequency and relative phase.

A second experiment was conducted to assess the effects of not only varying the frequency and phase, but also the driving voltages of the Mini-Shakers. This second experiment further served to show that the axial surface wave field, even in the nearly homogeneous, isotropic conditions of the sand tank, was a highly complex outcome of all variable source parameters.

Even though surface waves were generated in all test cases, the specific combination of source parameters needed to produce Rayleigh waves of sufficient amplitude and duration at the desired ranges for buried ordnance detection had yet to be

determined. It was evident from the initial testing that the appropriate combination would not be found in the laboratory. This is because, not only is the correct combination highly dependent on the individual properties of the vibration source and the ground coupling mechanism, but also on the local properties of the propagating medium at the time of testing. Furthermore, the limitations imposed by the tank, such as reflections from the tank walls and short ranges, made it impossible to quantify the source. To proceed any further in developing a discrete-mode, Rayleigh wave source would require designing a source that could be tested under actual field conditions.

C. FIELD TEST SOURCE – MOD I

To begin constructing a discrete-mode, Rayleigh wave, source that could be used in the field required that a suitable vibration source be identified. Once the vibration source was chosen, then the source-to-ground coupling mechanism could be appropriately designed and constructed. The vibration source needed to be rugged enough to withstand the beach and surf zone environment, yet inexpensive enough so that multiple pairs could be acquired, if arrays of paired vertical and horizontal sources could eventually be utilized.

1. Vibration Source

A test source that satisfied most of the necessary prerequisites was found manufactured by Aura Systems Inc., under the nomenclature of a Bass Shaker (See Appendix B3 for manufacturer specifications) [Ref. 16]. The Bass Shaker is a moving magnet transducer, intended to be used as a low frequency vibration source for a car stereo system. They are normally mounted under car seats or in door panels to provide listeners with the sensation of sound, without moving air like an ordinary speaker. The Bass Shaker generates a nominal force output of 10 lbf (44.5 N), independent of its mounting orientation.

2. Ground Coupling Mechanism

Since the Bass Shakers were considerably different in size and shape from the Mini-Shakers used previously, the source-to-ground coupling mechanism had to be redesigned. It was decided that the Bass Shakers should still be positioned at a 45-degree incline to the horizontal plane to provide the necessary degrees of freedom to produce all variations of elliptical motion. As shown in Figure 4.3, the ground

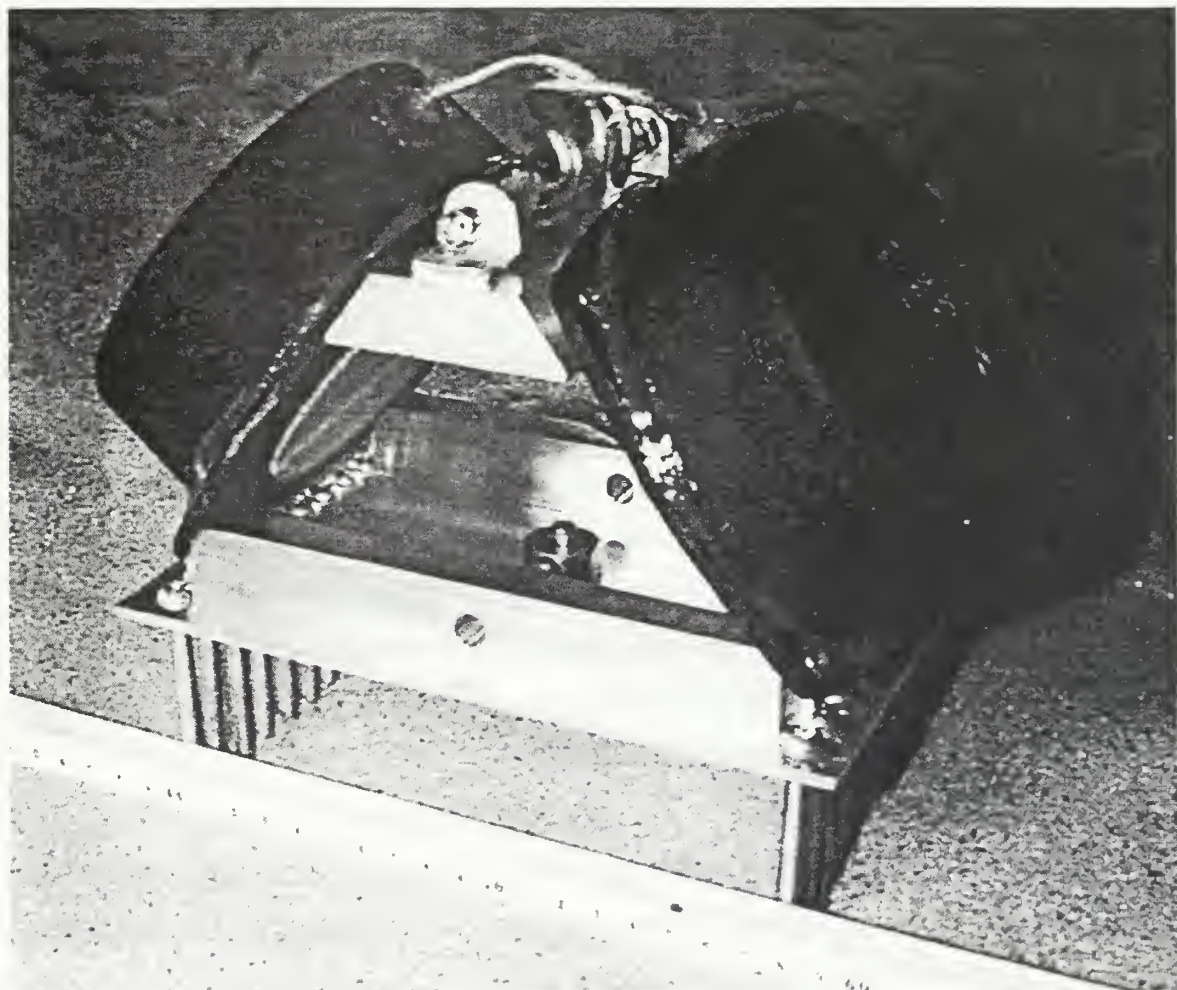


Figure 4.3. Picture of Field Test Source – Mod I

coupling mechanism was constructed from two pieces of aluminum. The top piece serving as a support brace for the upper part of the Bass Shakers and as a mounting surface for the electrical (BNC) connectors. The bottom piece serves as the attachment

point for the lower part of the Bass Shakers and provides the coupling mechanism to the medium through two rows of machine screws. Appendix C2 contains the Mod I technical drawings. A tri-axial accelerometer was positioned in the center of the base to monitor the source motion, and there was also an accelerometer mounted on the base of the support brace. Refer to Appendix B2 for accelerometer specifications.

3. Experimental Results

Before commencing any field experimentation, the new Rayleigh wave source was put through some operator familiarization and initial shakedown testing in the sand tank laboratory. Using the test equipment setup as described in Appendix D2, the same experiments were conducted as with the Mini-Shakers. These tests provided further verification that the axial surface wave field was a strong function of the input source parameters.

With the knowledge gained from the laboratory, it was clear that the first goal of any field experimentation should be to assess the Mod I source's ability to generate surface waves. To do this required finding a nearby location that was relatively free from any underground obstructions that would scatter the outgoing surface waves and make detection more difficult. The choice was made to use the NPS softball field as the first site for the field experiments. Progressing onto field experimentation from an equipment point of view proved to be quite a challenge at first, but as the research progressed, equipment difficulties were quickly overcome.

Once at the softball field, the lab equipment was setup as described in Appendix D3. Figure 4.4 illustrates the initial experimental layout. The initial distances were chosen based on expected Rayleigh wave speeds on the order of 100 m/sec and the maximum length of electrical cable available. Due to the hardness of the ground, trenches for the two rows of machine screws had to be dug in order to get the base of the source flush with the ground. After all the equipment was setup, attempts were made to detect the source motion above the background noise at the two seismometers located at ranges of 15.2 m (50 ft) and 30.5 m (100 ft). After many unsuccessful attempts to detect Rayleigh waves at these ranges, the decision was made to move back to ground zero.

The two seismometers were repositioned at distances of 1 m and 5 m from the source. From the variation in source parameters attempted, it was clear from the accelerometer output that the Mod I coupling mechanism had good horizontal coupling with the ground, but poor vertical coupling.

NPS Softball Field:

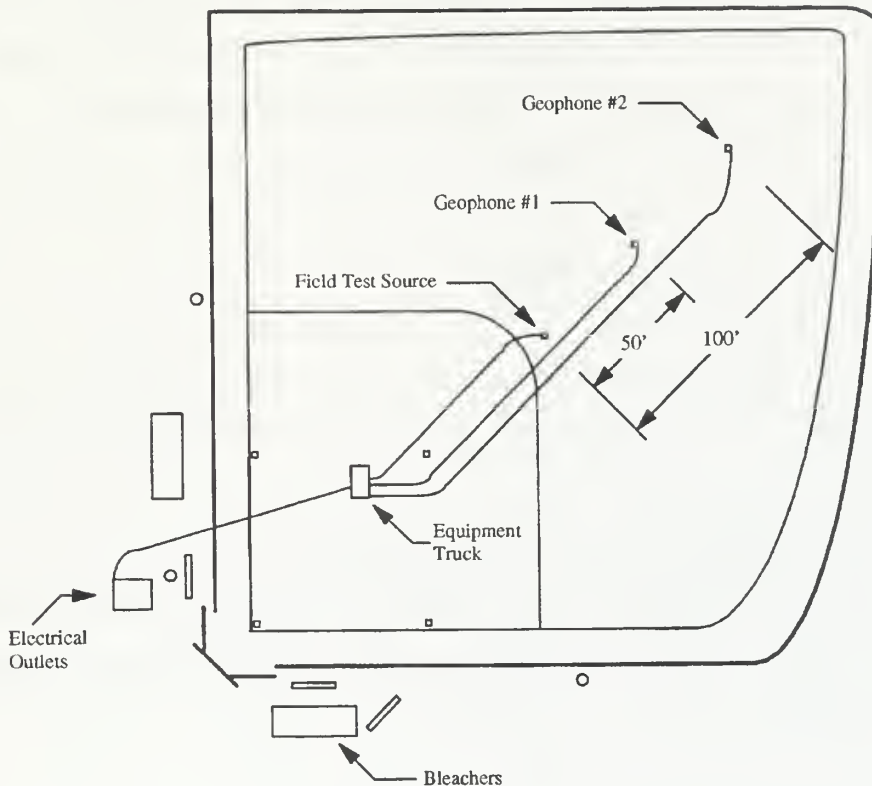


Figure 4.4. Field Source Testing Experimental Layout

At a distance of 1 m, the surface waves generated by the source motion were clearly visible, but at 5 m could not be separated from the background noise. This was clearly unacceptable, so to increase the chance of detection, improvement in the signal to noise ratio was required. First attempts were made by increasing the duty cycle, from 5 cycles to 20 cycles in increments of five. The increase in signal duration was clearly visible at 1 m, but at 5 m the signal was still buried within the background noise. The next effort was to increase the drive voltages of the two Bass Shakers. Starting at 5 Vrms, the drive voltage was increased in increments of five, until the current limit of the

power amplifiers was reached at approximately 39 Vrms. Even at 39 Vrms, the surface wave motion generated by the source was barely discernable at 5 m.

As a result of the first field experiment the following conclusions were drawn. First, to generate Rayleigh waves of sufficient amplitude to be detected at ranges of at least 10 m would require that the Bass Shakers be driven at the upper end of their linear response voltage limit. Second, that the ground coupling mechanism needed to be redesigned so as to enhance the vertical coupling. Furthermore, since there were so many channels of data that needed to be observed and ultimately processed, a method of recording all the field data was also required.

D. FIELD TEST SOURCE – MOD II

Using the lessons learned from the first field experiment, the next major milestones were to:

- Find the operating limits of the Bass Shaker.
- Modify the ground coupling mechanism to increase the vertical coupling.
- Incorporate into the field test equipment a method of obtaining multiple data channels.

1. Vibration Source

The manufacturer specifications that came with the Bass Shakers did not indicate any electrical operating limits. The installation guide (Appendix B3) did provide an advised maximum continuous power rating of 25 W per shaker. With an input impedance of 4Ω and a 25 W power rating, the maximum continuous drive voltage is only 10 Vrms. These ratings apply only to its intended use as a car stereo component and not for use as a vibration source for a seismic transducer. Consultation with the manufacturer provided no further information.

Without any formal documentation available, the only way to adequately assess the operating limits of the Bass Shakers was to see under what operating conditions

would failure occur. Sets of failure tests were conducted using the test equipment setup as described in Appendix D4. The goal of the failure testing was to estimate the amount of signal distortion as a function of frequency and drive voltage.

The HP35665A Signal Analyzer was used to simultaneously monitor the time series and total harmonic distortion of the Bass Shaker using the output signal of a uniaxial accelerometer mounted on the shaker case (See Appendix B4 for accelerometer specifications). The time series of the accelerometer output was used to visually detect any signs of failure or non-linearity as evidenced by changes in signal shape and/or duration. An estimate of the signal distortion over the first ten harmonics of the fundamental frequency, i.e. the drive frequency, was obtained using a built-in machine function.

The first set of failure tests were conducted by driving the shaker with 20 cycles of a sine wave, with a 2.00 sec repetition period, for fundamental frequencies of 100, 150, 200, 500, and 1000 Hz. While holding the frequency fixed, drive voltages of 10.1, 20.1, 30.1, and 38.6 Vrms were used, with 38.6 Vrms being the maximum voltage attainable without exceeding the current limit of the power amplifier. Figure 4.5 is a graphical representation of the signal distortion as a function of frequency and drive voltage for a 2.00 sec repetition period. Even though the overall signal distortion was low, the accelerometer time series for the 1000 Hz drive frequency showed evidence of non-linear behavior. The leading and trailing edges of the accelerometer signal were not as detailed as compared to the output signal from the function generator. There was also evidence of pulse elongation in the signal. The non-linear behavior was attributed to internal heating effects, as evidenced by noticeable case heating observed, but the shaker did not fail.

To stress the Bass Shaker further toward failure required that a more powerful amplifier be utilized. To hopefully alleviate the distortion caused by internal heating the repetition period was increased to 5.00 sec. A second set of failure tests were conducted with the new repetition period using a higher rated amplifier. During this second round of testing, the test shaker failed. The shaker was disassembled to locate the cause of the failure, but the internal design of the Bass Shaker only made the explanation speculative.

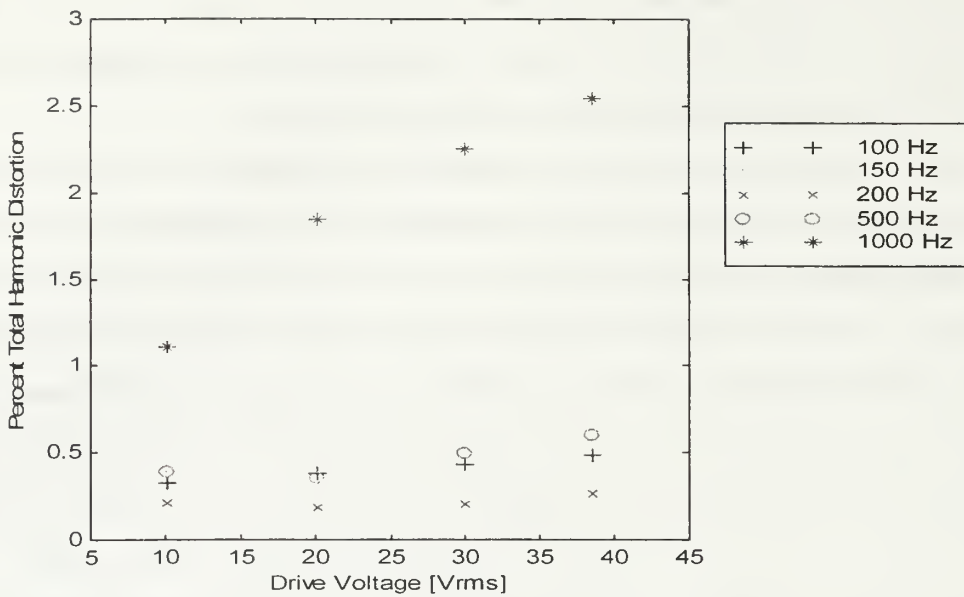


Figure 4.5. Signal Distortion for 2.00 sec Repetition Period

Since the cause of the failure of the first Bass Shaker was unknown, a second shaker was setup to complete the evaluation with the new amplifier. Figure 4.6 displays the results of the second set of tests.

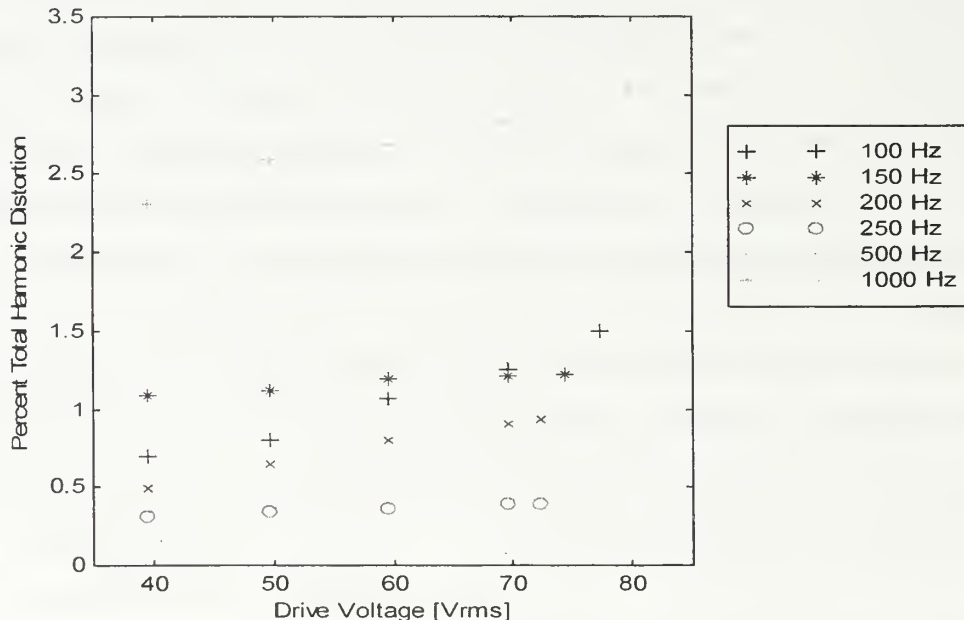


Figure 4.6. Signal Distortion for 5.00 sec Repetition Period

Using a repetition period of 5.00 sec seemed to effectively reduce the amount of internal heating and resulting distortion. As can be seen from Figure 4.6, the optimal drive frequency with respect to minimal signal distortion was 250 Hz. Again since the current limit of the power amplifier was exceeded before the shaker failed, it is safe to assume that with the current test equipment setup, shaker failure due to input drive voltage is not a major concern.

2. Ground Coupling Mechanism

To enhance the vertical coupling of the source to ground coupling mechanism, two end attachments were mated to the original base as shown in Figure 4.7. The attachments were constructed to hold three machine screws each, making the same 45-

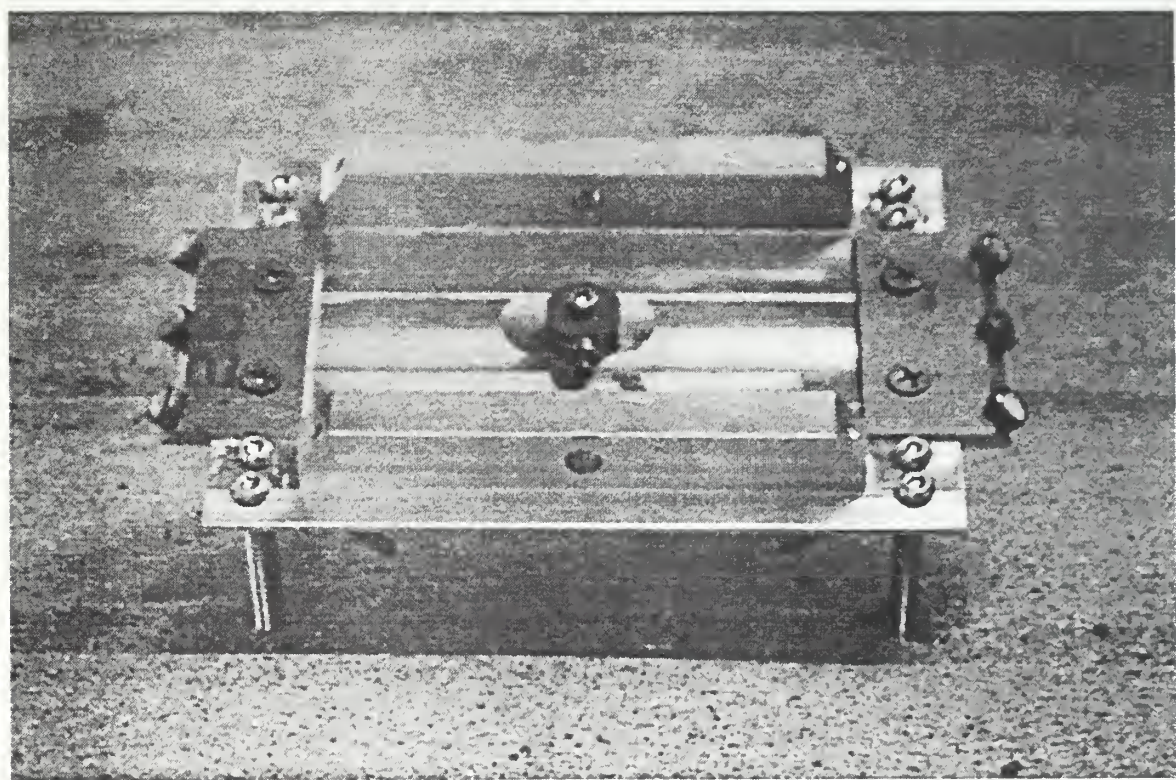


Figure 4.7. Picture of Mod II Base Modifications

degree angle with the horizontal surface plane as the Bass Shakers. It was hoped that these modifications to the base of the ground coupling mechanism would increase both the horizontal and vertical source coupling.

The upper support brace for the Bass Shakers was also modified. First, it was reduced in size to position the shakers closer to the desired 45-degree angle. Second, new BNC mounts were incorporated, making the Mod II source more rugged. Figure 4.8 is a picture of the redesigned Rayleigh wave source. Appendix C3 contains the technical drawings for the modifications.

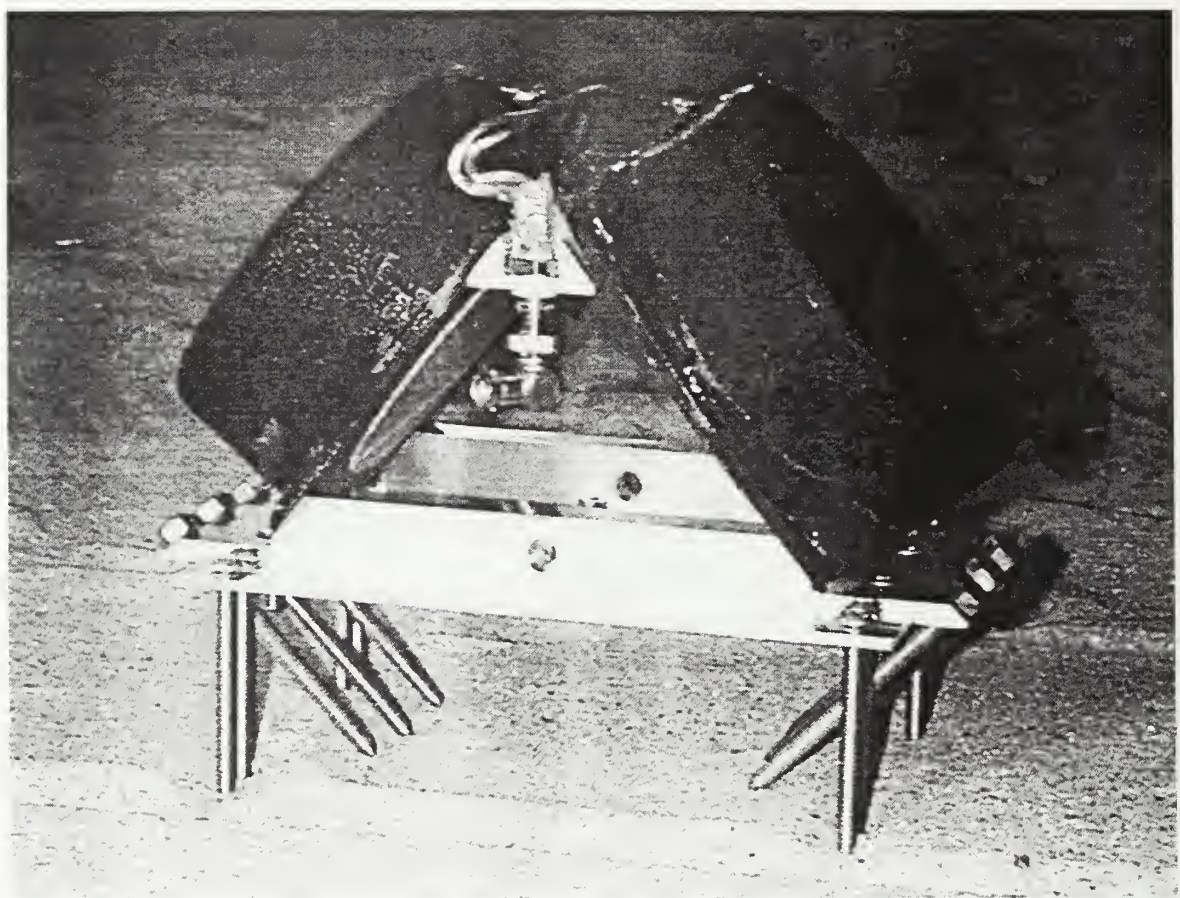


Figure 4.8. Picture of Field Test Source – Mod II

Addition of the two end attachments meant that emplacement of the source would first require placing the base into the ground in a similar fashion as the Mod I source,

then by using a cordless drill boring the six remaining angled machine screws into the ground.

3. Experimental Results

To resolve the data gathering issue, a SD390 Dynamic Signal Analyzer, made by Signal Processing Systems, was added to the test equipment setup described in Appendix D3. The SD390 is capable of receiving, displaying, and storing eight channels of information simultaneously, in real time. The eight channels provided data gathering capabilities for the:

- Radial and vertical components of the base-mounted accelerometer.
- Longitudinal, transverse, and vertical components of the two tri-axial seismometers.

Field testing of the Mod II source was also conducted at the softball field, using the equipment setup as shown in Appendix D5, but the source experimentation did not progress much farther than equipment setup. It was clear from the output signals of the accelerometer that the source was not exciting horizontal motion equally as well as it was exciting vertical motion. Thus generating the required elliptical motion to selectively stimulate Rayleigh waves would be nearly impossible. Attempts to replace the source were made, but did not significantly improve the operating conditions.

The results of the second field experiment prompted the need for further refinements to the design of the ground coupling mechanism and to rethink the utility of the softball field as the test location.

E. FIELD TEST SOURCE – MOD III

It is, of course, important to have good horizontal and vertical coupling to the ground for Rayleigh wave stimulation. Generating elliptical particle motion at the source requires moving the medium through a combination of both radial and vertical

excitations, such that, the semi-major axis of the ellipse is normal to the surface boundary and the semi-minor axis parallel to the interface in the direction of propagation. Therefore, having the correct design for the ground coupling mechanism is a major portion of discrete-mode source development.

1. Ground Coupling Mechanism

From the second field experiment it was noted that boring the machine screws into the ground with the cordless drill seemed to lock the source in place. The problems with the ineffective coupling arose from having to dig holes for the pre-positioned vertical machine screws. Hence, it only seemed logical that the source base be modified, so that all the screws could be positioned by screwing them into the ground. The Mod III base as shown in Figure 4.9 is the result.

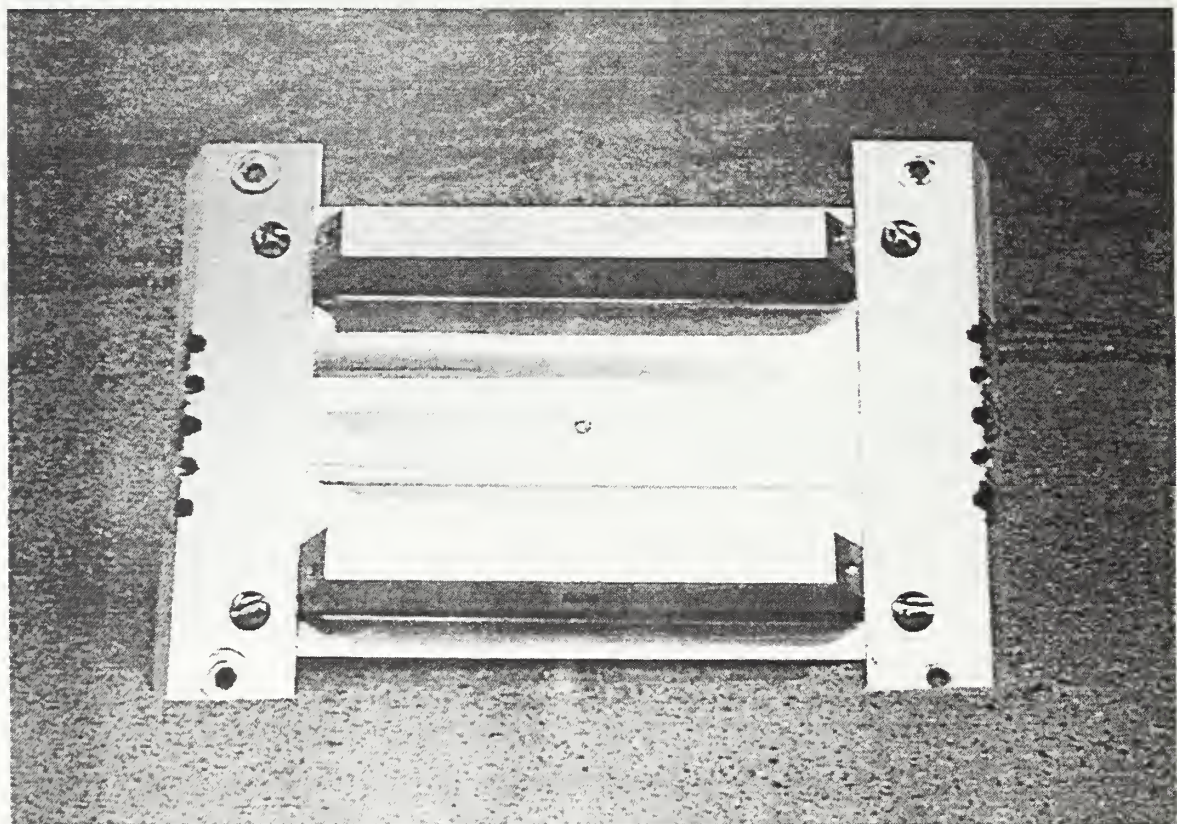


Figure 4.9. Picture of Mod III Base Modifications

The Mod III base modifications consisted of the addition of the two larger end attachments to the original base and the switch from 3 ½ inch machine screws to 6 inch machine screws. Reuse of the original base only served to reduce the turn-around time between field tests, since a whole new base did not have to be machined.

2. Experimental Results

Due to the equipment difficulties that arose from using the softball field as the test location, it was decided that any following ground phase experimentation be conducted from the lab in Spanagel Hall. Appendix D6 contains the new test location layout. The same equipment setup as described in Appendix D5 was used.

With the necessary modifications to the ground coupling mechanism completed, the next field experiment was used to ensure that the Mod III base provided the required horizontal and vertical coupling for Rayleigh wave stimulation. This phase of the source testing consisted of verifying, that with the correct phase settings for each of the Bass Shakers, both radial and vertical source motion could be individually stimulated. The stiffness of the ground to the source motion was quite noticeable, it was only through the manual manipulation of both phase and amplitude, that individual excitation of radial and vertical motion was possible.

The fourth, and final, ground phase field experiment was used to investigate the axial surface wave field effects for various drive voltages and relative phases of the Bass Shakers. Refer to Appendices D5 and D6 for the corresponding equipment and experimental setups. The effects to the surface wave field were characterized by measuring the coherence between the radial and vertical signal components at the furthest seismometer. Coherence on the order of unity would indicate a high degree of reliability in the magnitude and phase information of the received signals. The coherence was determined using a built-in processing option of the SD390 Signal Analyzer, using the average of ten received signals from a 250 Hz, 20 cycle sine wave burst, with a 5.00 sec repetition period. Driving voltages of 20, 40, 60, and 86 Vrms and relative phases of 0, 30, 60, 90, 120, 150, 180 degrees were chosen as the test values.

excitations, such that, the semi-major axis of the ellipse is normal to the surface boundary and the semi-minor axis parallel to the interface in the direction of propagation. Therefore, having the correct design for the ground coupling mechanism is a major portion of discrete-mode source development.

1. Ground Coupling Mechanism

From the second field experiment it was noted that boring the machine screws into the ground with the cordless drill seemed to lock the source in place. The problems with the ineffective coupling arose from having to dig holes for the pre-positioned vertical machine screws. Hence, it only seemed logical that the source base be modified, so that all the screws could be positioned by screwing them into the ground. The Mod III base as shown in Figure 4.9 is the result.

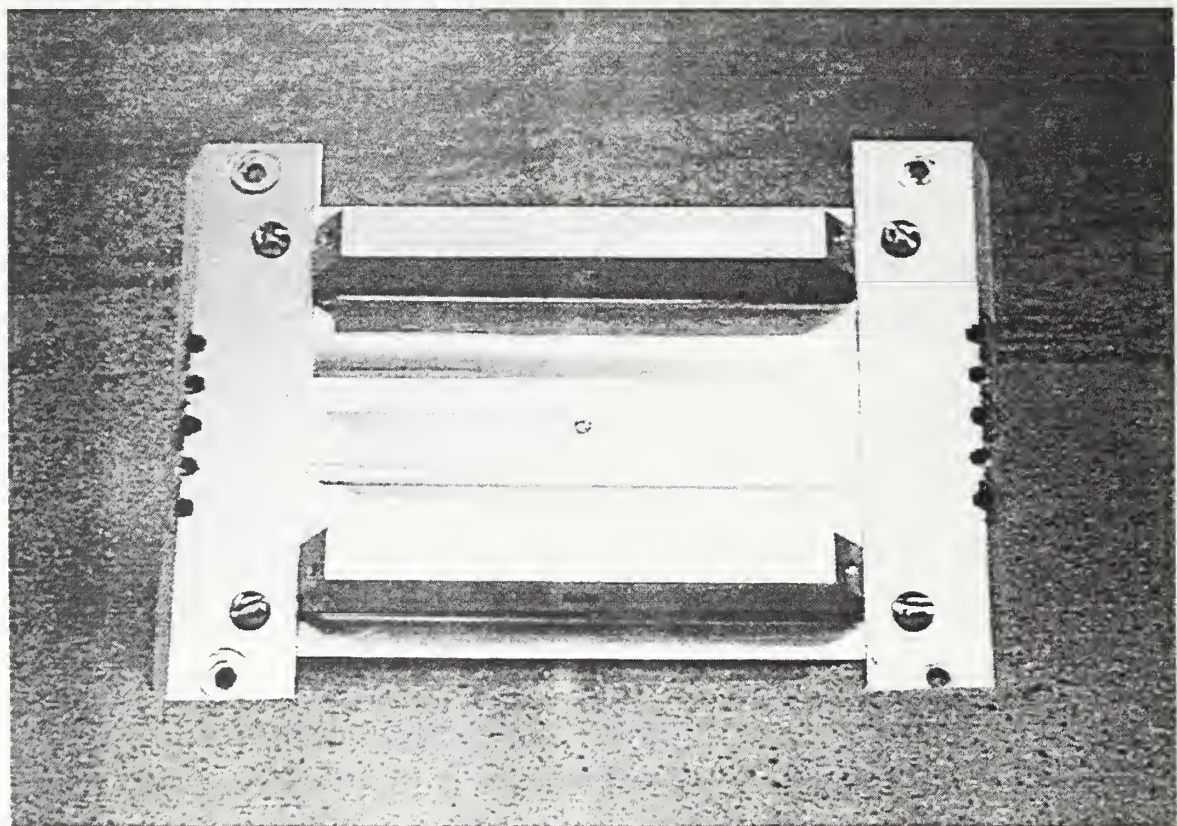


Figure 4.9. Picture of Mod III Base Modifications

The Mod III base modifications consisted of the addition of the two larger end attachments to the original base and the switch from 3 ½ inch machine screws to 6 inch machine screws. Reuse of the original base only served to reduce the turn-around time between field tests, since a whole new base did not have to be machined.

2. Experimental Results

Due to the equipment difficulties that arose from using the softball field as the test location, it was decided that any following ground phase experimentation be conducted from the lab in Spanagel Hall. Appendix D6 contains the new test location layout. The same equipment setup as described in Appendix D5 was used.

With the necessary modifications to the ground coupling mechanism completed, the next field experiment was used to ensure that the Mod III base provided the required horizontal and vertical coupling for Rayleigh wave stimulation. This phase of the source testing consisted of verifying, that with the correct phase settings for each of the Bass Shakers, both radial and vertical source motion could be individually stimulated. The stiffness of the ground to the source motion was quite noticeable, it was only through the manual manipulation of both phase and amplitude, that individual excitation of radial and vertical motion was possible.

The fourth, and final, ground phase field experiment was used to investigate the axial surface wave field effects for various drive voltages and relative phases of the Bass Shakers. Refer to Appendices D5 and D6 for the corresponding equipment and experimental setups. The effects to the surface wave field were characterized by measuring the coherence between the radial and vertical signal components at the furthest seismometer. Coherence on the order of unity would indicate a high degree of reliability in the magnitude and phase information of the received signals. The coherence was determined using a built-in processing option of the SD390 Signal Analyzer, using the average of ten received signals from a 250 Hz, 20 cycle sine wave burst, with a 5.00 sec repetition period. Driving voltages of 20, 40, 60, and 86 Vrms and relative phases of 0, 30, 60, 90, 120, 150, 180 degrees were chosen as the test values.

The quantitative results of the experiment are shown in Figure 4.10. As can be seen from the figure, the coherence between the radial and vertical components of the received signal increases as drive voltage increases, being nearly unity over most phase angles for a drive voltage of 86 Vrms. This final ground phase experiment illustrates that, the greater the input energy into the medium, the better the stimulation of reliable, repeatable, surface wave fields. The reason for the low coherence at 120 degrees is unknown.

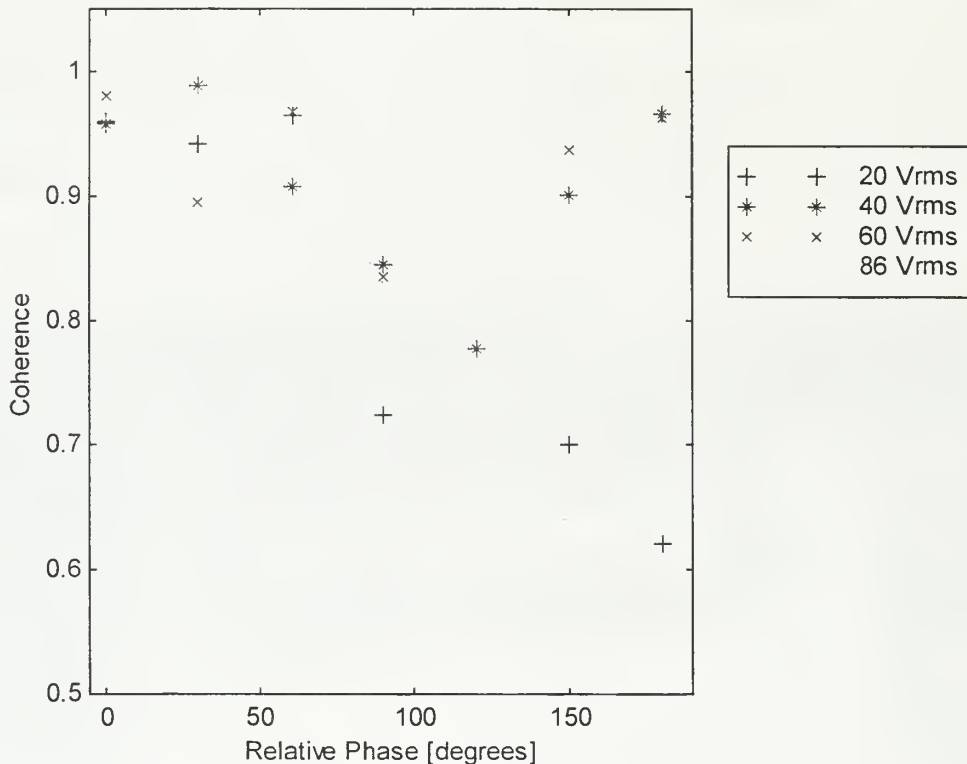


Figure 4.10. Coherence Measurements as a Function of Voltage and Phase

The time and effort spent in conducting the Ground Phase research provided a great amount of detail about the behavior of the field test sources and the associated surface wave fields. The choice of the Bass Shakers as the vibration source proved to be quite effective in generating the kinds of motion desired for discrete stimulation of Rayleigh waves.

Since the development of the seismo-acoustic sonar concept, the ultimate goal of the combined research efforts was to develop a mine detection system that was capable of locating buried ordnance, both in the surf zone and on land. Clearly, the surf zone is the more complicated environment to operate in, with regards to both the physics and the equipment required. The next chapter describes the development and experimental research conducted in this new environment. This portion of the research was identified as the Beach Phase.

V. DISCRETE-MODE SOURCE DEVELOPMENT AND TESTING (BEACH PHASE)

This chapter covers the beach and surf zone development and experimental testing of the discrete-mode, seismic wave source. Included within the chapter are individual sections documenting the different phases of the experimentation. The first section briefly addresses the final modifications made to the source-to-ground coupling mechanism. The next section covers the ambient background noise analysis and ground truthing experiments conducted at the test site location. The remaining sections describe the research efforts made to assess the ability of the test source to selectively excite Rayleigh waves.

During the ground phase experimentation, research efforts were mainly directed at investigating the operating characteristics of the field test sources, in order to find the most effective source-to-ground coupling design. Secondly, it was also concerned with qualitatively assessing the effects of various source parameters on the axial surface wave field. The ground phase research provided the necessary background information that was needed to successfully interpret the beach phase experimental results. Progressing onto beach and surf zone field experimentation was a major milestone in furthering the development of a discrete mode seismo-acoustic source and towards a greater understanding of the complex physics involved.

Using the lessons learned from the ground phase experimentation with respect to equipment transportation and logistics, it was evident that working out the bed of a pickup truck would not suffice for the beach phase experimentation. Thus, it was necessary to find a research platform that was large enough to transport all the equipment to the test site and that could provide the necessary electrical power. The mobile home owned by the Oceanography Department was the logical and most readily available solution.

A. FIELD TEST SOURCE – MOD IV

From the results obtained during the last set of ground phase experiments, the Mod III source-to-ground coupling mechanism, as shown in Figure 4.9, seemed to provide the necessary coupling in both the horizontal and vertical directions. As a result of its successful testing it was decided that this design be used as a model for the fabrication of the final ground coupling mechanism to be used for the beach phase experimentation. Figure 5.1 is a picture of the Mod IV ground coupling mechanism. Appendix C4 contains the technical drawings for the Mod IV base.

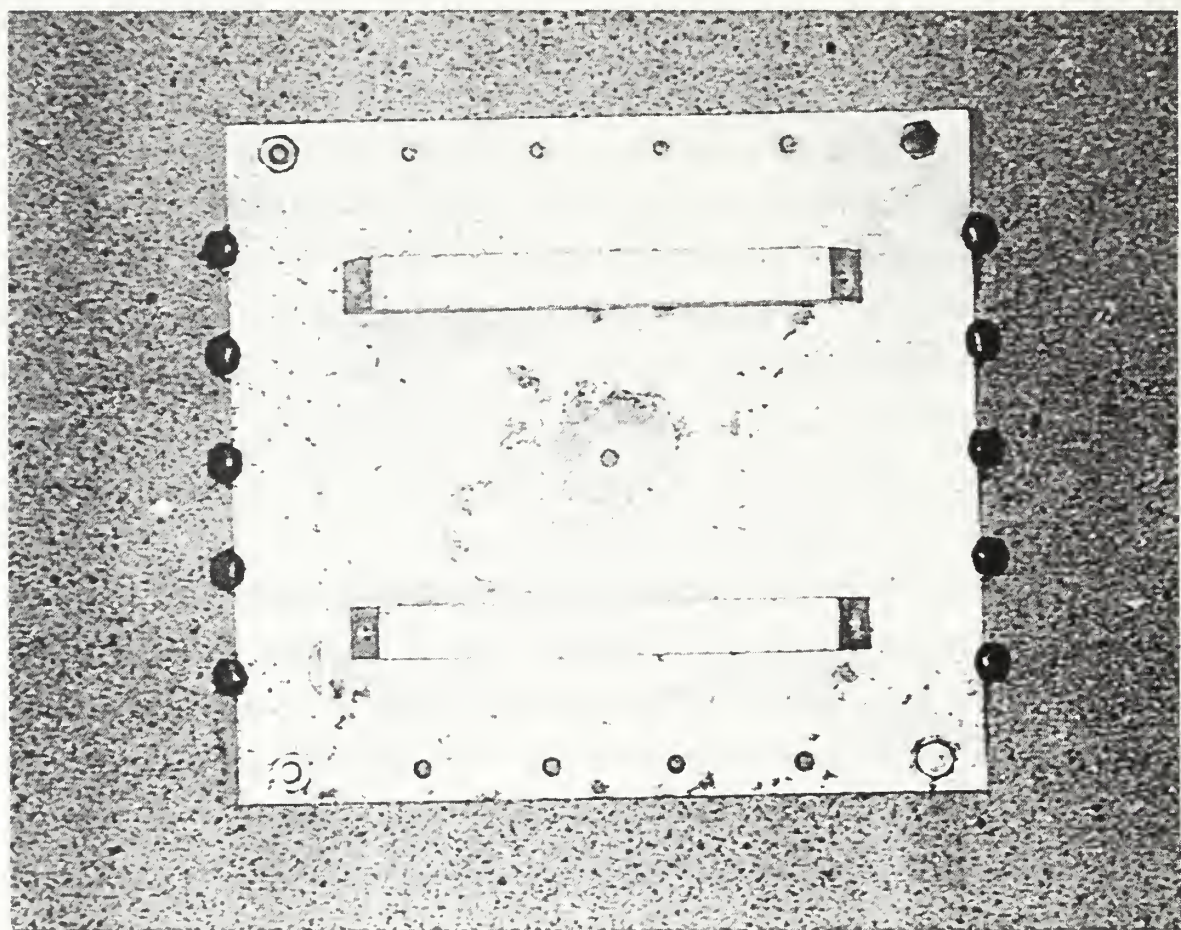


Figure 5.1. Picture of Mod IV Ground Coupling Mechanism

To help protect the sources from the harsh beach environment, all joints and access holes were filled with silicone. Furthermore, a waterproof accelerometer was also added (See Appendix B5 for manufacture specifications).

B. BACKGROUND NOISE AND GROUND TRUTHING EXPERIMENTS

Because of the highly complicated nature of the surface wave field, it was necessary to obtain a sufficient knowledge base of the ambient acoustic properties of the test medium. To obtain the required information meant that ambient background noise analyses and ground truthing experiments be conducted at the proposed source testing site. The test site chosen was a stretch of beach on the Monterey Bay coastline located behind the NPS Beach Research Facilities. The section of beach front area used, as shown in Figure 5.2, was approximately 80 feet wide from the surf zone to the sand dunes at low tide with a longitudinal extent far exceeding that required for the source testing.

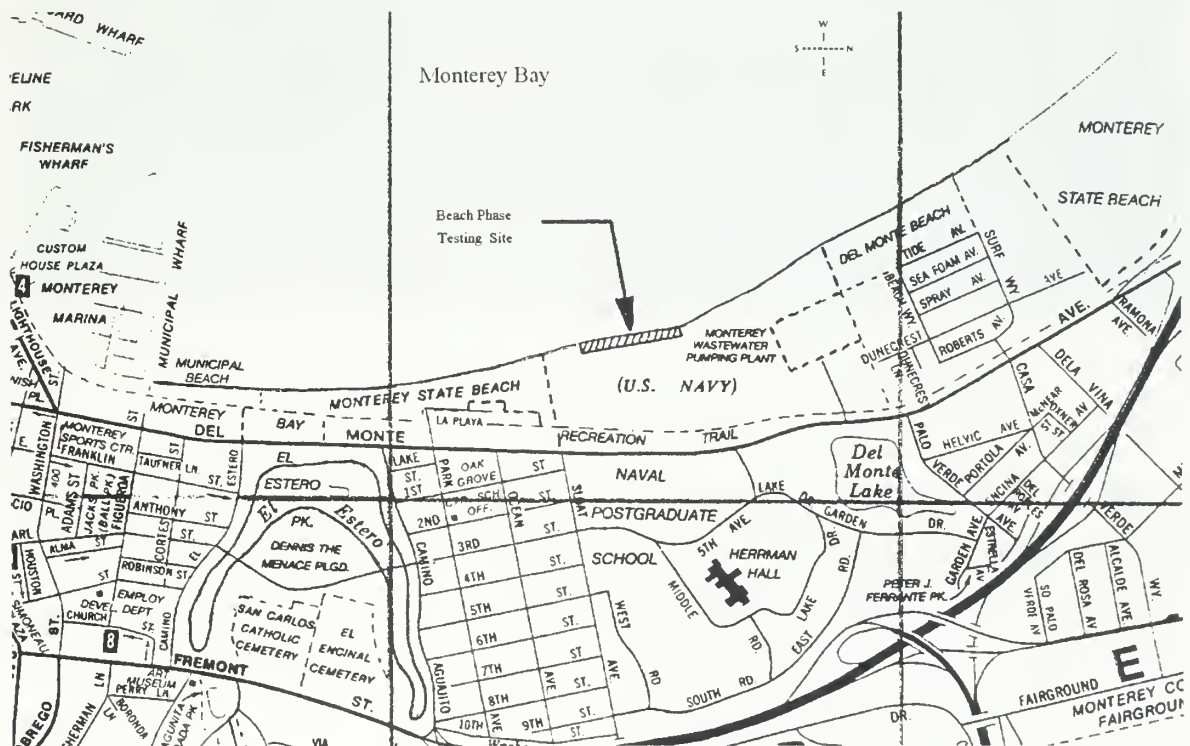


Figure 5.2. Beach Phase Testing Site

Map copyrighted 1994 by the California State Automobile Association. Reproduced by permission.

1. Background Noise Analysis

In order to make source testing and data interpretation as simple as possible it was desired that the source be operated in a frequency range for which competition with the background noise would be minimal. Background noise samples were taken at the test site using the seismometers as the receivers. Spectral analysis of the noise samples taken showed that the strongest noise components resided between 5-20 Hz as shown in Figure 5.3. Since these frequencies were well below the envisioned operating frequencies for the Bass Shakers filtering out the undesired background noise from the input signals would be relatively simple. Appendix F contains the MATLAB programs used to conduct the spectral analysis.

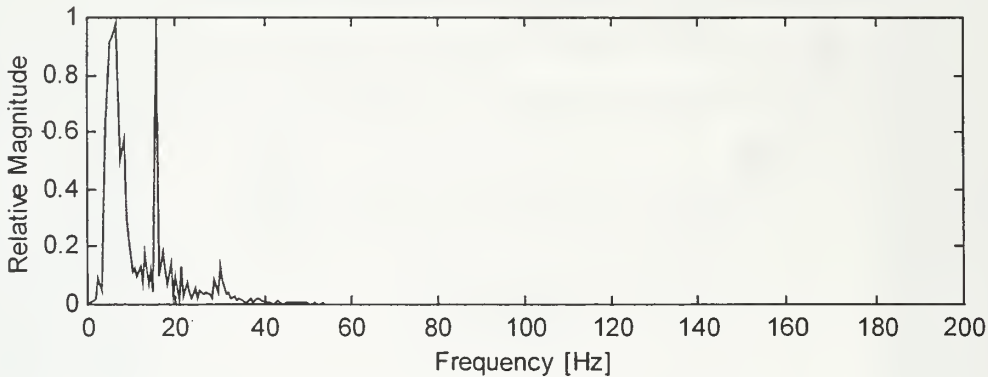


Figure 5.3. Ambient Background Noise

2. Ground Truthing

To obtain an accurate picture of the ambient acoustic properties of the test site a series of ground truthing experiments were conducted to estimate the group velocity of the Rayleigh wave. As was shown in section II C, Figure 2.6, a vertical point impulse generates a wave system comprised of P-, S- and R-waves, as well as other wave types not shown.

To simulate a vertical impulsive source a bowling ball with a self-contained uniaxial accelerometer was dropped from an average height of 45 inches, as shown in Figure 5.4. A bowling ball was used because it is spherically symmetric and impacts the ground

the same way on each drop. When the bowling ball impacts the ground several radially outward propagating wave systems are created. The impact of the bowling ball is sensed by the accelerometer, which triggers a multi-channel data acquisition system to record the response of a pre-positioned seismometer. Appendix B6 contains the manufacturer specifications for the uni-axial accelerometer and Appendix D7 the wiring diagram for the equipment setup.



Figure 5.4. Picture of Initial Ground Truthing Experiment

Since a seismometer is a velocity-sensing instrument, the particle motion induced by the propagating wave system is converted to an output voltage, which is proportional to the particle velocity, which can be used to obtain the wave velocities. The particle velocity data obtained from the seismometers were processed using a time versus frequency decomposition method. This method involves dividing the seismometer data records into equal length blocks with a pre-defined overlap. The midpoint of each block can be associated with an arrival time based on the separation between the bowling ball

and the seismometer, which in turn can be associated with a wave velocity. The power spectral density of each block is calculated and stored in a matrix, which associates frequency with velocity. The results of the data processing are then displayed in the form of a Gabor plot, named after its inventor Professor Gabor of the University of Delft, the Netherlands. The Gabor plot depicts the decomposition of the wave field as a contour plot of slowness (inverse speed) as a function of frequency. From the Gabor plots, estimates of the propagating velocity of various wave modes can be made.

Furthermore, since the particle displacement of the beach sediments is proportional to the particle velocity, the received seismometer signals can also be used to graphically display the average particle motion observed at the seismometer. The resulting particle motion can be displayed in the form of a Hankel plot or hodogram. By plotting the longitudinal component of motion versus the vertical component as a function of time, which is known as a Hankel plot, the motion can be used to determine the wave type, i.e. P, S, or R. A hodogram is the two-dimensional form of a Hankel plot. Appendix G contains the MATLAB programs used to analyze the ground truthing data.

The first set of ground truthing measurements were conducted as shown in Layout I of Appendix D7. Two series of bowling ball drops were made. The first series was conducted approximately 45 feet from the surf zone, in dry sand. The bowling ball was dropped at distances of 6, 12, 18, and 24 feet from the seismometer. The second series of drops were conducted at the edge of the surf zone using distances of 6, 12, 18, 24, 36, and 48 feet.

During the analysis of the seismometer data it became evident that even a source-receiver separation of 48 feet did not allow for the desired time separation of the propagating modes in the wavetrain. Thus, an accurate decomposition of the different wave types could not be accomplished. Figures 5.5 and 5.6 show the time series of the longitudinal and vertical velocity signals received at the seismometer for distances of 24 feet in dry sand and 48 feet in wet sand, respectively. The time series depicted have been adjusted so that 0 sec corresponds with the impact of the bowling ball. Figures 5.7 and 5.8 are Hankel plots of the particle motion at the seismometer for the associated time series.

Recalling that Rayleigh waves induce elliptical particle motion, it's clear from the Hankel plots that the motion shown at these distances is due to the presence of more than just the Rayleigh wave. Thus to adequately estimate the various wave speeds would require allowing greater time for wave separation to occur. This could only be accomplished by using larger separation distances between the seismic source and the seismometer.

To promote wave separation, the same experiment was conducted a second time using much larger distances. Figure 5.9 and Layout II in Appendix D7 show the experimental layout for the second phase of ground truthing experiments. Separation distances of 50, 70, 90, 110, and 130 feet were selected. Also, a second seismometer was placed at a distance of 10 feet behind the first to allow for the collection of five additional data sets at intermediate distances. Furthermore, it was decided that the ground truthing efforts be concentrated in the drier areas of the beach since the Bass Shakers were not waterproof.

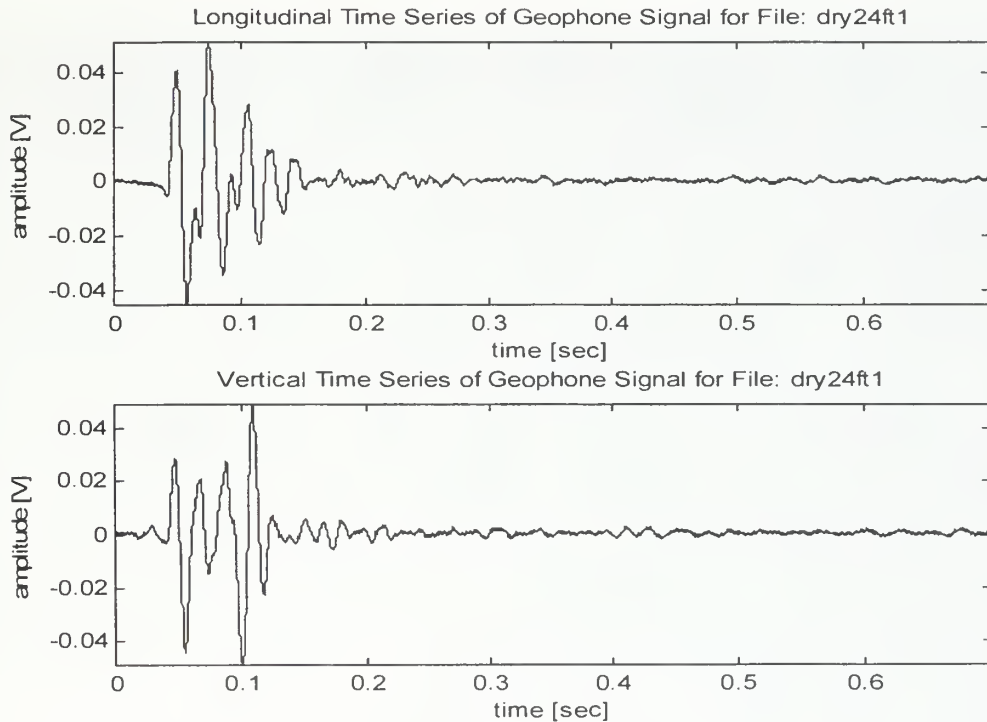


Figure 5.5. Time Series of Seismometer Velocity Signals for a 24 ft.
Source-Receiver Separation Distance

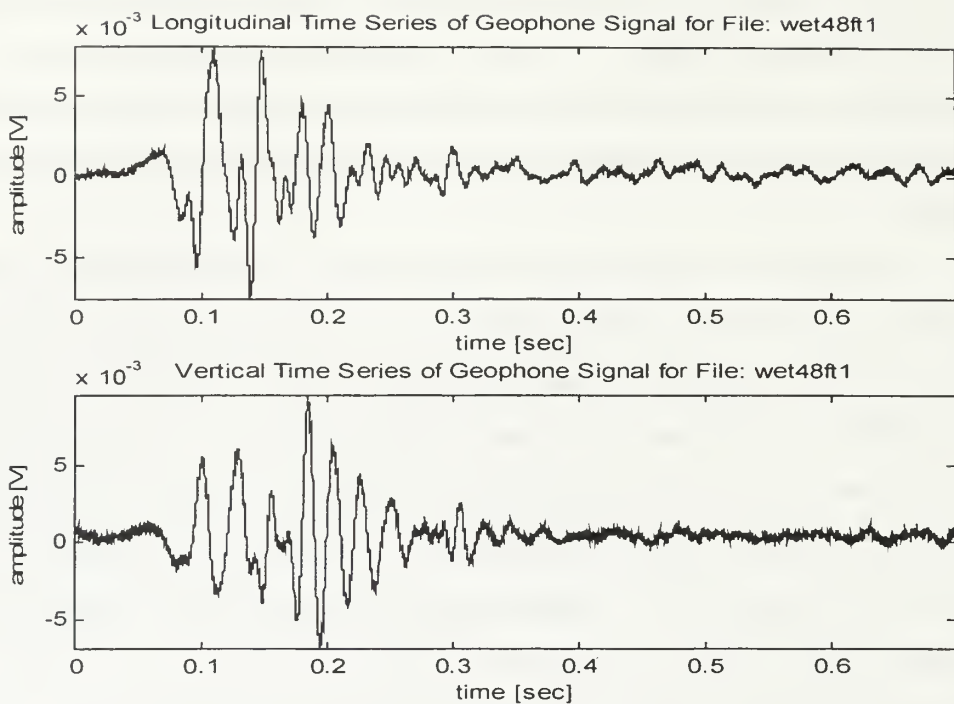


Figure 5.6. Time Series of Seismometer Velocity Signals for a 48 ft.
Source-Receiver Separation Distance

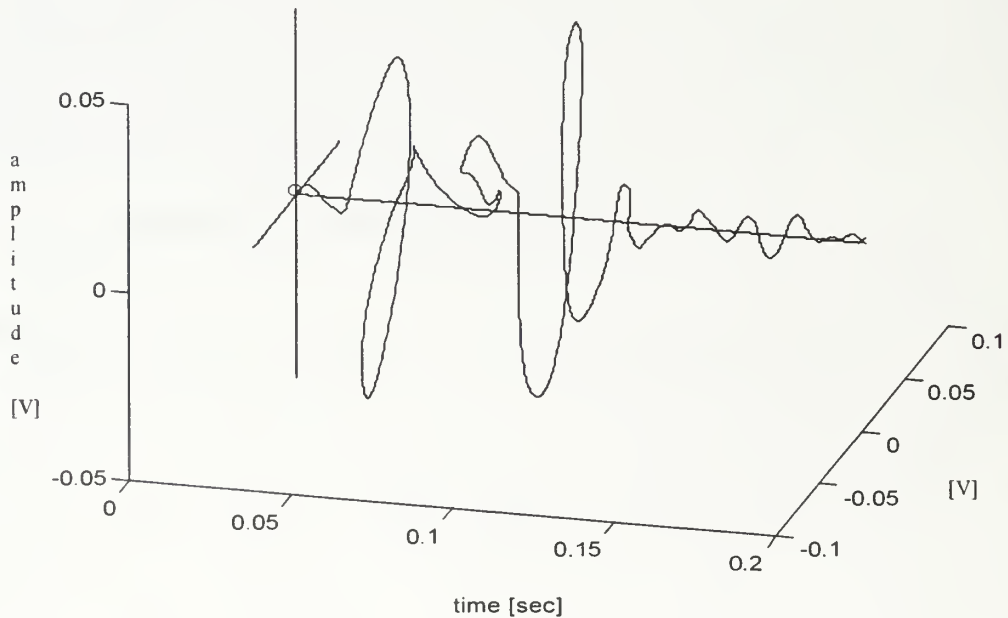


Figure 5.7. Hankel Plot of Seismometer Velocity Signals for a 24 ft.
Source-Receiver Separation Distance

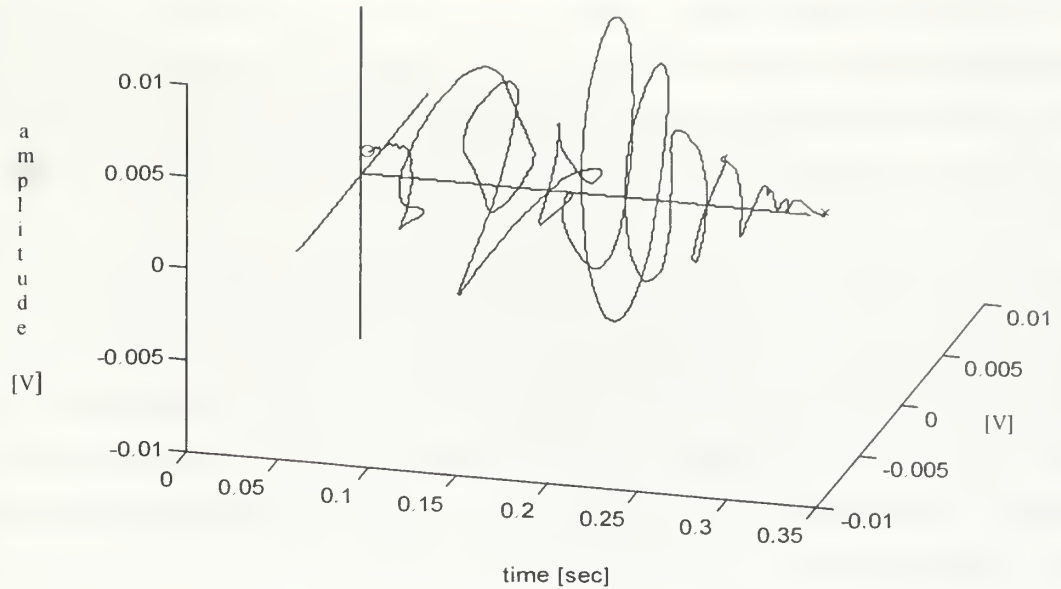


Figure 5.8. Hankel Plot of Seismometer Velocity Signals for a 48 ft.
Source-Receiver Separation Distance

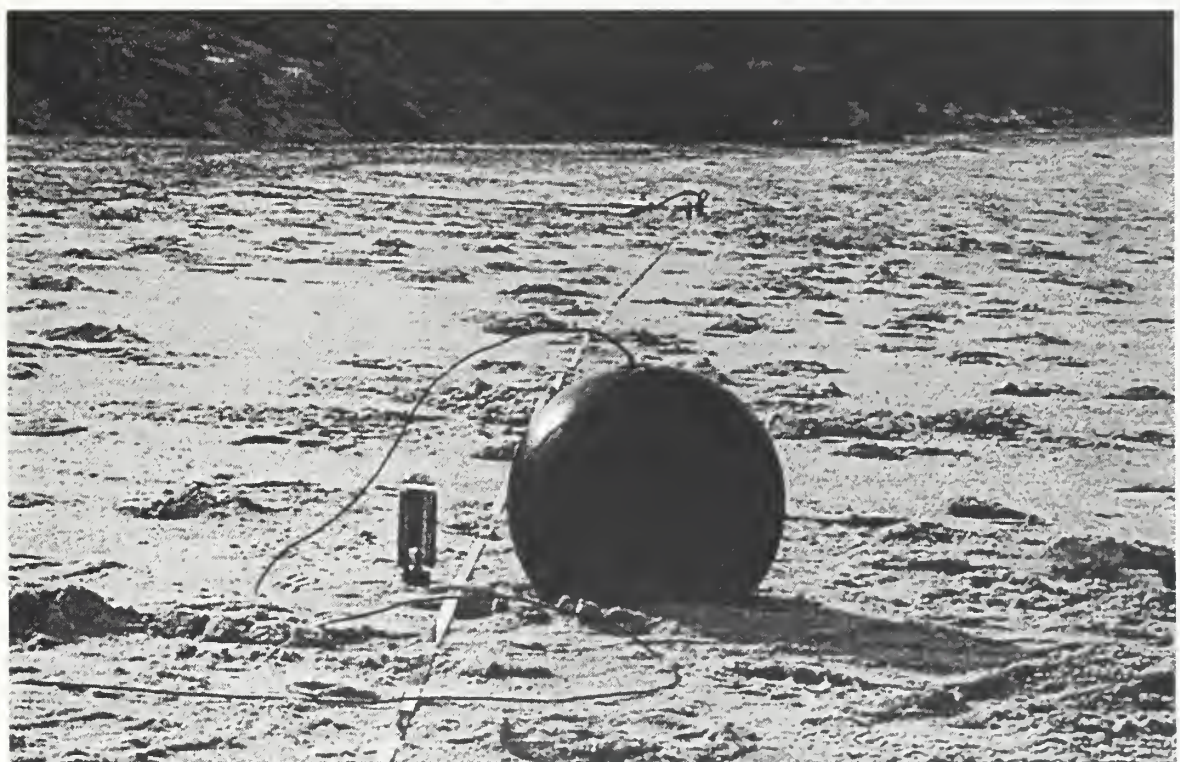


Figure 5.9. Picture of Second Ground Truthing Experiment

Increasing the separation distance between the drop location and the first seismometer greatly increased the ability to decompose the wave field. It was not until the data files for distances of 70 feet and greater were analyzed that modal separation in the Gabor plots became clear. Figure 5.10 is the Gabor plot for a separation distance of 70 ft (21.3 m). Figure 5.10 shows the existence of at least two wave modes, the slower mode being the Rayleigh wave as determined by analysis of the hodogram of the time series velocity signals. The group velocity of the Rayleigh wave at 40 Hz is approximately 88 m/sec (0.0114 sec/m) and the second mode is another wave with a group velocity of approximately 114 m/sec (0.0088 sec/m) at 60 Hz.. The identity of the second wave is unknown since its speed is not consistent with that expected for a shear wave in this sediment.

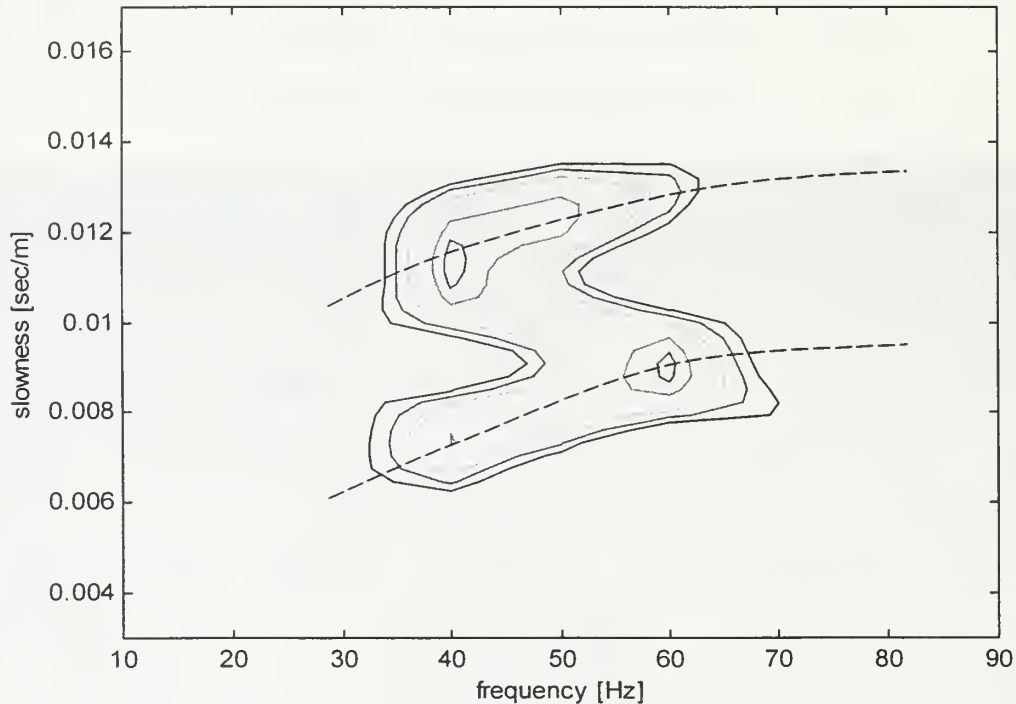


Figure 5.10. Gabor Plot for a 70 ft. Source-Receiver Separation Distance
(1dB contour separation)

The forces generated by the bowling ball impact with the beach sediments seems to generate larger amplitude body waves, as compared to the point source discussed in section II C. This is clearly evident in the time series for the seismometer longitudinal

section II C. This is clearly evident in the time series for the seismometer longitudinal velocity signal displayed in Figure 5.11. Even at a distance of 130 feet, the longitudinal particle motion caused by the body waves is comparable to that of the Rayleigh wave. The displacements in the vertical direction are almost entirely dominated by the Rayleigh wave.

Figures 5.12 and 5.13 are the Hankel plot and hodogram, respectively, for the time series of Figure 5.11. These figures serve to illustrate how much more prevalent is the retrograde elliptical motion of the Rayleigh wave at these larger distances. Figure 5.14 is the Gabor plot of the wave decomposition at a range of 130 ft (39.6 m). As can be seen from the figure, two propagating wave modes are present in the velocity range 60-250 m/sec. From the Gabor plot, the Rayleigh wave speed is estimated at approximately 89 m/sec (0.0112 sec/m) and the second wave has a speed of approximately 109 m/sec (0.0092 sec/m). The ratio of the Rayleigh and shear speeds obtained from this plot are within 10% of the theoretical ratio predicted by the theory of elasticity.

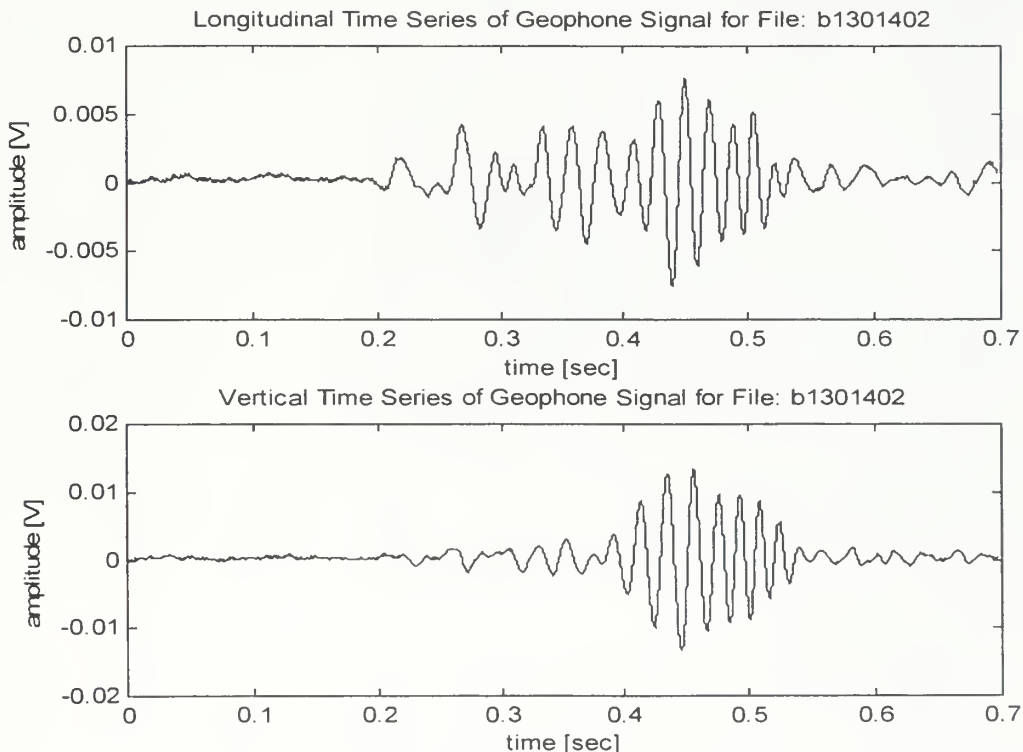


Figure 5.11. Time Series of Seismometer Velocity Signals for a 130 ft.
Source-Receiver Separation Distance

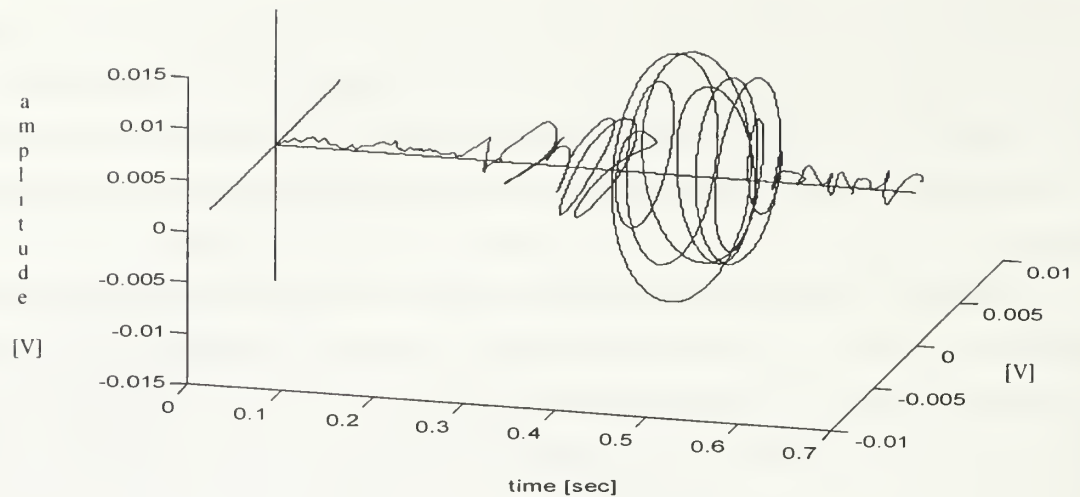


Figure 5.12. Hankel Plot of Seismometer Velocity Signals for a 130 ft.
Source-Receiver Separation Distance

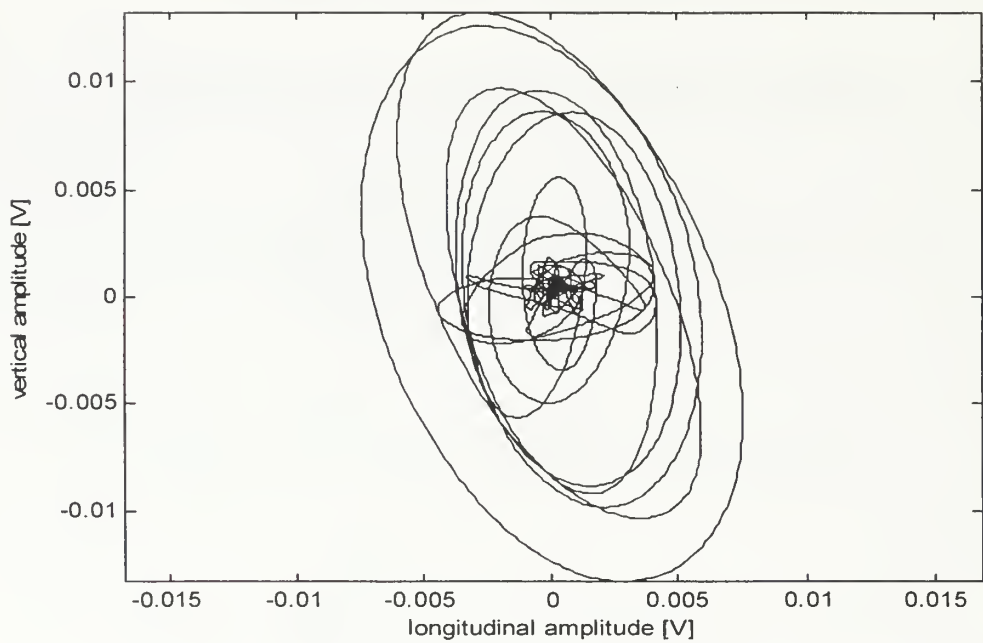


Figure 5.13. Hodogram of Seismometer Velocity Signals for a 130 ft.
Source-Receiver Separation Distance

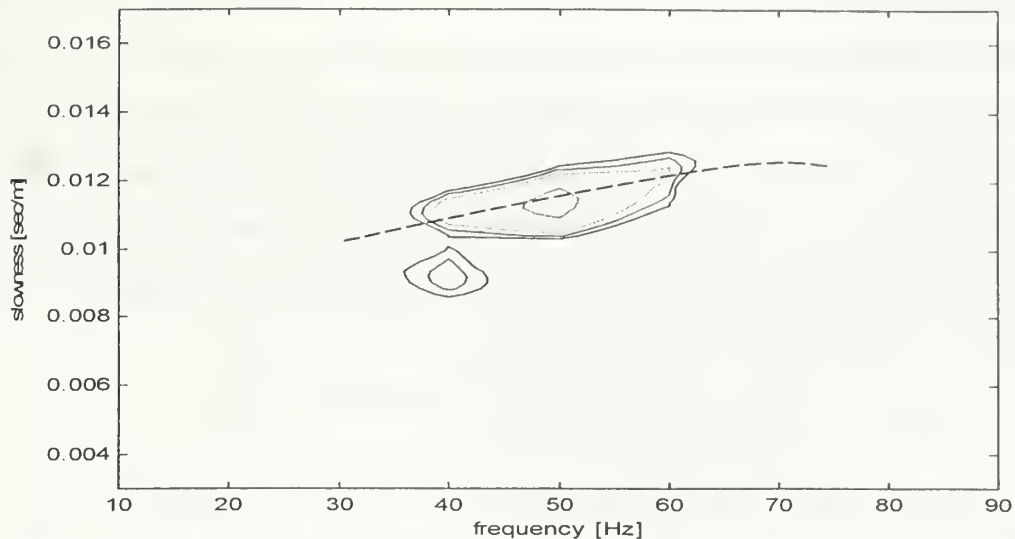


Figure 5.14. Gabor Plot for 130 ft. Source-Receiver Separation Distance
(1 dB contour intervals)

Figure 5.15 shows an aggregate display of the accelerometer trigger signal (lowest trace) and the seismometer vertical velocity versus time recorded for the bowling ball

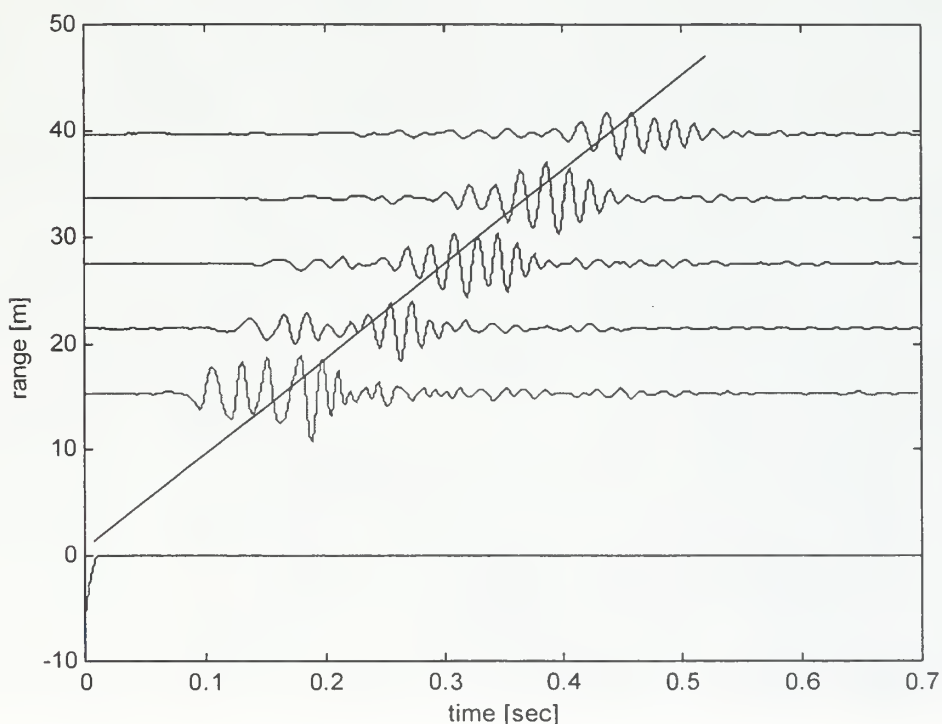


Figure 5.15. Rayleigh Wave Progression as a Function of Space and Time

drops between 50 ft (15.2 m) and 130 ft (39.6 m) range. The behavior of the velocity amplitude with range should not be considered indicative of what would be observed for an end-on array of five seismometers receiving a single signal, as site conditions probably changed over the duration of the data collection. The large vertical amplitude of the Rayleigh wave is easily distinguishable in the more distant traces. The extracted group velocity is approximately 90 m/sec (see straight line in Figure 5.15), which agrees well with speeds estimated from the Gabor plots.

C. DISCRETE-MODE EXCITATION

With the necessary ground truthing experiments completed, the next phase of the research was to begin testing the Mod IV field test source (See Figure 5.16). The goal of

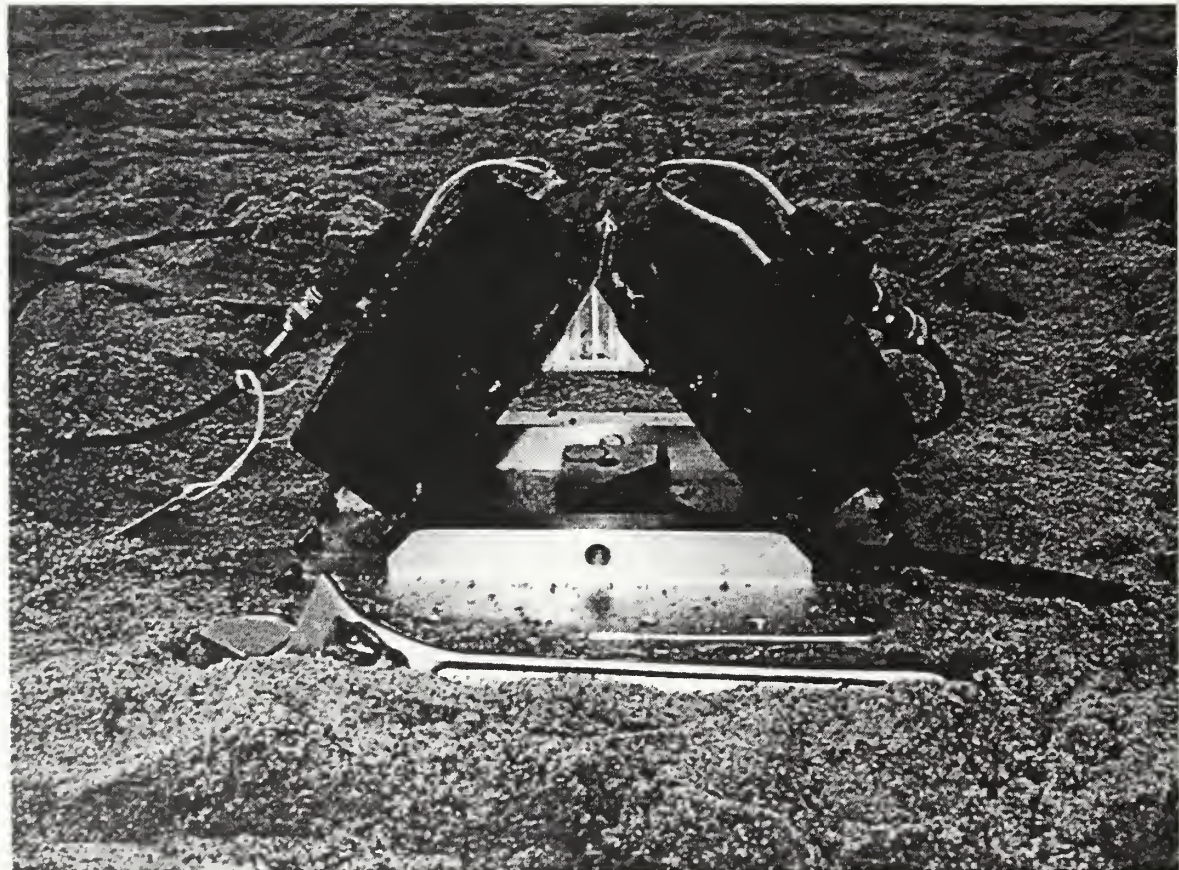


Figure 5.16. Picture of Mod IV Field Test Source

the research conducted from this point on was to prove that by inducing the appropriate elliptical particle motion into the beach sediments at the source, Rayleigh waves might be preferentially excited. Based on the theory for surface waves in a homogeneous, isotropic, elastic half-space, the particle motion induced by Rayleigh waves at the boundary surface is retrograde elliptical, with the vertical motion approximately 1-½ times the longitudinal motion.

1. Propagation Characteristics

Before moving onto assessing the Mod IV source's ability to selectively excite Rayleigh waves, some brief experimentation was conducted to see if the beach site itself had a preferential direction for energy propagation. To investigate this, the Mod IV field test source was positioned with two seismometers at equal distances, in the longitudinal direction, on both sides of the source, as shown in Figure 5.17 and layout I of Appendix



Figure 5.17. Picture of Wave Propagation Experiment

D8 (Also see Appendix D8 for associated test equipment setup).

The source as shown in Figures 5.16 and 5.17 was positioned so that, facing seaward, the port Bass Shaker faced in southerly direction along the beach and the starboard Bass Shaker to the north (See Figure 5.2 for orientation). Analysis of the shaker motion indicated that for an equal amplitude, positive input voltage, a negative phase for the port shaker and a positive phase for the starboard would generate retrograde elliptical source motion with respect to the southern positioned geophone. Reversing the phase would then induce a prograde elliptical motion.

For a homogeneous, isotropic, elastic medium the ratio of the longitudinal to vertical particle displacements for the Rayleigh wave at the boundary surface is a well-defined function of the Poisson's ratio. But since the Poisson's ratio for the beach sediments was not known, the specific ratio to be used in driving the test source was also unknown. As a result, it was decided that initial source testing be done using a 90 degree phase difference between the two shakers. This was accomplished by setting the port shaker to -45 degrees and the starboard shaker to +45 degrees, or vice versa. To distinguish between the two cases the following convention will be used: a -45 degree phase for the port shaker will be denoted by -45P and a +45 degree phase by +45P.

Since the Bass Shakers suffered the least distortion at 250 Hz, (See section IV.D.1, Figure 4.6), this frequency was chosen as the initial drive frequency. A 50 V peak, 20 cycle, 250 Hz, narrow-band filtered tone burst was used to drive the shakers. Even though this frequency was optimal for the shakers, it became immediately evident during data collection that this drive frequency was not optimal for energy propagation along the beach. As a result, it was decided to reduce the drive frequency to 100 Hz. It has been measures that, for this frequency, the harmonic distortion is less than 1% for a 50 Vrms drive voltage. Figures 5.18 and 5.19 are the Hankel plots for the seismometer signals at a range of 30 ft using a 50 V peak, 20 cycle, 100 Hz, narrow-band filtered tone burst and a -45P phase configuration. Figure 5.18 depicts the particle motion as observed at the southern seismometer and Figure 5.19 for the northern seismometer. In both figures the elliptical particle motion is prograde with respect to the seismic source and clearly shows the presence of the Rayleigh wave, but the northerly propagating wave is much more uniform. It can also see from the figures that the amplitude of the northerly

propagating wave is larger by a factor of two. Appendix H contains the MATLAB programs used to analyze the data gathered during the beach phase experimentation with the Mod IV source and to generate the accompanying figures.

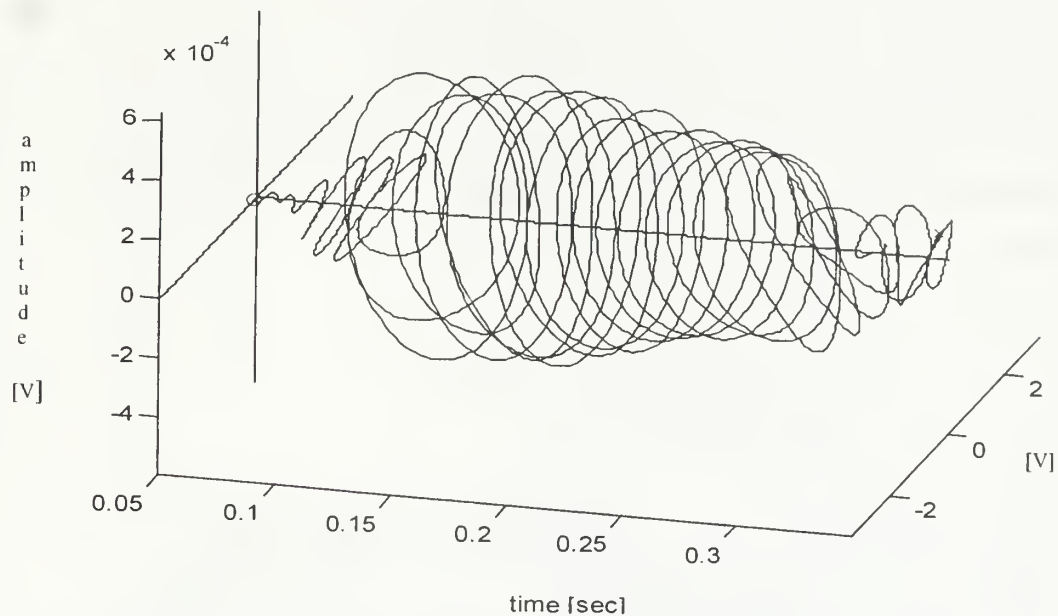


Figure 5.18. Hankel Plot of Southern Seismometer Velocity Signals for a 30 ft.
Source-Receiver Separation Distance (-45P)

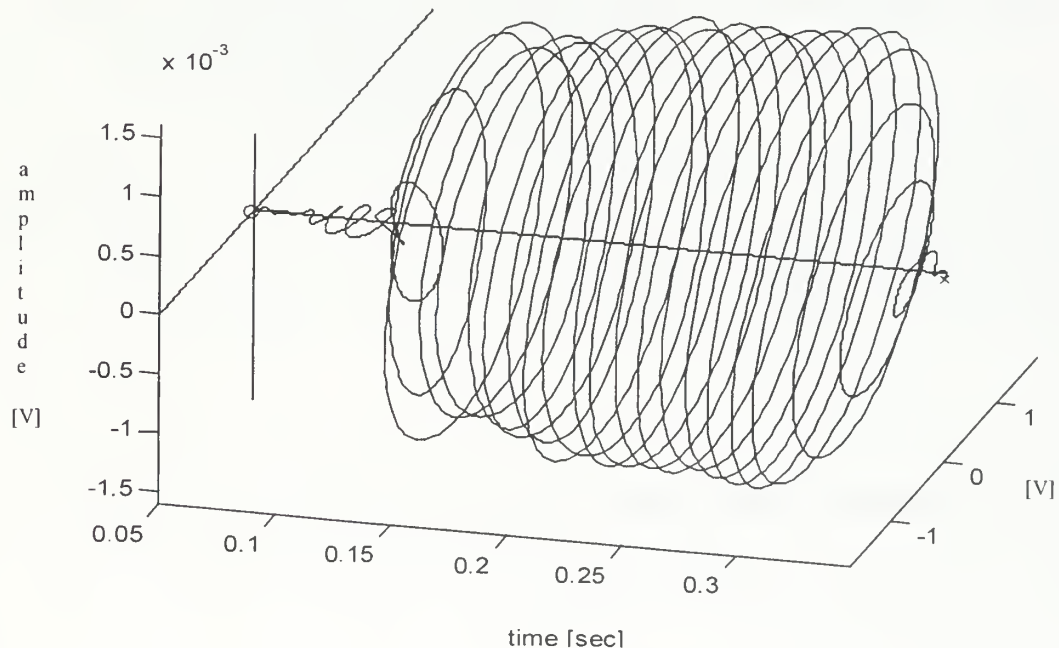


Figure 5.19. Hankel Plot of Northern Seismometer Velocity Signals for a 30 ft.
Source-Receiver Separation Distance (-45P)

Figures 5.20 and 5.21 are the Hankel plots for the same seismometer orientation and range, but for a +45P phase setting, which also produced an elliptical particle motion that was prograde with respect to the field test source. Again we see that the Hankel plot for the southern seismometer (Figure 5.20) is non-uniform and has a smaller amplitude as compared to the plot for the northern seismometer (Figure 5.21). Based on these figures, it would seem that the beach sediments either have a preferential direction of energy propagation or that the force generated by the motion of test source is different in the two directions.

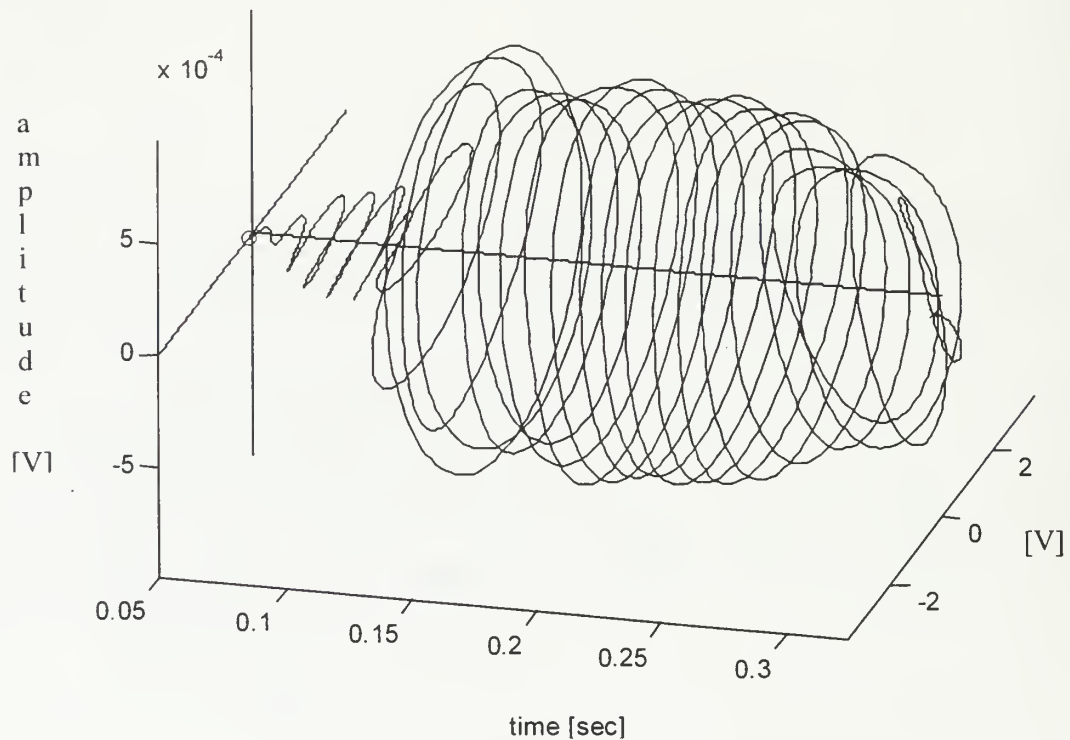


Figure 5.20. Hankel Plot of Southern Seismometer Velocity Signals for a 30 ft. Source-Receiver Separation Distance (+45P)

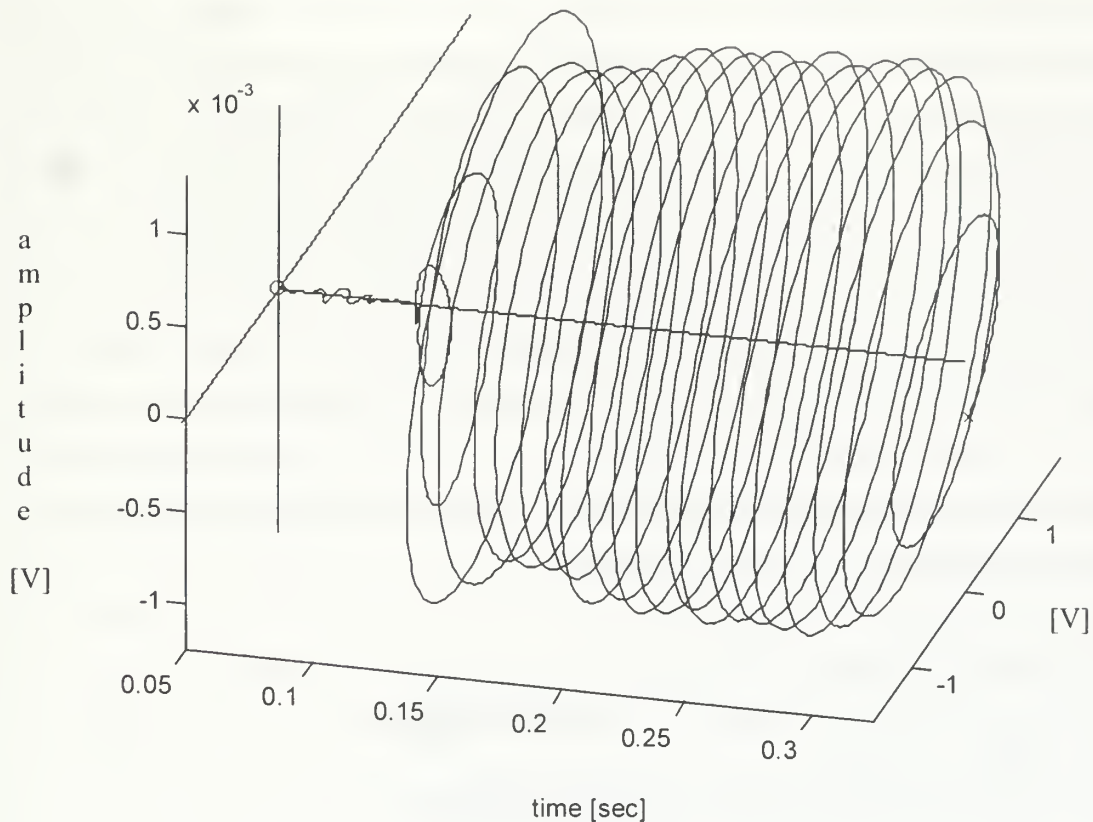


Figure 5.21. Hankel Plot of Northern Seismometer Velocity Signals for a 30 ft.
Source-Receiver Separation Distance (+45P)

The next set of the beach experiments was used to investigate the typical propagation distances that could be achieved with the discrete mode source. Since the results of the previous source tests were not available at the time of conducting this phase of the beach experimentation, the choice for follow-on seismometer position was completely arbitrary.

The two seismometers were initially positioned at distances of 30 and 45 ft and leapfrogged out to final distances of 90 and 105 ft, as shown in Layout II of Appendix D8. Using the same 50 V peak, 20 cycle, 100 Hz tone burst, sufficient Rayleigh wave signal strength was observed out to a distance of 90 ft, which far exceeded any of our initial expectations. Propagation distances of this order are just one of the features that make seismic sonar research so extremely important to mine warfare applications, since the maximum propagating distances for the best ground penetrating radar and

magnetometers is only 25 ft. Figure 5.22 shows an aggregate display of the source vertical acceleration (lowest trace) and the seismometer vertical velocity versus time at ranges from 30 ft (9.14 m) to 90 ft (27.43 m). Each seismometer signal trace has been normalized by the source vertical acceleration for that trace, as measured by the base mounted accelerometer. The behavior of the velocity amplitude with range should not be considered indicative of what would be observed for an end-on array of five seismometers receiving a single signal, as site conditions (e.g. tide, surface moisture, etc.) were evolving during the course of the data collection. The Rayleigh wave is clearly visible as the large amplitude wave train in each trace. The extracted group velocity is approximately 86 m/sec (see straight line in Figure 5.22), which agrees very well with that observed during ground truthing measurements.

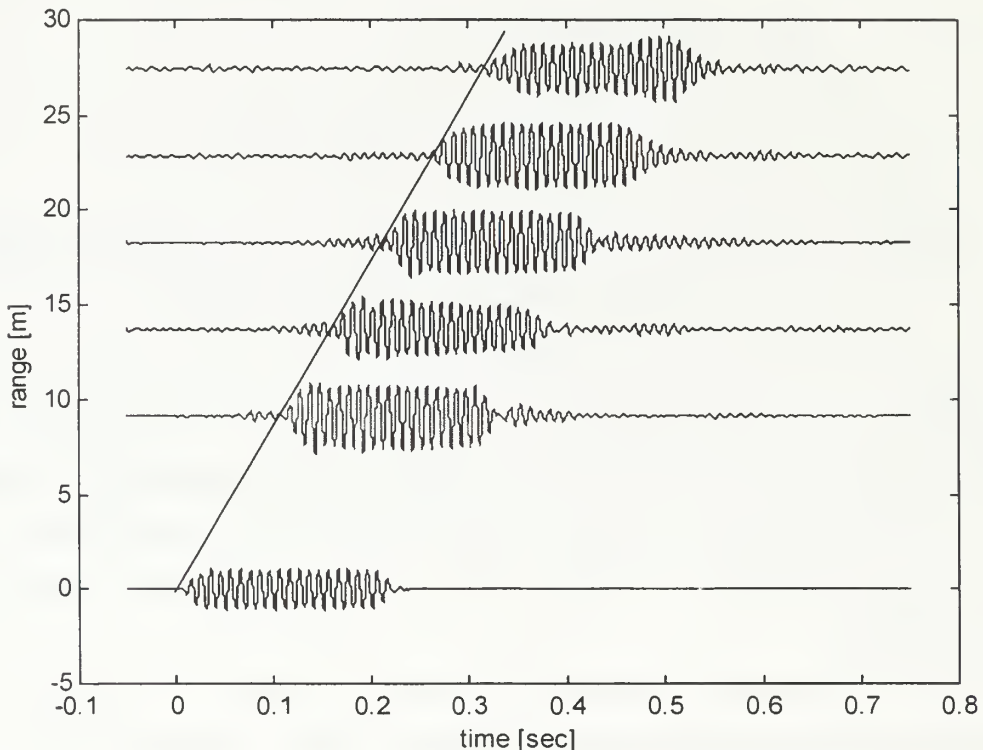


Figure 5.22. Rayleigh Wave Progression as a Function of Space and Time

Another interesting observation from this phase of the beach experimentation was that analysis of the particle motion observed at the seismometers showed prograde elliptical motion with respect to the source for all ranges, seismometer orientations, and

phase configurations. This result was unexpected, but can be explained. Assuming the beachfront to be a nearly homogeneous, isotropic, elastic medium, then the Rayleigh wave speed is independent of frequency (Refer to section II B). For a Rayleigh wave speed of 86 m/sec, a 100 Hz drive frequency corresponds to a Rayleigh wavelength of 0.86 m. Experimentation shows that the shift from retrograde to prograde elliptical motion for sediments occurs at approximately 0.1λ , or 8.6 cm (3.4 in) [Ref. 9]. Since the seismometers nominally sense the average particle motion and are nearly 25.4 cm (10 in) in length, most of their bulk resides below this depth. Thus, the observed motion is consistent with theory.

In order to verify this observation, another set of experiments were conducted using a 50 Hz drive frequency. At 50 Hz, assuming the same Rayleigh wave speed of 86 m/sec, the Rayleigh wavelength is 0.34 m. For this wavelength the corresponding turning point occurs at a depth of 17.2 cm (6.8 inches). To help eliminate any chance of misinterpreting the data the seismometers were only buried to a depth of 12.7 cm (5 in). Figures 5.23 and 5.24 are the Hankel plots of the seismometer velocity signals at 60 feet for drive frequencies of 100 Hz and 50 Hz, respectively.

As can be seen from the figures the sense of the particle motion is clearly different. Analysis of the Hankel plots showed that the particle motion as shown in Figure 5.23 was prograde elliptical and that of Figure 5.24 was retrograde elliptical. This illustration serves to show that accounting for the vector nature of the Rayleigh wave is extremely important, not only for discrete-mode propagation, but also for selective reception.

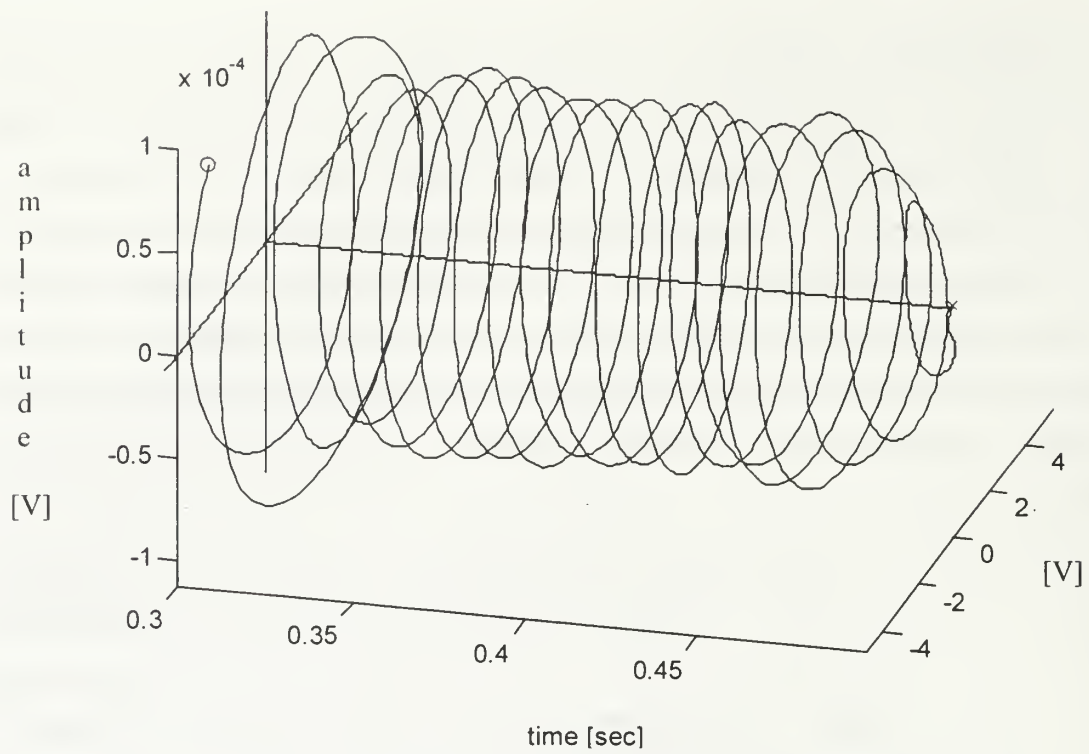


Figure 5.23. Hankel Plot of Seismometer Velocity Signals for a 60 ft.

Source-Receiver Separation Distance (100 Hz)

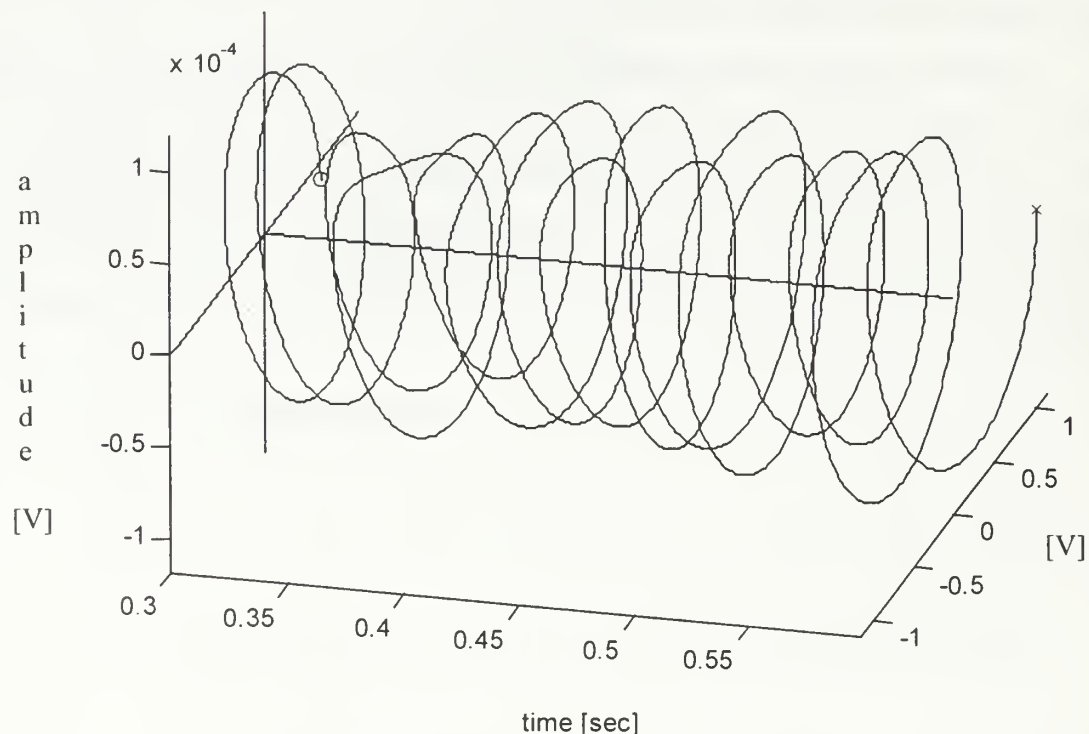


Figure 5.24. Hankel Plot of Seismometer Velocity Signals for a 60 ft.

Source-Receiver Separation Distance (50 Hz)

2. Selective Excitation

One of the goals of this thesis was to attempt to estimate how much of the input mechanical energy was being converted into Rayleigh waves. But because of the unpredictable nature of the source motion, this was not possible. It was assumed with the source design chosen and the information obtained on the operating characteristics of the Bass Shakers that it would be relatively easy to generate elliptical source motion. During the beach phase experimentation it was discovered that it was nearly impossible just to create circular motion at the source. Using equal amplitude drive voltages for the shakers and a -45° phase configuration should have produced retrograde circular motion and a $+45^\circ$, prograde circular motion. But, as can be seen from the hodograms of the base mounted accelerometer for the two cases, Figures 5.25 and 5.26, this was clearly not the result.

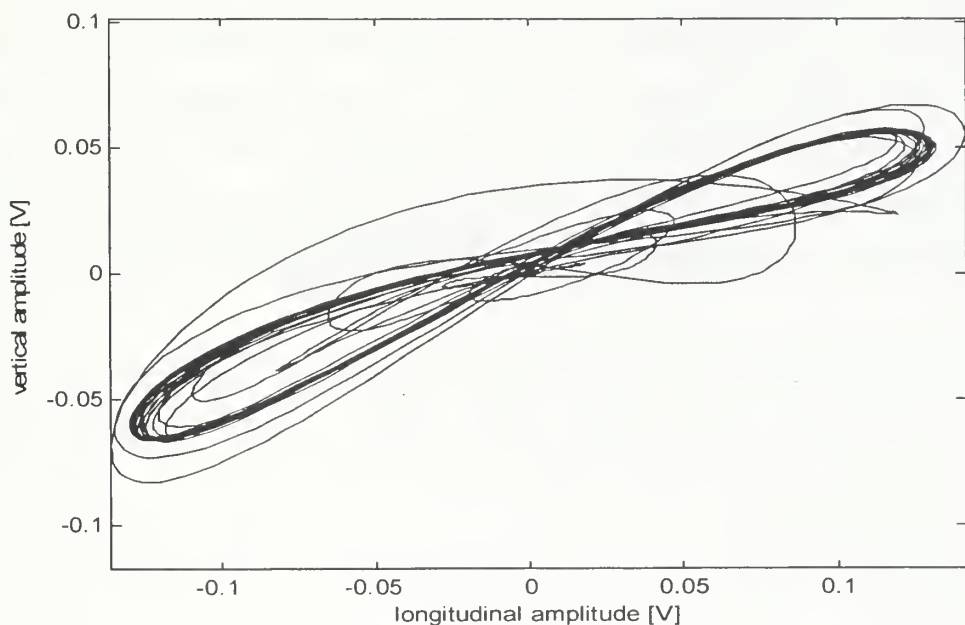


Figure 5.25. Hodogram of Accelerometer Signal (100 Hz, -45°)

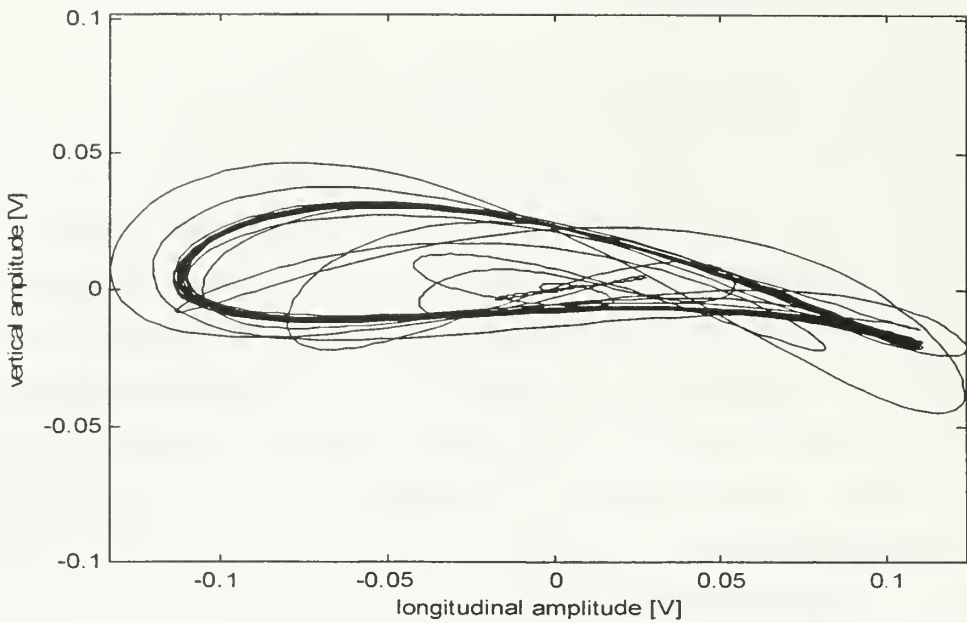


Figure 5.26. Hodogram of Accelerometer Signal (100 Hz, +45P)

Analysis of the hodograms from all the data files showed that the motion produced at the source depended explicitly on voltage, frequency, and phase. Furthermore, there is also a strong dependence on the elastic properties of the propagating medium. Examination of the accelerometer hodograms showed that longitudinal stimulation of the beach sediments was much more effective than vertical stimulation.

Follow-on experiments are planned in which it will be attempted to produce more optimum source motion. Even though the source motion was clearly not optimum, this did not seem to play a major part in stimulating the desired Rayleigh wave, at least at 100 Hz. Figure 5.27 is the Hankel plot of the seismometer velocity signals at 60 ft for a 20 V peak, 20 cycle, 100 Hz, tone burst with no phase difference between the shakers. Figure 5.28 displays the portion of the time record corresponding to the Rayleigh wave and the ratio of the longitudinal to vertical amplitude over the same time period.

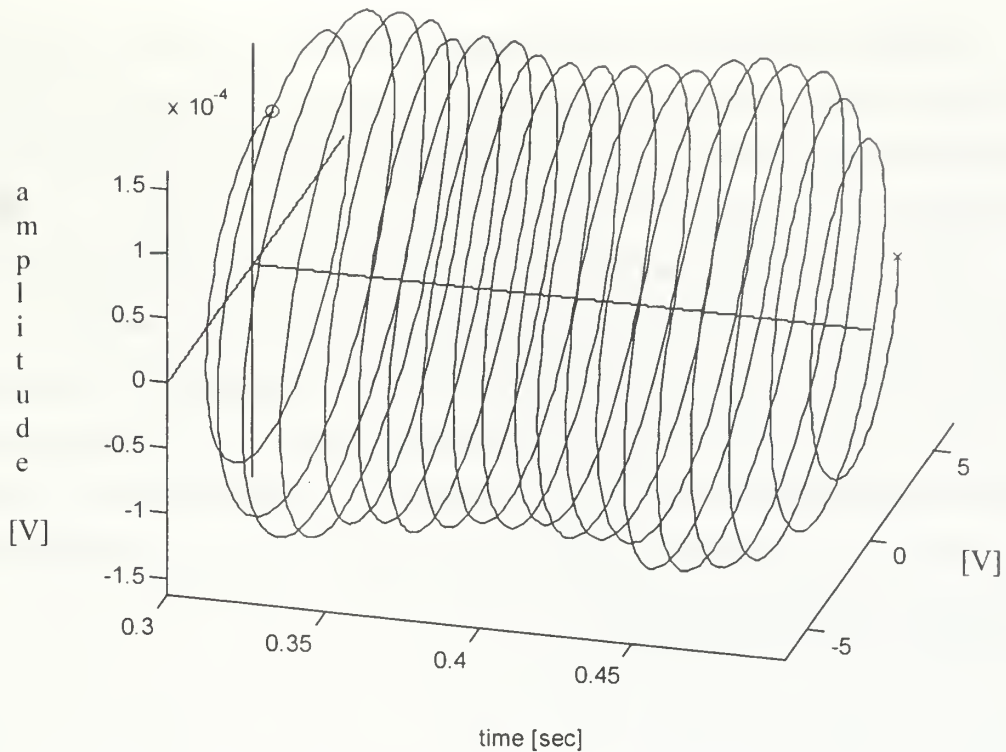


Figure 5.27. Hankel Plot of Seismometer Velocity Signals for a 60 ft. Source-Receiver Separation Distance

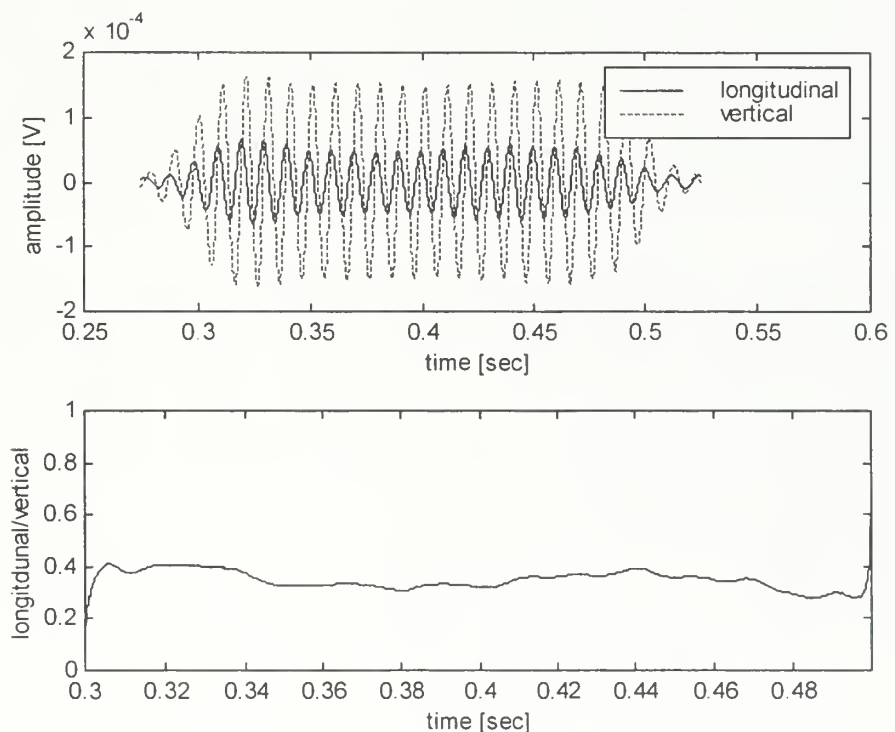


Figure 5.28. Ratio of Longitudinal and Vertical Rayleigh Wave Components

The uniformity of the wave is remarkable. Similar calculations were done for the seismometer velocity signals at 60 feet when phase differences of -45P, +45P, -32P, and +32P were used. In all four cases, similar looking Rayleigh waves were excited and the ratio of the wave components was nearly identical.

From analysis of the data files gathered during the beach phase experimentation it was obvious that the Rayleigh wave was the most significant disturbance along the interface boundary. At distances of 45 ft and smaller it appeared that no matter what phase configuration was used, all wave types were present, with the Rayleigh wave and vertically polarized shear wave the most dominant. But since body waves along the surface decay like $\frac{1}{r}$ and Rayleigh waves decay like $\frac{1}{\sqrt{r}}$, the influence of the body waves was negligible at distances over 60 ft.

VI. CONCLUSIONS AND RECOMMENDATIONS

This final chapter briefly synopsizes the noteworthy observations made during the conduct of the research described in this thesis and the conclusions that can be drawn from these observations. It also includes recommendations for follow-on research.

The major goal of this research project was to evaluate the concept of a discrete-mode interface (Rayleigh or Scholte) wave source. By selectively exciting the desired interface waves, it was theorized that significant reverberation suppression could be achieved, thus increasing the signal-to-noise ratio of a target echo in a seismic sonar detection system.

Based on the precepts from the theory of elasticity and the known characteristics of the desired interface waves, two different source concepts were designed and tested. The first discrete-mode source, i.e., the concept source as shown in Figure 4.1, was used to qualitatively probe in a laboratory environment the surface wave field created under various source motions. Experimentation with the concept source showed that a complex relationship existed between input source parameters, such as, frequency, phase, and driving voltage, and the propagating characteristics of the medium, and the resulting surface wave field. The limitations of the concept source and those imposed by the test tank made development of a field test source a necessity if any real progress was to be made.

To design a source that could be used under varying field conditions first required identifying a suitable vibration source and then constructing a matching source-to-ground coupling mechanism. Figure 4.3 shows the first version of the field test source. Again the beginning phases of the field experimentation were directed at evaluating the effects of varying source motions on the surface wave field. Results obtained during the various field tests lead to several modifications of the source-to-ground coupling mechanism until arriving at what was thought to be the best design (See Figure 5.16). It was with this final source design that all the beach phase testing was conducted.

Based on the known features of Rayleigh waves, it was believed that by stimulating the sediments at the source in an elliptical motion, Rayleigh waves could be selectively excited. To test this theory a series of experiments were conducted in which

the field test source was driven under several different modes of excitation. During these experiments it was observed that multiple types of interface waves and body waves were generated no matter what input source parameters were used. At source-to-receiver ranges greater than approximately 15 m (45 ft), the Rayleigh wave was clearly the largest interface disturbance, while the effects of the undesired waves quickly became negligible and were virtually undetectable at ranges greater than approximately 25 m (75 ft). Evaluation of the base-mounted accelerometer on the source showed that the field test source did not produce the elliptical motion expected for the applied input parameters. Because of this, it is difficult to determine whether the excitation of the undesired waves was due to the non-optimum nature of the source or that these undesired waves will always be present in practice. However, it was found that the medium itself acted as a selective filter for the interface waves after a few tens of meters of propagation.

Based on the experimental results obtained there are two major areas in which future discrete-mode excitation research efforts should be concentrated. The first area deals with correcting the deficiencies noted with the Bass Shakers and the source design. The Bass Shakers were not designed to be operated in the fashion utilized during the source testing. Thus, higher quality, greater power-handling excitors (e.g. shakers, actuators) must be incorporated into a new source. New sources must be identified that can be driven harder, but experience less distortion. Furthermore, complex source geometries such as the 45-degree orientation of the shakers used in the field test sources should be avoided. Such configurations simultaneously generate both longitudinal and vertical seismic motion. Future source designs should utilize simple vertical and horizontal excitation. This would serve two purposes, the first being that such an orientation still allows for the generation of elliptical motion at the source, and second that each component of the motion can be excited individually to study the resulting effects. Work has already begun in designing and constructing a new source made of orthogonal, servo-controlled, 20 lbf, linear actuators.

The second area deals with re-examining the experimental setups in order to better sample the various seismic wave types. This would serve to increase the researcher's knowledge of the different excitation potentials of the possible wave types and their associated excitation depths. Along these lines more experiments are needed to

further explore source control for optimal wave generation as a function of frequency and excitation depth. To better accomplish this task efforts should be made to computerize the source control so that the source motion can be monitored on a real-time basis.

Even though the results of this thesis were not as informative as initially desired the basic concept of discrete-mode excitation is promising. An important accomplishment of this thesis was to get the research out of the laboratory and onto the beach where the follow-on efforts can begin.

APPENDIX A. THEORETICAL PROPERTIES OF RAYLEIGH WAVES IN A HOMOGENEOUS, ISOTROPIC, ELASTIC HALF-SPACE

This appendix contains the various MATLAB programs that were used to reproduce the theoretical graphs contained within the reference texts on Rayleigh waves, some of which appear as figures within the body of the thesis. It also contains other programs written and their output, which provide further visual aid into the behavior of Rayleigh waves.

APPENDIX A1. VARIATIONS IN WAVE SPEED RATIOS AS A FUNCTION OF POISSON'S RATIO

```
% Filename: wavespeeds.m
% Written by: F.E. Gaghan
% Date Last Modified: 22 December 1997
% Purpose: This program numerically solves the Rayleigh wave equation
%           in an isotropic elastic half space. The wave equation
%           solutions are expressed as the ratio of the Rayleigh wave
%           speed to the shear wave speed as a function of the
%           Poisson's ratio. The ratio of the three wave types to the
%           shear wave speed is displayed graphically for Poisson's
%           ratios in the interval [0,1/2].
%
% Initialize required storage vectors
clear all;
speed_ratiosqd_root1=[]; speed_ratiosqd_root2=[];
speed_ratiosqd_root3=[];
longsqd_ratio1=[]; longsqd_ratio2=[]; longsqd_ratio3=[];
vertsqd_ratio1=[]; vertsqd_ratio2=[]; vertsqd_ratio3=[];
Rayleighsqd_root=[];

% For loop used to run through the desired Poisson's ratios
j=1;
for nu=[0:0.01:0.5];
    gammasqd(j)=(1-(2*nu))/(2-(2*nu));
    inv_gammasqd(j)=1/gammasqd(j);

    % Calculate the coefficients of the Rayleigh wave equation which is
    % cubic in the wave speed ratio
    p=-8;
    q=24-(16*gammasqd(j));
    r=(16*gammasqd(j))-16;
    a=((3*q)-(p^2))/3;
    b=((2*(p^3))-(9*p*q)+(27*r))/27;
    f=sqrt(((b^2)/4)+((a^3)/27));
    g=-(b/2)+f;
    h=-(b/2)-f;

    % Perform necessary manipulations of the coefficients to acquire
    % values in the correct quadrants when taking cube roots of complex
    % quantities
    if (f>0) & (g<0)
        A=(abs(g)^(1/3))^-1;
    else
        A=g^(1/3);
    end;%end-if (f>0) & (g<0)

    if (f>0) & (h<0)
        B=(abs(h)^(1/3))^-1;
    else
        B=h^(1/3);
    end;%end-if (f>0) & (h<0)
```

```

% Calculate and store the three roots of the square of the wave
% speed ratio
x1=A+B;
x2=(-(A+B)/2)+(((A-B)/2)*sqrt(-3));
x3=(-(A+B)/2)-(((A-B)/2)*sqrt(-3));
y1=x1-(p/3);
y2=x2-(p/3);
y3=x3-(p/3);
speed_ratiosqd_root1=[speed_ratiosqd_root1;y1];
speed_ratiosqd_root2=[speed_ratiosqd_root2;y2];
speed_ratiosqd_root3=[speed_ratiosqd_root3;y3];

% Calculate and store the ratio of longitudinal attenuation
% coefficient squared to the Rayleigh wave number squared
longsqd_ratio1=[longsqd_ratio1;1-(gammasqd(j)*y1)];
longsqd_ratio2=[longsqd_ratio2;1-(gammasqd(j)*y2)];
longsqd_ratio3=[longsqd_ratio3;1-(gammasqd(j)*y3)];

% Calculate and store the ratio of vertical attenuation coefficient
% squared to the Rayleigh wave number squared
vertsqd_ratio1=[vertsqd_ratio1;1-y1];
vertsqd_ratio2=[vertsqd_ratio2;1-y2];
vertsqd_ratio3=[vertsqd_ratio3;1-y3];

j=j+1;
end;%end-for nu

% Store the vectors into matrices
speed_ratiosqd_roots=[speed_ratiosqd_root1,speed_ratiosqd_root2,
speed_ratiosqd_root3];
longsqd_ratios=[longsqd_ratio1, longsqd_ratio2, longsqd_ratio3];
vertsqd_ratios=[vertsqd_ratio1, vertsqd_ratio2, vertsqd_ratio3];

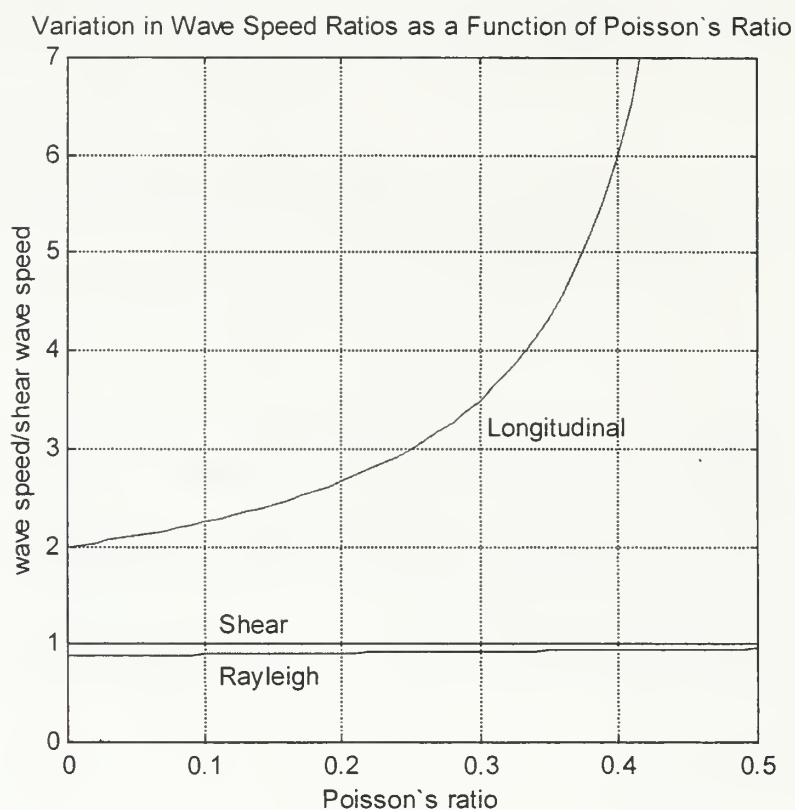
% Perform required logical comparisons to keep only the roots that
% satisfy the Rayleigh wave criteria
suitable=(longsqd_ratios>=0) & (vertsqd_ratios>=0);
for m=1:(j-1)
    for n=1:3
        if suitable(m,n)
            Rayleighsqd_root=[Rayleighsqd_root;speed_ratiosqd_roots(m,n)];
        end;%end-if suitable
    end;%end-for n
end;%end-for m

Rayleigh_root=sqrt(Rayleighsqd_root);
nu=[0:0.01:0.5];
shear_speed=ones(1,length(nu));

% Plot the ratio of Rayleigh wave speed to shear wave speed versus
% Poisson's ratio
figure(1);
plot(nu,shear_speed,nu,Rayleigh_root,nu,inv_gammasqd);
axis([0,0.5,0,7]);
grid on; axis square;
xlabel('Poisson's ratio'); ylabel('wave speed/shear wave speed');
text(.11,1.2,'Shear'); text(.11,0.65,'Rayleigh');
text(0.305,3.2,'Longitudinal');

```

```
title('Variation in Wave Speed Ratios as a Function of Poisson's Ratio');
```



APPENDIX A2. VARIATION IN RAYLEIGH WAVE SPEED AS A FUNCTION OF POISSON'S RATIO

```
% Filename: rayleighspeed.m
% Written by: F.E. Gaghan
% Date Last Modified: 02 December 1997
% Purpose: This program numerically solves the Rayleigh wave equation
%           in an isotropic elastic half space. The wave equation
%           solutions are expressed as the ratio of the Rayleigh wave
%           speed to the shear wave speed as a function of the
%           Poisson's ratio. The wave speed ratio is displayed
%           graphically for Poisson's ratios in the interval [-1,1/2].
```

```
% Initialize required storage vectors
clear all;
speed_ratiosqd_root1=[]; speed_ratiosqd_root2=[];
speed_ratiosqd_root3=[];
longsqd_ratio1=[]; longsqd_ratio2=[]; longsqd_ratio3=[];
vertsqd_ratio1=[]; vertsqd_ratio2=[]; vertsqd_ratio3=[];
Rayleighsqd_root=[];
```

```
% For loop used to run through the desired Poisson's ratios
j=1;
for nu=[0:0.05:0.5];
    gammasqd=(1-(2*nu))/(2-(2*nu));

    % Calculate the coefficients of the Rayleigh wave equation which is
    % cubic in the wave speed ratio
    p=-8;
    q=24-(16*gammasqd);
    r=(16*gammasqd)-16;
    a=((3*q)-(p^2))/3;
    b=((2*(p^3))-(9*p*q)+(27*r))/27;
    f=sqrt(((b^2)/4)+((a^3)/27));
    g=- (b/2)+f;
    h=- (b/2)-f;

    % Perform necessary manipulations of the coefficients to acquire
    % values in the correct quadrants when taking cube roots of complex
    % quantities
    if (f>0) & (g<0)
        A=(abs(g)^(1/3))^-1;
    else
        A=g^(1/3);
    end;%end-if (f>0) & (g<0)

    if (f>0) & (h<0)
        B=(abs(h)^(1/3))^-1;
    else
        B=h^(1/3);
    end;%end-if (f>0) & (h<0)
```

```

% Calculate and store the three roots of the square of the wave
% speed ratio
x1=A+B;
x2=(-(A+B)/2)+(((A-B)/2)*sqrt(-3));
x3=(-(A+B)/2)-(((A-B)/2)*sqrt(-3));
y1=x1-(p/3);
y2=x2-(p/3);
y3=x3-(p/3);
speed_ratiosqd_root1=[speed_ratiosqd_root1;y1];
speed_ratiosqd_root2=[speed_ratiosqd_root2;y2];
speed_ratiosqd_root3=[speed_ratiosqd_root3;y3];

% Calculate and store the ratio of longitudinal attenuation
% coefficient squared to the Rayleigh wave number squared
longsqd_ratio1=[longsqd_ratio1;1-(gammasqd*y1)];
longsqd_ratio2=[longsqd_ratio2;1-(gammasqd*y2)];
longsqd_ratio3=[longsqd_ratio3;1-(gammasqd*y3)];

% Calculate and store the ratio of vertical attenuation coefficient
% squared to the Rayleigh wave number squared
vertsqd_ratio1=[vertsqd_ratio1;1-y1];
vertsqd_ratio2=[vertsqd_ratio2;1-y2];
vertsqd_ratio3=[vertsqd_ratio3;1-y3];

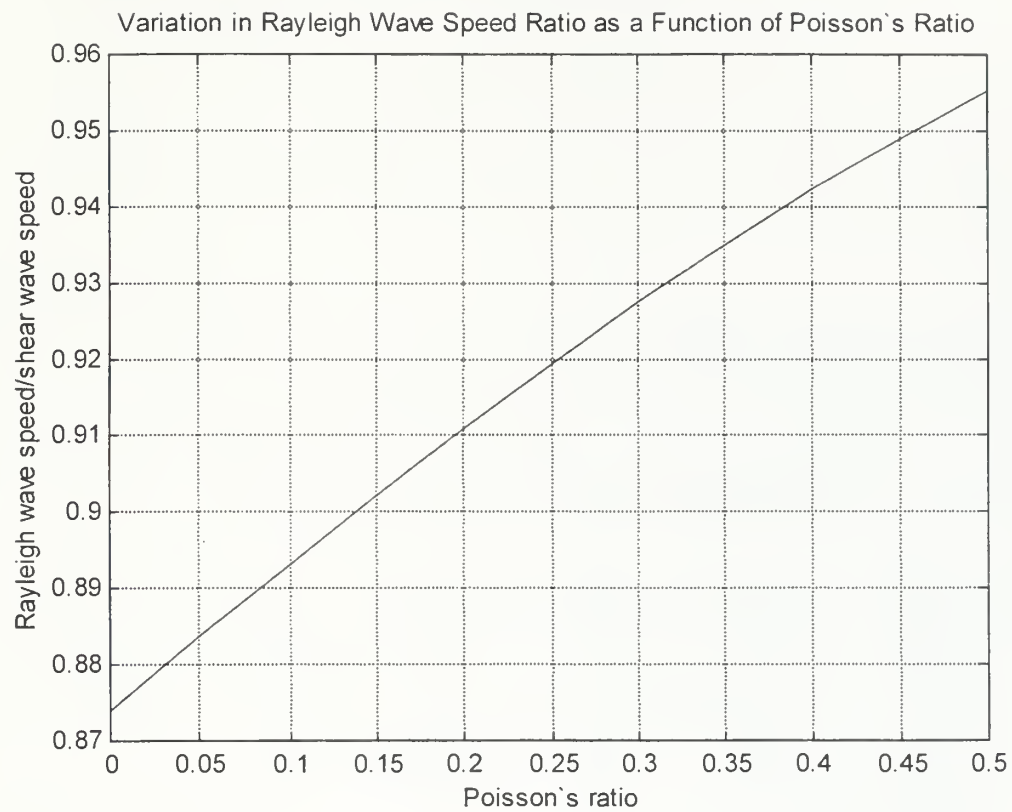
j=j+1;
end;%end-for nu

% Store the vectors into matrices
speed_ratiosqd_roots=[speed_ratiosqd_root1,speed_ratiosqd_root2,
speed_ratiosqd_root3];
longsqd_ratios=[longsqd_ratio1,longsqd_ratio2,longsqd_ratio3];
vertsqd_ratios=[vertsqd_ratio1,vertsqd_ratio2,vertsqd_ratio3];

% Perform required logical comparisons to keep only the roots that
% satisfy the Rayleigh wave criteria
suitable=(longsqd_ratios>=0) & (vertsqd_ratios>=0);
for m=1:(j-1)
    for n=1:3
        if suitable(m,n)
            Rayleighsqd_root=[Rayleighsqd_root;speed_ratiosqd_roots(m,n)];
        end;%end-if suitable
    end;%end-for n
end;%end-for m
Rayleigh_root=sqrt(Rayleighsqd_root);
nu=[0:0.05:0.5];

% Plot the ratio of Rayleigh wave speed to shear wave speed versus
% Poisson's ratio
figure(1);
plot(nu,Rayleigh_root);
grid on;
xlabel('Poisson's ratio'); ylabel('Rayleigh wave speed/shear wave
speed');
title('Variation in Rayleigh Wave Speed Ratio as a Function of
Poisson's Ratio');

```



APPENDIX A3. ELLIPTICAL PARTCILE MOTION INDUCED BY RAYLEIGH WAVE

```
% Filename: rayleighellipses.m
% Written by: F.E. Gaghan
% Date Last Modified: 02 December 1997
% Purpose: This program is used to graphically display the varying
%           particle motions induced by propagating Rayleigh waves in an
%           elastic medium. Specifically it is used to show how the
%           particle motion begins as retrograde elliptical and
%           progresses to prograde elliptical with depth.

% Initialize required space and wave parameters
clear all;
k=(2*pi*100)/300;
w=k*300;
t=[0:0.1:2]/200;
wt=w*t;
wt_t0=0;
C=0.2;

% Set special plot commands
axes('box','on'); hold on; grid on; axis equal;

% Outer for loop used to step through five various depths along the
% z-axis within the medium
for x3=[0,-0.3,-0.6,-0.9,-1.2]

    % Inner loop used to step through the longitudinal ranges in the
    % direction of propagation along the x-axis
    for x1=[0,0.5,1,1.5,2,2.5];

        % Algebraic manipulations required to calculate the longitudinal
        % particle displacement
        a1=exp(0.8475*k*x3)-0.5773*exp(0.3933*k*x3);
        c1=sin(wt-(k*x1));
        u1=C*(a1*c1);
        xl1=u1+x1;

        % Algebraic manipulations required to calculate the vertical
        % particle displacement
        a3=-0.8475*exp(0.8475*k*x3)+1.4679*exp(0.3933*k*x3);
        c3=cos(wt-(k*x1));
        u3=C*(a3*c3);
        x3u3=u3+x3;

        % Plot elliptical particle motion
        figure(1);
        plot(xl1,x3u3,'g.');

    end
end
```

```

% Algebraic manipulations required to calculate the wave motion
% in the longitudinal direction
x1_t0=[0:0.05:2.5];
last=length(x1_t0);
x3_t0=x3*ones(1,last);
c1_t0=sin(wt_t0-(k.*x1_t0));
u1_t0=C*(a1.*c1_t0);
x1u1_t0=u1_t0+x1_t0;

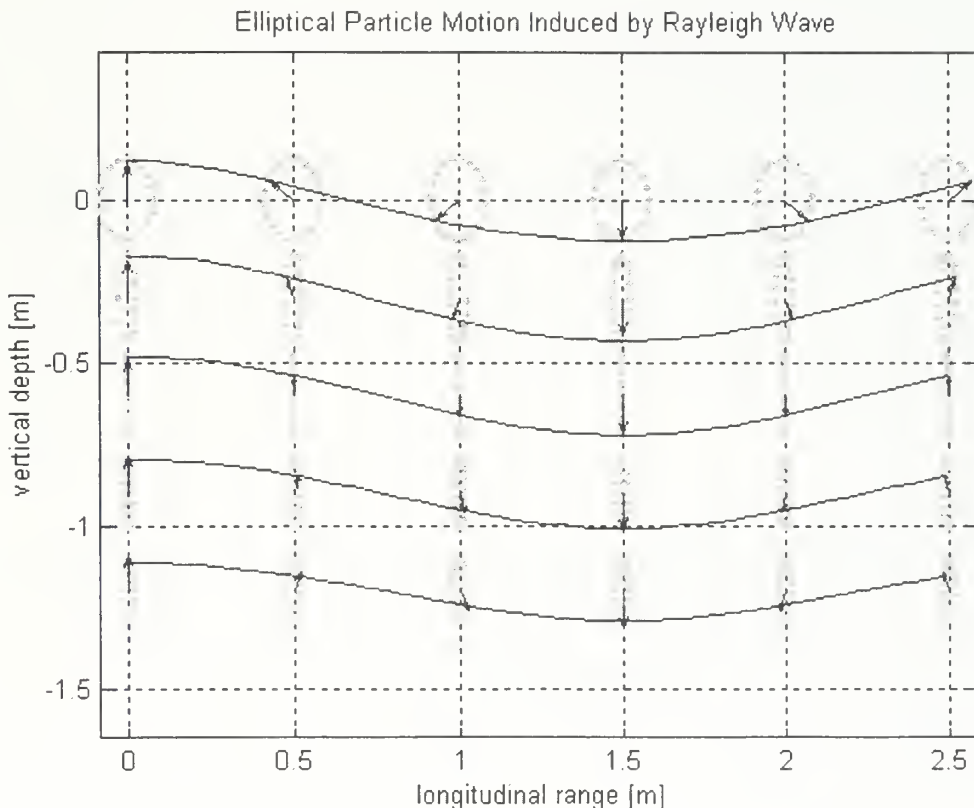
% Algebraic manipulations required to calculate the wave motion
% in the vertical direction
c3_t0=cos(wt_t0-(k.*x1_t0));
u3_t0=C*(a3.*c3_t0);
x3u3_t0=u3_t0+x3;
plot(x1u1_t0,x3u3_t0,'b');

% Plot Rayleigh wave motion
quiver(x1_t0(1:10:last),x3_t0(1:10:last),u1_t0(1:10:last),...
u3_t0(1:10:last),0.125,'k');

end;%end-for x1
end;%end-for x3

xlabel('longitudinal range [m]'); ylabel('vertical depth [m]');
title('Elliptical Particle Motion Induced by Rayleigh Wave');

```



APPENDIX A4. LONGITUDINAL AND VERTICAL PARTICLE DISPLACEMENTS

```
% Filename: rayleighdisplacements.m
% Written by: F.E. Gaghan
% Date Last Modified: 02 December 1997
% Purpose: This program is used to graphically display the horizontal
%           and vertical particle displacements induced by a propagating
%           Rayleigh wave for a specified value of Poisson's ratio. The
%           curves displayed are the particle displacement amplitudes
%           normalized by the vertical particle displacement at the
%           surface as a function of depth normalized by the Rayleigh
%           wave number.

% Initialize required storage vectors
clear all;
nu=0.25;
gammasqd=(1-(2*nu))/(2-(2*nu));

% Calculate the coefficients required to solve the Rayleigh wave
% equation which is cubic in the wave speed ratio
p=-8;
q=24-(16*gammasqd);
r=(16*gammasqd)-16;
a=((3*q)-(p^2))/3;
b=((2*(p^3))-(9*p*q)+(27*r))/27;
f=sqrt(((b^2)/4)+((a^3)/27));
g=-(b/2)+f;
h=-(b/2)-f;

% Perform necessary manipulations of the coefficients to acquire values
% in the correct quadrants when taking cube roots of complex quantities
if (f>0) & (g<0)
    A=(abs(g)^(1/3))*-1;
else
    A=g^(1/3);
end;%end-if (f>0) & (g<0)
if (f>0) & (h<0)
    B=(abs(h)^(1/3))*-1;
else
    B=h^(1/3);
end;%end-if (f>0) & (h<0)

% Calculate and store the three roots of the wave speed ratio squared
x1=A+B;
x2=(-(A+B)/2)+(((A-B)/2)*sqrt(-3));
x3=(-(A+B)/2)-(((A-B)/2)*sqrt(-3));
y1=x1-(p/3);
y2=x2-(p/3);
y3=x3-(p/3);
speed_ratiosqd_root1=y1;
speed_ratiosqd_root2=y2;
speed_ratiosqd_root3=y3;
speed_ratiosqd_roots=[y1,y2,y3];
```

```

% Calculate and store the ratio of longitudinal attenuation coefficient
% squared to the Rayleigh wave number squared
longsqd_ratio1=1-(gammasqd*y1);
longsqd_ratio2=1-(gammasqd*y2);
longsqd_ratio3=1-(gammasqd*y3);
longsqd_ratios=[longsqd_ratio1, longsqd_ratio2, longsqd_ratio3];

% Calculate and store the ratio of vertical attenuation coefficient
% squared to the Rayleigh wave number squared
vertsqd_ratio1=1-y1;
vertsqd_ratio2=1-y2;
vertsqd_ratio3=1-y3;
vertsqd_ratios=[vertsqd_ratio1, vertsqd_ratio2, vertsqd_ratio3];

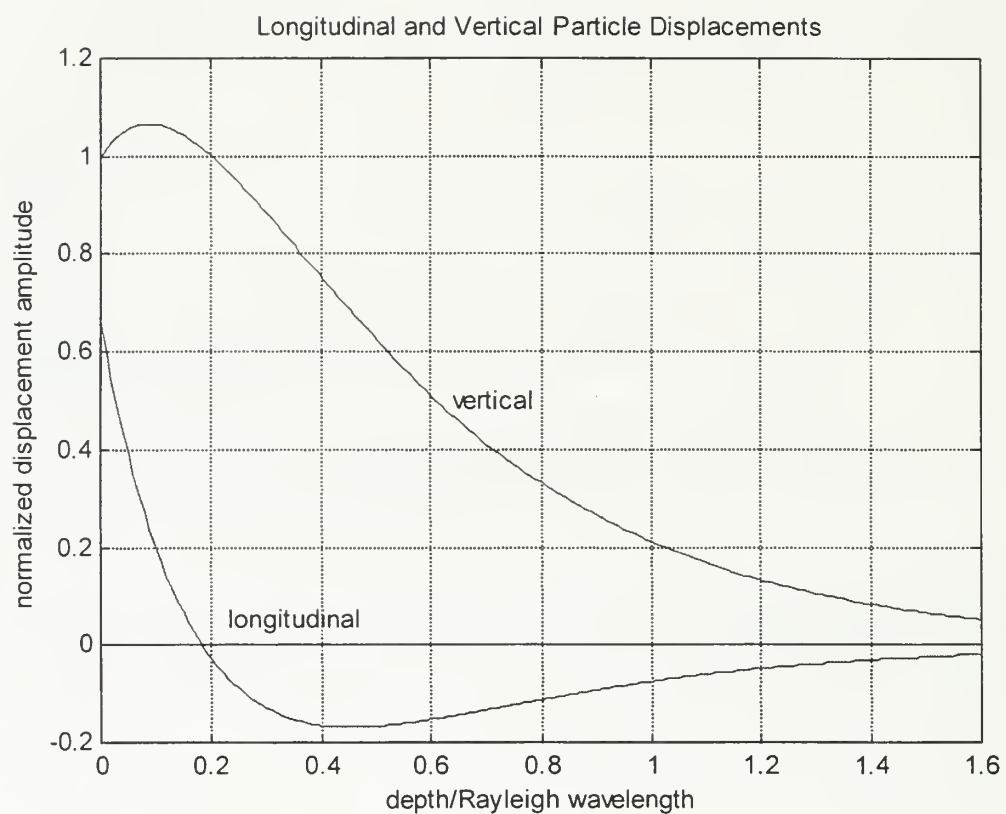
% Perform required logical comparisons to keep only the root that
% satisfies the Rayleigh wave criteria
suitable=(longsqd_ratios>=0) & (vertsqd_ratios>=0);
for m=1:3
    if suitable(m)
        Rayleighsqd_root=speed_ratiosqd_roots(m);
        index=m;
    end;%end-if suitable
end; %end-for m

% Calculate the values of the Rayleigh wave root and the attenuation
% ratios
Rayleigh_root=sqrt(Rayleighsqd_root);
Rayleigh_long_ratio=sqrt(longsqd_ratios(index));
Rayleigh_vert_ratio=sqrt(vertsqd_ratios(index));

% Calculate the normalized horizontal and vertical particle
% displacements
q=Rayleigh_long_ratio;
s=Rayleigh_vert_ratio;
long_const=(2*q*s)/((s^2)+1);
vert_const=2/((s^2)+1);
depth=[0:0.01:1.6];
surface_layer=zeros(1,length(depth));
krz=depth*(2*pi);
u3=(exp(-q*krz)-(vert_const*exp(-s*krz)));
u30=(1-vert_const);
u3_u30=u3/u30;
u1=exp(-q*krz)-(long_const*exp(-s*krz));
u1_u30=u1/(-q*u30);

% Plot the normalized horizontal and vertical particle displacements
figure(1);
plot(depth,surface_layer,depth,u3_u30,depth,u1_u30);
xlabel('depth/Rayleigh wave number');
ylabel('normalized displacement amplitude');
text(0.22,0.05,'longitudinal'); text(0.62,0.5,'vertical');
title('Longitudinal and Vertical Particle Displacements');
grid on;

```



APPENDIX A5. TENSILE AND SHEAR STRESSES

```
% Filename: rayleighstresses.m
% Written by: F.E. Gaghan
% Date Last Modified: 22 December 1997
% Purpose: This program is used to graphically display the horizontal
% and vertical particle stresses induced by a propagating
% Rayleigh wave for a specified value of Poisson's ratio. The
% curves displayed are the particle stress amplitudes
% normalized by the horizontal particle stress at the surface
% as a function of depth normalized by the Rayleigh wave
% number.

% Initialize required storage vectors
clear all;
nu=0.25;
gammasqd=(1-(2*nu))/(2-(2*nu));
gammasqdiv=1/gammasqd;
lame=(2*nu)/(1-(2*nu));

% Calculate the coefficients required to solve the Rayleigh wave
% equation which is cubic in the wave speed ratio
p=-8;
q=24-(16*gammasqd);
r=(16*gammasqd)-16;
a=((3*q)-(p^2))/3;
b=((2*(p^3))-(9*p*q)+(27*r))/27;
f=sqrt(((b^2)/4)+((a^3)/27));
g=-(b/2)+f;
h=-(b/2)-f;

% Perform necessary manipulations of the coefficients to acquire values
% in the correct quadrants when taking cube roots of complex quantities
if (f>0) & (g<0)
    A=(abs(g)^(1/3))*-1;
else
    A=g^(1/3);
end;%end-if (f>0) & (g<0)
if (f>0) & (h<0)
    B=(abs(h)^(1/3))*-1;
else
    B=h^(1/3);
end;%end-if (f>0) & (h<0)

% Calculate and store the three roots of the wave speed ratio squared
x1=A+B;
x2=(-(A+B)/2)+(((A-B)/2)*sqrt(-3));
x3=(-(A+B)/2)-(((A-B)/2)*sqrt(-3));
y1=x1-(p/3);
y2=x2-(p/3);
y3=x3-(p/3);
speed_ratiosqd_root1=y1;
speed_ratiosqd_root2=y2;
speed_ratiosqd_root3=y3;
speed_ratiosqd_roots=[y1,y2,y3];
```

```

% Calculate and store the ratio of longitudinal attenuation coefficient
% squared to the Rayleigh wave number squared
longsqd_ratio1=1-(gammasqd*y1);
longsqd_ratio2=1-(gammasqd*y2);
longsqd_ratio3=1-(gammasqd*y3);
longsqd_ratios=[longsqd_ratio1, longsqd_ratio2, longsqd_ratio3];

% Calculate and store the ratio of vertical attenuation coefficient
% squared to the Rayleigh wave number squared
vertsqd_ratio1=1-y1;
vertsqd_ratio2=1-y2;
vertsqd_ratio3=1-y3;
vertsqd_ratios=[vertsqd_ratio1, vertsqd_ratio2, vertsqd_ratio3];

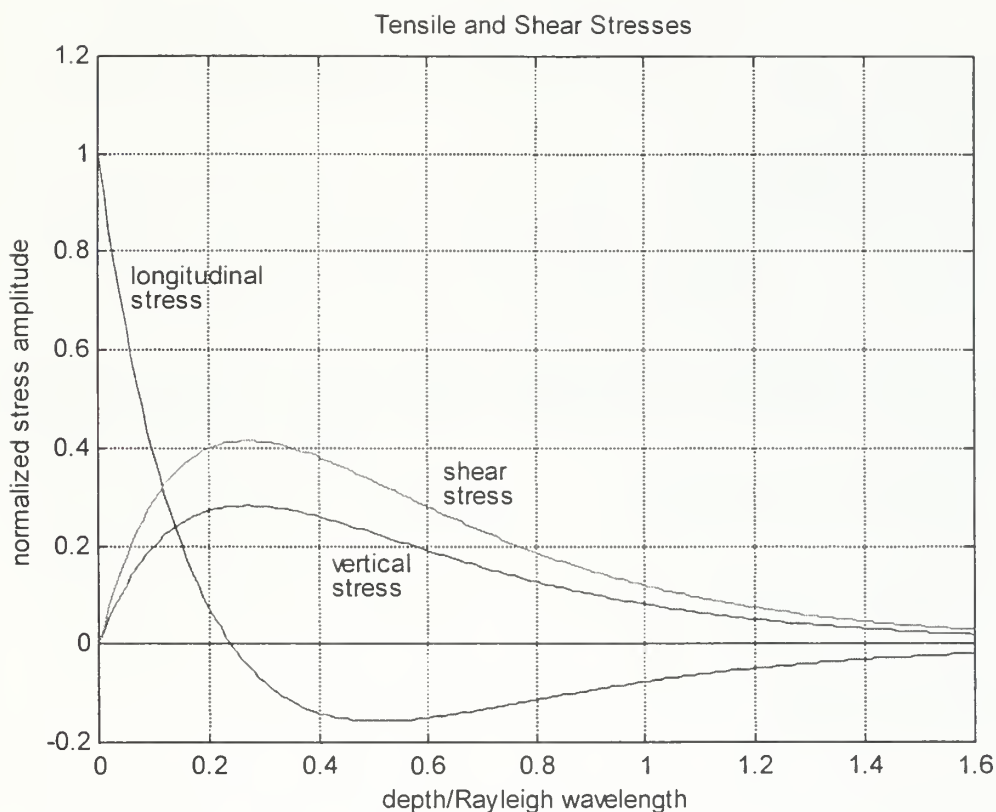
% Perform required logical comparisons to keep only the root that
% satisfies the Rayleigh wave criteria
suitable=(longsqd_ratios>=0) & (vertsqd_ratios>=0);
for m=1:3
    if suitable(m)
        Rayleighsqd_root=speed_ratiosqd_roots(m);
        index=m;
    end;%end-if suitable
end; %end-for m

% Calculate the values of the Rayleigh wave root and the attenuation
% ratios
Rayleigh_root=sqrt(Rayleighsqd_root);
Rayleigh_long_ratio=sqrt(longsqd_ratios(index));
Rayleigh_vert_ratio=sqrt(vertsqd_ratios(index));

% Calculate the normalized horizontal and vertical particle stresses
q=Rayleigh_long_ratio;
s=Rayleigh_vert_ratio;
long_const=(2*q*s)/((s^2)+1);
vert_const=2/((s^2)+1);
depth=[0:0.01:1.6];
surface_layer=zeros(1,length(depth));
krz=depth*(2*pi);
sigmaxx=(gammasqdin*exp(-q*krz))-
(lame*(q^2)*exp(-q*krz))-(2*long_const*exp(-s*krz));
sigmaxx0=gammasqdin-(lame*(q^2))-(2*long_const);
sigmaxx_xx0=sigmaxx/sigmaxx0;
sigmazz=(-gammasqdin*(q^2)*exp(-q*krz))+
(lame*exp(-q*krz))+(2*long_const*exp(-s*krz));
sigmazz_xx0=sigmazz/sigmaxx0;
sigmaxz=(-2*q*exp(-q*krz))+(2*q*exp(-s*krz));
sigmaxz_xx0=sigmaxz/sigmaxx0;

```

```
% Plot the normalized horizontal and vertical particle stresses
figure(1);
plot(depth,surface_layer,depth,sigmaxx_xx0,depth,sigmazz_xx0,
depth,sigmaxz_xx0);
xlabel('depth/Rayleigh wave number');
ylabel('normalized stress amplitude');
text(0.06,0.75,'longitudinal'); text(0.63,0.35,'shear');
text(0.42,0.16,'vertical');
text(0.06,0.7,'stress'); text(0.63,0.3,'stress');
text(0.42,0.11,'stress');
title('Tensile and Shear Stresses');
grid on;
```



APPENDIX A6. VARIATION IN RATIO OF LONGITUDINAL TO VERTICAL PARTICLE DISPLACEMENT AS A FUNCTION OF POISSON'S RATIO

```
% Filename: rayleighaxesratio.m
% Written by: F.E. Gaghan
% Date Last Modified: 10 February 1998
% Purpose: This program is used to graphically display the ratio of the
%           longitudinal to vertical particles displacements at the
%           surface during Rayleigh wave propagation as a function of
%           the Poisson's ratio. The calculations are for a homogeneous,
%           isotropic, elastic half-space.

% Establish desired Poisson's ratio values
clear all;
nu=[0.0:0.01:0.5];
for i=1:length(nu)
    gammasqd=(1-(2*nu(i)))/(2-(2*nu(i)));
    % Calculate the coefficients required to solve the Rayleigh wave
    % equation which is cubic in the wave speed ratio
    p=-8;
    q=24-(16*gammasqd);
    r=(16*gammasqd)-16;
    a=((3*q)-(p^2))/3;
    b=((2*(p^3))-(9*p*q)+(27*r))/27;
    f=sqrt(((b^2)/4)+((a^3)/27));
    g=-(b/2)+f;
    h=-(b/2)-f;
    % Perform necessary manipulations of the coefficients to acquire
    % values in the correct quadrants when taking cube roots of complex
    % quantities
    if (f>0) & (g<0)
        A=(abs(g)^(1/3))*-1;
    else
        A=g^(1/3);
    end;%end-if (f>0) & (g<0)
    if (f>0) & (h<0)
        B=(abs(h)^(1/3))*-1;
    else
        B=h^(1/3);
    end;%end-if (f>0) & (h<0)
    % Calculate and store the three roots of the wave speed ratio
    % squared
    x1=A+B;
    x2=(-(A+B)/2)+(((A-B)/2)*sqrt(-3));
    x3=(-(A+B)/2)-(((A-B)/2)*sqrt(-3));
    y1=x1-(p/3);
    y2=x2-(p/3);
    y3=x3-(p/3);
    speed_ratiosqd_root1=y1;
    speed_ratiosqd_root2=y2;
    speed_ratiosqd_root3=y3;
    speed_ratiosqd_roots=[y1,y2,y3];
```

```

% Calculate and store the ratio of longitudinal attenuation
% coefficient squared to the Rayleigh wave number squared
longsqd_ratio1=1-(gammasqd*y1);
longsqd_ratio2=1-(gammasqd*y2);
longsqd_ratio3=1-(gammasqd*y3);
longsqd_ratios=[longsqd_ratio1, longsqd_ratio2, longsqd_ratio3];

% Calculate and store the ratio of vertical attenuation coefficient
% squared to the Rayleigh wave number squared
vertsqd_ratio1=1-y1;
vertsqd_ratio2=1-y2;
vertsqd_ratio3=1-y3;
vertsqd_ratios=[vertsqd_ratio1, vertsqd_ratio2, vertsqd_ratio3];

% Perform required logical comparisons to keep only the root that
% satisfies the Rayleigh wave criteria
suitable=(longsqd_ratios>=0) & (vertsqd_ratios>=0);
for m=1:3
    if suitable(m)
        Rayleighsqd_root=speed_ratiosqd_roots(m);
        index=m;
    end;%end-if suitable
end; %end-for m

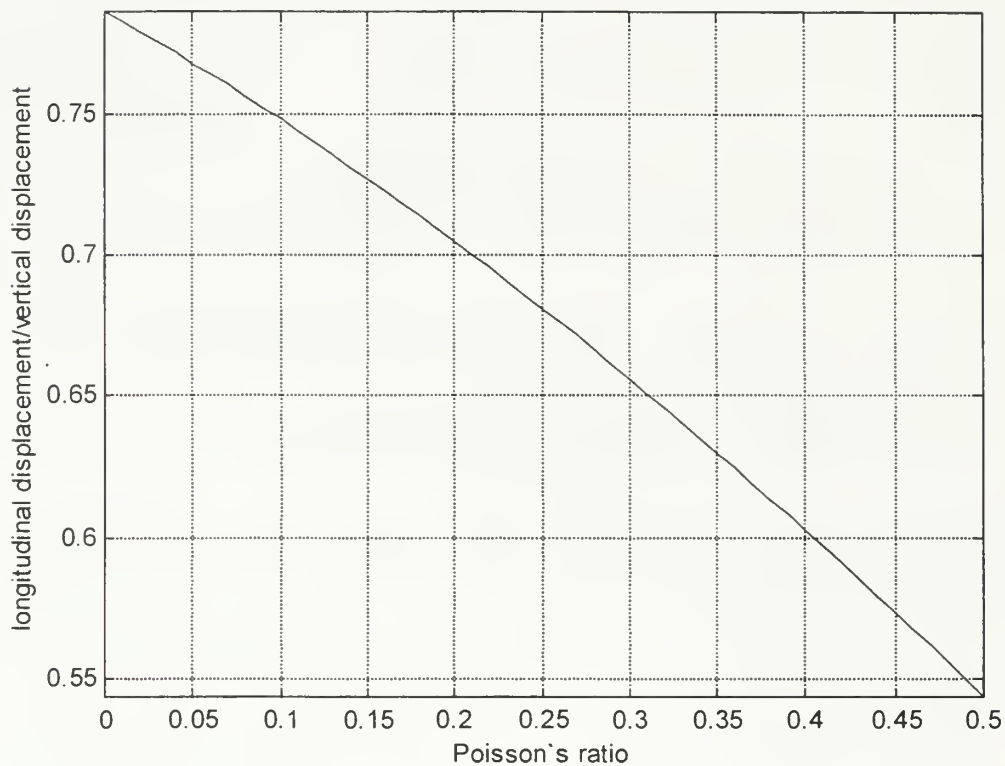
% Calculate the values of the Rayleigh wave root and the
% attenuation ratios
Rayleigh_root=sqrt(Rayleighsqd_root);
Rayleigh_long_ratio=sqrt(longsqd_ratios(index));
Rayleigh_vert_ratio=sqrt(vertsqd_ratios(index));

% Calculate the normalized horizontal and vertical particle
% displacements and the ratio of horizontal to vertical particle
% displacements
q=Rayleigh_long_ratio;
s=Rayleigh_vert_ratio;
long_const=(2*q*s)/((s^2)+1);
vert_const=2/((s^2)+1);
u30=1-vert_const;
u10=1-long_const;
axesratio(i)=u10/(-q*u30);
end; %end-for i

% Plot the ratio of horizontal to vertical particle displacements as a
% function of the Poisson's ratio
figure(1);
plot(nu, axesratio);
xlabel('Poisson's ratio');
ylabel('longitudinal displacement/vertical displacement');
title('Longitudinal and Vertical Particle Displacements');
axis([nu(1), nu(i), min(axesratio), max(axesratio)]);
grid on;

```

Variation in Ratio of Longitudinal to Vertical Particle Displacements



APPENDIX A7. VARIATION IN RAYLEIGH WAVES AS A FUNCTION OF DEPTH

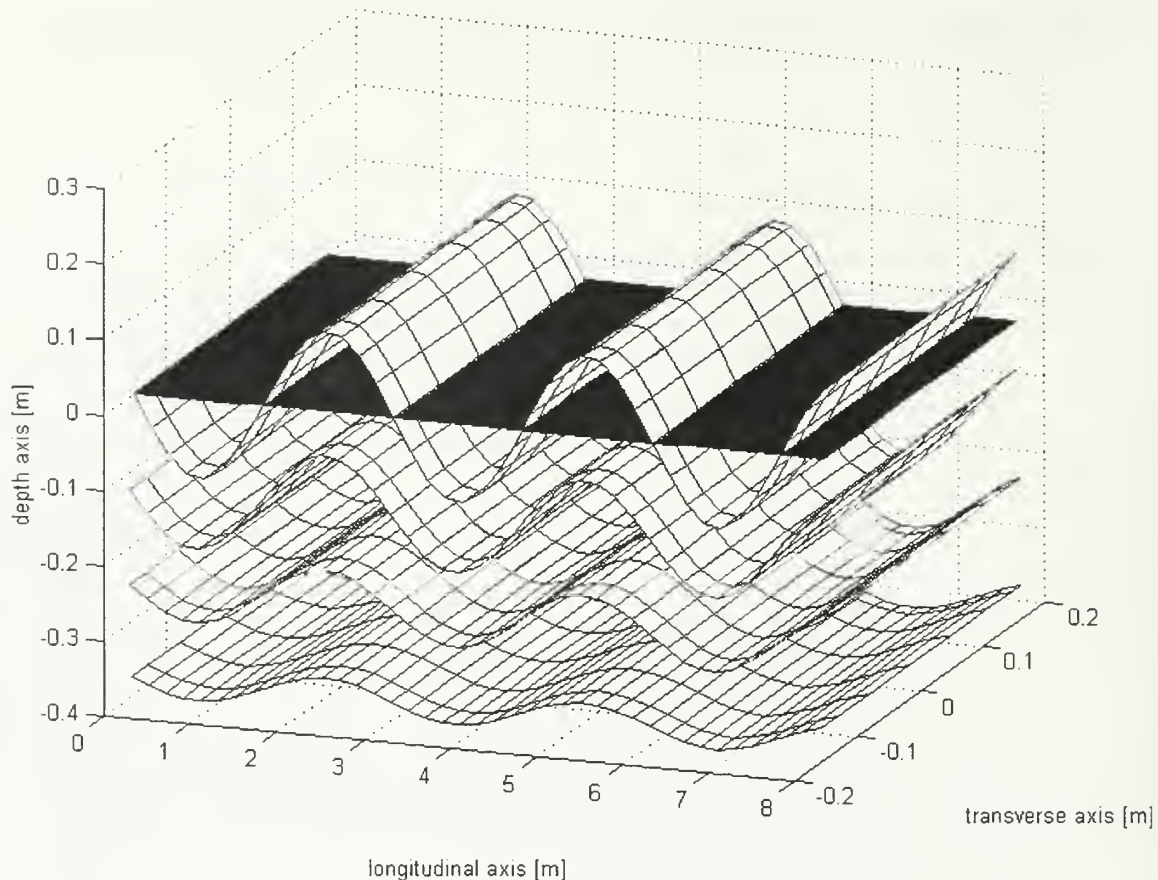
```
% Filename: rayleighwaves3d.m
% Written by: F.E. Gaghan
% Date Last Modified: 22 December 1997
% Purpose: This program produces a 3D graphical representation of
% Rayleigh waves in an isotropic elastic half space from which
% can be seen the exponential decay with depth into the
% medium.

% Initialize required space and wave parameters
clear all;
x1=[0:0.2:8];
k=(2*pi*100)/300;
kx1=k*x1;
w=k*300;
t=[0:0.2:8];
wt=w*t;
C=0.25;
[X1]=meshgrid(x1);

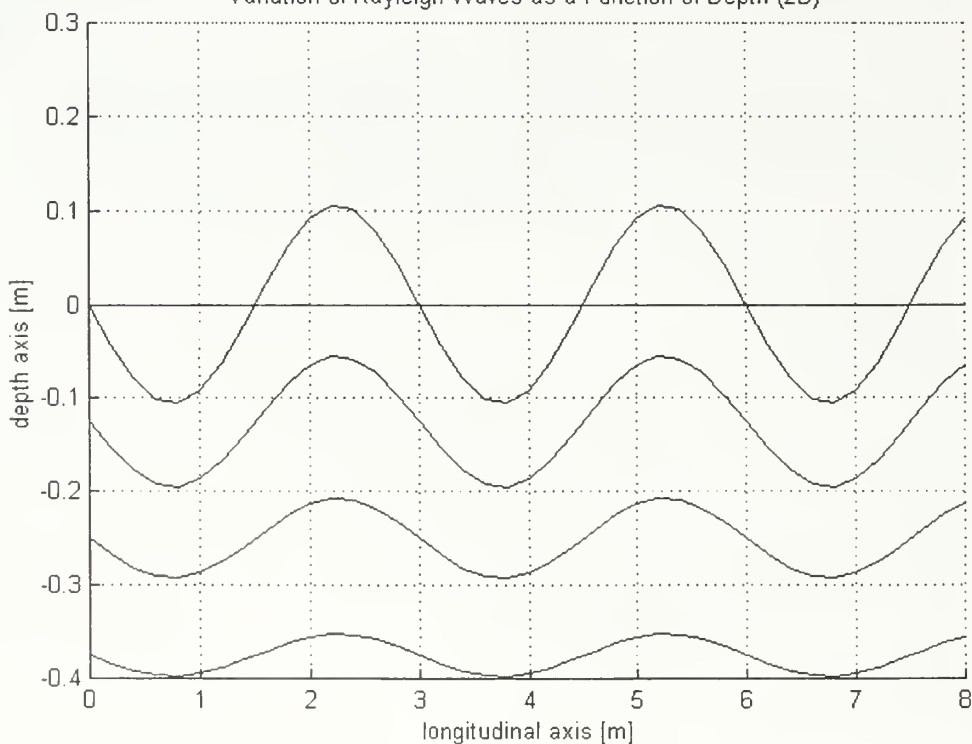
% Loop through various depths in the medium to calculate the horizontal
% and vertical particle displacements.
i=0;
for x3=[0,-0.125,-0.25,-0.375];
    % Calculate the horizontal particle displacement
    a1=exp(0.8475*k*x3)-(0.5773*exp(0.3933*k*x3));
    c1=sin(wt-kx1);
    u1=C*(a1*c1);
    u1=u1+x3;
    % Calculate the vertical particle displacement
    a3=(-0.8475*exp(0.8475*k*x3))+(1.4679*exp(0.3933*k*x3));
    c3=cos(wt-kx1);
    u3=C*(a3*c3);
    % Conditional statement used to display surface layer
    if i==0
        [LX,LY]=meshgrid(x1,u3);
        [LZ]=0*LX;
        figure(1);
        surf(LX,LY,LZ);
    end;%end-if i

    % Plot the waves for each of the four different depths within the
    % medium
    [U3,U1]=meshgrid(u1,u3);
    hold on;
    mesh(X1,U1,U3);
    xlabel('longitudinal axis [m]'); ylabel('transverse axis [m]');
    zlabel('depth axis [m]');
    title('Variation of Rayleigh Waves as a Function of Depth (3D)');
    view(20,20);
    i=i+1;
end;%end-for x3
```

Variation of Rayleigh Waves as a Function of Depth (3D)



Variation of Rayleigh Waves as a Function of Depth (2D)



APPENDIX B. MANUFACTURER SPECIFICATION SHEETS

The appendix contains the specification sheets from the manufacturer catalogs for the various equipment components used during the experimental testing phases.

APPENDIX B1. MANUFACTURER SPECIFICATIONS FOR ELECTRO-MAGNETIC SHAKERS (MINI-SHAKERS)



**WILCOXON
RESEARCH**



The Model F5B Vibration Generator is a reaction-type shaker generating dynamic forces for structural excitation in vibration research and testing. The reaction principle of operation, light weight and compact configuration allow this generator to be stud mounted in any position, directly to structures without external support or critical shaft alignment problems.

The Model F5B Electromagnetic Shaker is a cylindrical permanent magnet shaker. The magnet is in rigid contact with the outer case. A moving coil wound on an aluminum bobbin surrounds the magnet. This coil and bobbin is suspended from two flat, circular metal springs ensuring pure axial motion. A low center of gravity minimizes rotation excitation by the shaker. The added dynamic weight is low since the suspended weight does not effect rotational or axial inertia above its resonance. This prevents inconsistencies often encountered whenever the rotational impedance of structures is low compared to the axial impedance.

The Model F5B is designed for operation over a very wide range of audio frequencies. It can be supplied with a sensing transducer containing an accelerometer and a force gage (Model Z11 Impedance Head). The shaker drives the tested structure through the impedance head.

The Model Z11 Impedance Head is a cylindrical structure containing a piezoelectric accelerometer and a piezoelectric force gage. The transducer base can be used to measure applied force and structure motion. From these measurements mechanical impedance can be obtained.

The high impedance charge signals from the piezoelectric force gage and accelerometer should be conditioned using charge amplifiers or charge converters (CC701), and high impedance voltage amplifiers (AMS).

The Model Z11 Impedance Head has a specimen contact diameter of 0.25 inches preventing excessive filtering by impedance head attachment. The very low mass below the force gage (1 gram) makes it possible to take measurements on relatively light structures, such as aircraft, models and light machinery.

Model F5B/Z11 Electromagnetic Shaker System

SPECIFICATIONS OF MODEL F5B ELECTROMAGNETIC VIBRATION GENERATOR

Usable Frequency Range	10 - 10,000 Hz
Blocked Force Output	see graph
Maximum Continuous Current	0.1 amp rms
Nominal Electrical Impedance	115 Ω
DC Electrical Resistance	56 Ω
Resonance Frequency blocked	35 Hz
Connector	BNC

SPECIFICATIONS OF MODEL Z11 / IMPEDANCE HEAD

Accelerometer Nominal Values

Charge Sensitivity	3.5 pC/g
Voltage Sensitivity*	4.4 mV/g
Capacitance*	800 pF
Frequency Range, +3 dB	10 - 10,000 Hz
Connector*	Microdot 10 - 32
Cable	R13 J2-6

Force Gage Nominal Values

Charge Sensitivity	350 pC/lb
Voltage Sensitivity*	440 mV/lb
Capacitance*	800 pF
Frequency Range, +3 dB	10 - 10,000 Hz
Connector*	Microdot 10 - 32
Cable	R13 J2-6

Mass Below Force Gage

(force gage attached to specimen)

1 gram

Mass Below Force Gage

(accelerometer attached to specimen)

10 grams

Effective Stiffness

(force gage attached to specimen)

4×10^5 lb/in

Effective Stiffness

(accelerometer attached to specimen)

2×10^6 lb/in

Diameter of Mounting Surface

0.25 inch

Mounting Stud, integral

8 - 32

Temperature Range

0 to 80°C

Maximum Screw Down Torque

15 in-lb

Base Material

titanium

Weight of F5B

160 grams

Weight of Z11

10 grams

Total Weight

170 grams

NOTES:

- * Blocked force output refers to the force output against a mass of infinite mechanical impedance.
- † Refers to connector at the end of cable.
- ‡ Refers to condition at the end of the 6 foot, low-noise cable (180 pF).

ACCESSORIES SUPPLIED:

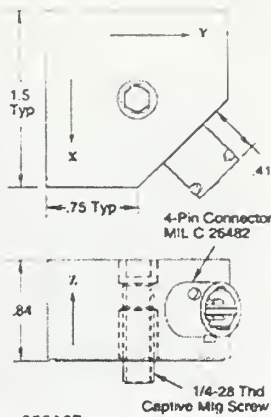
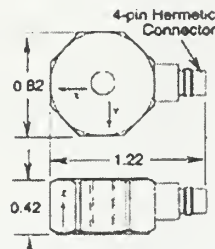
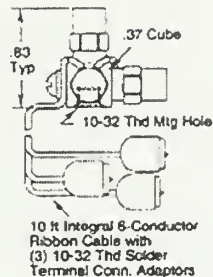
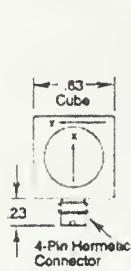
- Output cables

ACCESSORIES AVAILABLE:

- Amplifiers; signal conditioners.

APPENDIX B2. MANUFACTURER SPECIFICATIONS FOR TRI-AXIAL ACCELEROMETER

Dimensions shown in inches except where noted.



339B01 & 339B10

354B17

354B33

356A27

MODEL NUMBER	UNIT	GENERAL PURPOSE				INDUSTRIAL
		339B01	339B10	354B17	354B33	356A27
Voltage Sensitivity (1)	mV/g	100	10	10	100	100
Frequency Range ($\pm 5\%$)	Hz	1 to 2 000	1 to 3 000	1 to 5 000	1 to 2 000	3 to 2 000
($\pm 10\%$)	Hz	0.7 to 4 000	0.7 to 5 000	0.7 to 7 000	0.7 to 4 000	2 to 5 000
Resonant Frequency	kHz	≥ 20	≥ 40	> 15	≥ 12	≥ 12
Amplitude Range	$\pm g$ pk	50	500	500	50	50
Resolution (broadband)	g pk	0.002	0.01	0.01	0.003	0.0005
Mechanical Shock Limits	$\pm g$ pk	8 000	5 000	10 000	3 000	10 000
Temperature Range	°F	-65 to +250	-65 to +250	-65 to +250	-65 to +250	-65 to +250
Temperature Coefficient	%/°F	≤ 0.03	≤ 0.03	≤ 0.03	≤ 0.03	≤ 0.05
Amplitude Linearity	%	± 1	± 1	± 1	± 1	± 1
Transverse Sensitivity	%	≤ 5	≤ 5	≤ 5	≤ 5	≤ 5
Base Strain Sensitivity	$\mu\varepsilon$	≤ 0.0004	≤ 0.0003	≤ 0.002	≤ 0.02	≤ 0.002
Excitation Voltage	VDC	20 to 30	18 to 30	18 to 30	20 to 30	20 to 30
Constant Current Supply	mA	2 to 20	2 to 20	2 to 20	2 to 20	2 to 20
Output Impedance	ohm	≤ 100	≤ 100	≤ 100	≤ 100	≤ 250
Output Bias Voltage	VDC	8 to 14	8 to 14	8 to 12	8 to 12	8 to 14
Discharge Time Constant	second	≥ 0.5	≥ 0.5	≥ 0.5	≥ 0.5	≥ 0.2
Ground Isolation (2)	ohm	optional	optional	no	$\geq 10^8$	$\geq 10^8$
Sensing Element	type	quartz	quartz	quartz	quartz	ceramic
Element Configuration	structure	shear	shear	shear	shear	shear
Connector	type	4-pin microtech	4-pin microtech	integral cable	4-pin microtech	MIL-C-26482
Sealing	type	welded/hermetic	welded/hermetic	weld/herm	weld/herm	welded/hermetic
Mounting Thread	size	10-32	10-32	5-40	10-32 thru bolt	1/4-28
Housing	material	titanium	titanium	titanium	titanium	stainless steel
Weight	gram (oz)	15 (0.53)	15 (0.53)	23 (0.8)	15.5 (0.55)	150 (5.3)
SUPPLIED ACCESSORIES: (3)						
Adhesive Petro Wax		060A24	060A24	080A24	080A24	080A24
Mounting Stud (5)		061B05	061B05	081B05	081A54	081A56
Mounting Base (6)		060A12	080A12	080A	N/A	N/A
OPTIONAL ACCESSORIES: (3)						
Magnetic Mounting Base	type	Y	Y	N/A	A, H, K, W	N
CABLING (3)	series	010	010	N/A	002	059

NOTES:

- All models have a sensitivity tolerance of $\pm 10\%$.
- Models 354B17 and 339B11 obtain ground isolation when used with supplied mounting base. Models 356A27 and 354B33 are case isolated.
- See cables/accessories section beginning on page 78 for a complete description of the supplied and optional accessories.
- NIST traceable calibration certificate from 10 Hz to $\pm 5\%$ frequency point supplied with each accelerometer.
- Model 061B05 mounting stud is 10-32 to 10-32. Model 081A27 mounting stud is threaded 5-40 to 5-40. Model 081A52 is a 0-80 threaded cap screw. Model 081A53 is a 4-40 threaded cap screw. Models 081A54 and 081A55 are 10-32 threaded cap screws.
- Models 080A33 and 080A51 are electrically insulated mounting washer pads.

APPENDIX B1. MANUFACTURER SPECIFICATIONS FOR ELECTRO-MAGNETIC SHAKERS (MINI-SHAKERS)



**WILCOXON
RESEARCH**



KNOCKDOWN



The Model F5B Vibration Generator is a reaction-type shaker generating dynamic forces for structural excitation in vibration research and testing. The reaction principle of operation, light weight and compact configuration allow this generator to be stud mounted in any position, directly to structures without external support or critical shaft alignment problems.

The Model F5B Electromagnetic Shaker is a cylindrical permanent magnet shaker. The magnet is in rigid contact with the outer case. A moving coil wound on an aluminum bobbin surrounds the magnet. This coil and bobbin is suspended from two flat circular metal springs ensuring pure axial motion. A low center of gravity minimizes rotation excitation by the shaker. The added dynamic weight is low since the suspended weight does not effect rotational or axial inertia above its resonance. This prevents inconsistencies often encountered whenever the rotational impedance of structures is low compared to the axial impedance.

The Model F5B is designed for operation over a very wide range of audio frequencies. It can be supplied with a sensing transducer containing an accelerometer and a force gage (Model Z11 Impedance Head). The shaker drives the tested structure through the impedance head.

The Model Z11 Impedance Head is a cylindrical structure containing a piezoelectric accelerometer and a piezoelectric force gage. The transducer base can be used to measure applied force and structure motion. From these measurements mechanical impedance can be obtained.

The high impedance charge signals from the piezoelectric force gage and accelerometer should be conditioned using charge amplifiers or charge converters (CC701), and high impedance voltage amplifiers (AMS).

The Model Z11 Impedance Head has a specimen contact diameter of 0.25 inches preventing excessive stiffening by impedance head attachment. The very low mass below the force gage (1 gram) makes it possible to take measurements on relatively light structures, such as airframes, models and light machinery.

Model F5B/Z11 Electromagnetic Shaker System

SPECIFICATIONS OF MODEL F5B ELECTROMAGNETIC VIBRATION GENERATOR

Usable Frequency Range	10 - 10,000 Hz
Blocked Force Output	see graph*
Maximum Continuous Current	0.1 amp rms
Nominal Electrical Impedance	115 Ω
DC Electrical Resistance	56 Ω
Resonance Frequency blocked	35 Hz
Connector	BNC

SPECIFICATIONS OF MODEL Z11 / IMPEDANCE HEAD

Accelerometer Nominal Values

Charge Sensitivity	3.5 pC/g
Voltage Sensitivity†	4.4 mV/g
Capacitance‡	800 pF
Frequency Range, +3 dB	10 - 10,000 Hz
Connector‡	Microdot 10 - 32
Cable	R13-J2-6

Force Gage Nominal Values

Charge Sensitivity	350 pC/lb
Voltage Sensitivity†	440 mV/lb
Capacitance‡	800 pF
Frequency Range, +3 dB	10 - 10,000 Hz
Connector‡	Microdot 10 - 32
Cable	R13-J2-6

Mass Below Force Gage

(force gage attached to specimen) 1 gram

Mass Below Force Gage
(accelerometer attached to specimen) 10 grams

Effective Stiffness
(force gage attached to specimen) 4×10^5 lb/in

Effective Stiffness
(accelerometer attached to specimen) 2×10^5 lb/in

Diameter of Mounting Surface 0.25 inch

Mounting Stud, integral 8 - 32

Temperature Range 0 to 80 °C

Maximum Screw Down Torque 15 in-lb

Base Material titanium

Weight of F5B 160 grams

Weight of Z11 10 grams

Total Weight 170 grams

NOTES:

* Blocked force output refers to the force output against a mass of infinite mechanical impedance.

† Refers to connector at the end of cable.

‡ Refers to condition at the end of the 6 foot, low-noise cable (180 pF).

ACCESSORIES SUPPLIED: Output cables.

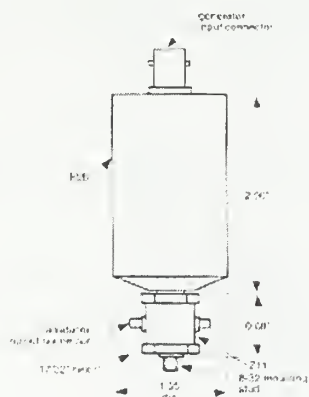
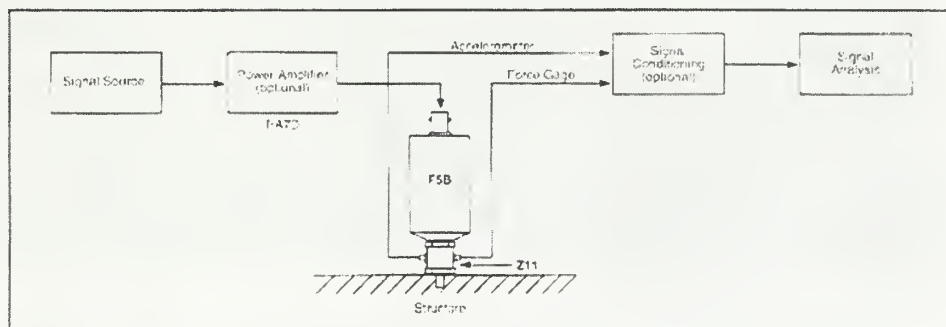
ACCESSORIES AVAILABLE: Amplifiers; signal conditioners.



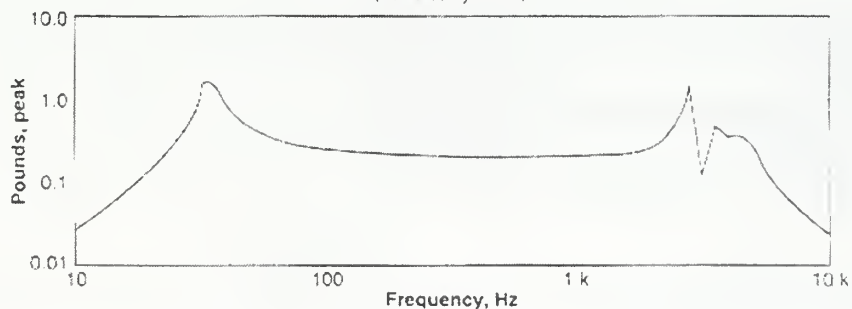
WILCOXON
RESEARCH

Model F5B/Z11

RECOMMENDED SYSTEM DIAGRAM

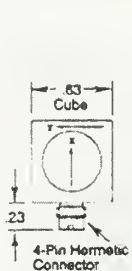


TYPICAL BLOCKED FORCE OUTPUT
(Powered by PA7D)

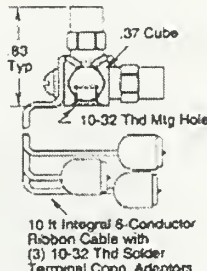


APPENDIX B2. MANUFACTURER SPECIFICATIONS FOR TRI-AXIAL ACCELEROMETER

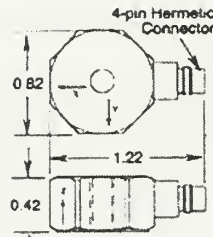
Dimensions shown in inches except where noted.



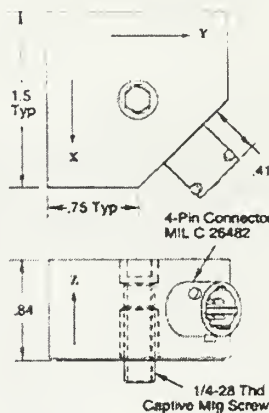
339B01 & 339B10



354B17



354B33



356A27

MODE NUMBER	UNIT	GENERAL PURPOSE			INDUSTRIAL	
		339B01	339B10	354B17	354B33	356A27
Voltage Sensitivity (1)	mV/g	100	10	10	100	100
Frequency Range ($\pm 5\%$)	Hz	1 to 2 000	1 to 3 000	1 to 5 000	1 to 2 000	3 to 2 000
($\pm 10\%$)	Hz	0.7 to 4 000	0.7 to 5 000	0.7 to 7 000	0.7 to 4 000	2 to 5 000
Resonant Frequency	kHz	≥ 20	≥ 40	≥ 15	≥ 12	≥ 12
Amplitude Range	$\pm g$ pk	50	500	500	50	50
Resolution (broadband)	g pk	0.002	0.01	0.01	0.003	0.0005
Mechanical Shock Limits	$\pm g$ pk	8 000	5 000	10 000	3 000	10 000
Temperature Range	°F	-85 to +250	-65 to +250	-65 to +250	-65 to +250	-65 to +250
Temperature Coefficient	%/°F	≤ 0.03	≤ 0.03	≤ 0.03	≤ 0.03	≤ 0.05
Amplitude Linearity	%	± 1	± 1	± 1	± 1	± 1
Transverse Sensitivity	%	≤ 5	≤ 5	≤ 5	≤ 5	≤ 5
Base Strain Sensitivity	g/ μ E	≤ 0.0004	≤ 0.0003	≤ 0.002	≤ 0.02	≤ 0.002
Excitation Voltage	VDC	20 to 30	18 to 30	18 to 30	20 to 30	20 to 30
Constant Current Supply	mA	2 to 20	2 to 20	2 to 20	2 to 20	2 to 20
Output Impedance	ohm	≤ 100	≤ 100	≤ 100	≤ 100	≤ 250
Output Bias Voltage	VDC	8 to 14	8 to 14	8 to 12	8 to 12	8 to 14
Discharge Time Constant	second	≥ 0.5	≥ 0.5	≥ 0.5	≥ 0.5	≥ 0.2
Ground Isolation (2)	ohm	optional	optional	no	$\geq 10^8$	$> 10^8$
Sensing Element	type	quartz	quartz	quartz	quartz	ceramic
Element Configuration	structure	shear	shear	shear	shear	shear
Connector	type	4-pin microtech	4-pin microtech	integral cable	4-pin microtech	Mil-C-26482
Sealing	type	welded/hermetic	welded/hermetic	weld/herm	weld/herm	welded/hermetic
Mounting Thread	size	10-32	10-32	5-40	10-32 thru bolt	1/4-28
Housing	material	titanium	titanium	titanium	titanium	stainless steel
Weight	gram (oz)	15 (0.53)	15 (0.53)	23 (0.8)	15.5 (0.55)	150 (5.3)
SUPPLIED ACCESSORIES (3, 4)						
Adhesive Petro Wax		080A24	080A24	080A24	080A24	080A24
Mounting Stud (5)		081B05	081B05	081B05	081A54	081A56
Mounting Base (6)		080A12	080A12	080A	N/A	N/A
OPTIONAL ACCESSORIES (3)						
Magnetic Mounting Base		080A27	080A27	080A27	N/A	N/A
CABLING (3)						
Mating Cable Connectors	type	Y	Y	N/A	A, H, K, W	N
Recommended Cable	series	010	010	N/A	002	059

NOTES:

- All models have a sensitivity tolerance of $\pm 10\%$.
- Models 354B17 and 339B11 obtain ground isolation when used with supplied mounting base. Models 356A27 and 354B33 are case isolated.
- See cables/accessories section beginning on page 78 for a complete description of the supplied and optional accessories.
- NIST traceable calibration certificate from 10 Hz to $\pm 5\%$ frequency point supplied with each accelerometer.
- Model 081B05 mounting stud is 10-32 to 10-32. Model 081A27 mounting stud is threaded 5-40 to 5-40. Model 081A52 is a 0-80 threaded cap screw. Model 081A53 is a 4-40 threaded cap screw. Models 081A54 and 081A55 are 10-32 threaded cap screws.
- Models 080A33 and 080A51 are electrically insulated mounting washer pads.

APPENDIX B3. MANUFACTURER SPECIFICATIONS FOR BASS SHAKERS

AURA SYSTEMS INC.

EXTENDED SERVICE PLAN \$12.99

SPECIAL LOW PRICE!

**Bass Shakers™ Let You
Feel All the Bass without
Breaking the Sound Barrier**

The Bass Shaker is a transducer that generates the sensation of sound by vibration, not by moving air. The result is a big bass effect without a high pressure level that could distort sound or blow your speakers. They are also great for adding bass to vehicles with poor sound insulation, such as trucks. Mount these Bass Shakers under your front seats and you will feel the punch of the drums and the kick of the percussion, as if you were on stage or in the studio when the music was recorded! Hooks up easily to any standard audio amplifier output channel, and can be used with existing subwoofers for an extra kick. Each Bass Shaker requires only 25W RMS of power.

Model AST1B4. Item No. B-40070-492383 S/H \$9.99 FREE wt 3 lbs

40 Hz resonan

Specifications:	AST-1B-4 Bass Shaker
Frame Size: 4.75" dia. X 2.35" h
Magnet Type: Ceramic
Power Rating: Nominal 25 W
Force, Nominal: 10 lbf (44.5 N)
Weight: 2.5 lbs each
Resonance Frequency (fo):	... 42 Hz
Usable Frequency Range: 20-100 Hz

Configuring Shakers.

The Aura Bass Shaker™ has a nominal impedance of 4 ohms. Depending on the amplifier driving them, they can be hooked up in stereo or bridged/mono configuration, just as regular Subwoofers. Please consult the amplifier manual for connection details.

Connecting Multiple Shakers

Two Shakers can be wired together to increase the delivered power . This can be accomplished by connecting them in either series or in parallel. Connecting in series increases the impedance to 8 ohms (see figure A), whereas, a parallel connection (figure B) reduces the impedance down to 2 ohms. Consult the amplifier manual to figure out the delivered power at various impedances. **In either case do not exceed the rated 25 Watts RMS per Shaker (50Watts RMS, total).**

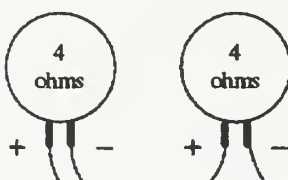


Figure A, Series connection, 8 Ohms

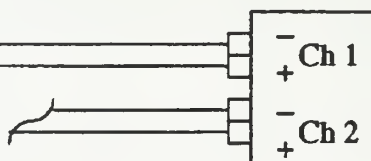
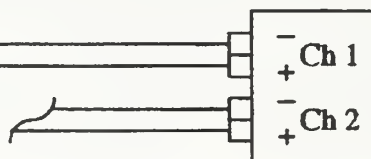
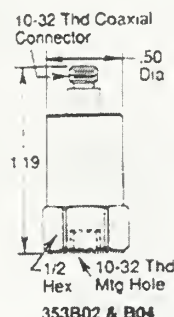


Figure B, Parallel connection, 2 Ohms



APPENDIX B4. MANUFACTURER SPECIFICATIONS FOR UNI-AXIAL ACCELEROMETER

Dimensions shown in inches except where noted.



353B02 & B04

MODEL NUMBER	Unit
Voltage Sensitivity (1)	mV/g
Frequency Range ($\pm 5\%$)	Hz
($\pm 10\%$)	Hz
Resonant Frequency	KHz
Amplitude Range	$\pm g$ pk
Resolution (broadband)	g pk
Mechanical Shock Limits	$\pm g$ pk
Temperature Range	°F
Temperature Coefficient	%/°F
Amplitude Linearity	%
Transverse Sensitivity (2)	%
Base Strain Sensitivity	g/ μ E
Excitation Voltage	VDC
Constant Current Excitation	mA
Output Impedance	ohm
Output Bias Voltage	VDC
Discharge Time Constant	second
Sensing Element	quartz
Connector (3)	type
Sealing	type
Mounting Thread	size
Housing	material
Weight	gram (oz)
OPTIONAL MODELS (4)	
High Sensitivity (100 mV/g); (5)	
Ground Isolated ($>10^8$ ohms)	
Adhesive Mount	
Low Freq: ≥ 10 sec. DTC (6, 10)	
Water Resistant Connection	
Low Output Bias (4.5 to 6.5 V)	
SUPPLIED ACCESSORIES: (7)	
Adhesive Petro Wax	
Mounting Stud (8)	
Adhesive Mounting Base	
OPTIONAL ACCESSORIES: (7)	
Magnetic Mounting Base	
Triaxial Mounting Adaptor	
CABLING: (7)	
Mating Cable Connectors	type
Recommended Stock Cables	series

NOTES:

1. Sensitivity tolerance is $\pm 5\%$; tighter tolerances ($\pm 2\%$) available upon request.
2. Transverse sensitivity on shear structured accelerometers is typically $\leq 3\%$.
3. Models 353B13, 353B17 and 353B67 supplied with 10 ft. ribbon cable terminating in a 10-32 coaxial plug. Cable is user repairable.
4. See page B for a description of the optional models. (Specifications may differ slightly. Consult factory before ordering.)
5. Optional high sensitivity Models (353B65, 353B66, 353B67 and 353B68) not available with low output bias option. Output bias voltage range: 12-17V.

6. High frequency/low mass sensors will have ≥ 5 sec. discharge time constant (typically 8 seconds) with low frequency ('C') option.
7. See cables/accessories section beginning on page 78 for a complete description of the supplied and optional accessories.
8. NIST traceable calibration certificate supplied with each accelerometer.
9. Supplied mounting stud is threaded 10-32 to 10-32.
10. Models Q353B43, Q353B44, Q353B51, Q353B52 have a maximum temperature of 180°F (82°C).

**APPENDIX B5. MANUFACTURER SPECIFICATIONS FOR WATERPROOF
TRI-AXIAL ACCELEROMETER**

APPLICATION	REVISIONS				
	REV	DESCRIPTION	ECN	DATE	APP'D
329-1110-95					
	MODEL 081A56 MOUNTING BOLT 1/4-28 UNF-2A THREAD BY .750(19.05) LONG (SUPPLIED)				
	MOLDED 059 CABLE 10 FEET(3 METERS) TERMINATING TO PIGTAIL				
<p>FOR METRIC TRIAXIAL ACCELEROMETER (M329A11) USE MOUNTING BOLT MODEL M081A59, M6 X 1.00-6g BY .787(20.0) LONG.</p>					
UNLESS SPECIFIED TOLERANCES DIMENSIONS IN INCHES DECIMALS $XX \pm .01$ $XXX \pm .005$ ANGLES ± 2 DEGREES FILLETS AND RADIUS $.003 - .005$ (0.07 - 0.13)		DRAWN CHK'D APP'D	IMP 5/16-14 S/1/94	5100A ENGR 12	KJA 7/15/94 7/15/94
		OUTLINE DRAWING 329A11 SERIES TRIAXIAL ACCELEROMETER			PCB PIEZOTRONICS, INC. 3425 WALDEN AVE., DEPUE, NEW YORK 14043 PHONE: (716) 684-0001
		FILE CODE IDENT. NO. 52681	DWG. NO. 329-1110-95	SCALE: 2X SHEET 1 OF 1	

— Calibration Certificate —

Per ISA-RP37.2

Model No. 329A11/200AC

Serial No. 1038 (Z-AXIS)

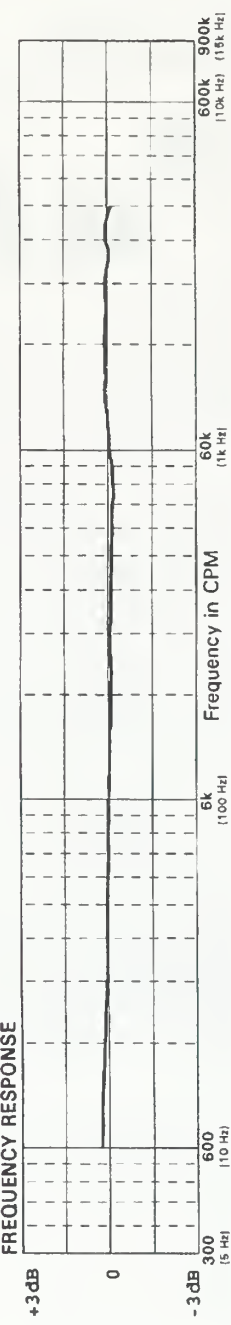
On Us

Calibration traceable to NIST thru Project No. 822/256889

CALIBRATION DATA

KEY SPECIFICATIONS

Settling Time (within 1% of output bias)		s						Reference Freq.						
Frequency	CPM	600	900	1800	3000	6000	18000	30000	60000	180000	300000			
Amplitude Deviation	%	3.0	2.5	0.8	0.7	0.0	-0.5	-1.3	-0.5	0.9	-1.5			



**INDUSTRIAL
MONITORING
INSTRUMENTATION**
A Division of PCB Piezotronics, Inc.

Phone: 1-800-959-4IMI
Fax: 1-716-684-3823

Calibrated by Andrew Shwec
Date 01-13-1998

APPENDIX B6. MANUFACTURER SPECIFICATIONS FOR BOWLING BALL UNI-AXIAL ACCELEROMETER

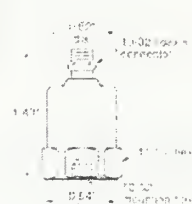


FEATURES:

- Rugged
 - Wide frequency range
 - High resonance frequency
 - Low base strain sensitivity
 - Lightweight
 - Mechanical & thermal isolation
 - Hermetically sealed



Model 352



Model 352T

NOTES: As measured at the end of a standard 6 ft. cable, 18C pF.

The cable supplied with the H-10 is limited to 80 °C. For higher temperatures (lowest 120 °C)

OPTIONS: Higher temperature ranges, customer specified sensitivities.

OPTIONS: High temperature range extension, strain rate sensors.

ACCESSORIES SUPPLIED: SF1 mounting stud, RT110-16 cable assembly, calibration data
ACCESSORIES AVAILABLE: Magnetic mounting bases, SFE cementing stents, SF4 isolation mounting base, CC704 amplifiers, signal conditioners.

1000000000000000

Models 352/352T

DYNAMIC	
Sensitivity, 25°C, nominal	16 pC/g
Amplitude Nonlinear nearly, to 500 g	15%
Frequency Response: ¹	
-5%	3.0 - 5,000 Hz
-10%	2.0 - 10,000 Hz
-3 dB	1.0 - 15,000 Hz
Resonance Frequency	40 kHz
Transverse Sensitivity, mix.	5% of axial
Temperature Response	see graph

ELECTRICAL

ELECTRICAL	
Capacitance, nominal	500 pF
Resistance 25°C min.	1,000 MΩ
Gounding	case grounded
352	
352T	base isolated

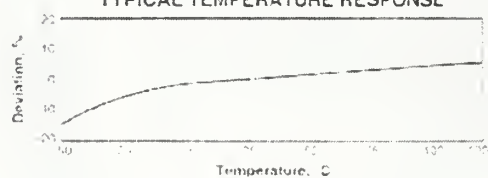
ENVIRONMENTAL

Temperature Range	-50 to 120 °C
Vibration Limit	750 g peak
Shock Limit	5 000 g peak
Electromagnetic Sensitivity, equiv.	40 uG/gauss
Base Strain Sensitivity	0.005 microstrain

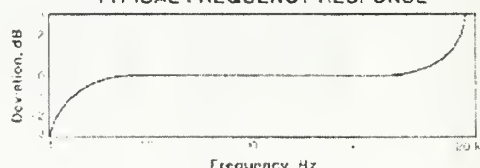
PHYSICAL

PHYSICAL	
Weight:	352 ..
	3521 ..
Case Material	316L stainless steel
Mounting	10-32 tapped hole
Output Connector	10-32 coaxial
Cabling, Mating Connector	Wilcoxon R1, 10-32 coaxial
Standard Cable	J1 6R, SW noise, PVC nickel 20 pE%

TYPICAL TEMPERATURE RESPONSE



TYPICAL FREQUENCY RESPONSE

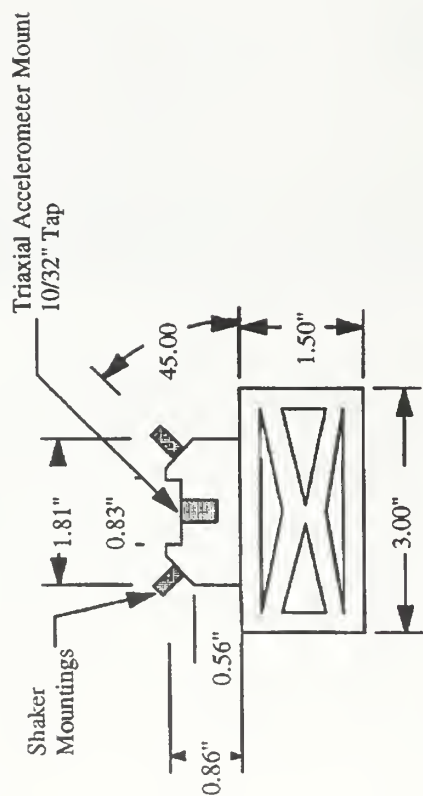


APPENDIX C. DISCRETE MODE SOURCE TECHNICAL DRAWINGS

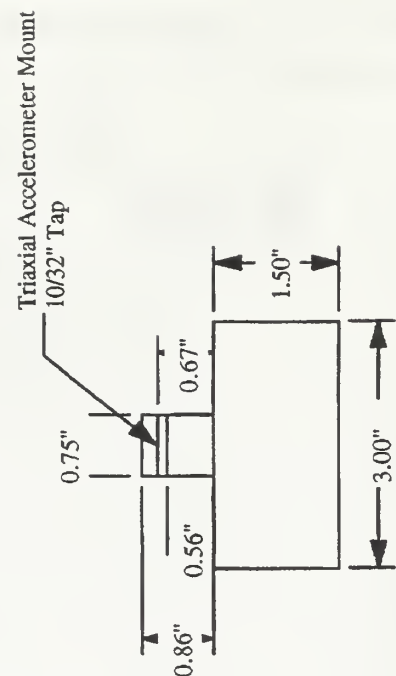
This appendix contains the technical drawings for the various source-to-ground coupling mechanisms designed during the course of the research.

APPENDIX C1. CONCEPT SOURCE TECHNICAL DRAWINGS

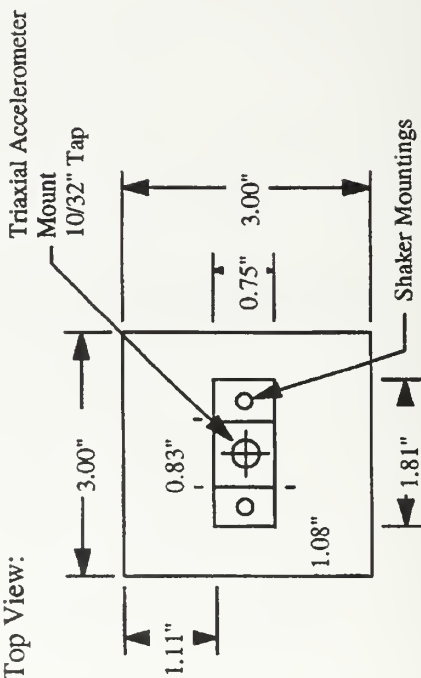
Front View:

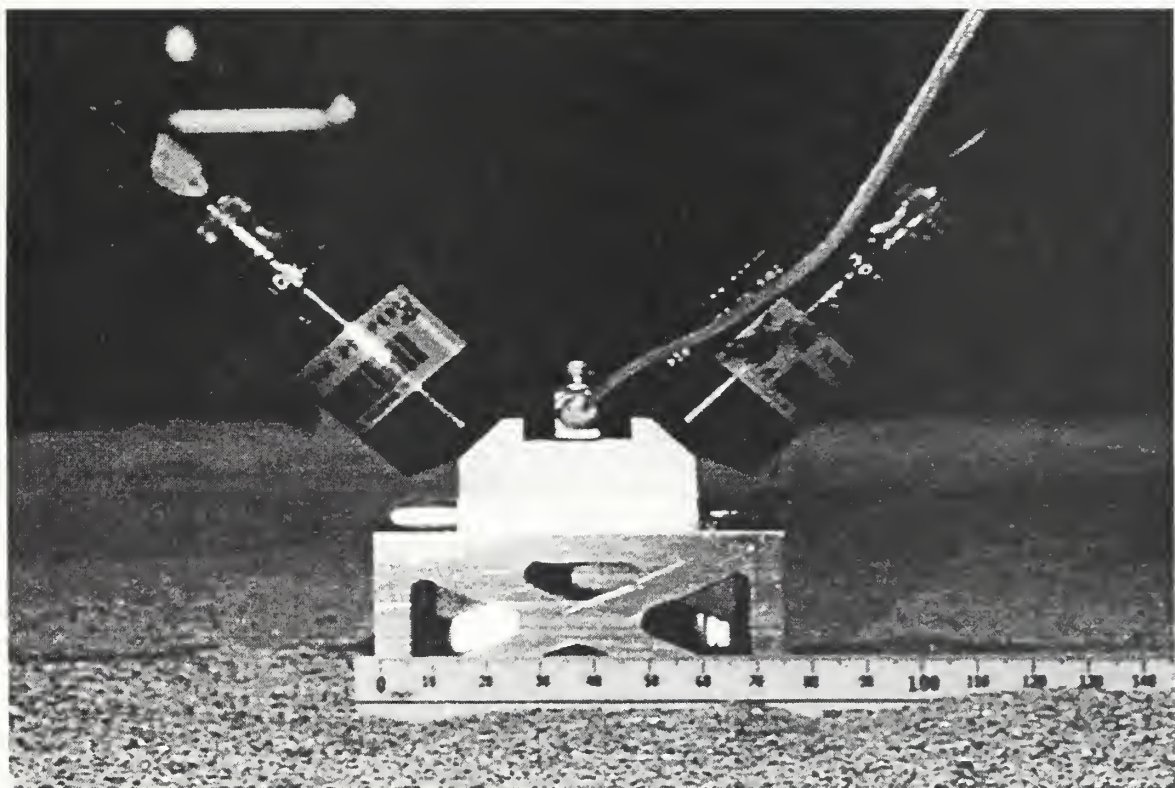
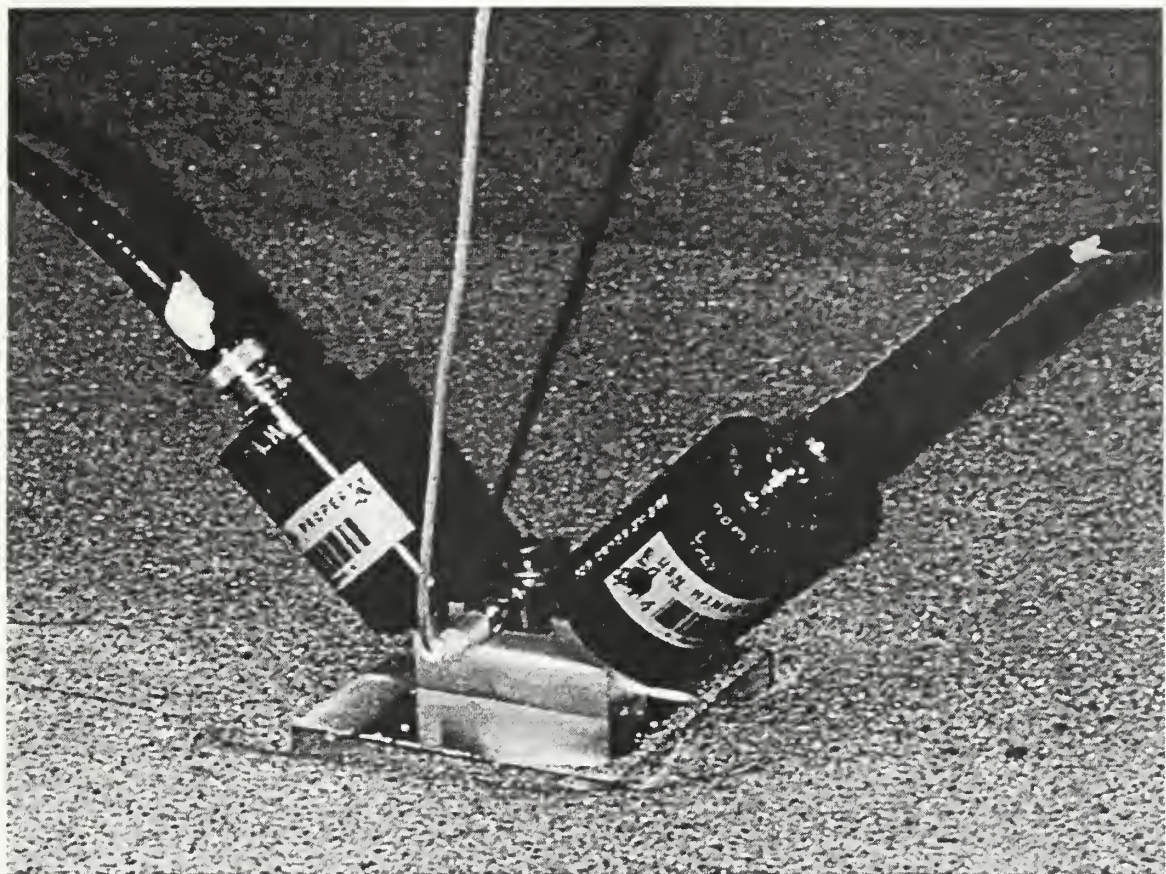


Side View:



Top View:

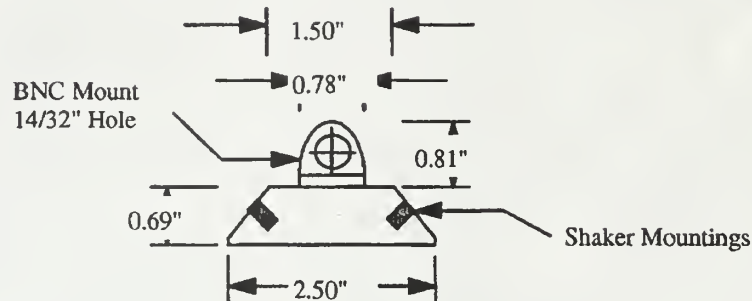




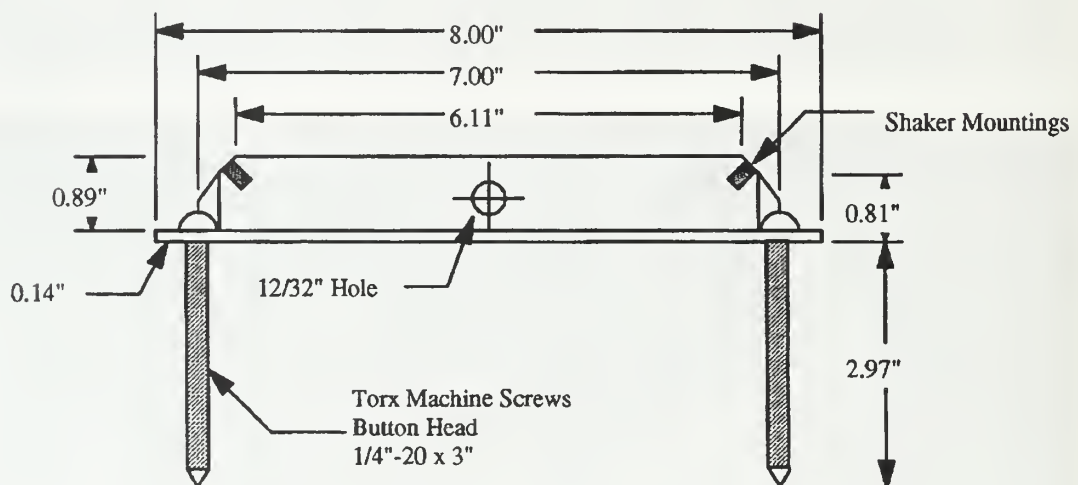
APPENDIX C2. FIELD TEST SOURCE – MOD I TECHNICAL DRAWINGS

Front View:

Top Piece:

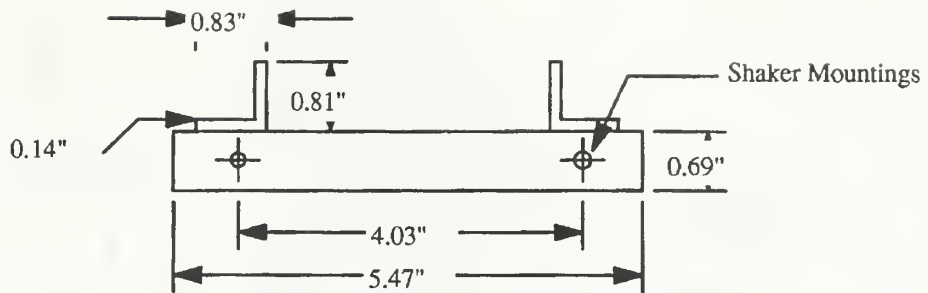


Bottom Piece:

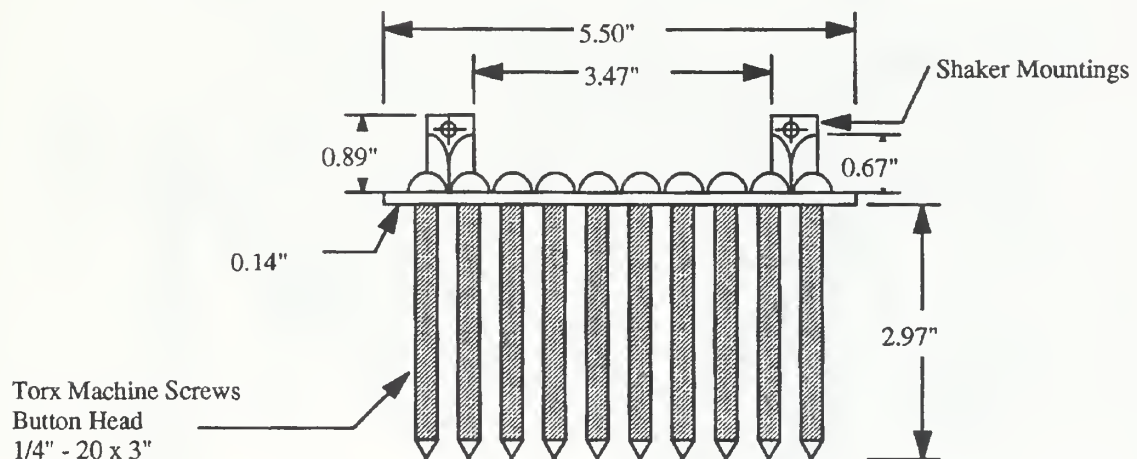


Side View:

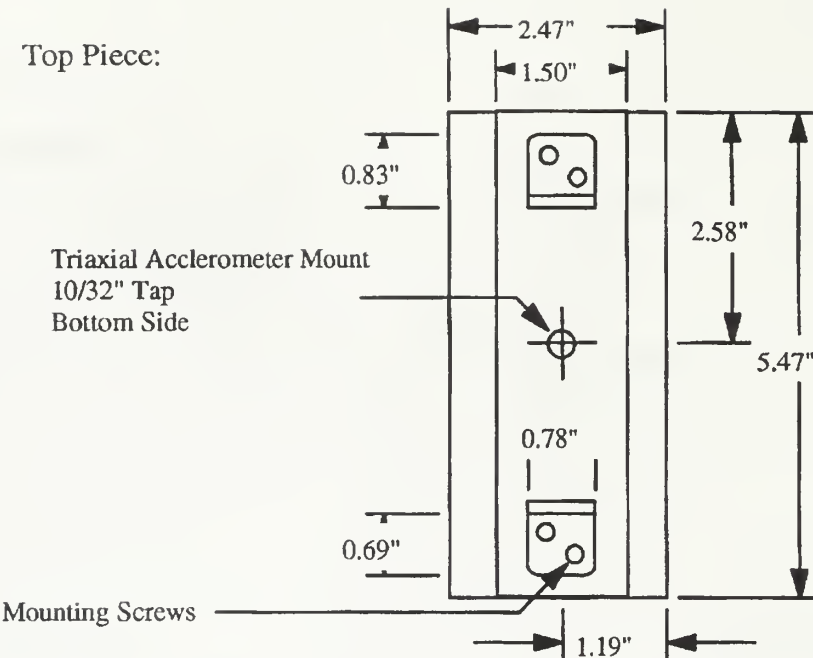
Top Piece:



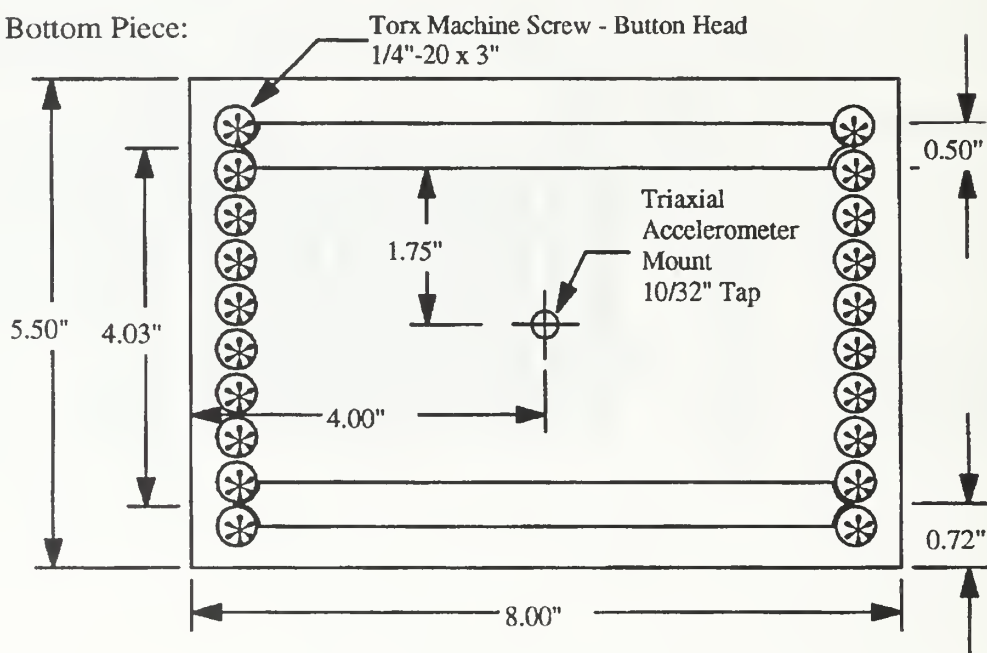
Bottom Piece:



Top View:



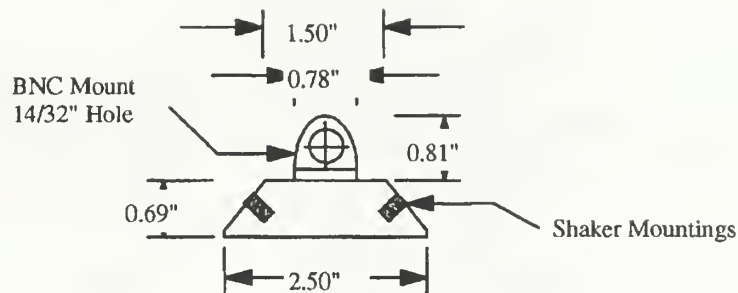
Bottom Piece:



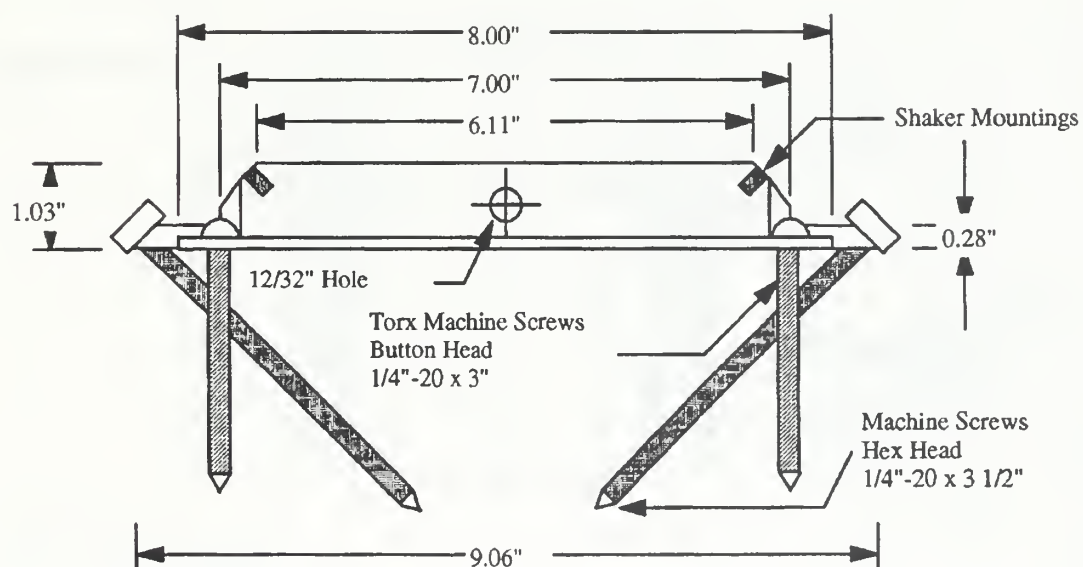
APPENDIX C3. FIELD TEST SOURCE – MOD II TECHNICAL DRAWINGS

Front View:

Top Piece:

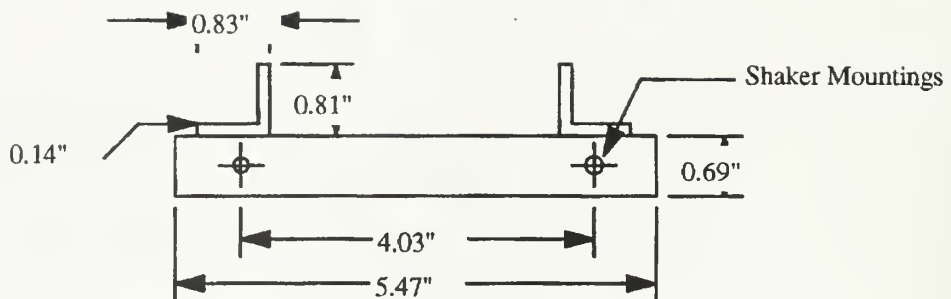


Bottom Piece:

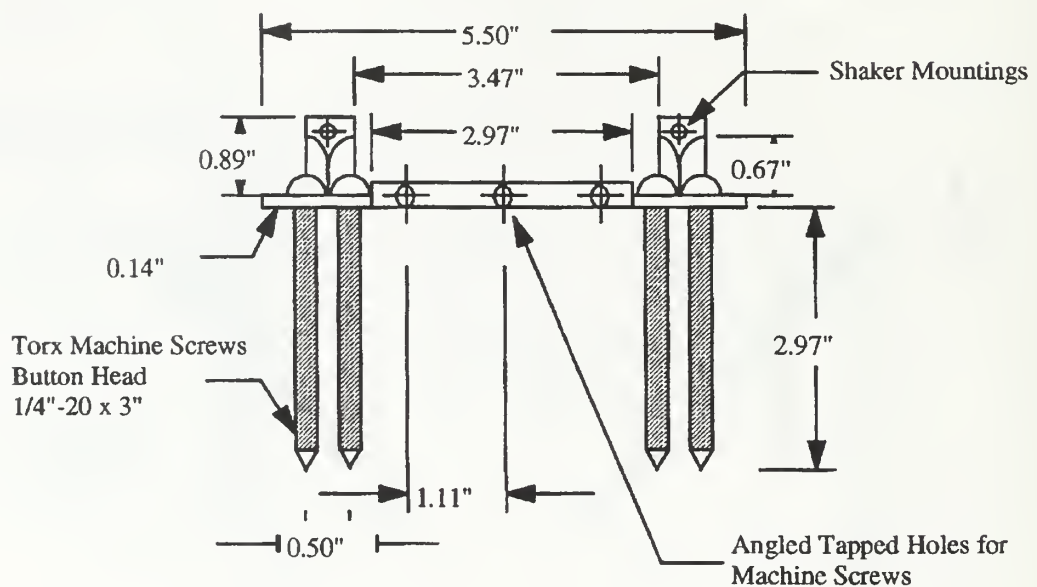


Side View:

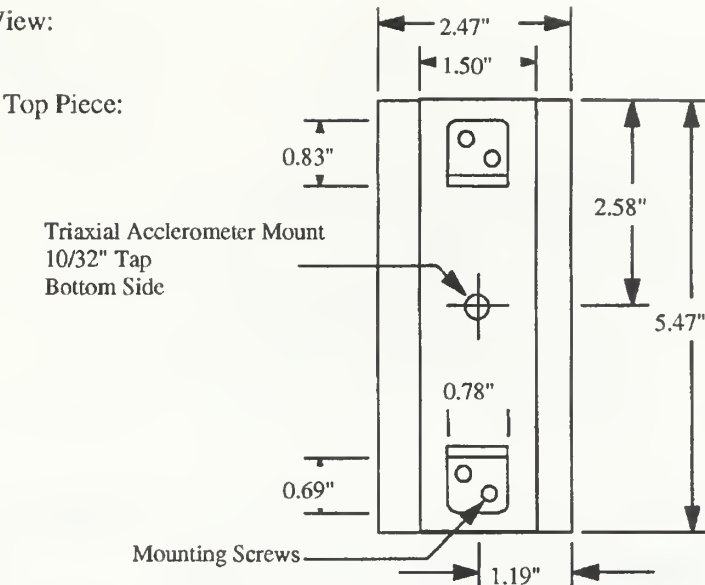
Top Piece:



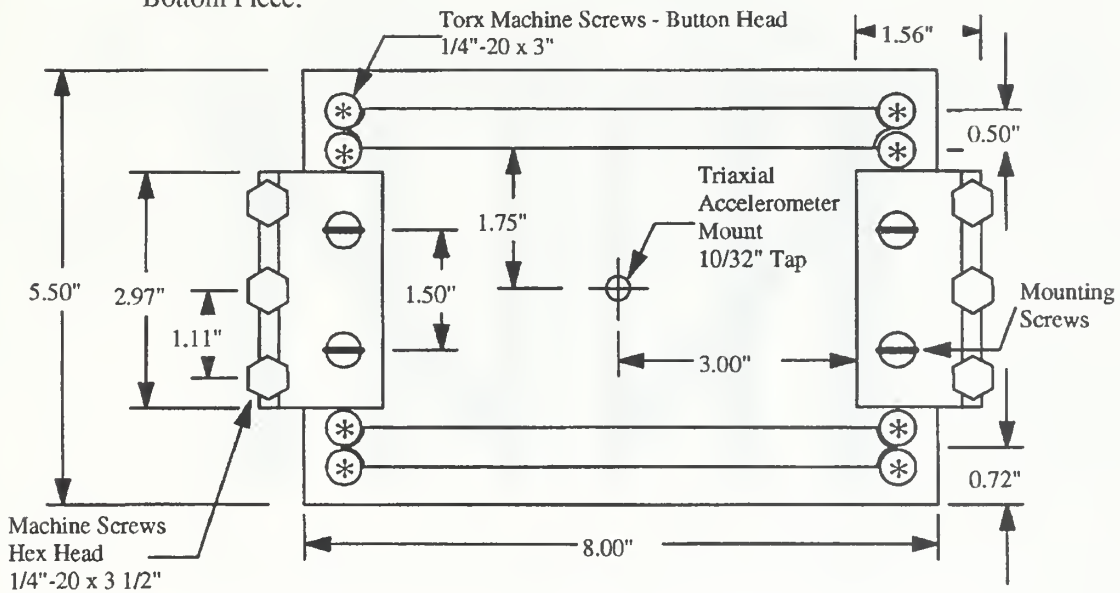
Bottom Piece:



Top View:



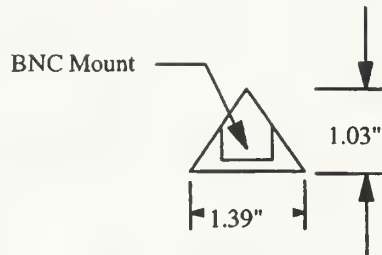
Bottom Piece:



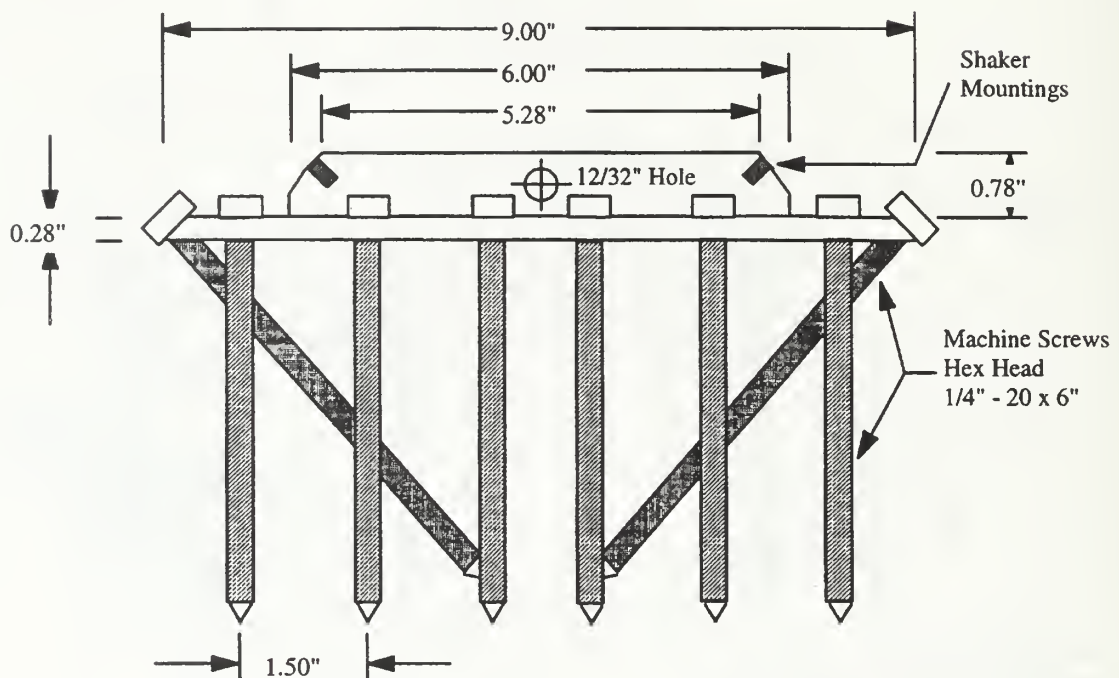
APPENDIX C4. FIELD TEST SOURCE – MOD IV TECHNICAL DRAWINGS

Front View:

Top Piece:

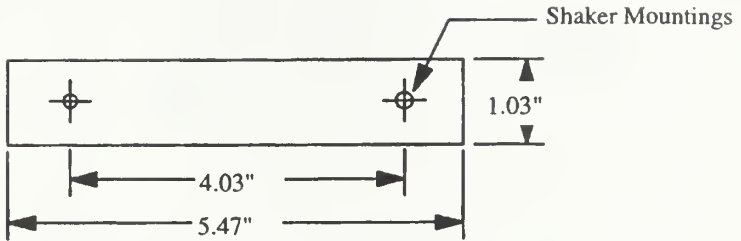


Bottom Piece:

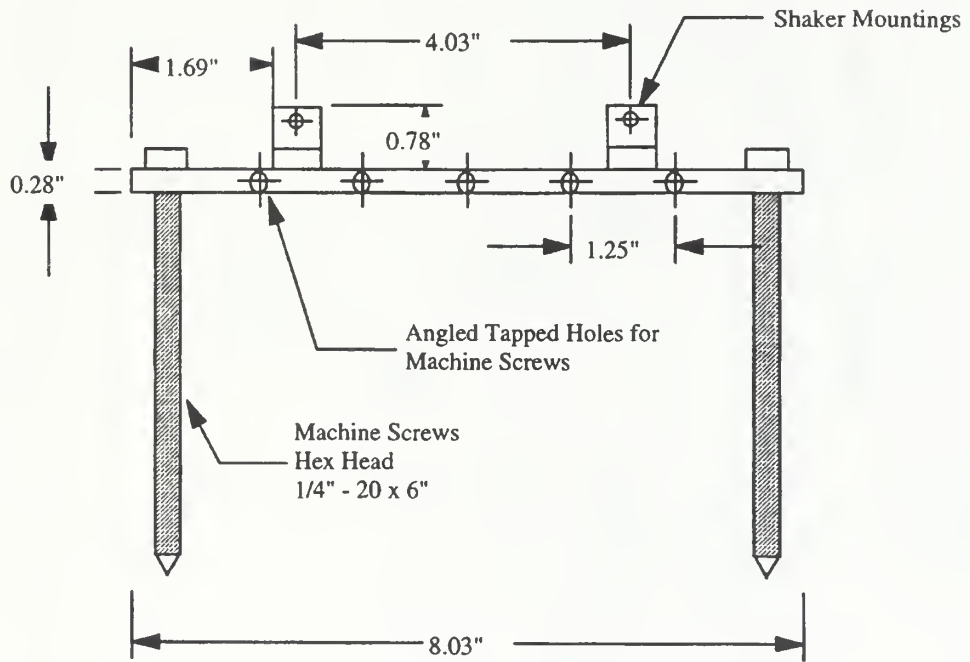


Side View:

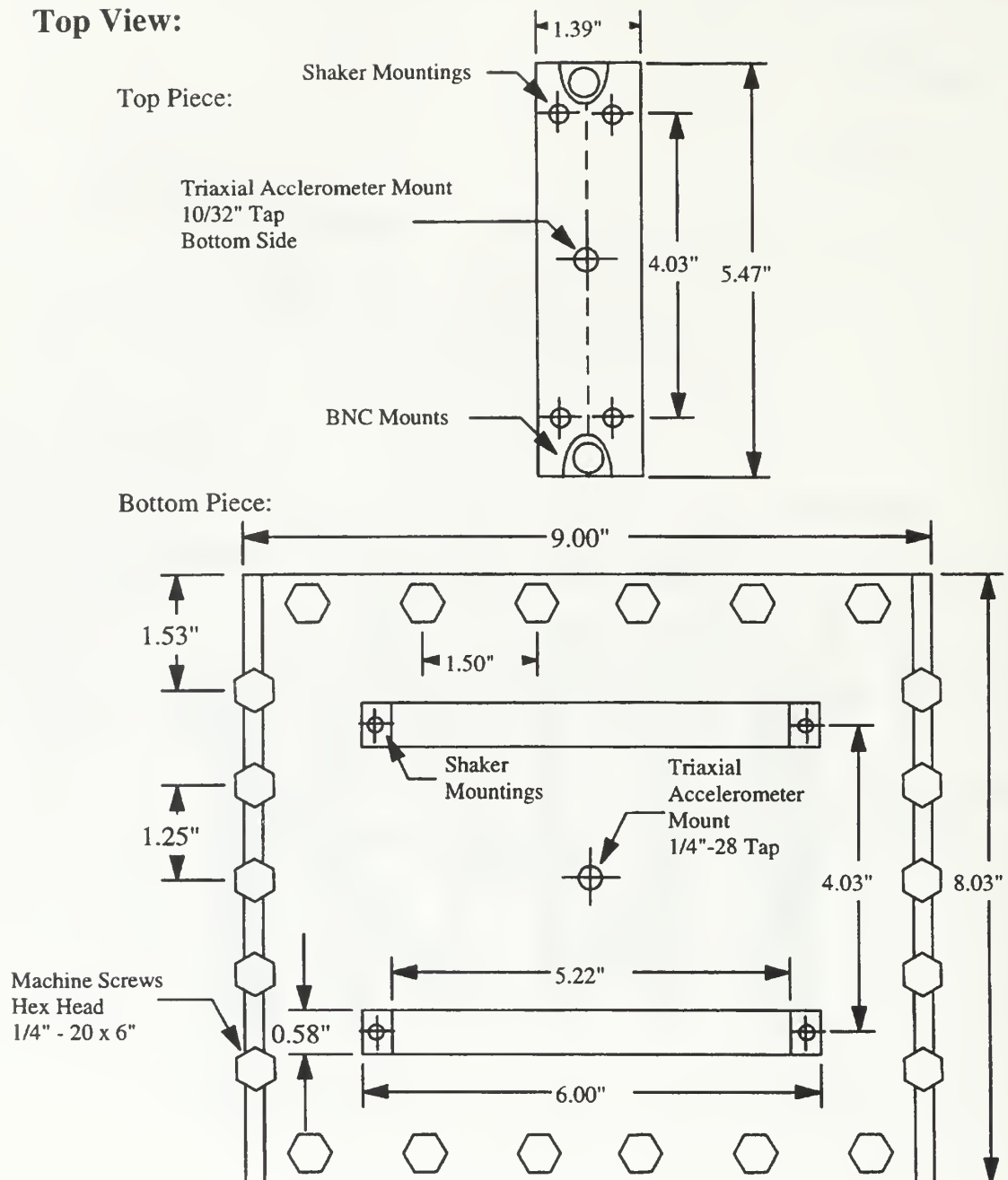
Top Piece:



Bottom Piece:



Top View:



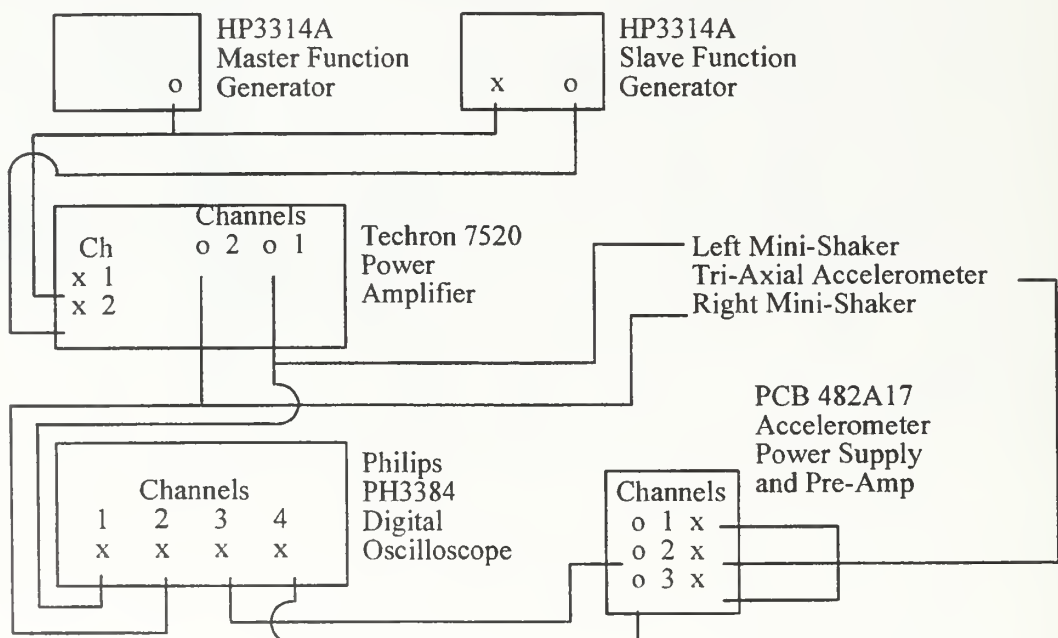
APPENDIX D. TEST EQUIPMENT WIRING DIAGRAMS AND EXPERIMENTAL SETUPS

This appendix contains the test equipment wiring schematics and diagrams of the experimental setups utilized during source experimentation.

APPENDIX D1. CONCEPT SOURCE LABORATORY TEST EQUIPMENT AND SETUP

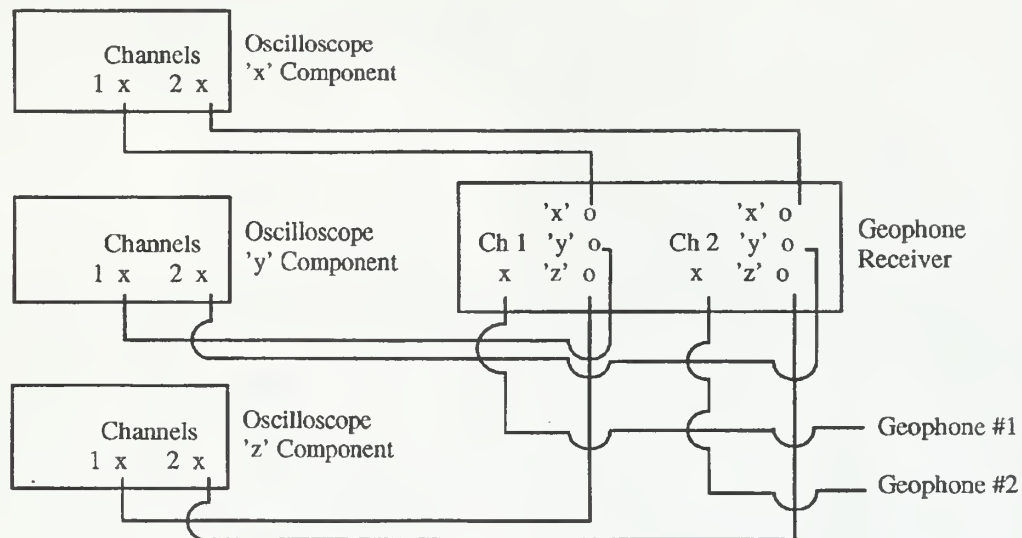
The following diagrams provide the wiring schematics and tank layout for the laboratory test equipment used for concept source experimentation. The equipment setup consisted of two units, a signal generating rack, and a signal receiving rack. The signal generating rack consisted of two phase-locked function generators, with the master function generator controlling the left Mini-Shaker and the slave function generator controlling the right. The output from the function generators was sent through a voltage amplifier then to the two vibration sources, with the resulting signals displayed on the oscilloscope. The pre-amp provided power for the source mounted tri-axial accelerometer with only the longitudinal and vertical components as outputs to the oscilloscope.

Signal Generating Rack:



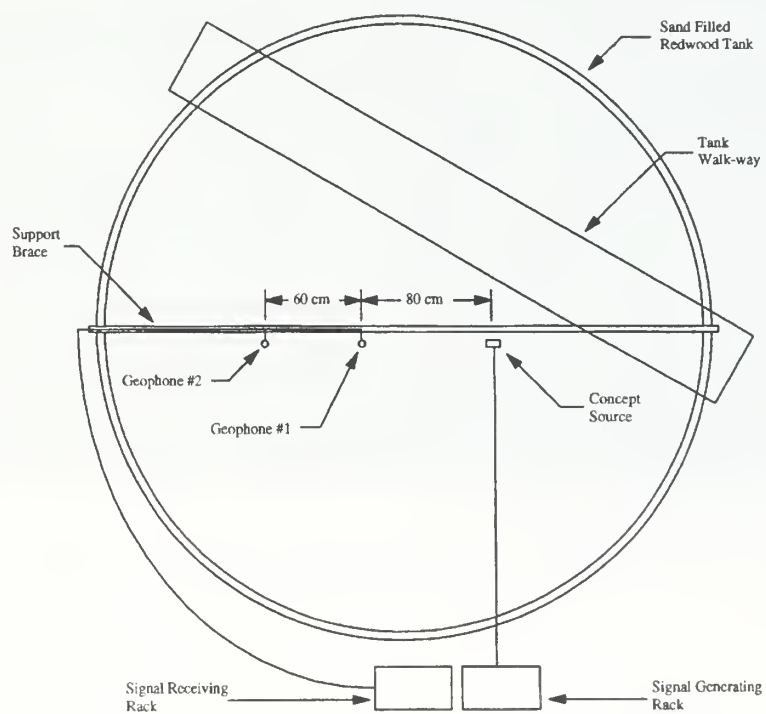
The signal receiving rack consisted of a unit built by ARL:UT, which provided power to the two tri-axial geophones and output connections for each of the three components of motion. The three oscilloscopes displayed the received signals from the two geophones.

Signal Receiving Rack:



The source and geophones were positioned in the test tank as shown below.

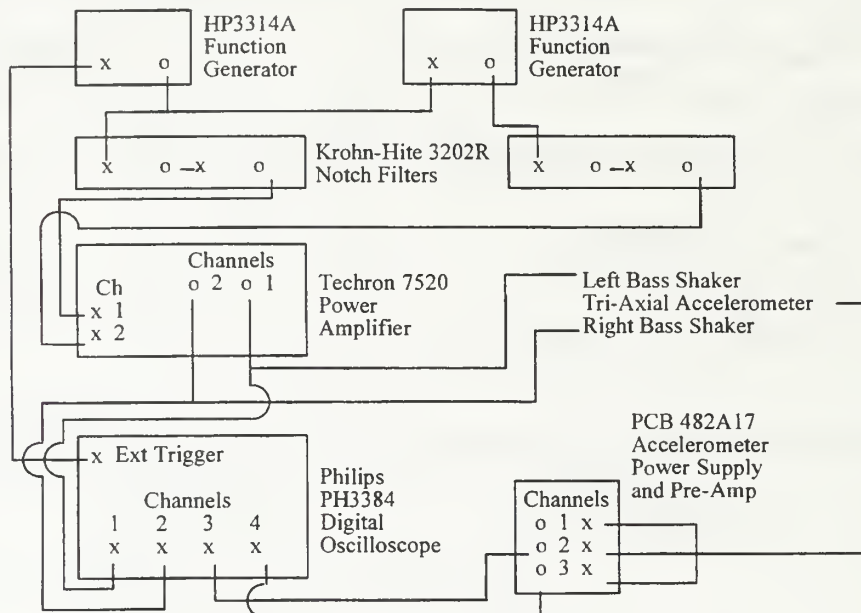
Sand Tank Setup:



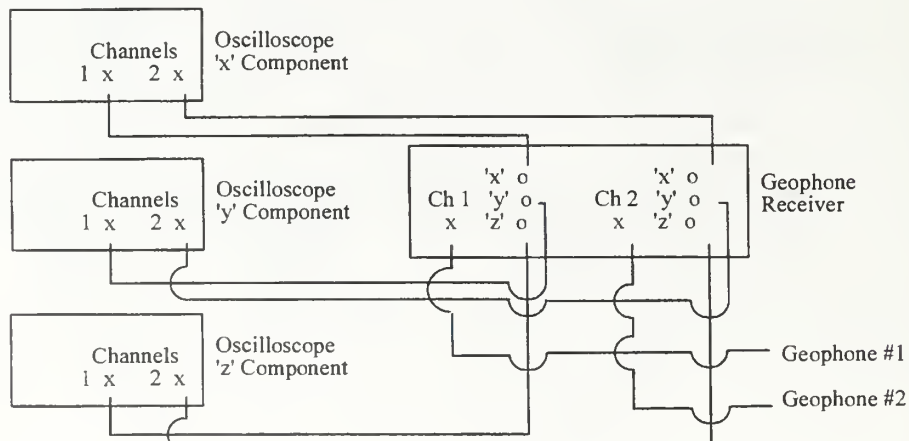
APPENDIX D2. FIELD TEST SOURCE – MOD I LABORATORY TEST EQUIPMENT AND SETUP

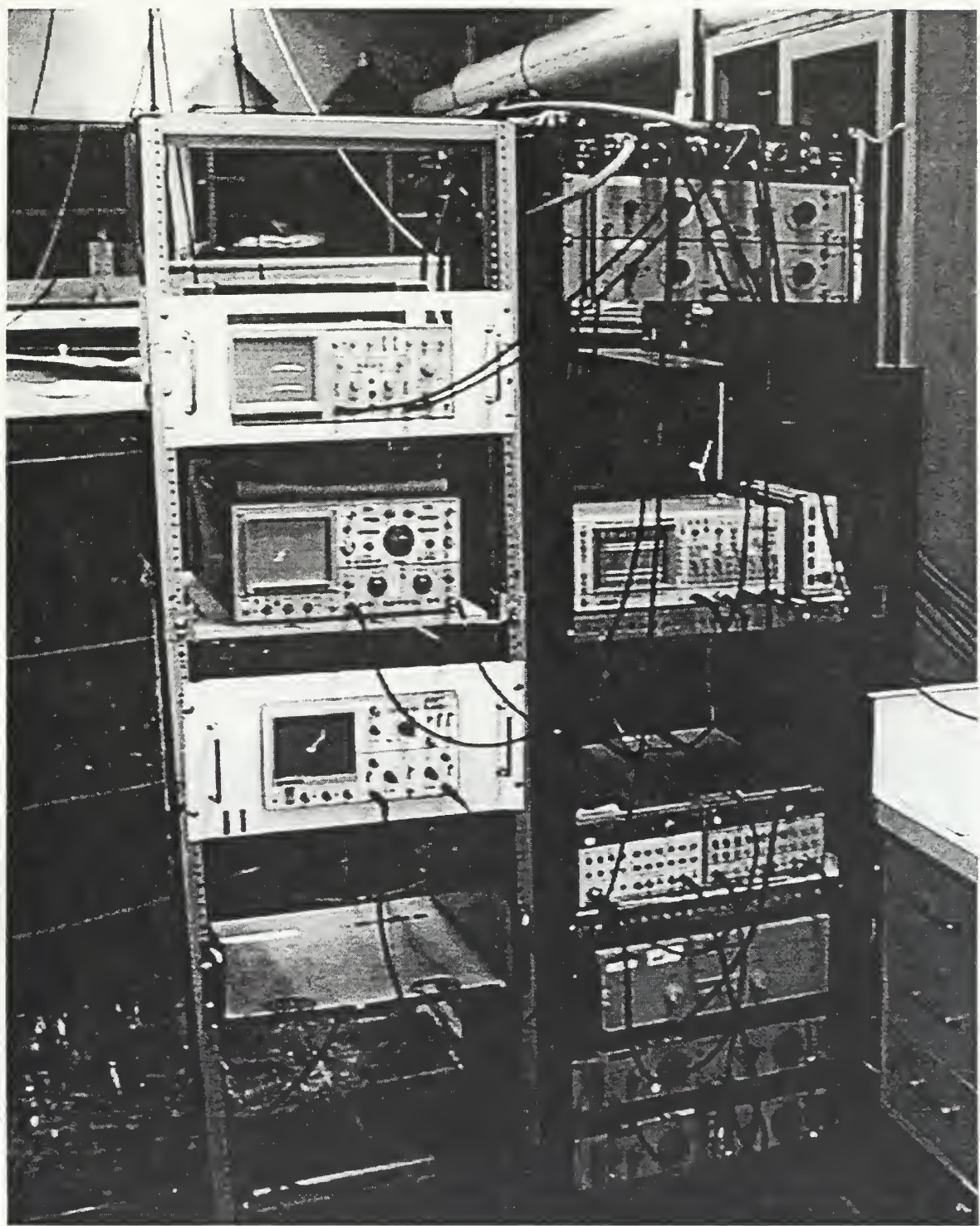
The following diagrams provide the wiring schematics and tank layout for the laboratory test equipment used while conducting source experimentation with the Mod I Field Test Source. The equipment setup and tank layout shown below are the same as the setups described in Appendix D1, except for the addition of two notch filters in between the function generators and the voltage amplifier in the signal generating rack.

Signal Generating Rack:

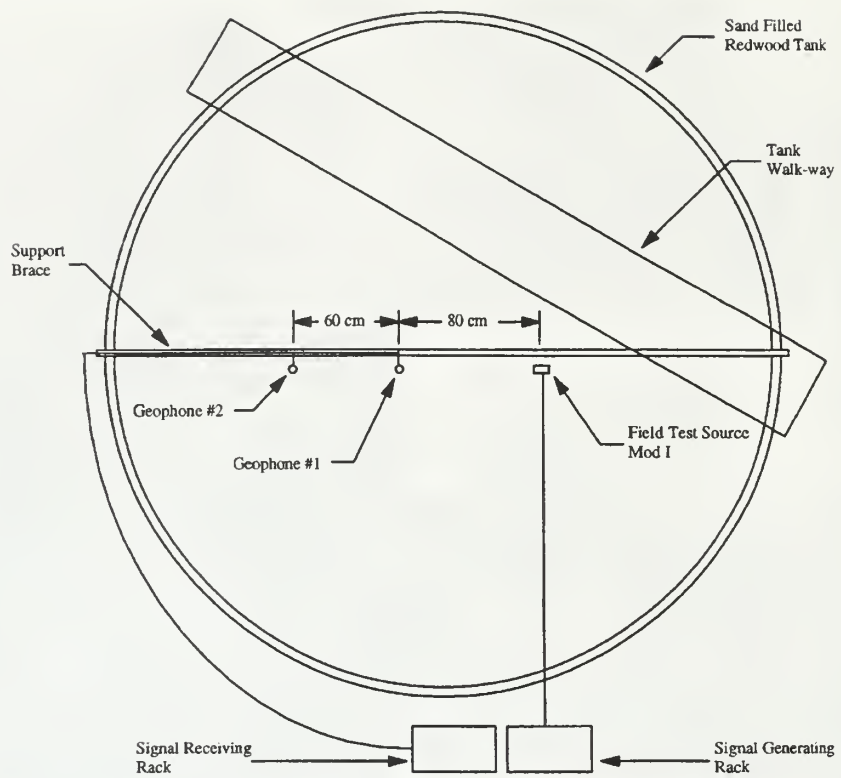


Signal Receiving Rack:





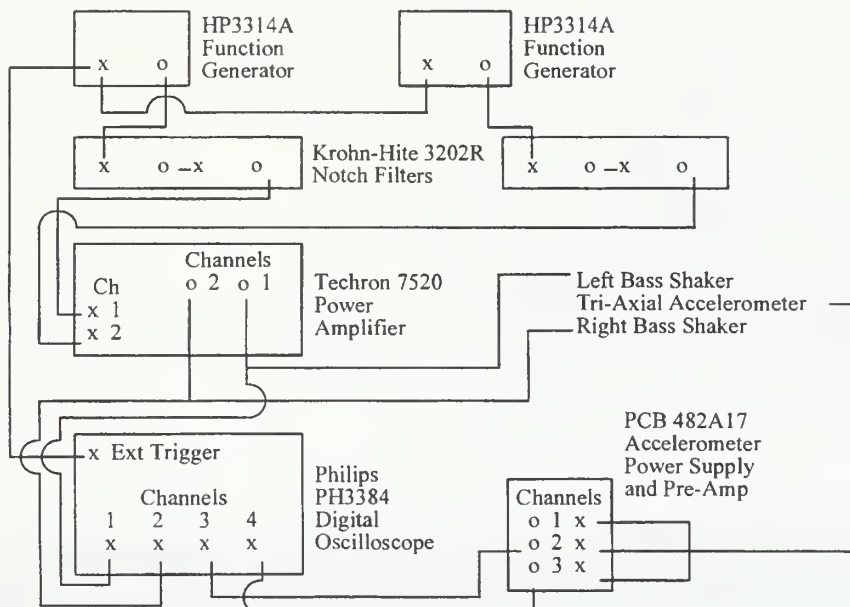
Sand Tank Setup:



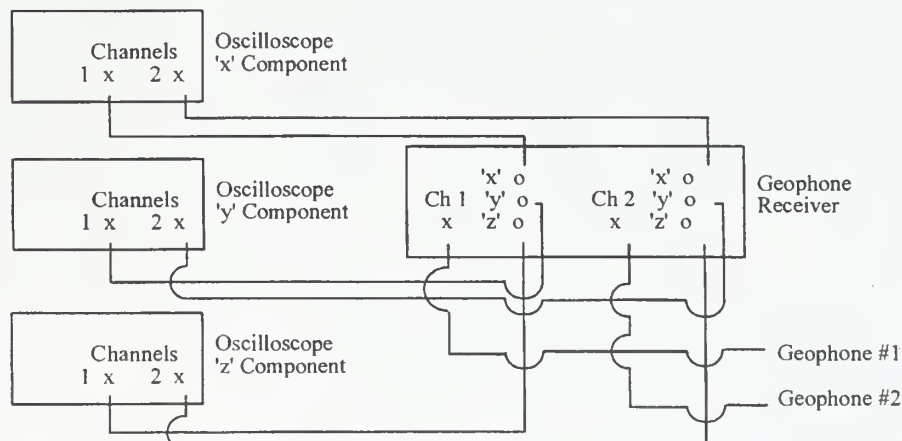
APPENDIX D3. FIELD TEST SOURCE – MOD I SOFTBALL FIELD TEST EQUIPMENT AND SETUP

The following diagrams describe the equipment and experimental layout utilized for the field experimentation of the Mod I Field Test Source. The equipment setup is nearly identical to the setup as described in Appendix D2, except that the two Bass Shakers were now operated independently.

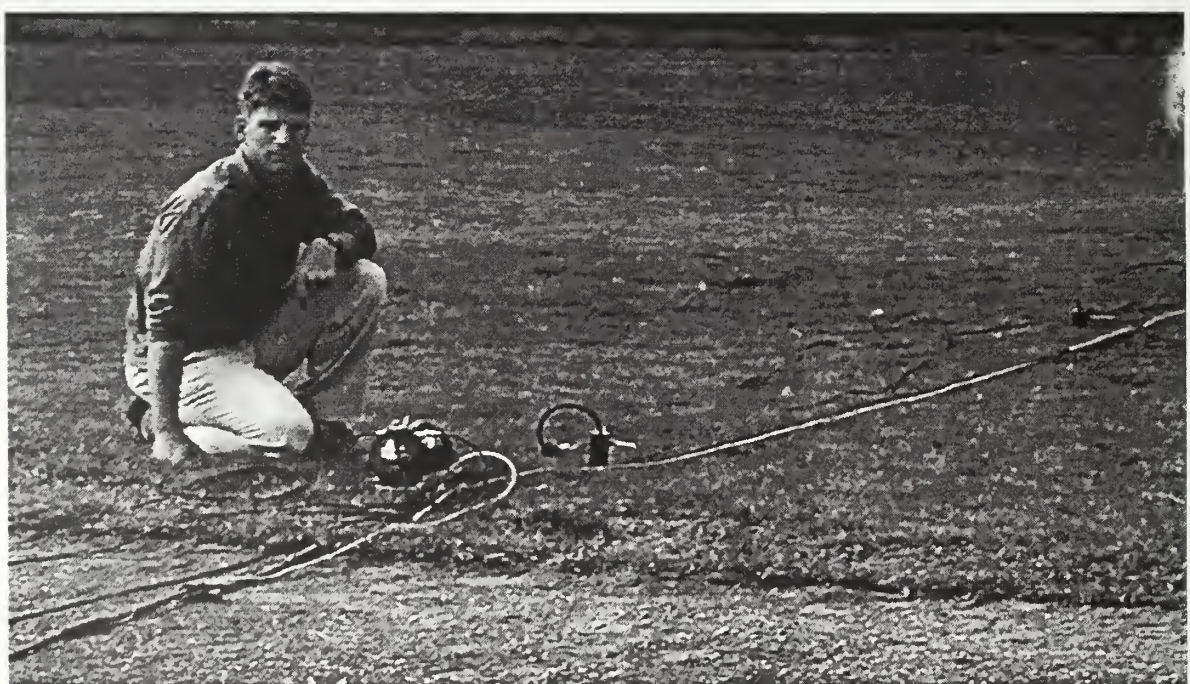
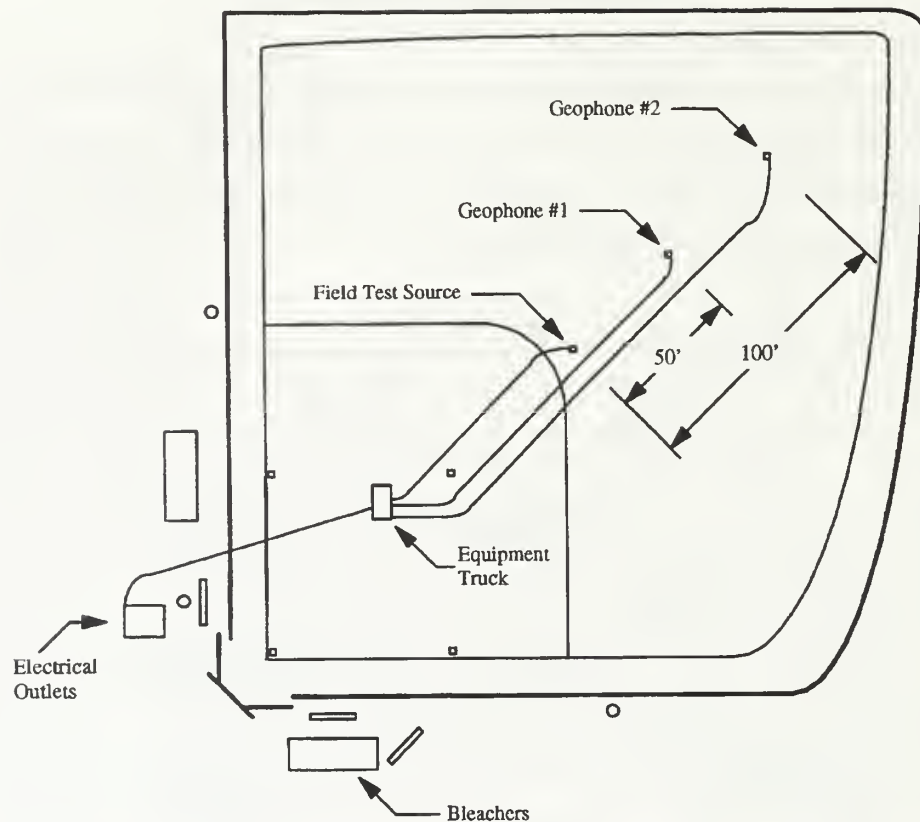
Signal Generating Rack:



Signal Receiving Rack:



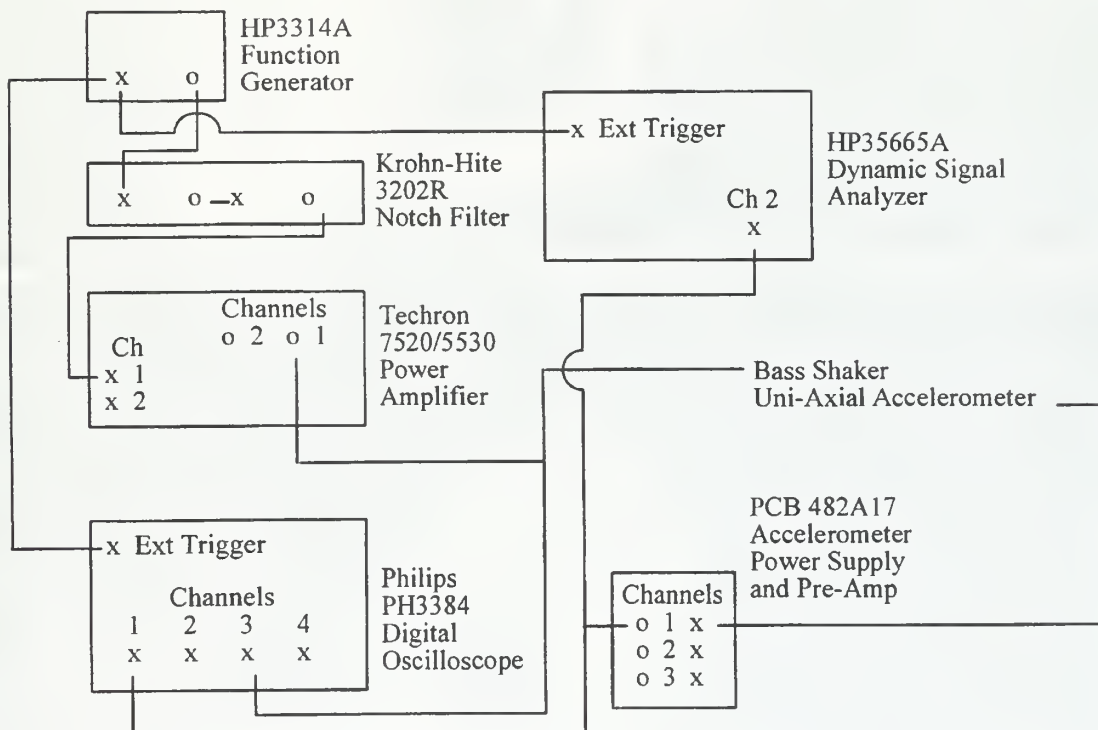
NPS Softball Field:

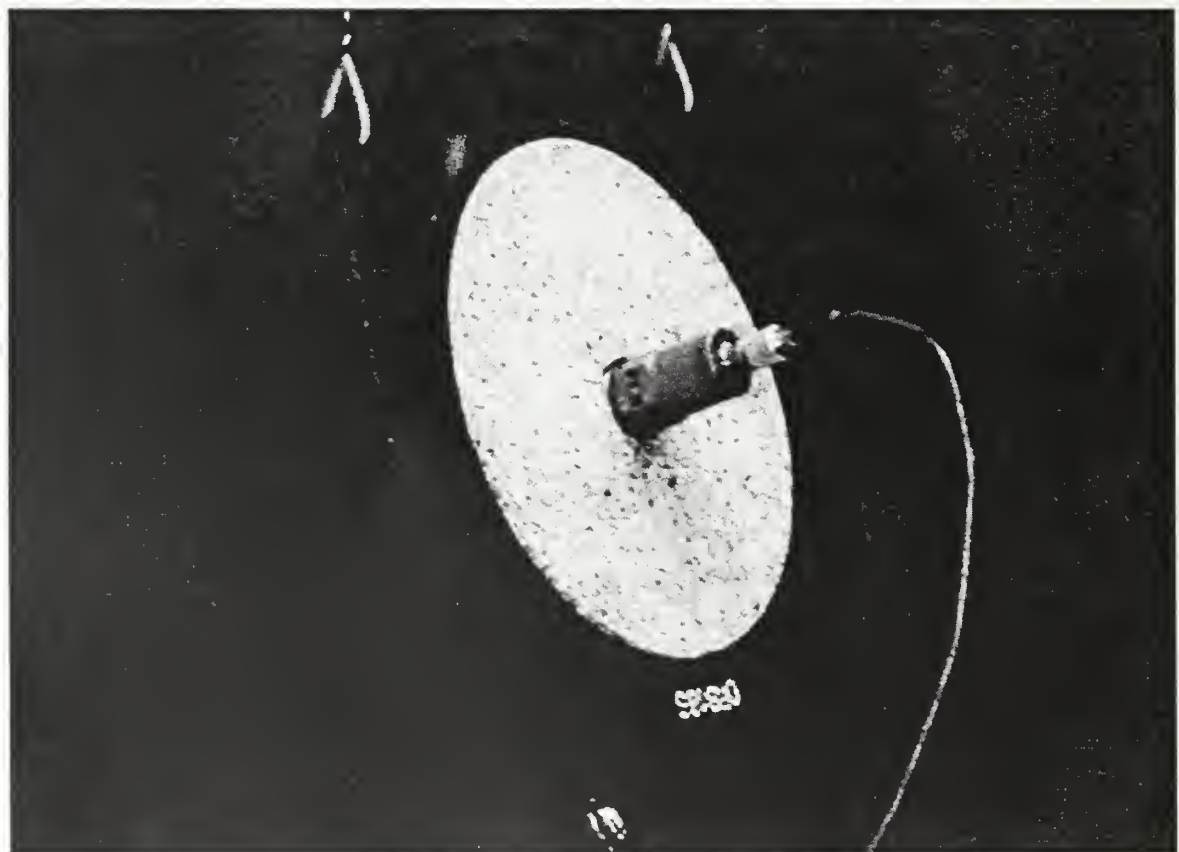
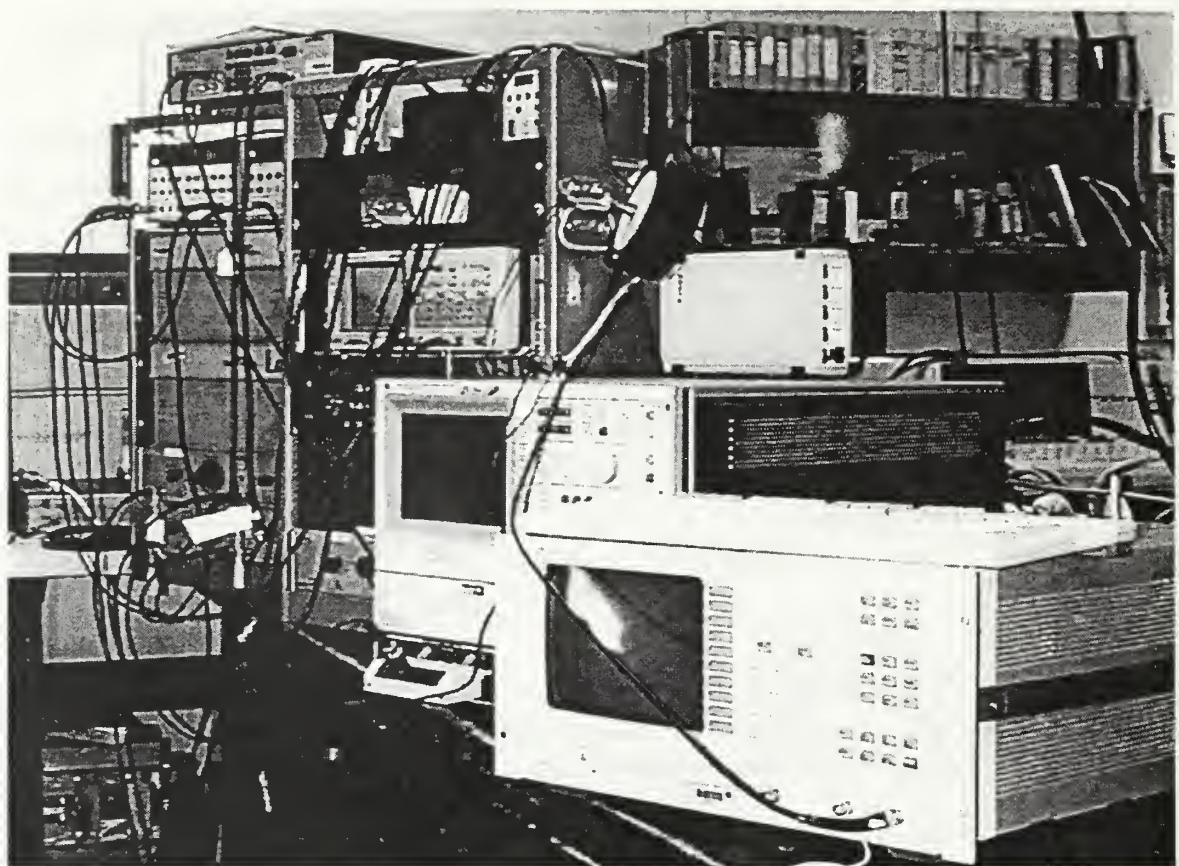


APPENDIX D4. BASS SHAKER FAILURE TEST EQUIPMENT AND SETUP

The test equipment used in investigating the operating limits of the Bass Shakers is shown below. For the necessary testing, only one side of the signal generating rack, as described in Appendix D3, was required. The HP35665A Signal Analyzer was used to monitor the output signal of the case mounted uni-axial accelerometer.

Bass Shaker Failure Test Equipment:

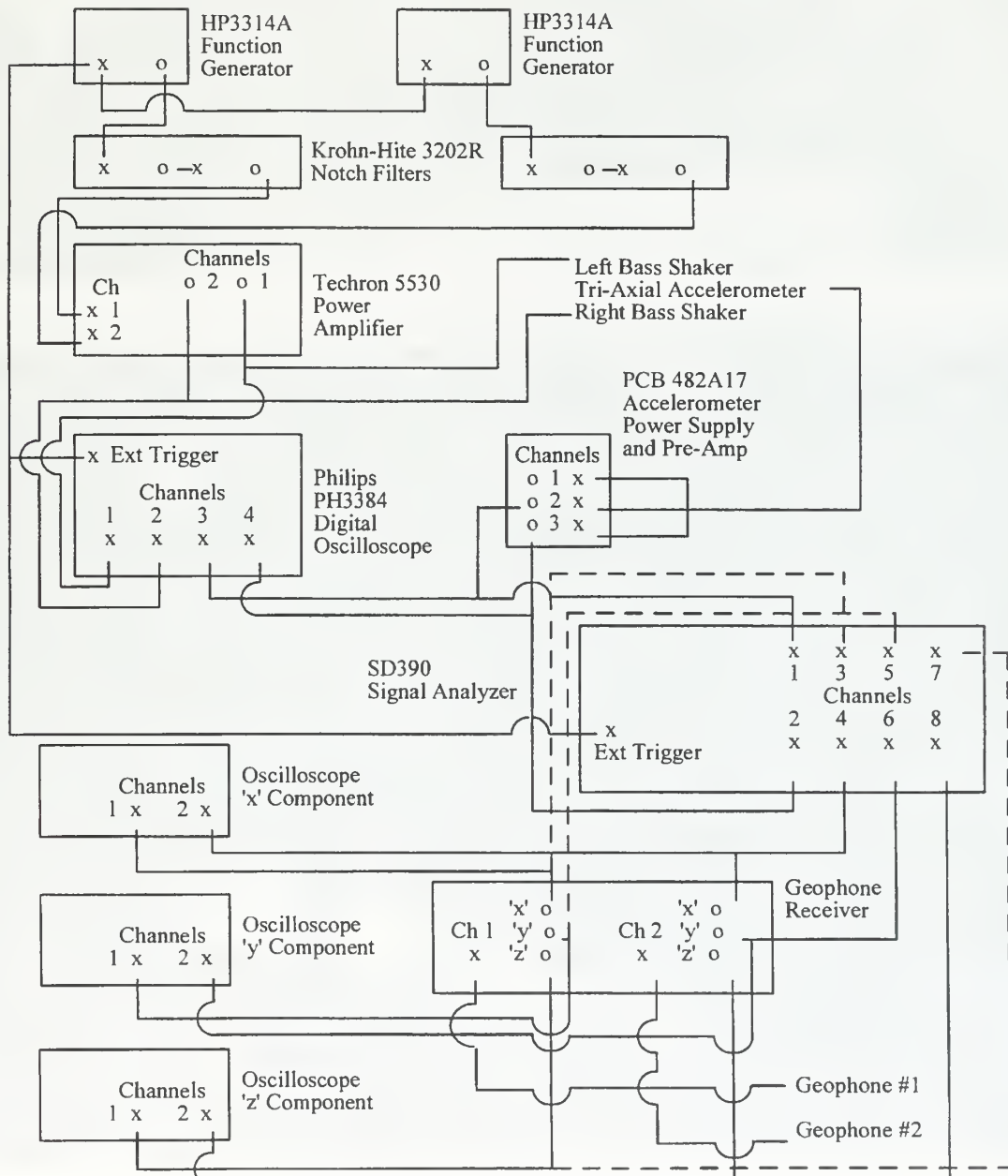


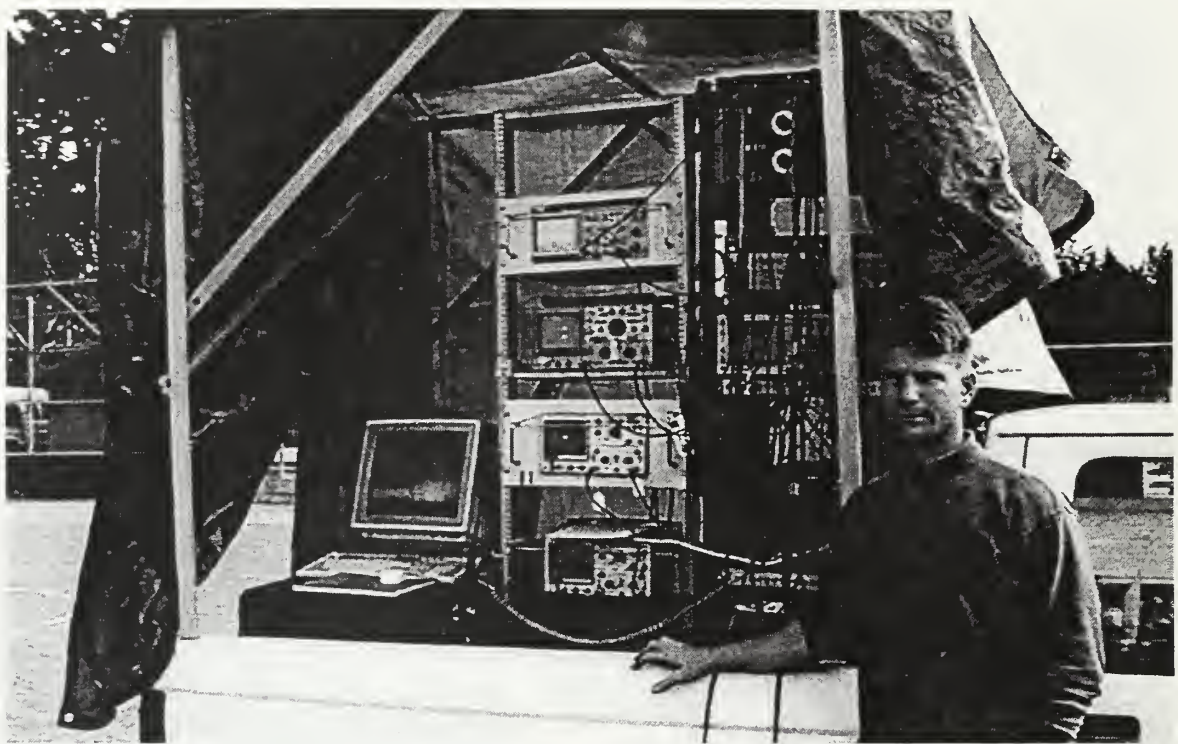


APPENDIX D5. FIELD TEST SOURCE – MOD II SOFTBALL FIELD TEST EQUIPMENT AND SETUP

The equipment diagram shown below is identical to the setup shown in Appendix D3, except for the addition of the SD390 Signal Analyzer. Incorporation of the SD390, allowed for acquisition of eight data channels. The dotted lines in the diagram are used only for clarity of the test equipment setup.

Field Equipment Diagram:

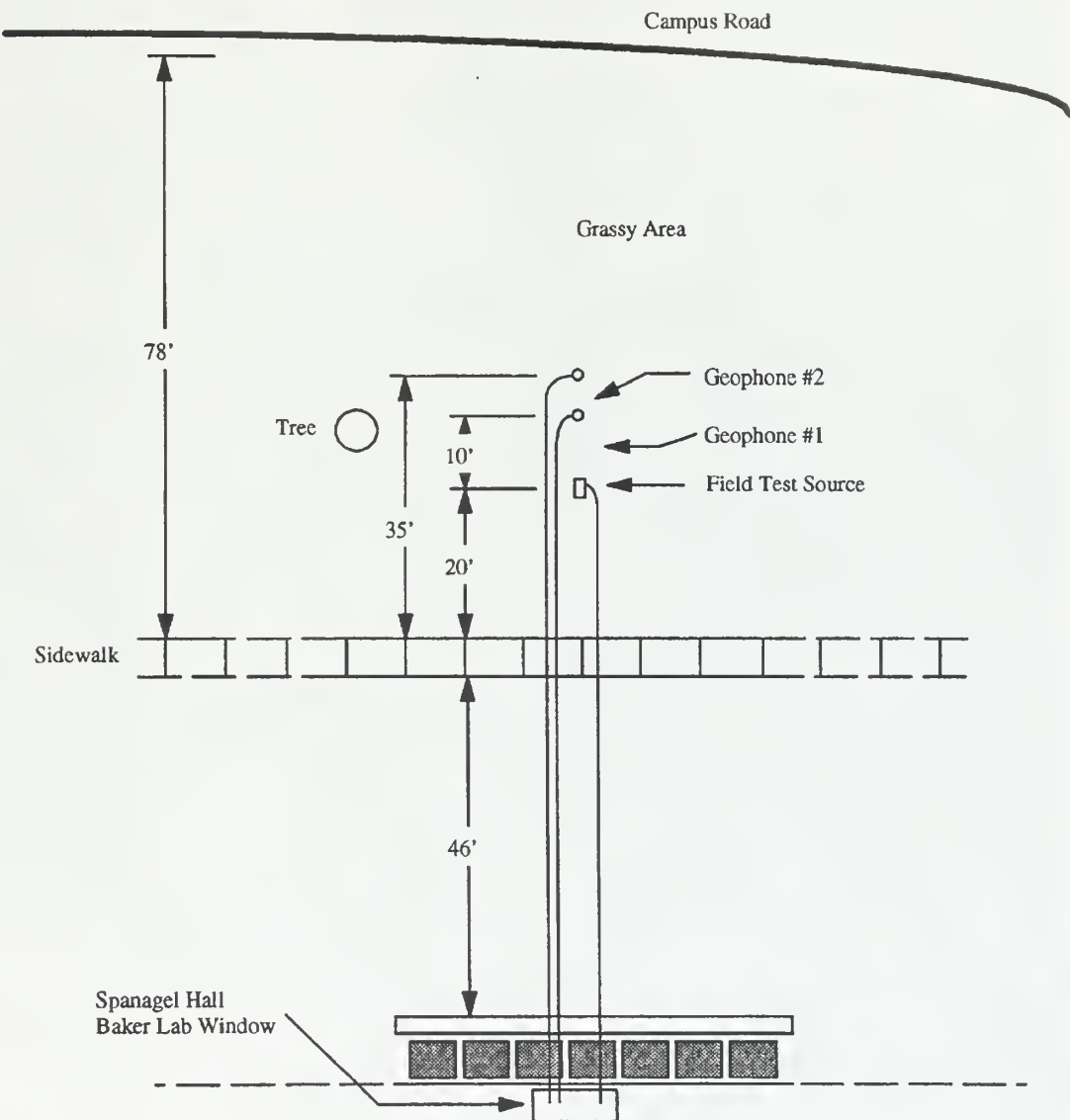




APPENDIX D6. FIELD TEST SOURCE – MOD III FIELD SETUP

The diagram shown below describes the experimental layout for the final ground phase testing of the Mod III Field Test Source.

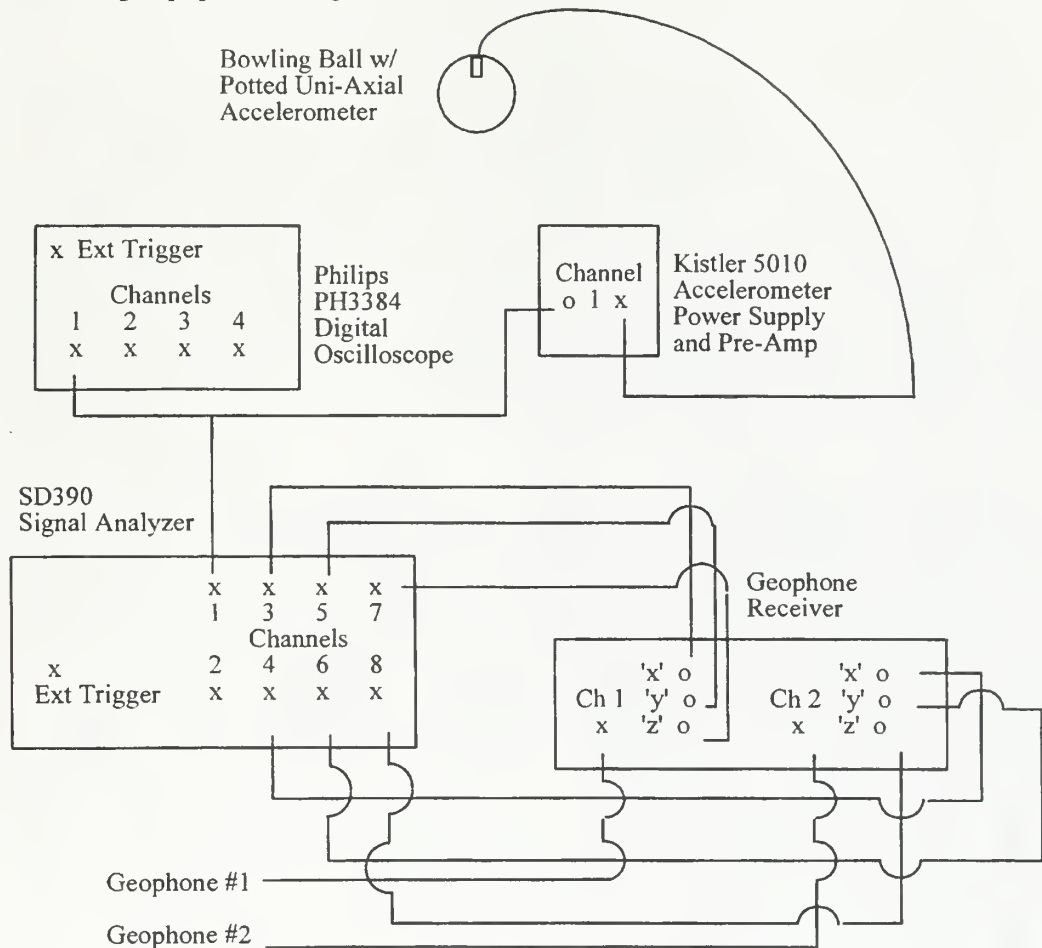
Field Test Source - Mod III Experimental Layout



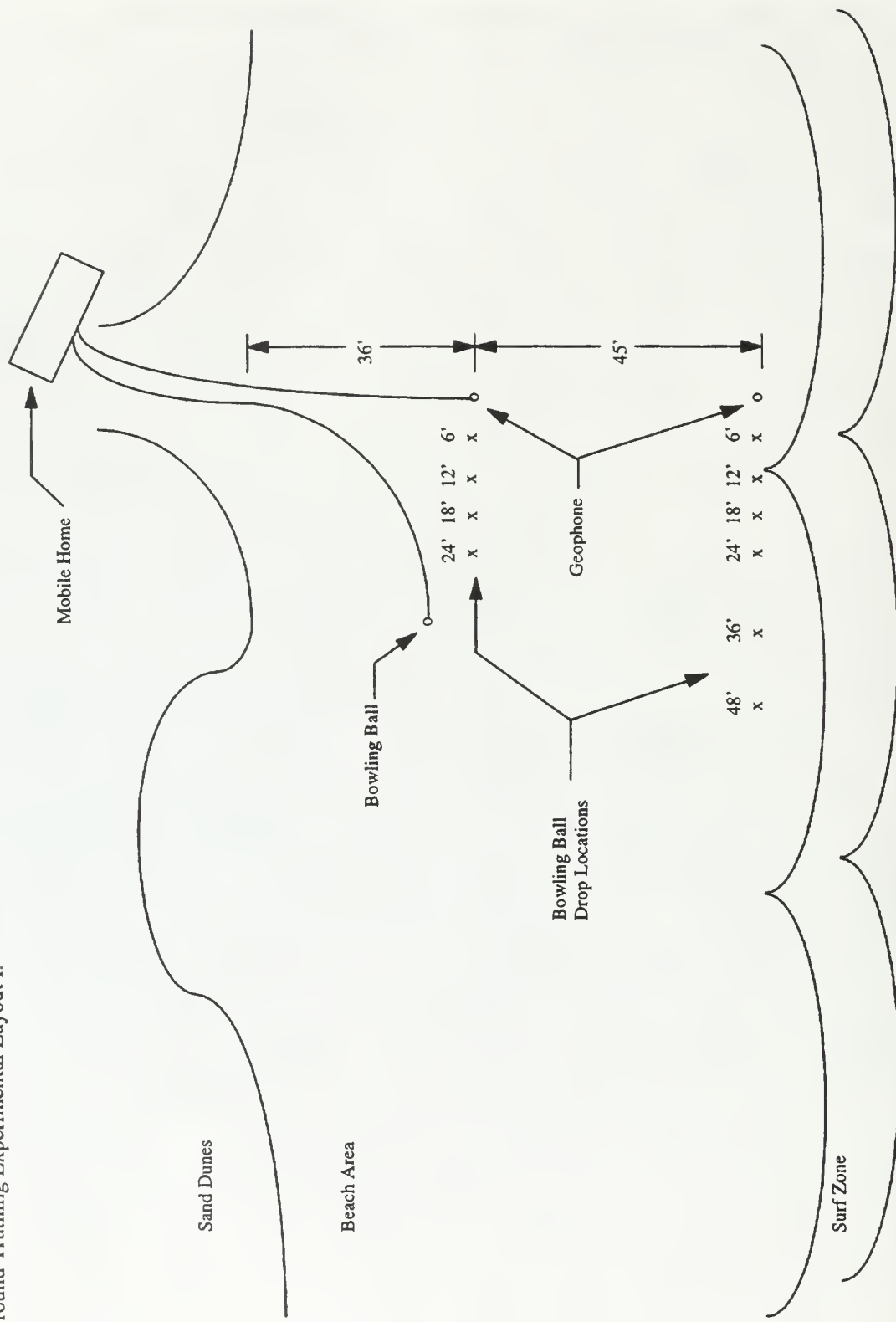


APPENDIX D7. GROUND TRUTHING TEST EQUIPMENT AND SETUP

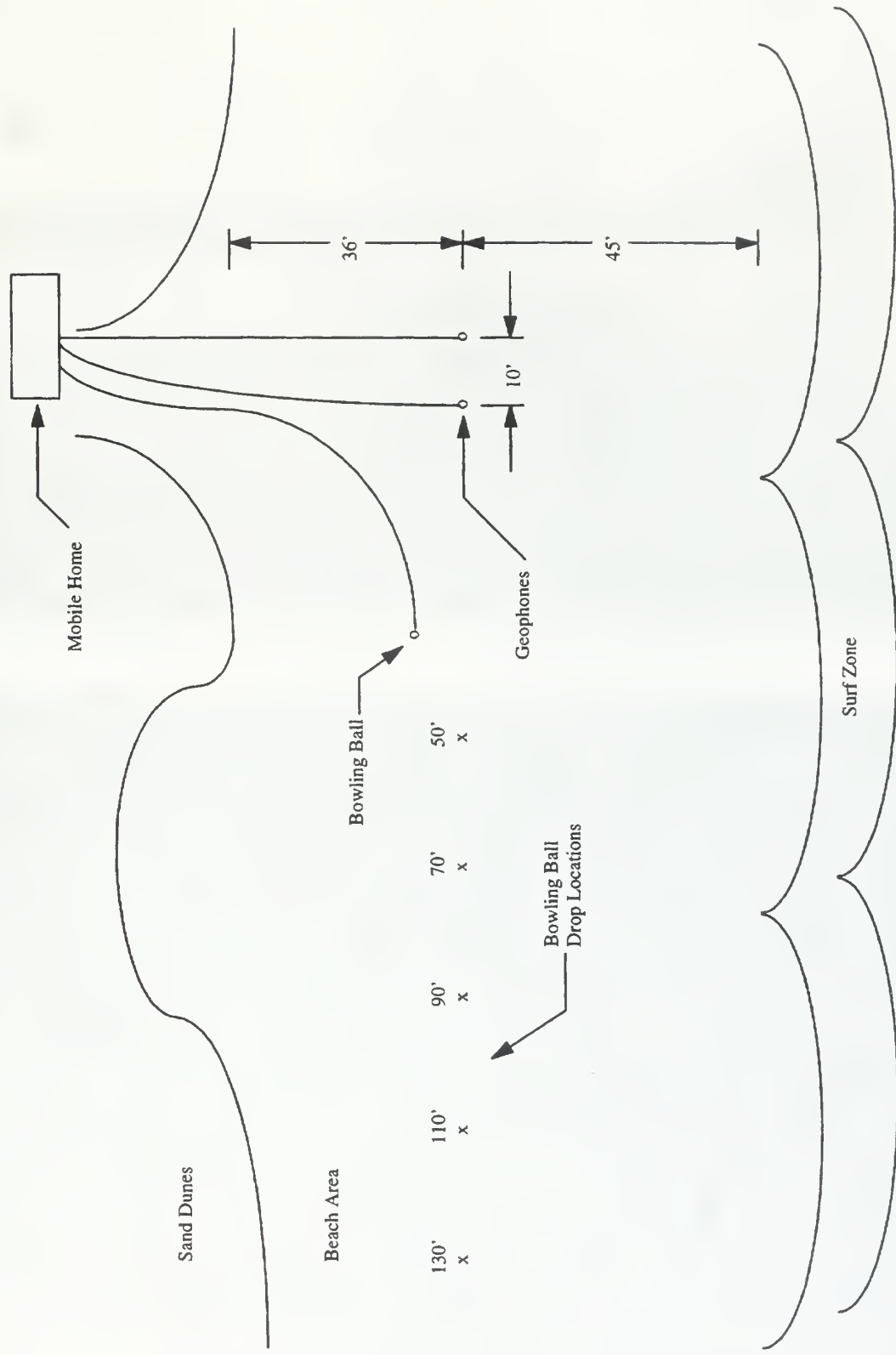
Ground Truthing Equipment Diagram:

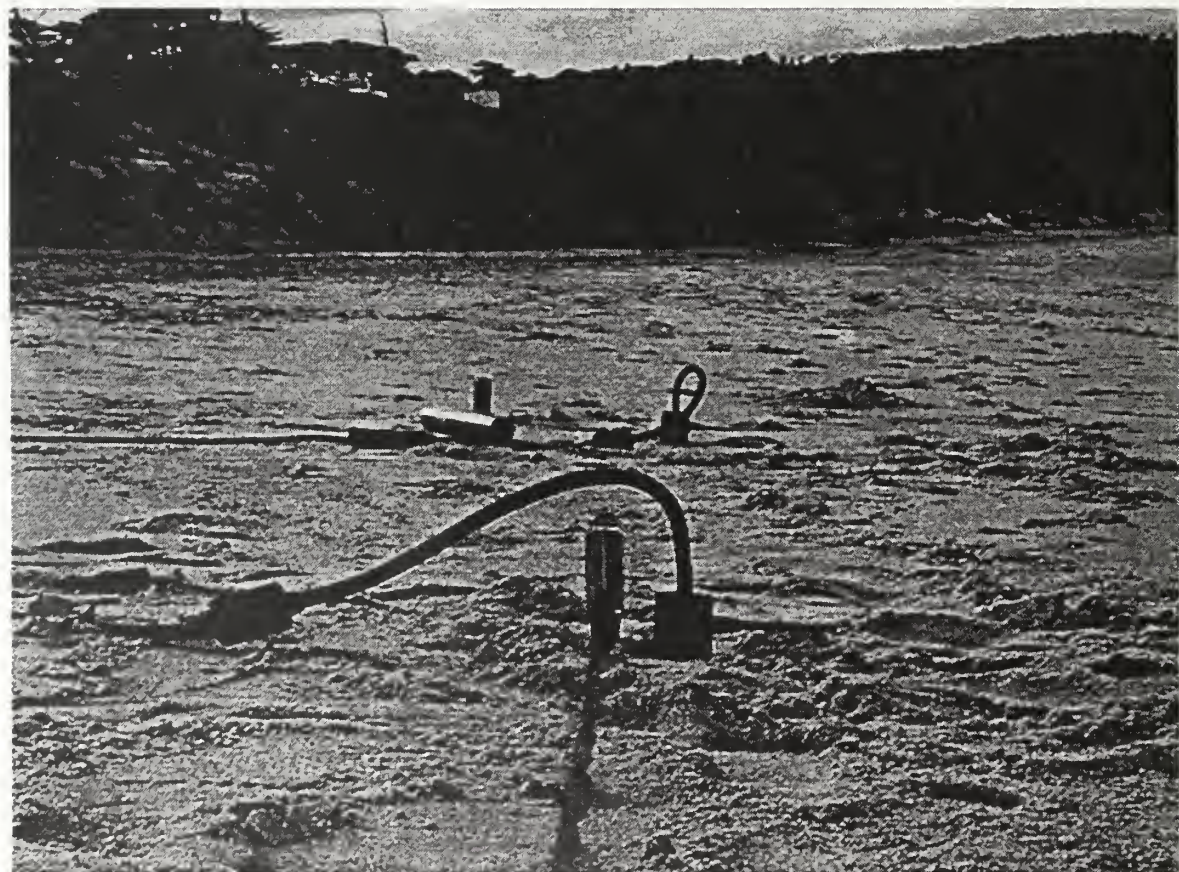


Ground Truthing Experimental Layout I:



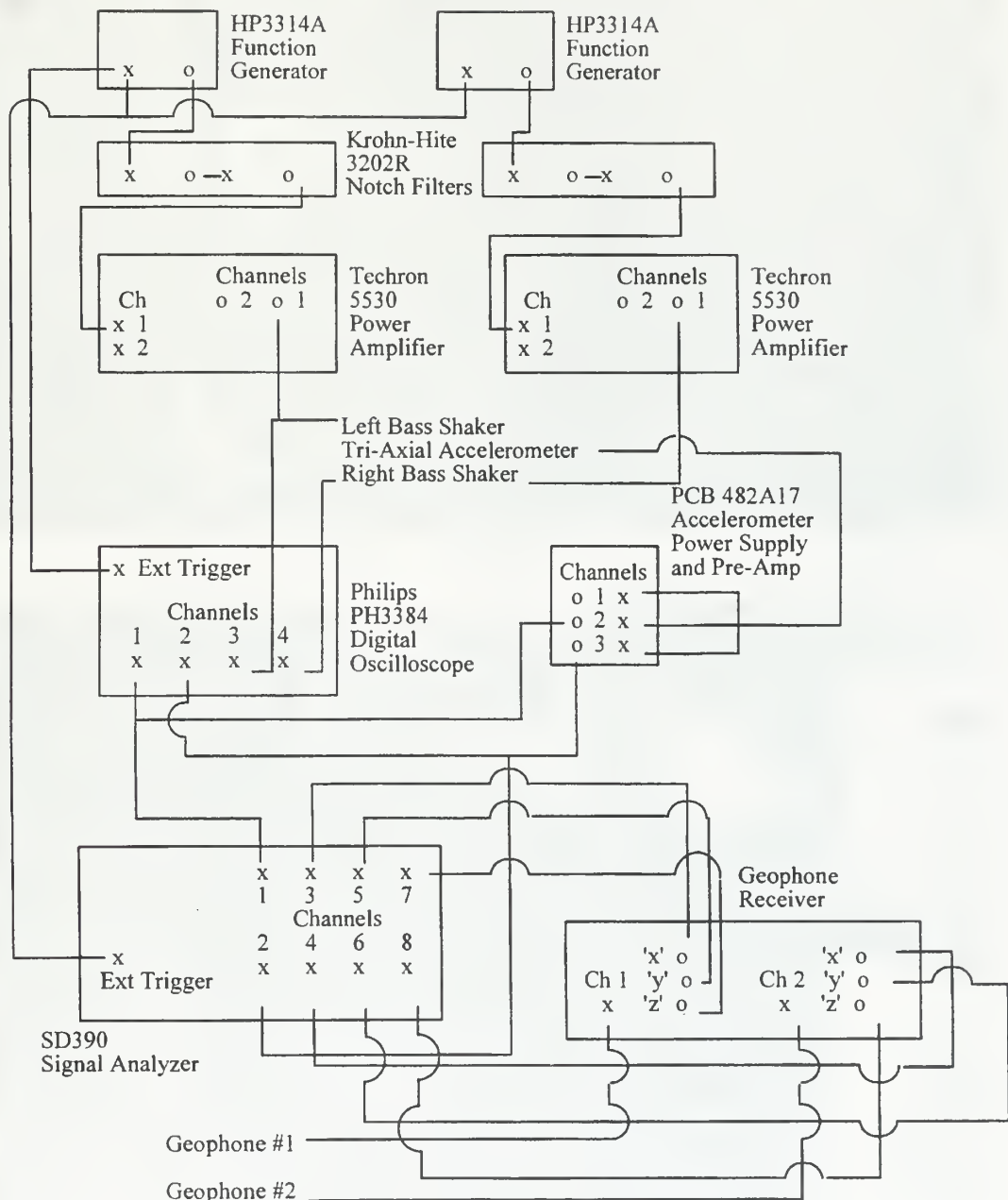
Ground Truthing Experimental Layout II:

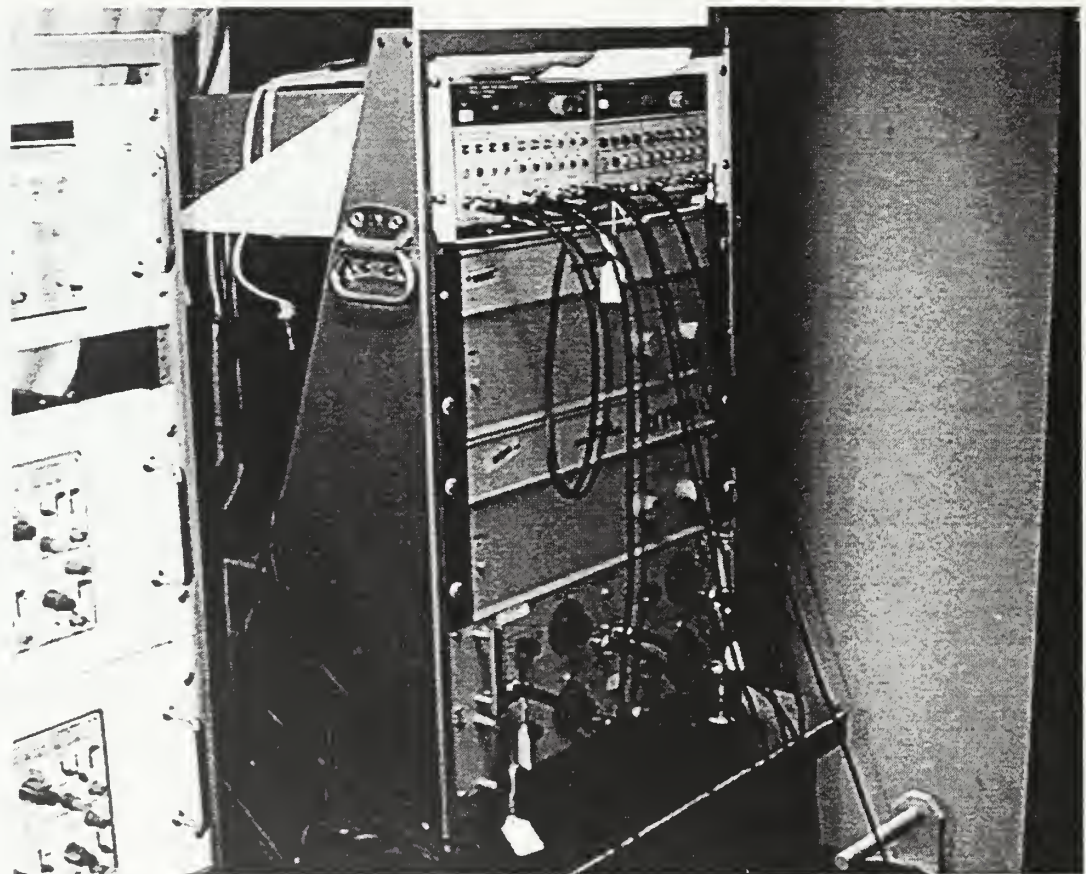
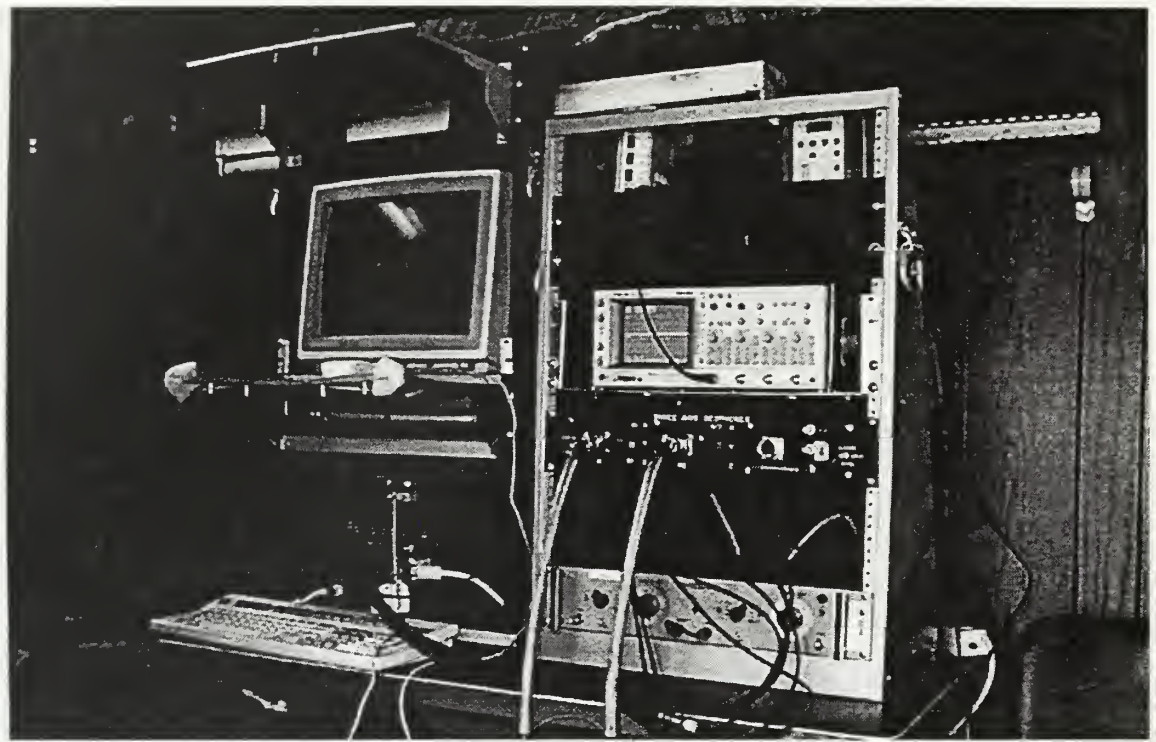




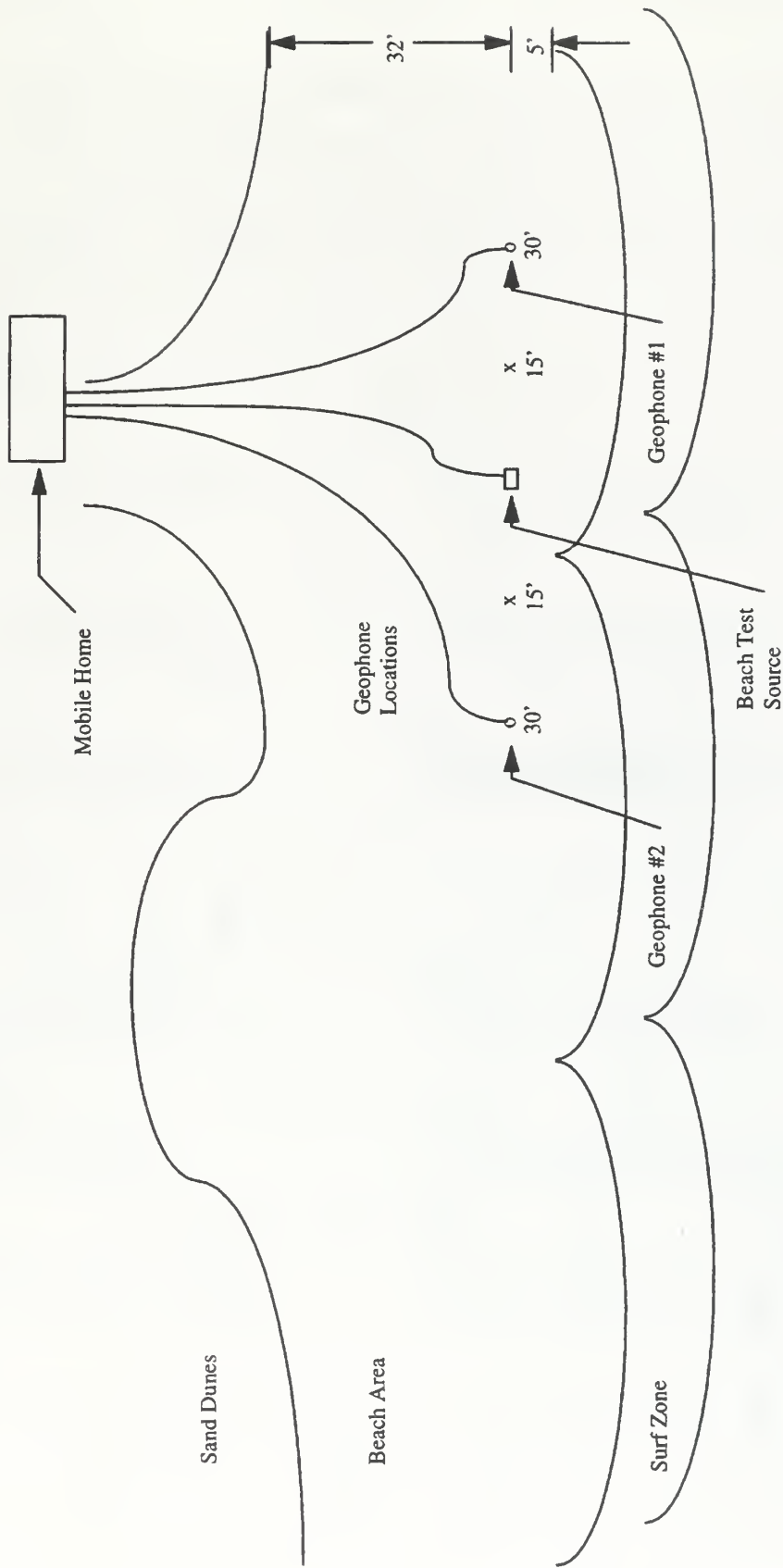
APPENDIX D8. FIELD TEST SOURCE – MOD IV BEACH SETUP

Beach Equipment Diagram:

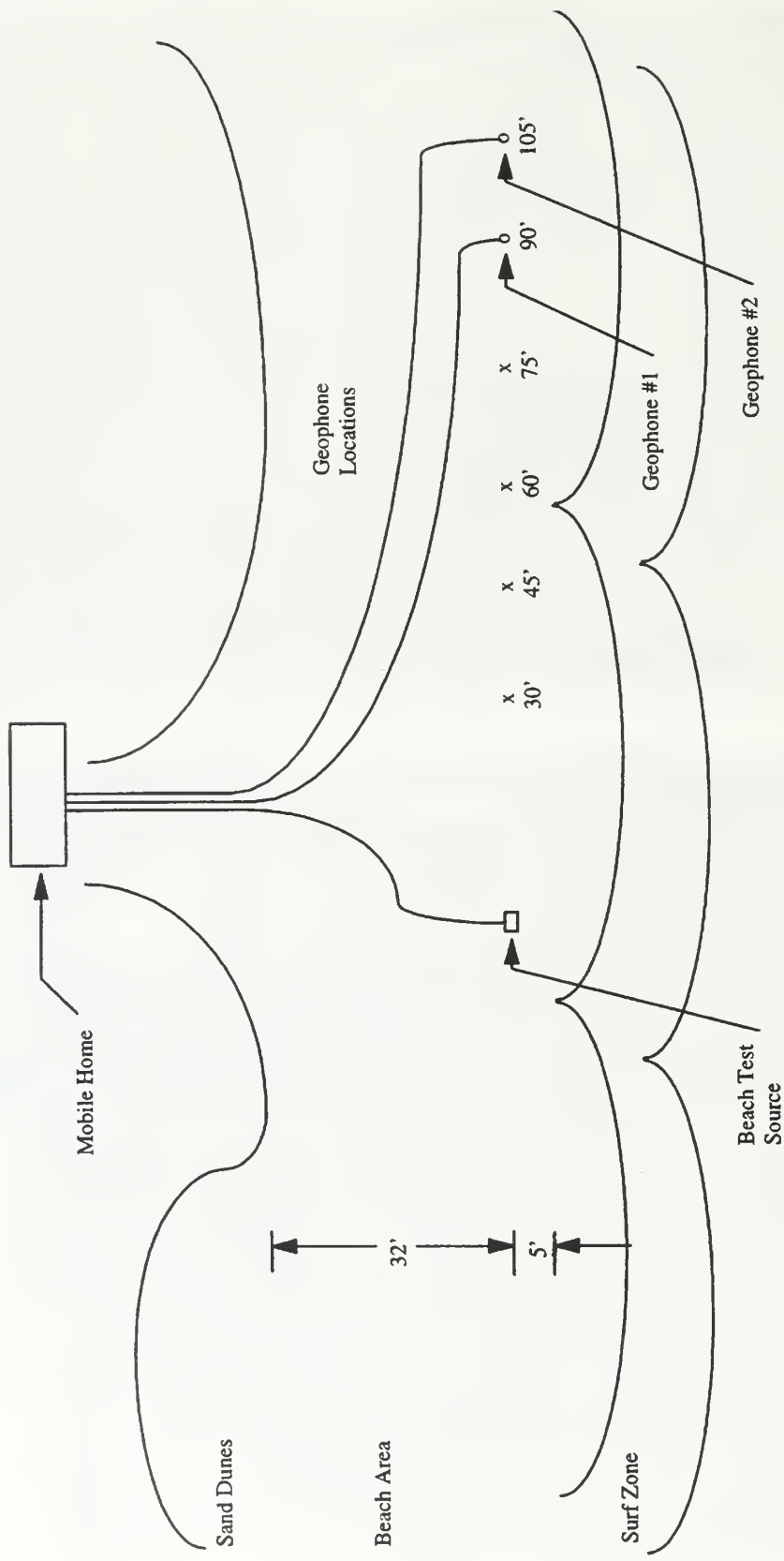




Beach Test Source Experimental Layout I:



Beach Test Source Experimental Layout II:



APPENDIX E. CONCEPT SOURCE EXPERIMENTAL RESULTS

This appendix contains the qualitative results for the effects of frequency and phase on the axial surface wave field for the concept source. The effects were characterized by the amplitude of the longitudinal and vertical signals of the geophone farthest from the source compared to those of the geophone closest to the source, as observed on the oscilloscopes.

Frequency: 100 Hz

Case 1

Radial: No Noticeable Difference
Vertical: Visible Reduction

Case 3

Radial: Visible Reduction
Vertical: No Noticeable Difference

Case 5

Radial: Visible Reduction
Vertical: Visible Reduction

Case 2

Radial: No Noticeable Difference
Vertical: Visible Reduction

Case 4

Radial: Visible Reduction
Vertical: No Noticeable Difference

Case 6

Radial: No Noticeable Difference
Vertical: Visible Reduction

Frequency: 150 Hz

Case 1

Radial: Visible Reduction
Vertical: No Noticeable Difference

Case 3

Radial: Visible Reduction
Vertical: Visible Reduction

Case 5

Radial: No Noticeable Difference
Vertical: No Noticeable Difference

Case 2

Radial: Visible Reduction
Vertical: Visible Reduction

Case 4

Radial: Visible Reduction
Vertical: No Noticeable Difference

Case 6

Radial: Visible Increase
Vertical: No Noticeable Difference

Frequency: 200 Hz

Case 1

Radial: Visible Increase
Vertical: No Noticeable Difference

Case 3

Radial: No Noticeable Difference
Vertical: No Noticeable Difference

Case 5

Radial: No Noticeable Difference
Vertical: No Noticeable Difference

Case 2

Radial: Visible Reduction
Vertical: No Noticeable Difference

Case 4

Radial: Visible Reduction
Vertical: No Noticeable Difference

Case 6

Radial: Visible Reduction
Vertical: No Noticeable Difference

Frequency: 250 Hz

Case 1

Radial: Visible Reduction
Vertical: No Noticeable Difference

Case 3

Radial: Visible Reduction
Vertical: No Noticeable Difference

Case 5

Radial: No Noticeable Difference
Vertical: No Noticeable Difference

Case 2

Radial: Visible Reduction
Vertical: Visible Reduction

Case 4

Radial: Visible Reduction
Vertical: Visible Reduction

Case 6

Radial: Visible Reduction
Vertical: No Noticeable Difference

Frequency: 300 Hz

Case 1

Radial: Visible Reduction
Vertical: Visible Reduction

Case 3

Radial: Visible Reduction
Vertical: No Noticeable Difference

Case 5

Radial: No Noticeable Difference
Vertical: Visible Reduction

Case 2

Radial: Visible Reduction
Vertical: No Noticeable Difference

Case 4

Radial: Visible Reduction
Vertical: Visible Reduction

Case 6

Radial: No Noticeable Difference
Vertical: Visible Reduction

Frequency: 500 Hz

Case 1

Radial: No Noticeable Difference
Vertical: Visible Reduction

Case 3

Radial: Visible Reduction
Vertical: Visible Reduction

Case 5

Radial: No Noticeable Difference
Vertical: Visible Reduction

Case 2

Radial: Visible Reduction
Vertical: Visible Reduction

Case 4

Radial: No Noticeable Difference
Vertical: Visible Reduction

Case 6

Radial: No Noticeable Difference
Vertical: Visible Reduction

APPENDIX F. AMBIENT BACKGROUND NOISE ANALYSIS

This appendix contains the MATLAB program and output figures used to conduct the spectral analysis of the ambient background noise at the beach test site.

```
% Filename: noise2geos.m
% Written by: F.E. Gaghan
% Date Last Modified: 27 January 1998
% Purpose: This program is used to calculate the frequency spectrum and
%           power spectral density of the background noise from one of
%           two geophone signals for the various test sites. The user
%           has the option to perform the analysis for a single data
%           file or to perform an incoherent average for a number of
%           data files.

% Initialize user interface
average=input('Do you want to average the noise plots
(y or n): ','s');
directory=input('Input the noise file directory: ','s');
file_directory=[directory];

if average=='y'
    num_average=3;
else
    num_average=1;
end; %end-if average

% Assign noise signal component to appropriate data channel
geophone=input('Do you want the data from geophone 1 or 2: ');
if geophone==1
    rcvr_horiz_column=4;
    rcvr_vert_column=6;
else
    rcvr_horiz_column=5;
    rcvr_vert_column=7;
end; %end-if geophone
sampling_rate=5120;

% Loop structure used for signal averaging
for iteration=1:num_average
    disp(' ');
    if iteration==1
        file=input('Input the noise filename: ','s');
    else
        file=input('Input the next noise filename: ','s');
    end; %end-if iteration
    filename=[file];
    eval(['load ' file_directory,'\',filename]);

    horiz_noise=xrc390(:,rcvr_horiz_column)-
        mean(xrc390(:,rcvr_horiz_column));
    vert_noise=xrc390(:,rcvr_vert_column)-
        mean(xrc390(:,rcvr_vert_column));
```

```

% Calculate frequency response
fft_length=length(horiz_noise);
freqs_Hz=sampling_rate*(0:(fft_length/2)-1)/fft_length;
fft_horiz_noise=abs(fft(horiz_noise,fft_length))/fft_length;
fft_horiz_noise=fft_horiz_noise/max(fft_horiz_noise);
fft_vert_noise=abs(fft(vert_noise,fft_length))/fft_length;
fft_vert_noise=fft_vert_noise/max(fft_vert_noise);

% Calculate power spectral density
psd_horiz_noise=psd(horiz_noise,fft_length,sampling_rate)
    .* (2/sampling_rate);
dBpsd_horiz_noise=10*log10(psd_horiz_noise);
horiz_density_amp=10.^^(dBpsd_horiz_noise/10);

psd_vert_noise=psd(vert_noise,fft_length,sampling_rate)
    .* (2/sampling_rate);
dBpsd_vert_noise=10*log10(psd_vert_noise);
vert_density_amp=10.^^(dBpsd_vert_noise/10);

% Perform incoherent average of frequency spectrum and power
% spectral density
if iteration==1
    horiz_spectrum=zeros(size(fft_horiz_noise));
    horiz_spectrum=horiz_spectrum+(fft_horiz_noise.^2);
    vert_spectrum=zeros(size(fft_vert_noise));
    vert_spectrum=vert_spectrum+(fft_vert_noise.^2);
    horiz_density=zeros(size(horiz_density_amp));
    horiz_density=horiz_density+horiz_density_amp;
    vert_density=zeros(size(vert_density_amp));
    vert_density=vert_density+vert_density_amp;
else
    horiz_spectrum=horiz_spectrum+(fft_horiz_noise.^2);
    vert_spectrum=vert_spectrum+(fft_vert_noise.^2);
    horiz_density=horiz_density+horiz_density_amp;
    vert_density=vert_density+vert_density_amp;
end; %end-if iteration
end; % end-for iteration

% Identify maximum frequency of interest
freq_marker=0;
for i=1:length(freqs_Hz)
    if freqs_Hz(i)<=500, freq_marker=freq_marker+1; end
end; %end for i

% Normalize frequency spectrum
avg_horiz_spectrum=sqrt(horiz_spectrum);
avg_horiz_spectrum=avg_horiz_spectrum/max(avg_horiz_spectrum);
avg_vert_spectrum=sqrt(vert_spectrum);
avg_vert_spectrum=avg_vert_spectrum/max(avg_vert_spectrum);

if iteration==1
    avg_horiz_density=horiz_density;
    avg_vert_density=vert_density;
else
    avg_horiz_density=horiz_density/3;
    avg_vert_density=vert_density/3;
end; %end-if iteration

```

```

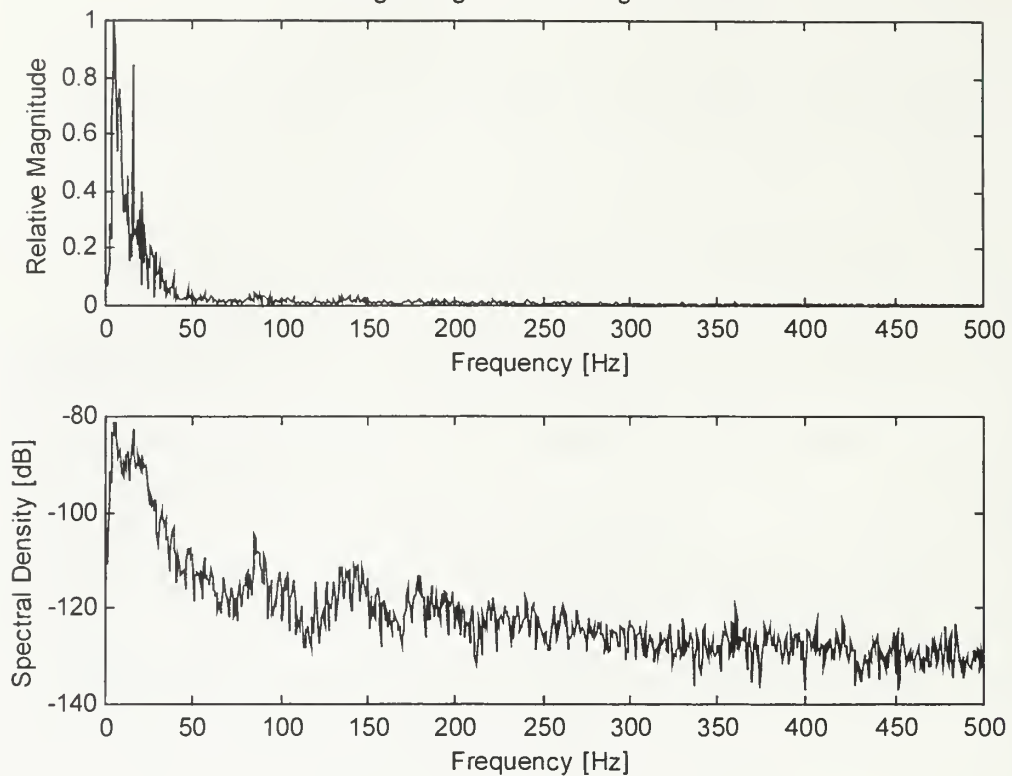
dBavg_horiz_density=10*log10(avg_horiz_density);
dBavg_vert_density=10*log10(avg_vert_density);

% Plot normalized longitudinal frequency spectrum and power spectral
% density
figure(1);
subplot(211);
plot(freqs_Hz(2:freq_marker),avg_horiz_spectrum(2:freq_marker));
title('Average Longitudinal Background Noise');
xlabel('Frequency [Hz]'); ylabel('Relative Magnitude');
subplot(212);
plot(freqs_Hz(2:freq_marker),dBavg_horiz_density(2:freq_marker));
xlabel('Frequency [Hz]'); ylabel('Spectral Density [dB]');

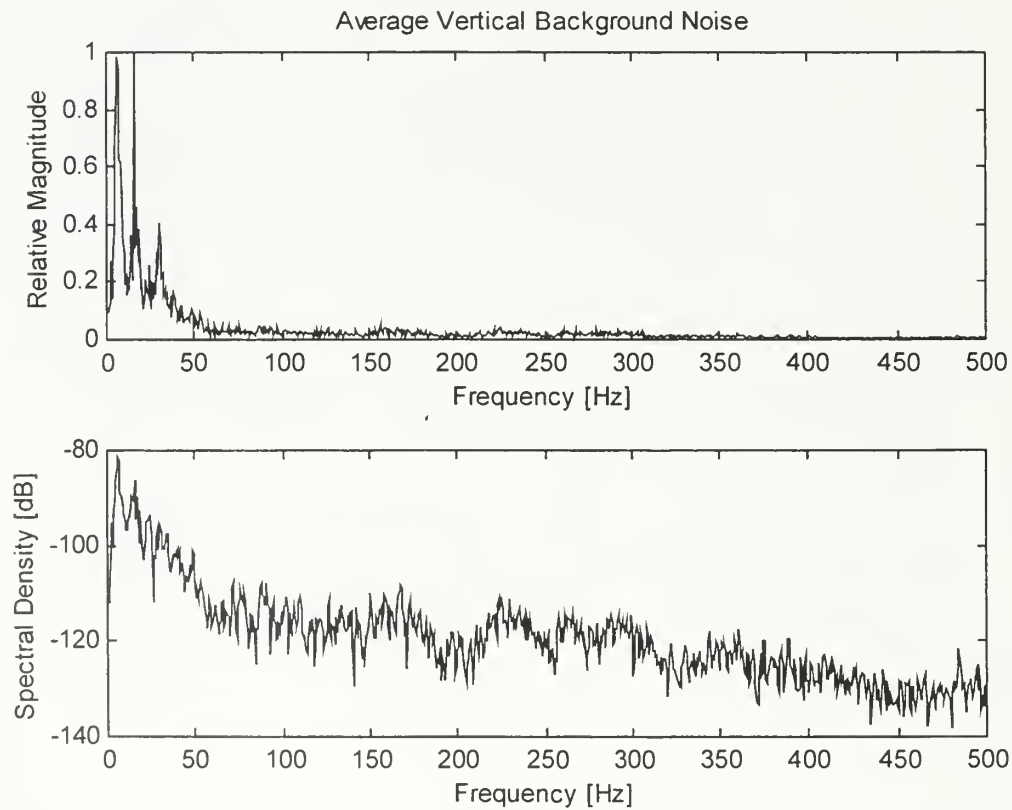
% Plot normalized vertical frequency spectrum and power spectral
% density
figure(2);
subplot(211);
plot(freqs_Hz(2:freq_marker),avg_vert_spectrum(2:freq_marker));
title('Average Vertical Background Noise');
xlabel('Frequency [Hz]'); ylabel('Relative Magnitude');
subplot(212);
plot(freqs_Hz(2:freq_marker),dBavg_vert_density(2:freq_marker));
xlabel('Frequency [Hz]'); ylabel('Spectral Density [dB]');

```

Average Longitudinal Background Noise



Average Vertical Background Noise



APPENDIX G. GROUND TRUTHING

This appendix contains the various MATLAB programs written to analyze the ground truthing data collected.

```
% Filename: truthtingdisplay.m
% Written by: F.E. Gaghan
% Date Last Modified: 14 February 1998
% Purpose: This program is used to graphically display the evolution of
%           the wave packet generated by the dropping the bowling ball
%           in both the longitudinal and vertical directions as a
%           function of time and range. The Rayleigh wave speed can be
%           estimated from the graph.

% Establish user interface to control data input
directory=input('Input the data file directory: ','s');
file_directory=[directory];
freq_span=input('Input the frequency span in kHz: ');
sampling_rate=freq_span*1000*2.56;
sample_delay=input('Input the number of delay samples: ');
sample_delay=abs(sample_delay);

% Assign input channels to correct data columns
trigger_col=1;
geo1_long_col=4; geo1_vert_col=6;
geo2_long_col=5; geo2_vert_col=7;

% While loop used to control data file input sequence
iteration=1;
continue='y';
while continue=='y'
    % Input and load data file
    disp(' ');
    if iteration==1
        file=input('Input the data filename: ','s');
    else
        file=input('Input the next data filename: ','s');
    end; % end-if iteration
    filename=[file];
    eval(['load ' file_directory, '\',filename]);

    range_ft=input('Input the range in ft to the first geophone: ');
    range_m=range_ft/3.2808;

    % Select desired geophone
    geophone=input('Input the geophone number for that range:
    1-#1, 2-#2 ');
    if geophone==1
        geo_long_col=geo1_long_col;
        geo_vert_col=geo1_vert_col;
    else
        geo_long_col=geo2_long_col;
        geo_vert_col=geo2_vert_col;
    end; %end-if geophone
```

```

% Adjust geophone timeseries in accordance with trigger signal
trigger_timeseries=xrc390(:,trigger_col);
[trigger_value,trigger_pt]=
min(trigger_timeseries(1:sample_delay+500));
start_pt=trigger_pt-2;
record_length=length(trigger_timeseries);

time_scale=[0:(1/sampling_rate):((record_length-
start_pt)/sampling_rate)]';

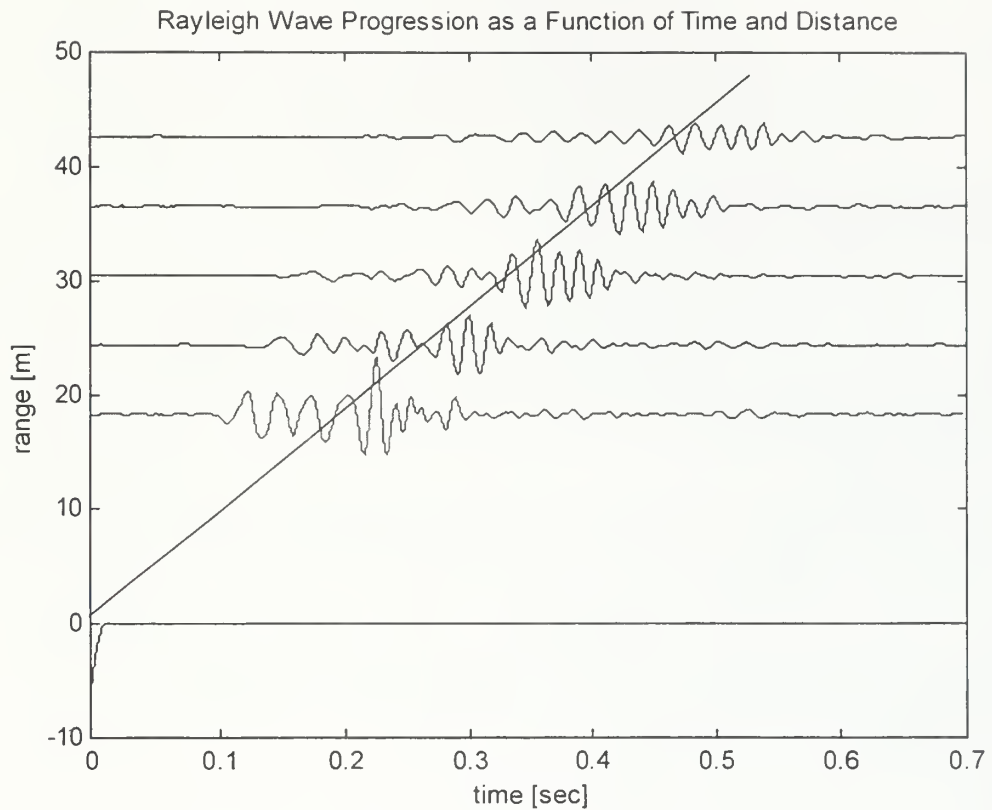
geo_long_timeseries=xrc390((start_pt:record_length),
geo_long_col);
geo_vert_timeseries=xrc390((start_pt:record_length),
geo_vert_col);

% Filter and scale geophone signals
b=ones(1,10)/10; a=1;
geo_long_filtered=filtfilt(b,a,geo_long_timeseries)*200;
geo_vert_filtered=filtfilt(b,a,geo_vert_timeseries)*200;
trigger_timeseries=trigger_timeseries*20;

% Plot the timeseries of the filtered geophone signals linearly
% scaled by the range to the geophone
adjust_yaxis=range_m;
range=sprintf('%2.2f',range_m);
if iteration==1
    hold on;
    figure(1);
    plot(time_scale,trigger_timeseries(start_pt:record_length),
        time_scale,geo_long_filtered+adjust_yaxis);
    text(0.7,geo_long_filtered(record_length)+adjust_yaxis+0.45,
        [range,' m']);
    xlabel('time [sec]'); ylabel('range [m]');
    hold on;
    figure(2);
    plot(time_scale,trigger_timeseries(start_pt:record_length),
        time_scale,geo_vert_filtered+adjust_yaxis);
    text(0.7,geo_vert_filtered(record_length)+adjust_yaxis+0.45,
        [range,' m']);
    xlabel('time [sec]'); ylabel('range [m]');
else
    hold on;
    figure(1);
    plot(time_scale,geo_long_filtered+adjust_yaxis);
    text(0.7,geo_long_filtered(record_length)+adjust_yaxis+0.45,
        [range,' m']);
    hold on;
    figure(2);
    plot(time_scale,geo_vert_filtered+adjust_yaxis);
    text(0.7,geo_vert_filtered(record_length)+adjust_yaxis+0.45,
        [range,' m']);
end; %end-if iteration

```

```
% Check for additional data file inputs  
iteration=iteration+1;  
disp(' ');  
continue=input('Do you want to input another data file?  
(y or n) ','s');  
end; %end-while continue
```



```

% Filename: gabormain2.m
% Written by: F.E. Gaghan
% Date Last Modified: 10 February 1998
% Purpose: This program is used to calculate the time versus frequency
% components from one of two geophone signals generated by a
% dropped bowling ball in order to analyze the wave speed
% characteristics of a propagating medium. The user has the
% ability to chose from three different processing methods.
% The results are displayed in the form of a gabor matrix
% (contour plot).

% Declare global variables
global slowness velocity freqs_Hz freq_marker

% Establish user interface to control data input
directory=input('Input the data file directory: ','s');
file_directory=[directory];

% Assign input channels to correct data columns
trigger_col=1;
geo1_long_col=4; geo1_vert_col=6;
geo2_long_col=5; geo2_vert_col=7;

% Enable user to incoherently average the gabor matrices
disp(' ');
average=input('Do you want to average the gabor matrices?
(y or n): ','s');
if average=='y'
    num_average=3;
else
    num_average=1;
end; %end-if average

% Select geophone signal to process
disp(' ');
geophone=input('Select geophone number: 1-#1, 2-#2 ');
if geophone==1
    geo_long_col=geo1_long_col;
    geo_vert_col=geo1_vert_col;
else
    geo_long_col=geo2_long_col;
    geo_vert_col=geo2_vert_col;
end; %end-if geophone

% For loop used to control data file input sequence
for iteration=1:num_average
    disp(' ');
    if iteration==1
        file=input('Input the data filename: ','s');
    else
        file=input('Input the next data filename: ','s');
    end; %end-if iteration
    filename=[file];
    eval(['load ' file_directory, '\',filename]);

```

```

if iteration==1
range_ft=input(['Input the range to geophone ',
    num2str(geophone),' in ft: ']);
range_m=range_ft/3.2808;
freq_span=input('Input the frequency span in kHz: ');
sampling_rate=freq_span*1000*2.56;
sample_delay=input('Input the number of delay samples: ');
sample_delay=abs(sample_delay);
end; % end-if iteration

% Adjust geophone timeseries in accordance with trigger signal
trigger_timeseries=xrc390(:,trigger_col);
[trigger_value,trigger_pt]=
    min(trigger_timeseries(1:sample_delay+500));
start_pt=trigger_pt-2;
record_length=length(trigger_timeseries);
time_scale=[0:(1/sampling_rate):((record_length-
    start_pt)/sampling_rate)]';
long_timeseries=xrc390((start_pt:record_length),geo_long_col);
vert_timeseries=xrc390((start_pt:record_length),geo_vert_col);

% Filter geophone signals
b=ones(1,10)/10; a=1;
long_filtered=filtfilt(b,a,long_timeseries);
vert_filtered=filtfilt(b,a,vert_timeseries);

% Plot longitudinal and vertical timeseries of geophone signals
figure(1);
subplot(211);
plot(time_scale,long_timeseries)
title(['Longitudinal Time Series of Geophone Signal for File: ', 
    file]);
xlabel('time [sec]'); ylabel('amplitude [V]');
subplot(212);
plot(time_scale,vert_timeseries);
title(['Vertical Time Series of Geophone Signal for File: ', 
    file]);
xlabel('time [sec]'); ylabel('amplitude [V]');

% Plot hodogram of geophone signals
figure(2);
plot(long_filtered,vert_filtered);
xlabel('longitudinal amplitude [V]');
ylabel('vertical amplitude [V]');
axis equal;

% Display geophone signals in a hankel plot
xyz_axis=zeros(length(time_scale),1);
y_axis=linspace(min(long_filtered),max(long_filtered),
    length(time_scale));
z_axis=linspace(min(vert_filtered),max(vert_filtered),
    length(time_scale));
figure(3);
plot3(time_scale,long_filtered,vert_filtered, ...
    time_scale,xyz_axis,xyz_axis,'k',...
    xyz_axis,y_axis,xyz_axis,'k',...
    xyz_axis,xyz_axis,z_axis,'k');

```

```

xlabel('time [sec]');
ylabel('longitudinal amplitude [V]');
zlabel('vertical amplitude [V]');
view(15,30);

% Enable the user the ability to display selected portions of the
% time record
disp(' ');
isolate=input('Do you want to isolate the Rayleigh wave?
(y or n): ','s');
if isolate=='y'
    continue='y';

while continue~='q'
    time1=input('Input the start time of the hodogram: ');
    point1=floor(time1*sampling_rate);
    time2=input('Input the stop time of the hodogram: ');
    point2=floor(time2*sampling_rate);

    % Plot hodogram of user selected portions of timeseries
    figure(4);
    plot(long_filtered(point1:point2),
        vert_filtered(point1:point2),...
        long_filtered(point1),vert_filtered(point1),'o',...
        long_filtered(point2),vert_filtered(point2),'x');
    xlabel('longitudinal amplitude [V]');
    ylabel('vertical amplitude [V]');
    axis equal;

    % Display hankel plot of user selected portions of timeseries
    x_axis=ones(point2-point1+1,1)*time_scale(point1);
    y_axis=linspace(min(long_filtered(point1:point2)),
        max(long_filtered(point1:point2)),point2-point1+1);
    z_axis=linspace(min(vert_filtered(point1:point2)),
        max(vert_filtered(point1:point2)),point2-point1+1);
    figure(5);
    plot3(time_scale(point1:point2),
        long_filtered(point1:point2),
        vert_filtered(point1:point2),...
        time_scale(point1),long_filtered(point1),
        vert_filtered(point1),'o',...
        time_scale(point2),long_filtered(point2),
        vert_filtered(point2),'x',...
        time_scale(point1:point2),xyz_axis(point1:point2),
        xyz_axis(point1:point2),'k',...
        x_axis,y_axis,xyz_axis(point1:point2),'k',...
        x_axis,xyz_axis(point1:point2),z_axis,'k');
    xlabel('time [sec]');
    ylabel('longitudinal amplitude [V]');
    zlabel('vertical amplitude [V]');
    axis([time_scale(point1),time_scale(point2),
        min(long_filtered),max(long_filtered),
        min(vert_filtered),max(vert_filtered)]);
    view(15,30);

```

```

% Graphically display ratio of longitudinal to vertical
% signal amplitudes
ellipse=input('Do you want to calculate ratio of elliptical
    axes (y or n): ','s');
if ellipse=='y'
    long_hilbert=abs(hilbert(long_filtered(point1:point2)));
    vert_hilbert=abs(hilbert(vert_filtered(point1:point2)));
    amp_ratio=long_hilbert./vert_hilbert;

    figure(6);
    subplot(211);
    plot(time_scale(point1-512:point2+512),
        long_filtered(point1-512:point2+512),...
        time_scale(point1-512:point2+512),
        vert_filtered(point1-512:point2+512), '--');
    xlabel('time [sec]'); ylabel('amplitude [V]');
    legend('longitudinal','vertical');
    subplot(212);
    plot(time_scale(point1:point2),amp_ratio);
    xlabel('time [sec]'); ylabel('longitudinal/vertical');
end; %end-if ellipse

continue=input('Press any key to continue isolation or "q" to
    quit: ','s');
end; %end-while
end; %end-if isolate

% Select data processing method
if iteration==1
    disp(' ');
    processing_method=input('Select processing method: 1-slowness;
        2-velocity; 3-S transform ');
end; %end-if iteration

if processing_method==1
    gabor_matrix=gaborslowness(file,long_filtered,sampling_rate,
        range_m);
elseif processing_method==2
    gabor_matrix=gaborvelocity(file,long_filtered,sampling_rate,
        range_m);
else
    S_matrix=stransform(file,long_filtered,sampling_rate,range_m);
end; %end-if processing_method

% Incoherently average the gabor matrices for three data files
amplitude_matrix=10.^((gabor_matrix/10));
if iteration==1
    amplitude_average=zeros(size(gabor_matrix));
    amplitude_average=amplitude_average+amplitude_matrix;
else
    amplitude_average=amplitude_average+amplitude_matrix;
end; %end-if iteration
end; %end-for iteration

```

```

% Plot incoherently averaged gabor matrix
if average=='y'
    amplitude_average=amplitude_average/3;
    gabor_average=10*log10(amplitude_average);
    dbmax=max(max(gabor_average));
    contour_levels=[dbmax:-1:dbmax-6];
    figure(7);
    contour(freqs_Hz(2:freq_marker),slowness,
        gabor_matrix(2:freq_marker,:)',contour_levels);
    title('Average Propagation Speed as a Function of Frequency');
    xlabel('frequency [Hz]'); ylabel('slowness [sec/m]');
end; %end-if average

% Enable user to plot a fitted group velocity curve to gabor matrix
disp(' ');
group=input('Do you want a group veolcity curve for the gabor plot
(y or n): ','s');
if group=='y'
    gaborgroup
end; %end-if group

% Enable user to cross correlate the geophone signals
disp(' ');
correlate=input('Do you want to correlate the geophone signals?
(y or n) ','s');
if correlate=='y'
    long1_timeseries=xrc390((start_pt:record_length),geo1_long_col);
    long2_timeseries=xrc390((start_pt:record_length),geo2_long_col);
    vert1_timeseries=xrc390((start_pt:record_length),geo1_vert_col);
    vert2_timeseries=xrc390((start_pt:record_length),geo2_vert_col);

    b=ones(1,10)/10; a=1;
    long1_filtered=filtfilt(b,a,long1_timeseries);
    long2_filtered=filtfilt(b,a,long2_timeseries);
    long12_corr=xcorr(long1_filtered, long2_filtered, 'coeff');
    long12_hilbert=abs(hilbert(long12_corr));
    vert1_filtered=filtfilt(b,a,vert1_timeseries);
    vert2_filtered=filtfilt(b,a,vert2_timeseries);
    vert12_corr=xcorr(vert1_filtered, vert2_filtered, 'coeff');
    vert12_hilbert=abs(hilbert(vert12_corr));

    % Plot the cross correlation of the longitudinal geophone signals
    figure(8);
    plot(long12_hilbert);
    title('Longitudinal Cross Correlation');
    axis([length(long1_filtered),length(long12_hilbert),
        0,max(long12_hilbert)]);

    % Plot the cross correlation of the vertical geophone signals
    figure(9);
    plot(vert12_hilbert);
    title('Vertical Cross Correlation');
    axis([length(vert1_filtered),length(vert12_hilbert),
        0,max(vert12_hilbert)]);
end; %end-if correlate

```

```

% Filename: gaborslowness.m
% Written by: F.E. Gaghan
% Date Last Modified: 10 February 1998
% Purpose: This program is a subroutine used to calculate the time
% versus frequency components of a geophone signal using the
% element location within the timeseries record to determine
% the time of arrival which is converted to slowness (inverse
% speed). The subroutine returns the gabor matrix to
% gabormain.

function gabor_matrix=gaborslowness(datafile,timeseries,
    sampling_freq,separation)

% Declare global variables
global slowness freqs_Hz freq_marker

% Initialize control variables and storage vectors
fft_length=1024;
last_index=length(timeseries);
fft_index=last_index-(fft_length-1);
fft_overlap=fft_length/16;
gabor_matrix=[];
slowness=[];
i=1;

% Conduct time versus frequency decomposition of geophone signal
for index=1:fft_overlap:fft_index-1
    block_midpoint=index+(fft_length/2)-1;
    arrival_time=block_midpoint/sampling_freq;
    slow=arrival_time/separation;
    slowness=[slowness,slow];

    fft_block=[timeseries(index:index+fft_length-1)];
    [psd_fft_block,freqs_Hz]=psd(fft_block,fft_length,sampling_freq);
    dB_fft_block=10*log10(psd_fft_block);
    gabor_matrix=[gabor_matrix,dB_fft_block];
    i=i+1;
end; %end for index

% Determine element addresses for major frequency components
freq_marker=0;
for i=1:length(freqs_Hz)
    if freqs_Hz(i)<=100, freq_marker=freq_marker+1; end
end; %end for i

% Plot the contours of the gabor matrix
dBmax=max(max(gabor_matrix));
contour_levels=[dBmax:-1:dBmax-6];
figure(7);
contour(freqs_Hz(2:freq_marker),slowness,
    gabor_matrix(2:freq_marker,:)',contour_levels);
title(['Propagation Speed as a Function of Frequency for File: ',
    datafile]);
xlabel('frequency [Hz]'); ylabel('slowness [sec/m]');
return; %end-function

```

```

% Filename: gaborvelocity.m
% Written by: F.E. Gaghan
% Date Last Modified: 10 February 1998
% Purpose: This program is a subroutine used to calculate the time
% versus frequency components of a geophone signal using wave
% speed to identify the associated element location within the
% timeseries. The subroutine returns the gabor matrix to
% gabormain.

function gabor_matrix=gaborvelocity(datafile,timeseries,
    sampling_freq,separation)

% Declare global variables
global velocity freqs_Hz freq_marker

% Initialize control variables and storage vectors
fft_length=1024;
max_velocity=200;
min_velocity=50;
velocity_increment=4.5;
number_increments=
    floor((max_velocity-min_velocity)/velocity_increment);
gabor_matrix=[];

% Conduct time versus frequency decomposition of geophone signal
for index=0:number_increments
    velocity(index+1)=max_velocity-(index*velocity_increment);
    block_midpoint=floor((separation/velocity(index+1))*sampling_freq);

    if block_midpoint < (fft_length/2)
        padding=(fft_length/2)-block_midpoint;
        zero_padding=zeros(padding,1);
        block_end=block_midpoint+(fft_length/2)-1;
        fft_block=[zero_padding;timeseries(1:block_end)];
    else
        block_start=block_midpoint-(fft_length/2)+1;
        block_end=block_midpoint+(fft_length/2);
        if block_end > length(timeseries)
            padding=block_end-length(timeseries);
            zero_padding=zeros(padding,1);
            fft_block=
                [timeseries(block_start:length(timeseries));zero_padding];
        else
            fft_block=timeseries(block_start:block_end);
        end; %end-if block_end
    end; %end-if block_midpoint

    [psd_fft_block,freqs_Hz]=psd(fft_block,fft_length,sampling_freq);
    dB_fft_block=10*log10(psd_fft_block);
    gabor_matrix=[gabor_matrix,dB_fft_block];
end; %end-for index

% Determine element addresses for major frequency components
freq_marker=0;
for i=1:length(freqs_Hz)
    if freqs_Hz(i)<=100, freq_marker=freq_marker+1; end
end; %end-for i

```

```

% Plot the contours of the gabor matrix
dBmax=max(max(gabor_matrix));
contour_levels=[dBmax:-1: dBmax-6];
figure(7);
contour(freqs_Hz(2:freq_marker),
    velocity,gabor_matrix(2:freq_marker,:)',contour_levels);
title(['Propagation Speed as a Function of Frequency for file: ',
    datafile]);
xlabel('frequency [Hz]'); ylabel('velocity [m/sec]');

return; %end-function

% Filename: gaborgroup.m
% Written by: F.E. Gaghan
% Date Last Modified: 09 February 1998
% Purpose: This program is a subroutine used to fit a group velocity
%           curve to the gabor matrix plot created by gabormain.

function gaborgroup

% Declare global variables
global freq speed type_fit

% Establish minimum user interface
disp(' ');
disp('Pick off the group speed points from the gabor plot with
the mouse');
disp('Press return when done');
[freq,speed]=ginput;

% Determine desired curve-fitting routine
type_fit=input('Pick the type of fit: 1-linear 2-spline ');
fit_steps=100;
lower_freq=freq(1);
upper_freq=freq(length(freq));
freq_step=(upper_freq-lower_freq)/fit_steps;
frequencies=lower_freq:freq_step:upper_freq;
fit_steps=length(freq_step);

% Calculate fitted curve values
if type_fit==1
    speeds=interp1(freq,speed,frequencies);
else
    speeds=spline(freq,speed,frequencies);
end; %end-if type_fit

% Plot fitted curve
hold on;
plot(frequencies,speeds,'--k');

return; %end-function

```


APPENDIX H. DISCRETE-MODE ANALYSIS

This appendix contains the MATLAB programs written to analyze the data collected during the beach phase experimentation with the MOD IV source.

```
% Filename: filtereddisplay.m
% Written by: F.E. Gaghan
% Date Last Modified: 09 February 1998
% Purpose: This program is used to graphically display the evolution of
%           the wave packet generated by the field test source in both
%           the longitudinal and vertical directions as a function of
%           time and range. The Rayleigh wave speed can be estimated
%           from the graph. It also displays the associated hodograms of
%           each Rayleigh wave.

% Establish user interface to control data input
directory=input('Input the data file directory: ','s');
file_directory=[directory];
drive_freq=input('Input the shaker drive frequency in Hz: ');
freq_span=input('Input the frequency span in kHz: ');
sampling_rate=freq_span*1000*2.56;
sample_delay=input('Input the number of delay samples: ');

record_length=8192;
time_scale=[(sample_delay/sampling_rate):(1/sampling_rate):
    ((record_length+sample_delay-1)/sampling_rate)]';

% Assign input channels to correct data columns
accel_long_col=1; accel_vert_col=2;
geo1_long_col=5; geo1_vert_col=7;
geo2_long_col=6; geo2_vert_col=8;

% Create band pass filter centered at the drive frequency
pass_freq=drive_freq/(sampling_rate/2);
[b_highpass,a_highpass]=butter(2,pass_freq,'high');
[b_lowpass,a_lowpass]=butter(2,pass_freq);
fft_length=1024;

% While loop used to control data file input sequence
iteration=1;
continue='y';
while continue=='y'
    % Input and load data file
    disp(' ');
    if iteration==1
        file=input('Input the data filename: ','s');
    else
        file=input('Input the next data filename: ','s');
    end; % end-if iteration
    filename=[file];
    eval(['load ' file_directory, '\',filename]);

    range_ft=input('Input the range in ft to the first geophone: ');
    range_m=range_ft/3.2808;
```

```

% Select desired geophone
geophone=input('Input the geophone number for that range:
    1-#1, 2-#2 ');
if geophone==1
    geo_long_col=geo1_long_col;
    geo_vert_col=geo1_vert_col;
else
    geo_long_col=geo2_long_col;
    geo_vert_col=geo2_vert_col;
end; %end-if geophone

% Filter accelerometer signals
accel_long_timeseries=xrc390(:,accel_long_col);
accel_vert_timeseries=xrc390(:,accel_vert_col);
accel_long_filtered=filtfilt(b_highpass,a_highpass,
    accel_long_timeseries);
accel_vert_filtered=filtfilt(b_highpass,a_highpass,
    accel_vert_timeseries);
accel_long_filtered=filtfilt(b_lowpass,a_lowpass,
    accel_long_filtered);
accel_vert_filtered=filtfilt(b_lowpass,a_lowpass,
    accel_vert_filtered);

[power,freqs_Hz]=
    psd(accel_long_filtered,record_length,sampling_rate);

% Determine element address for drive frequency
freq_marker=0;
for i=1:length(freqs_Hz)
    if freqs_Hz(i)==drive_freq, freq_marker=i; end;
end; %end for i

% Normalize filtered accelerometer signals by magnitude of
% accelerometer fft at the drive frequency
accel_long_fft=abs(fft(accel_long_filtered)/fft_length);
accel_vert_fft=abs(fft(accel_vert_filtered)/fft_length);
accel_long_filtered=
    accel_long_filtered/accel_long_fft(freq_marker);
accel_vert_filtered=
    accel_vert_filtered/accel_vert_fft(freq_marker);

% Filter the geophone signals
geo_long_timeseries=xrc390(:,geo_long_col);
geo_vert_timeseries=xrc390(:,geo_vert_col);
geo_long_filtered=
    filtfilt(b_highpass,a_highpass,geo_long_timeseries);
geo_vert_filtered=
    filtfilt(b_highpass,a_highpass,geo_vert_timeseries);
geo_long_filtered=
    filtfilt(b_lowpass,a_lowpass,geo_long_filtered);
geo_vert_filtered=
    filtfilt(b_lowpass,a_lowpass,geo_vert_filtered);

```

```

% Normalize the filtered geophone signals by magnitude of
% accelerometer fft at the drive frequency
geo_long_filtered=
    1.75*(geo_long_filtered/accel_long_fft(freq_marker));
geo_vert_filtered=
    1.75*(geo_vert_filtered/accel_vert_fft(freq_marker));
geo_long_filtered=
    1.75*(geo_long_filtered/max(geo_long_filtered));
geo_vert_filtered=
    1.75*(geo_vert_filtered/max(geo_vert_filtered));

% Plot the timeseries of the filtered geophone signals linearly
% scaled by the range to the geophone
adjust_yaxis=range_m;
range=sprintf('%2.2f',range_m);
if iteration==1
    hold on;
    figure(1);
    plot(time_scale,accel_long_filtered,time_scale,
        geo_long_filtered+adjust_yaxis);
    text(0.7,geo_long_filtered(record_length)+adjust_yaxis+0.45,
        [range,' m']);
    xlabel('time [sec]'); ylabel('range [m]');
    hold on;
    figure(2);
    plot(time_scale,accel_vert_filtered,time_scale,
        geo_vert_filtered+adjust_yaxis);
    text(0.7,geo_vert_filtered(record_length)+adjust_yaxis+0.45,
        [range,' m']);
    xlabel('time [sec]'); ylabel('range [m]');
else
    hold on;
    figure(1);
    plot(time_scale,geo_long_filtered+adjust_yaxis);
    text(0.7,geo_long_filtered(record_length)+adjust_yaxis+0.45,
        [range,' m']);
    hold on;
    figure(2);
    plot(time_scale,geo_vert_filtered+adjust_yaxis);
    text(0.7,geo_vert_filtered(record_length)+adjust_yaxis+0.45,
        [range,' m']);
end; %end-if iteration

% Plot hodograms of filtered signals
offset=513;
if iteration==1
    timel_a=
        input('Input the start time of accelerometer hodogram: ');
    point1_a=floor(timel_a*sampling_rate)+offset;
    time2_a=
        input('Input the stop time of accelerometer hodogram: ');
    point2_a=floor(time2_a*sampling_rate)+offset;

    timel_g=input('Input the start time of geophone hodogram: ');
    point1_g=floor(timel_g*sampling_rate)+offset;
    time2_g=input('Input the stop time of geophone hodogram: ');
    point2_g=floor(time2_g*sampling_rate)+offset;

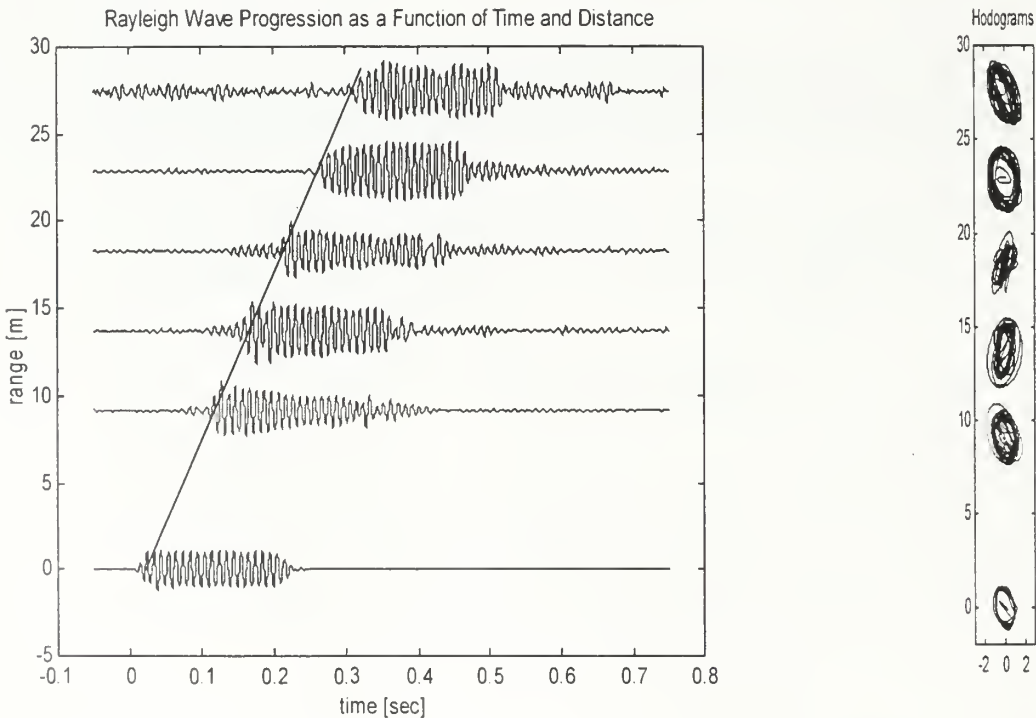
```

```

hold on;
figure(3);
plot(accel_long_filtered(point1_a:point2_a),
     accel_vert_filtered(point1_a:point2_a),...
     geo_long_filtered(point1_g:point2_g),
     geo_vert_filtered(point1_g:point2_g)+adjust_yaxis);
xlabel('longitudinal displacement');
ylabel('vertical displacement');
axis equal;
else
    time1_g=input('Input the start time of geophone hodogram: ');
    point1_g=floor(time1_g*sampling_rate)+offset;
    time2_g=input('Input the stop time of geophone hodogram: ');
    point2_g=floor(time2_g*sampling_rate)+offset;
    hold on;
    figure(3);
    plot(geo_long_filtered(point1_g:point2_g),
         geo_vert_filtered(point1_g:point2_g)+adjust_yaxis);
    xlabel('longitudinal displacement');
    ylabel('vertical displacement');
    axis equal;
end; %end-if iteration

% Check for additional data file inputs
iteration=iteration+1;
disp(' ');
continue=input('Do you want to input another data file?
(y or n) ','s');
end; %end-while continue

```



```

% Filename: sourcecorr.m
% Written by: F.E. Gaghan
% Date Last Modified: 10 February 1998
% Purpose: This program is used to calculate the cross correlation
%           between the input drive signal to the bass shakers and the
%           received accelerometer and geophone signals. From the output
%           of the cross correlation estimates for P-wave and R-wave
%           speeds are labeled.

% Establish user interface to control data input
directory=input('Input the data file directory: ','s');
file_directory=[directory];
file=input('Input the data filename: ','s');
filename=[file];
eval(['load ' file_directory,'\',filename]);

drive_freq=input('Input the shaker drive frequency in Hz: ');
range1_ft=input(['Input the range to the geophone #1 in ft: ']);
range1_m=range1_ft/3.2808;
range2_ft=input(['Input the range to the geophone #2 in ft: ']);
range2_m=range2_ft/3.2808;

freq_span=input('Input the frequency span in kHz: ');
sampling_rate=freq_span*1000*2.56;
sample_delay=input('Input the number of delay samples: ');

record_length=8192;
time_scale=[(sample_delay/sampling_rate):(1/sampling_rate):
            ((record_length+sample_delay-1)/sampling_rate)]';

% Assign input channels to correct data columns
accel_long_col=1; accel_vert_col=2;
geol_long_col=5;  geol_vert_col=7;
geo2_long_col=6; geo2_vert_col=8;

% Assign storage locations to data file columns
accel_long_timeseries=xrc390(:,accel_long_col);
accel_vert_timeseries=xrc390(:,accel_vert_col);
geol_long_timeseries=xrc390(:,geol_long_col);
geol_vert_timeseries=xrc390(:,geol_vert_col);
geo2_long_timeseries=xrc390(:,geo2_long_col);
geo2_vert_timeseries=xrc390(:,geo2_vert_col);

% Generate the reference input drive signal
N=sampling_rate/drive_freq;
n=[0:20*N];
drive_signal=sin(2*pi*n/N);
front_padding=zeros(abs(sample_delay),1);
padding=record_length-(length(front_padding)+length(drive_signal));
rear_padding=zeros(padding,1);
reference_signal=[front_padding;drive_signal';rear_padding];

% Create band pass filter centered at the drive frequency
pass_freq=drive_freq/(sampling_rate/2);
[b_highpass,a_highpass]=butter(2,pass_freq,'high');
[b_lowpass,a_lowpass]=butter(2,pass_freq);

```

```

% Filter the accelerometer and geophone signals
reference_filtered=
filtfilt(b_highpass,a_highpass,reference_signal);
accel_long_filtered=
filtfilt(b_highpass,a_highpass,accel_long_timeseries);
accel_vert_filtered=
filtfilt(b_highpass,a_highpass,accel_vert_timeseries);
geol_long_filtered=
filtfilt(b_highpass,a_highpass,geol_long_timeseries);
geol_vert_filtered=
filtfilt(b_highpass,a_highpass,geol_vert_timeseries);
geo2_long_filtered=
filtfilt(b_highpass,a_highpass,geo2_long_timeseries);
geo2_vert_filtered=
filtfilt(b_highpass,a_highpass,geo2_vert_timeseries);
reference_filtered=filtfilt(b_lowpass,a_lowpass,reference_signal);
accel_long_filtered=
filtfilt(b_lowpass,a_lowpass,accel_long_filtered);
accel_vert_filtered=
filtfilt(b_lowpass,a_lowpass,accel_vert_filtered);
geol_long_filtered=filtfilt(b_lowpass,a_lowpass,geol_long_filtered);
geol_vert_filtered=filtfilt(b_lowpass,a_lowpass,geol_vert_filtered);
geo2_long_filtered=filtfilt(b_lowpass,a_lowpass,geo2_long_filtered);
geo2_vert_filtered=filtfilt(b_lowpass,a_lowpass,geo2_vert_filtered);

% Calculate the cross correlation between the reference signal and the
% accelerometer signals
[accel_long_corr,accel_long_lags]=
xcorr(reference_signal,accel_long_filtered,'coeff');
accel_long_corr=abs(hilbert(accel_long_corr));
accel_long_lags=accel_long_lags./sampling_rate;
[accel_vert_corr,accel_vert_lags]=
xcorr(reference_signal,accel_vert_filtered,'coeff');
accel_vert_corr=abs(hilbert(accel_vert_corr));
accel_vert_lags=accel_vert_lags./sampling_rate;

% Plot the cross correlation as a function of time
figure(1);
subplot(211);
plot(accel_long_lags,accel_long_corr);
title('Cross Correlation of Reference and Longitudinal Accelerometer
      Signals');
xlabel('lags [sec]');
subplot(212);
plot(accel_vert_lags,accel_vert_corr);
title('Cross Correlation of Reference and Vertical Accelerometer
      Signals');
xlabel('lags [sec]');

% Establish the boundary criteria for the various wave speeds at
% geophone #1
plower_lag=rangel_m/1000; pupper_lag=rangel_m/500;
pwave_lower=record_length+floor(plower_lag*sampling_rate);
pwave_upper=record_length+floor(pupper_lag*sampling_rate);
rlower_lag=rangel_m/100; rupper_lag=rangel_m/50;
rwave_lower=record_length+floor(rlower_lag*sampling_rate);
rwave_upper=record_length+floor(rupper_lag*sampling_rate);

```

```

% Calculate the cross correlation between the reference signal and the
% longitudinal signal for geophone #1
[geol_long_corr,geol_long_lags]=
    xcorr(reference_signal,geol_long_filtered,'coeff');
geol_long_corr=abs(hilbert(geol_long_corr));
[rmax_long_val,rmax_long_loc]=
    max(geol_long_corr(rwave_lower:rwave_upper));
[long_val,long_loc]=max(geol_long_corr(pwave_lower:pwave_upper));
dont_plot='n';
if long_val > geol_long_corr(record_length)
    pmax_long_loc=long_loc;
else
    dont_plot='y';
end; %end-if long_val

% Calculate the cross correlation between the reference signal and the
% vertical signal for geophone #1
[geol_vert_corr,geol_vert_lags]=
    xcorr(reference_signal,geol_vert_filtered,'coeff');
geol_vert_corr=abs(hilbert(geol_vert_corr));
[rmax_vert_val,rmax_vert_loc]=
    max(geol_vert_corr(rwave_lower:rwave_upper));
[vert_val,vert_loc]=max(geol_vert_corr(pwave_lower:pwave_upper));
if vert_val > geol_vert_corr(record_length)
    pmax_vert_loc=vert_loc;
else
    dont_plot='y';
end; %end-if vert_val

% Plot the longitudinal cross correlation as a function of slowness
(inverse speed)
slowness_long=geol_long_lags/(sampling_rate*rang1_m);
slowness_vert=geol_vert_lags/(sampling_rate*rang1_m);
if dont_plot=='y'
    figure(2);
    subplot(211);
    plot(slowness_long,geol_long_corr,...
        slowness_long(rwave_lower+rmax_long_loc),
        geol_long_corr(rwave_lower+rmax_long_loc),'o');
    text(slowness_long(1)+0.0025,rmax_long_val-0.25,
        ['rwave velocity = ',
        num2str(1/slowness_long(rwave_lower+rmax_long_loc)), ' m/sec']);
    text(slowness_long(1)+0.0025,rmax_long_val-0.35,
        ['rwave corr = ',
        num2str(geol_long_corr(rwave_lower+rmax_long_loc))]);
    title('Cross Correlation of Reference and Geophone #1 Longitudinal
        Signals');
    xlabel('slowness [sec/m]');
    subplot(212);
    plot(slowness_vert,geol_vert_corr,...
        slowness_vert(rwave_lower+rmax_vert_loc),
        geol_vert_corr(rwave_lower+rmax_vert_loc),'o');
    text(slowness_vert(1)+0.0025,rmax_vert_val-0.25,
        ['rwave velocity = ',
        num2str(1/slowness_vert(rwave_lower+rmax_vert_loc)), ' m/sec']);

```

```

text(slowness_vert(1)+0.0025,rmax_vert_val-0.35,
    ['rwave corr = ',
     num2str(geol_vert_corr(rwave_lower+rmax_vert_loc))]);
title('Cross Correlation of Reference and Geophone #1 Vertical
      Signals');
xlabel('slowness [sec/m]');
else
    figure(2);
    subplot(211);
    plot(slowness_long,geol_long_corr, ...
        slowness_long(pwave_lower+pmax_long_loc),
        geol_long_corr(pwave_lower+pmax_long_loc),'o',...
        slowness_long(rwave_lower+rmax_long_loc),
        geol_long_corr(rwave_lower+rmax_long_loc),'o');
    text(slowness_long(1)+0.0025,rmax_long_val-0.05,
        ['pwave velocity = ',
         num2str(1/slowness_long(pwave_lower+pmax_long_loc)), ' m/sec']);
    text(slowness_long(1)+0.0025,rmax_long_val-0.15,
        ['rwave corr = ',
         num2str(geol_long_corr(pwave_lower+pmax_long_loc))]);
    text(slowness_long(1)+0.0025,rmax_long_val-0.25,
        ['rwave velocity = ',
         num2str(1/slowness_long(rwave_lower+rmax_long_loc)), ' m/sec']);
    text(slowness_long(1)+0.0025,rmax_long_val-0.35,
        ['rwave corr = ',
         num2str(geol_long_corr(rwave_lower+rmax_long_loc))]);
title('Cross Correlation of Reference and Geophone #1 Longitudinal
      Signals');
xlabel('slowness [sec/m]');
subplot(212);
plot(slowness_vert,geol_vert_corr, ...
    slowness_vert(pwave_lower+pmax_vert_loc),
    geol_vert_corr(pwave_lower+pmax_vert_loc),'o',...
    slowness_vert(rwave_lower+rmax_vert_loc),
    geol_vert_corr(rwave_lower+rmax_vert_loc),'o');
text(slowness_vert(1)+0.0025,rmax_vert_val-0.05,
    ['pwave velocity = ',
     num2str(1/slowness_vert(pwave_lower+pmax_vert_loc)), ' m/sec']);
text(slowness_vert(1)+0.0025,rmax_vert_val-0.15,
    ['rwave corr = ',
     num2str(geol_vert_corr(pwave_lower+pmax_long_loc))]);
text(slowness_vert(1)+0.0025,rmax_vert_val-0.25,
    ['rwave velocity = ',
     num2str(1/slowness_vert(rwave_lower+rmax_vert_loc)), ' m/sec']);
text(slowness_vert(1)+0.0025,rmax_vert_val-0.35,
    ['rwave corr = ',
     num2str(geol_vert_corr(rwave_lower+rmax_long_loc))]);
title('Cross Correlation of Reference and Geophone #1 Vertical
      Signals');
xlabel('slowness [sec/m]');
end; %end-if dont_plot

```

```

% Establish the boundary criteria for the various wave speeds at
% geophone #2
plower_lag=range2_m/1000; pupper_lag=range2_m/500;
pwave_lower=record_length+floor(plower_lag*sampling_rate);

```

```

pwave_upper=record_length+floor(pupper_lag*sampling_rate);
rlower_lag=range2_m/100; rupper_lag=range2_m/50;
rwave_lower=record_length+floor(rlower_lag*sampling_rate);
rwave_upper=record_length+floor(rupper_lag*sampling_rate);

% Calculate the cross correlation between the reference signal and the
% longitudinal signal for geophone #2
[geo2_long_corr,geo2_long_lags]=
    xcorr(reference_signal,geo2_long_filtered,'coeff');
geo2_long_corr=abs(hilbert(geo2_long_corr));
[rmax_long_val,rmax_long_loc]=
    max(geo2_long_corr(rwave_lower:rwave_upper));
[long_val,long_loc]=max(geo2_long_corr(pwave_lower:pwave_upper));
dont_plot='n';
if long_val > geo2_long_corr(record_length)
    pmax_long_loc=long_loc;
else
    dont_plot='y';
end; %end-if long_val

% Calculate the cross correlation between the reference signal and the
% vertical signal for geophone #2
[geo2_vert_corr,geo2_vert_lags]=
    xcorr(reference_signal,geo2_vert_filtered,'coeff');
geo2_vert_corr=abs(hilbert(geo2_vert_corr));
[rmax_vert_val,rmax_vert_loc]=
    max(geo2_vert_corr(rwave_lower:rwave_upper));
[vert_val,vert_loc]=max(geo2_vert_corr(pwave_lower:pwave_upper));
if vert_val > geo2_vert_corr(record_length)
    pmax_vert_loc=vert_loc;
else
    pmax_vert_loc=rmax_vert_loc;
end; %end-if vert_val

% Plot the longitudinal cross correlation as a function of slowness
% (inverse speed)
slowness_long=geo2_long_lags/(sampling_rate*range2_m);
slowness_vert=geo2_vert_lags/(sampling_rate*range2_m);
if dont_plot=='y'
    figure(3);
    subplot(211);
    plot(slowness_long,geo2_long_corr, ...
        slowness_long(rwave_lower+rmax_long_loc),
        geo2_long_corr(rwave_lower+rmax_long_loc),'o');
    text(slowness_long(1)+0.0025,rmax_long_val-0.25,
        ['rwave velocity = ',
        num2str(1/slowness_long(rwave_lower+rmax_long_loc)), ' m/sec']);
    text(slowness_long(1)+0.0025,rmax_long_val-0.35,
        ['rwave corr = ',
        num2str(geo2_long_corr(rwave_lower+rmax_long_loc))]);
    title('Cross Correlation of Reference and Geophone #2 Longitudinal
          Signals');
    xlabel('slowness [sec/m]');
    subplot(212);
    plot(slowness_vert,geo2_vert_corr, ...
        slowness_vert(rwave_lower+rmax_vert_loc),
        geo2_vert_corr(rwave_lower+rmax_vert_loc),'o');

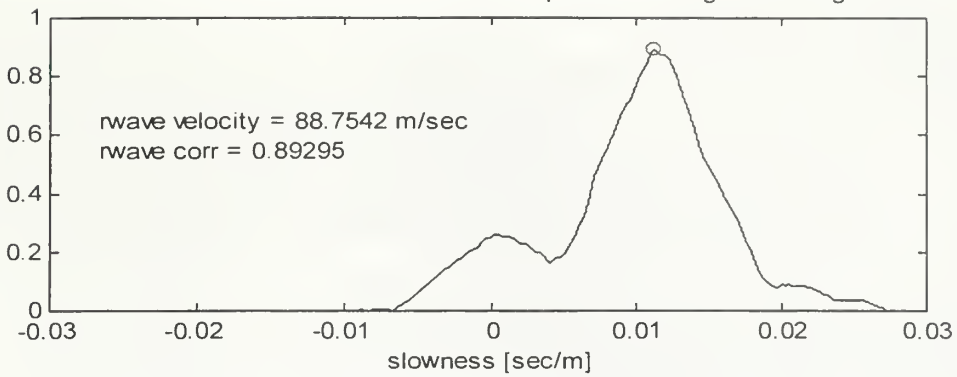
```

```

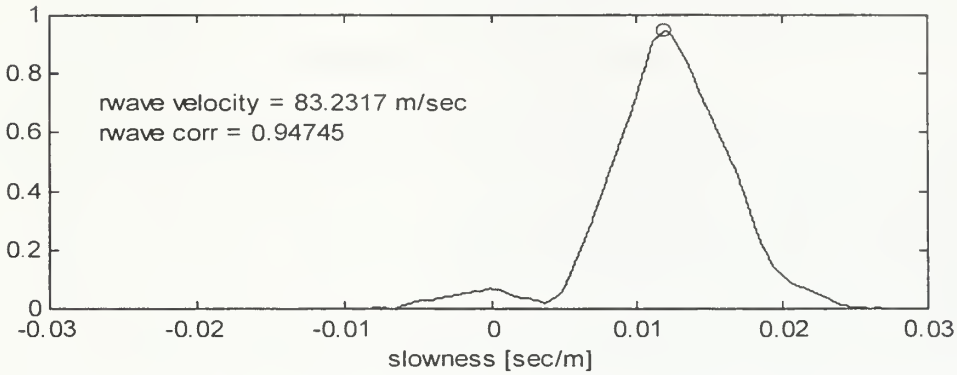
text(slowness_vert(1)+0.0025,rmax_vert_val-0.25,
    ['rwave velocity = ',
     num2str(1/slowness_vert(rwave_lower+rmax_vert_loc)), ' m/sec']);
text(slowness_vert(1)+0.0025,rmax_vert_val-0.35,
    ['rwave corr = ',
     num2str(geo2_vert_corr(rwave_lower+rmax_long_loc))]);
title('Cross Correlation of Reference and Geophone #2 Vertical
      Signals');
xlabel('slowness [sec/m]');
else
    figure(3);
    subplot(211);
    plot(slowness_long,geo2_long_corr, ...
          slowness_long(pwave_lower+pmax_long_loc),
          geo2_long_corr(pwave_lower+pmax_long_loc), 'o',...
          slowness_long(rwave_lower+rmax_long_loc),
          geo2_long_corr(rwave_lower+rmax_long_loc), 'o');
    text(slowness_long(1)+0.0025,rmax_long_val-0.05,
        ['pwave velocity = ',
         num2str(1/slowness_long(pwave_lower+pmax_long_loc)), ' m/sec']);
    text(slowness_long(1)+0.0025,rmax_long_val-0.15,
        ['pwave corr = ',
         num2str(geo2_long_corr(pwave_lower+pmax_long_loc))]);
    text(slowness_long(1)+0.0025,rmax_long_val-0.25,
        ['rwave velocity = ',
         num2str(1/slowness_long(rwave_lower+rmax_long_loc)), ' m/sec']);
    text(slowness_long(1)+0.0025,rmax_long_val-0.35,
        ['rwave corr = ',
         num2str(geo2_long_corr(rwave_lower+rmax_long_loc))]);
    title('Cross Correlation of Reference and Geophone #2 Longitudinal
          Signals');
    xlabel('slowness [sec/m]');
    subplot(212);
    plot(slowness_vert,geo2_vert_corr, ...
          slowness_vert(pwave_lower+pmax_vert_loc),
          geo2_vert_corr(pwave_lower+pmax_vert_loc), 'o',...
          slowness_vert(rwave_lower+rmax_vert_loc),
          geo2_vert_corr(rwave_lower+rmax_vert_loc), 'o');
    text(slowness_vert(1)+0.0025,rmax_vert_val-0.05,
        ['pwave velocity = ',
         num2str(1/slowness_vert(pwave_lower+pmax_vert_loc)), ' m/sec']);
    text(slowness_vert(1)+0.0025,rmax_vert_val-0.15,
        ['pwave corr = ',
         num2str(geo2_vert_corr(pwave_lower+pmax_long_loc))]);
    text(slowness_vert(1)+0.0025,rmax_vert_val-0.25,
        ['rwave velocity = ',
         num2str(1/slowness_vert(rwave_lower+rmax_vert_loc)), ' m/sec']);
    text(slowness_vert(1)+0.0025,rmax_vert_val-0.35,
        ['rwave corr = ',
         num2str(geo2_vert_corr(rwave_lower+rmax_long_loc))]);
    title('Cross Correlation of Reference and Geophone #2 Vertical
          Signals');
    xlabel('slowness [sec/m]');
end; %end-if dont_plot

```

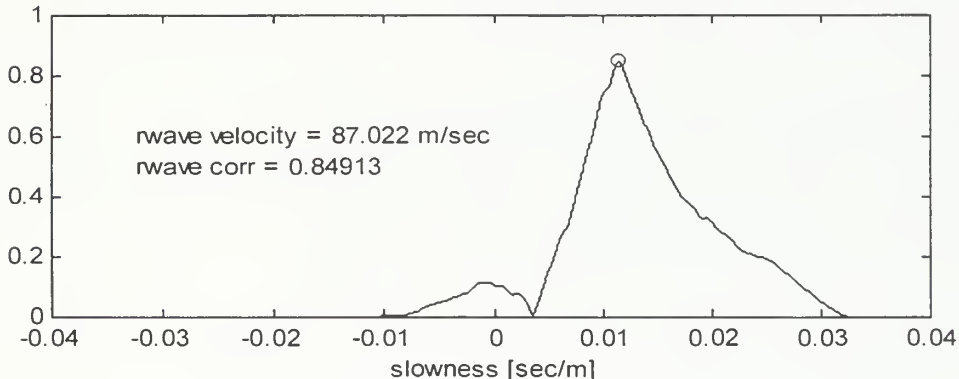
Cross Correlation of Reference and Geophone #1 Longitudinal Signals



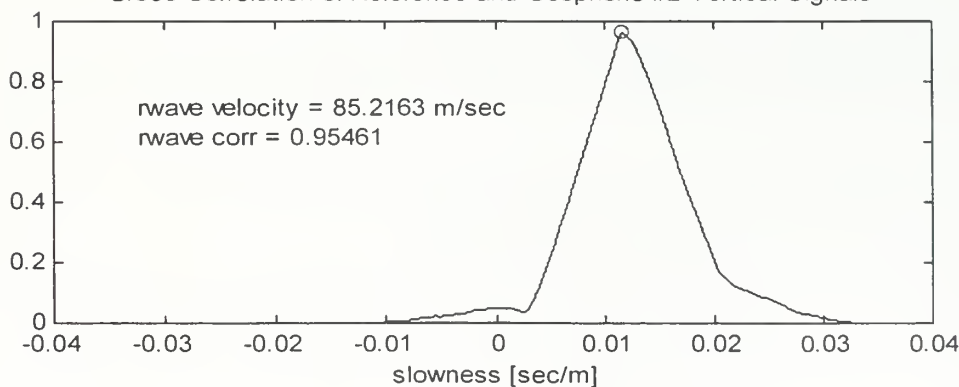
Cross Correlation of Reference and Geophone #1 Vertical Signals



Cross Correlation of Reference and Geophone #2 Longitudinal Signals



Cross Correlation of Reference and Geophone #2 Vertical Signals



```

% Filename: sourcesignals.m
% Written by: F.E. Gaghan
% Date Last Modified: 10 February 1998
% Purpose: This program allows the user to display the timeseries of
% the filtered and unfiltered received accelerometer and
% geophone signals. The user can also display the hodograms
% and hankel plots of each of the signals. It also enables the
% user to isolate selected portions of the geophone signals
% for ease of display.

% Establish user interface to control data input
directory=input('Input the data file directory: ','s');
file_directory=[directory];
file=input('Input the data filename: ','s');
filename=[file];
eval(['load ' file_directory,'\',filename]);

drive_freq=input('Input the shaker drive frequency in Hz: ');
range_ft=input(['Input the range to the geophone #1 in ft: ']);
range_m=range_ft/3.2808;
freq_span=input('Input the frequency span in kHz: ');
sampling_rate=freq_span*1000*2.56;
sample_delay=input('Input the number of delay samples: ');
record_length=8192;
time_scale=[(sample_delay/sampling_rate):(1/sampling_rate):
            ((record_length+sample_delay-1)/sampling_rate)]';

% Assign input channels to correct data columns
accel_long_col=1; accel_vert_col=2;
geo1_long_col=5; geo1_vert_col=7;
geo2_long_col=6; geo2_vert_col=8;

% Assign storage locations to data file columns
accel_long_timeseries=xrc390(:,accel_long_col);
accel_vert_timeseries=xrc390(:,accel_vert_col);
geo1_long_timeseries=xrc390(:,geo1_long_col);
geo1_vert_timeseries=xrc390(:,geo1_vert_col);
geo2_long_timeseries=xrc390(:,geo2_long_col);
geo2_vert_timeseries=xrc390(:,geo2_vert_col);

% Plot unfiltered timeseries of accelerometer signals
figure(1);
subplot(211);
plot(time_scale,accel_long_timeseries);
axis([time_scale(1),time_scale(record_length),
      min(accel_long_timeseries)-0.2,max(accel_long_timeseries)+0.2]);
title(['Longitudinal Time Series of Accelerometer Signal for File: ',
       file]);
xlabel('time [sec]'); ylabel('amplitude [V]');
subplot(212);
plot(time_scale,accel_vert_timeseries);
axis([time_scale(1),time_scale(record_length),
      min(accel_long_timeseries)-0.2,max(accel_long_timeseries)+0.2]);
title(['Vertical Time Series of Accelerometer Signal for File: ',
       file]);
xlabel('time [sec]'); ylabel('amplitude [V]');

```

```

% Create band pass filter centered at the drive frequency
pass_freq=drive_freq/(sampling_rate/2);
[b_highpass,a_highpass]=butter(2,pass_freq,'high');
[b_lowpass,a_lowpass]=butter(2,pass_freq);

% Filter the accelerometer and geophone signals
accel_long_filtered=
    filtfilt(b_highpass,a_highpass,accel_long_timeseries);
accel_vert_filtered=
    filtfilt(b_highpass,a_highpass,accel_vert_timeseries);
geo1_long_filtered=
    filtfilt(b_highpass,a_highpass,geo1_long_timeseries);
geo1_vert_filtered=
    filtfilt(b_highpass,a_highpass,geo1_vert_timeseries);
geo2_long_filtered=
    filtfilt(b_highpass,a_highpass,geo2_long_timeseries);
geo2_vert_filtered=
    filtfilt(b_highpass,a_highpass,geo2_vert_timeseries);
accel_long_filtered=
    filtfilt(b_lowpass,a_lowpass,accel_long_filtered);
accel_vert_filtered=
    filtfilt(b_lowpass,a_lowpass,accel_vert_filtered);
geo1_long_filtered=
    filtfilt(b_lowpass,a_lowpass,geo1_long_filtered);
geo1_vert_filtered=
    filtfilt(b_lowpass,a_lowpass,geo1_vert_filtered);
geo2_long_filtered=
    filtfilt(b_lowpass,a_lowpass,geo2_long_filtered);
geo2_vert_filtered=
    filtfilt(b_lowpass,a_lowpass,geo2_vert_filtered);

% Plot the filtered and unfiltered timeseries signals for geophone #1
figure(2);
subplot(211);
plot(time_scale,geo1_long_timeseries);
title(['Longitudinal Time Series of Geophone #1 Signal for File: ', file]);
xlabel('time [sec]'); ylabel('amplitude [V]');
subplot(212);
plot(time_scale,geo1_long_filtered);
title(['Vertical Time Series of Geophone #1 Signal for File: ', file]);
xlabel('time [sec]'); ylabel('amplitude [V]');

% Plot the filtered and unfiltered timeseries signals for geophone #2
figure(3);
subplot(211);
plot(time_scale,geo2_long_timeseries);
title(['Longitudinal Time Series of Geophone #2 Signal for File: ', file]);
xlabel('time [sec]'); ylabel('amplitude [V]');
subplot(212);
plot(time_scale,geo2_long_filtered);
title(['Vertical Time Series of Geophone #2 Signal for File: ', file]);
xlabel('time [sec]'); ylabel('amplitude [V]');

```

```

% Plot the hodogram of the filtered and unfiltered timeseries signals
% of the accelerometer
figure(4);
subplot(211);
plot(accel_long_timeseries,accel_vert_timeseries);
xlabel('longitudinal amplitude [V]');
ylabel('vertical amplitude [V]');
axis equal;
subplot(212);
plot(accel_long_filtered,accel_vert_filtered);
xlabel('longitudinal amplitude [V]');
ylabel('vertical amplitude [V]');
axis equal;

% Plot the hodogram of the filtered and unfiltered timeseries signals
% for geophone #1
figure(5);
subplot(211);
plot(geol_long_timeseries,geol_vert_timeseries);
xlabel('longitudinal amplitude [V]');
ylabel('vertical amplitude [V]');
axis equal;
subplot(212);
plot(geol_long_filtered,geol_vert_filtered);
xlabel('longitudinal amplitude [V]');
ylabel('vertical amplitude [V]');
axis equal;

% Plot the hodogram of the filtered and unfiltered timeseries signals
% for geophone #2
figure(6);
subplot(211);
plot(geo2_long_timeseries,geo2_vert_timeseries);
xlabel('longitudinal amplitude [V]');
ylabel('vertical amplitude [V]');
axis equal;
subplot(212);
plot(geo2_long_filtered,geo2_vert_filtered);
xlabel('longitudinal amplitude [V]');
ylabel('vertical amplitude [V]');
axis equal;

% Display hankel plot for geophone #1
xyz_axis=zeros(length(time_scale),1);
y_max1=max(abs(min(geol_long_timeseries)),max(geol_long_timeseries));
y_axis1=linspace(-y_max1,y_max1,length(time_scale));
z_max1=max(abs(min(geol_vert_timeseries)),max(geol_vert_timeseries));
z_axis1=linspace(-z_max1,z_max1,length(time_scale));
y_max1f=max(abs(min(geol_long_filtered)),max(geol_long_filtered));
y_axis1f=linspace(-y_max1f,y_max1f,length(time_scale));
z_max1f=max(abs(min(geol_vert_filtered)),max(geol_vert_filtered));
z_axis1f=linspace(-z_max1f,z_max1f,length(time_scale));
figure(7);
subplot(211);
plot3(time_scale,geol_long_timeseries,geol_vert_timeseries, ...
    time_scale,xyz_axis,xyz_axis,'k',...
    xyz_axis,y_axis1,xyz_axis,'k',...

```

```

xyz_axis,xyz_axis,z_axis1,'k');
xlabel('time [sec]');
ylabel('longitudinal amplitude [V]');
zlabel('vertical amplitude [V]');
view(15,30);
subplot(212);
plot3(time_scale,geo1_long_filtered,geo1_vert_filtered, ...
    time_scale,xyz_axis,xyz_axis,'k',...
    xyz_axis,y_axis1f,xyz_axis,'k',...
    xyz_axis,xyz_axis,z_axis1f,'k');
axis([time_scale(512),time_scale(length(time_scale)), ...
    min(geo1_long_filtered),max(geo1_long_filtered), ...
    min(geo1_vert_filtered),max(geo1_vert_filtered)]);
xlabel('time [sec]');
ylabel('longitudinal amplitude [V]');
zlabel('vertical amplitude [V]');
view(15,30);

% Display hankel plot for geophone #2
y_max2=max(abs(min(geo2_long_timeseries)),max(geo2_long_timeseries));
y_axis2=linspace(-y_max2,y_max2,length(time_scale));
z_max2=max(abs(min(geo2_vert_timeseries)),max(geo2_vert_timeseries));
z_axis2=linspace(-z_max2,z_max2,length(time_scale));
y_max2f=max(abs(min(geo2_long_filtered)),max(geo2_long_filtered));
y_axis2f=linspace(-y_max2f,y_max2f,length(time_scale));
z_max2f=max(abs(min(geo2_vert_filtered)),max(geo2_vert_filtered));
z_axis2f=linspace(-z_max2f,z_max2f,length(time_scale));
figure(8);
subplot(211);
plot3(time_scale,geo2_long_timeseries,geo2_vert_timeseries, ...
    time_scale,xyz_axis,xyz_axis,'k',...
    xyz_axis,y_axis2,xyz_axis,'k',...
    xyz_axis,xyz_axis,z_axis2,'k');
xlabel('time [sec]');
ylabel('longitudinal amplitude [V]');
zlabel('vertical amplitude [V]');
view(15,30);
subplot(212);
plot3(time_scale,geo2_long_filtered,geo2_vert_filtered, ...
    time_scale,xyz_axis,xyz_axis,'k',...
    xyz_axis,y_axis2f,xyz_axis,'k',...
    xyz_axis,xyz_axis,z_axis2f,'k');
axis([time_scale(512),time_scale(length(time_scale)), ...
    min(geo2_long_filtered),max(geo2_long_filtered), ...
    min(geo2_vert_filtered),max(geo2_vert_filtered)]);
xlabel('time [sec]');
ylabel('longitudinal amplitude [V]');
zlabel('vertical amplitude [V]');
view(15,30);

```

```

% Enable the user the ability to display selected portions of the time
% record
disp(' ');
isolate=input('Do you want to isolate the Rayleigh wave?
(y or n): ','s');
if isolate=='y'
    continue='y';

while continue=='q'
    disp(' ');
    time1_1=
        input('Input the start time of the hodogram for figure(7): ');
    point1_1=floor(time1_1*sampling_rate);
    time2_1=
        input('Input the stop time of the hodogram for figure(7): ');
    point2_1=floor(time2_1*sampling_rate);

    x_axis1=ones(point2_1-point1_1+1,1)*time_scale(point1_1);
    y_max1_timeseries=
        max(abs(min(geol_long_timeseries(point1_1:point2_1))), ...
            max(geol_long_timeseries(point1_1:point2_1)));
    z_max1_timeseries=
        max(abs(min(geol_vert_timeseries(point1_1:point2_1))), ...
            max(geol_vert_timeseries(point1_1:point2_1)));
    y_axis1_timeseries=
        linspace(-y_max1_timeseries,y_max1_timeseries,
            point2_1-point1_1+1);
    z_axis1_timeseries=
        linspace(-z_max1_timeseries,z_max1_timeseries,
            point2_1-point1_1+1);

    y_max1_filtered=
        max(abs(min(geol_long_filtered(point1_1:point2_1))), ...
            max(geol_long_filtered(point1_1:point2_1)));
    z_max1_filtered=
        max(abs(min(geol_vert_filtered(point1_1:point2_1))), ...
            max(geol_vert_filtered(point1_1:point2_1)));
    y_axis1_filtered=
        linspace(-y_max1_filtered,y_max1_filtered,point2_1-point1_1+1);
    z_axis1_filtered=
        linspace(-z_max1_filtered,z_max1_filtered,point2_1-point1_1+1);

% Plot hodogram of user selected portions of geophone #1
figure(5);
plot(geol_long_filtered(point1_1:point2_1),
    geol_vert_filtered(point1_1:point2_1));
xlabel('longitudinal amplitude [V]');
ylabel('vertical amplitude [V]');
axis equal;

```

```

% Display hankel plot of user selected portions of geophone #1
figure(9);
subplot(211)
plot3(time_scale(point1_1:point2_1),
       geol_long_timeseries(point1_1:point2_1),
       geol_vert_timeseries(point1_1:point2_1),...
       time_scale(point1_1),geol_long_timeseries(point1_1),
       geol_vert_timeseries(point1_1),'o',...
       time_scale(point2_1),geol_long_timeseries(point2_1),
       geol_vert_timeseries(point2_1),'x',...
       time_scale(point1_1:point2_1),
       xyz_axis(point1_1:point2_1),
       xyz_axis(point1_1:point2_1),'k',...
       x_axis1,y_axis1_timeseries,
       xyz_axis(point1_1:point2_1),'k',...
       x_axis1,xyz_axis(point1_1:point2_1),
       z_axis1_timeseries,'k');
xlabel('time [sec]');
ylabel('longitudinal amplitude [V]');
zlabel('vertical amplitude [V]');
axis([time_scale(point1_1),time_scale(point2_1),
      min(geol_long_timeseries),max(geol_long_timeseries),
      min(geol_vert_timeseries),max(geol_vert_timeseries)]));
view(15,30);
subplot(212);
plot3(time_scale(point1_1:point2_1),
       geol_long_filtered(point1_1:point2_1),
       geol_vert_filtered(point1_1:point2_1),...
       time_scale(point1_1),geol_long_filtered(point1_1),
       geol_vert_filtered(point1_1),'o',...
       time_scale(point2_1),geol_long_filtered(point2_1),
       geol_vert_filtered(point2_1),'x',...
       time_scale(point1_1:point2_1),
       xyz_axis(point1_1:point2_1),
       xyz_axis(point1_1:point2_1),'k',...
       x_axis1,y_axis1_filtered,
       xyz_axis(point1_1:point2_1),'k',...
       x_axis1,xyz_axis(point1_1:point2_1),
       z_axis1_filtered,'k');
xlabel('time [sec]');
ylabel('longitudinal amplitude [V]');
zlabel('vertical amplitude [V]');
axis([time_scale(point1_1),time_scale(point2_1),
      min(geol_long_filtered),max(geol_long_filtered),
      min(geol_vert_filtered),max(geol_vert_filtered)]));
view(15,30);

disp(' ');
timel_2=
    input('Input the start time of the hodogram for figure(8): ');
point1_2=floor(timel_2*sampling_rate);
time2_2=
    input('Input the stop time of the hodogram for figure(8): ');
point2_2=floor(time2_2*sampling_rate);

```

```

x_axis2=ones(point2_2-point1_2+1,1)*time_scale(point1_2);
y_max2_timeseries=
max(abs(min(geo2_long_timeseries(point1_2:point2_2))),
max(geo2_long_timeseries(point1_2:point2_2)));
z_max2_timeseries=
max(abs(min(geo2_vert_timeseries(point1_2:point2_2))),
max(geo2_vert_timeseries(point1_2:point2_2)));
y_axis2_timeseries=
linspace(-y_max2_timeseries,y_max2_timeseries,
point2_2-point1_2+1);
z_axis2_timeseries=
linspace(-z_max2_timeseries,z_max2_timeseries,
point2_2-point1_2+1);

y_max2_filtered=
max(abs(min(geo2_long_filtered(point1_2:point2_2))),
max(geo2_long_filtered(point1_2:point2_2)));
z_max2_filtered=
max(abs(min(geo2_vert_filtered(point1_2:point2_2))),
max(geo2_vert_filtered(point1_2:point2_2)));
y_axis2_filtered=
linspace(-y_max2_filtered,y_max1_filtered,
point2_2-point1_2+1);
z_axis2_filtered=
linspace(-z_max2_filtered,z_max1_filtered,
point2_2-point1_2+1);

% Plot hodogram of user selected portions of geophone #2
figure(6);
plot(geo2_long_filtered(point1_2:point2_2),
geo2_vert_filtered(point1_2:point2_2));
xlabel('longitudinal amplitude [V]');
ylabel('vertical amplitude [V]');
axis equal;

% Display hankel plot of user selected portions of geophone #2
figure(10);
subplot(211)
plot3(time_scale(point1_2:point2_2),
geo2_long_timeseries(point1_2:point2_2),
geo2_vert_timeseries(point1_2:point2_2),...
time_scale(point1_2),geo2_long_timeseries(point1_2),
geo2_vert_timeseries(point1_2),'o',...
time_scale(point2_2),geo2_long_timeseries(point2_2),
geo2_vert_timeseries(point2_2),'x',...
time_scale(point1_2:point2_2),
xyz_axis(point1_2:point2_2),
xyz_axis(point1_2:point2_2),'k',...
x_axis2,y_axis2_timeseries,
xyz_axis(point1_2:point2_2),'k',...
x_axis2,xyz_axis(point1_2:point2_2),
z_axis2_timeseries,'k');
xlabel('time [sec]');
ylabel('longitudinal amplitude [V]');
zlabel('vertical amplitude [V]');
axis([time_scale(point1_2),time_scale(point2_2),
min(geo2_long_timeseries),max(geo2_long_timeseries),

```

```

min(geo2_vert_timeseries),max(geo2_vert_timeseries)));
view(15,30);
subplot(212);
plot3(time_scale(point1_2:point2_2),
geo2_long_filtered(point1_2:point2_2),
geo2_vert_filtered(point1_2:point2_2),...
time_scale(point1_2),geo2_long_filtered(point1_2),
geo2_vert_filtered(point1_2),'o',...
time_scale(point2_2),geo2_long_filtered(point2_2),
geo2_vert_filtered(point2_2),'x',...
time_scale(point1_2:point2_2),
xyz_axis(point1_2:point2_2),
xyz_axis(point1_2:point2_2),'k',...
x_axis2,y_axis2_filtered,
xyz_axis(point1_2:point2_2),'k',...
x_axis2,xyz_axis(point1_2:point2_2),
z_axis2_filtered,'k');
xlabel('time [sec]');
ylabel('longitudinal amplitude [V]');
zlabel('vertical amplitude [V]');
axis([time_scale(point1_2),time_scale(point2_2),
min(geo2_long_filtered),max(geo2_long_filtered),
min(geo2_vert_filtered),max(geo2_vert_filtered)]);
view(15,30);

% Graphically display ratio of longitudinal to vertical signal
% amplitudes
disp(' ');
ellipse=
input('Do you want to calculate ratio of elliptical axes
(y or n): ','s');
if ellipse=='y'
geol_long_hilbert=
abs(hilbert(geol_long_filtered(point1_1:point2_1)));
geol_vert_hilbert=
abs(hilbert(geol_vert_filtered(point1_1:point2_1)));
geol_amp_ratio=geol_long_hilbert./geol_vert_hilbert;
figure(11);
subplot(211);
plot(time_scale(point1_1-256:point2_1+256),
geol_long_filtered(point1_1-256:point2_1+256),...
time_scale(point1_1-256:point2_1+256),
geol_vert_filtered(point1_1-256:point2_1+256),'--');
xlabel('time [sec]'); ylabel('amplitude [V]');
legend('longitudinal','vertical');
subplot(212);
plot(time_scale(point1_1:point2_1),geol_amp_ratio);
xlabel('time [sec]'); ylabel('longitudinal/vertical');
axis([time_scale(point1_1),time_scale(point2_1),0,1]);

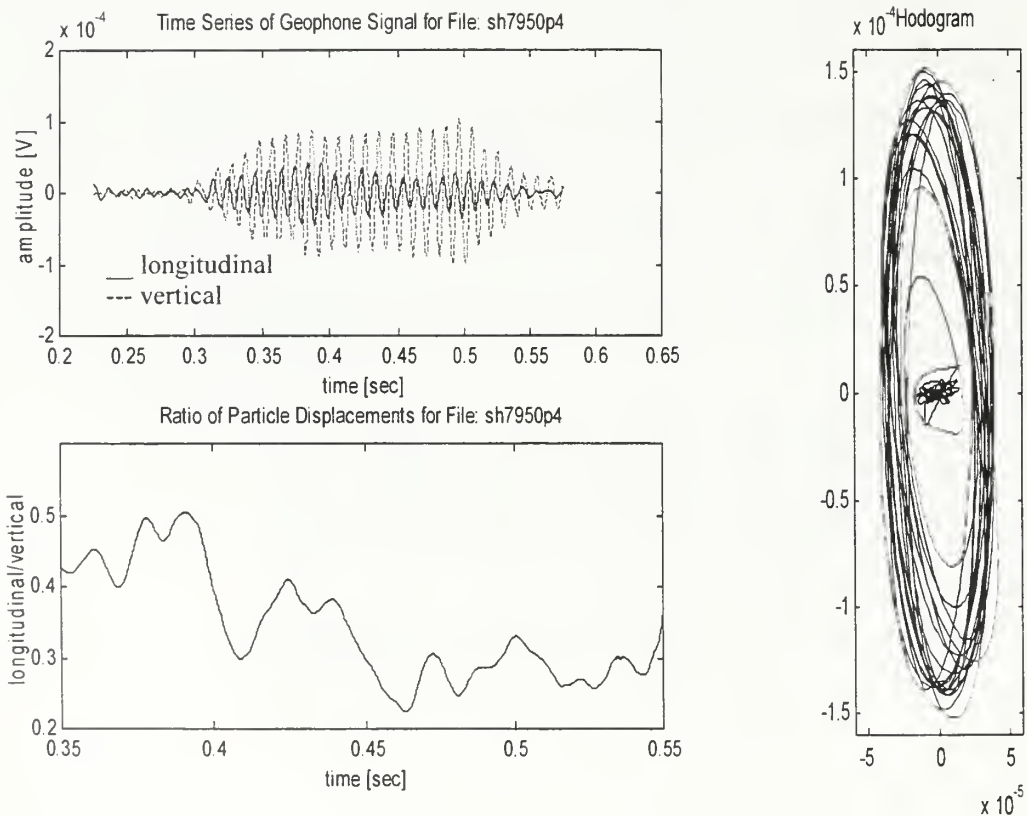
```

```

geo2_long_hilbert=
    abs(hilbert(geo2_long_filtered(point1_2:point2_2)));
geo2_vert_hilbert=
    abs(hilbert(geo2_vert_filtered(point1_2:point2_2)));
geo2_amp_ratio=geo2_long_hilbert./geo2_vert_hilbert;
figure(12);
subplot(211);
plot(time_scale(point1_2-256:point2_2+256),
    geo2_long_filtered(point1_2-256:point2_2+256),...
    time_scale(point1_2-256:point2_2+256),
    geo2_vert_filtered(point1_2-256:point2_2+256),'--');
xlabel('time [sec]'); ylabel('amplitude [V]');
legend('longitudinal','vertical');
subplot(212);
plot(time_scale(point1_2:point2_2),geo2_amp_ratio);
xlabel('time [sec]'); ylabel('longitudinal/vertical');
axis([time_scale(point1_2),time_scale(point2_2),0,1]);
end; %end-if ellipse

disp(' ');
continue=
    input('Press any key to continue isolation or "q" to quit: ',
    's');
end; %end-while
end; %end-if isolate

```



LIST OF REFERENCES

1. Muir, T.G., Smith, D.E., Wilson, P.S., "Seismo-Acoustic Sonar for Buried Object Detection," Proceedings of the Symposium, *Technology and the Mine Problem*, Naval Postgraduate School, Monterey, CA, Nov. 1996.
2. U.S. Navy, Chief of Naval Operations, "Mine Countermeasures – An Integral Part of Our Strategy and Our Forces," Washington, DC, Dec. 1995.
3. "United Nations Demining," [<http://www.un.org/Depts/Landmine/policy.html>], Oct. 1997.
4. Naval Explosive Ordnance Disposal Technology Center Final Report TR-311, *Technology Assessment for the Detection of Buried Metallic and Non-Metallic Cased Ordnance*, Jan. 1993.
5. Applied Research Laboratories, University of Texas at Austin, *Semi-Annual Performance Report on Physics of Buried Mine Detection and Classification*, by N.P. Chotiros and T.G. Muir, Aug. 1994.
6. Rayleigh, Lord (J.W. Strutt), "On Waves Propagated along the Plane Surface of an Elastic Solid," Proceedings London Mathematical Society, 1885, vol. 17, no. 4.
7. Kolsky, H., *Stress Waves in Solids*, pp.1-23, Dover Publications, Inc., 1963.
8. Viktorov, I.A., *Rayleigh and Lamb Waves Physical Theory and Application*, Plenum Press, 1967.
9. Personal communication between D. Rauch, SACLANT ASW Research Center, La Spezia, Italy and T.G. Muir, Applied Research Laboratories, University of Texas at Austin.
10. Richart, F.E., Hall, J.R., Woods, R.D., *Vibration of Soils and Foundations*, pp.88-92, Prentice-Hall, Inc., 1970.
11. Stewart, W.F., *Buried Object Detection Using Surface Waves*, Master's Thesis, Naval Postgraduate School, Monterey, CA, Sep. 1995.
12. BBN Systems and Technologies Final Report 7677, *Feasibility of Acoustic Landmine Detection*, May 1992.
13. Smith, E., "Scattering of Interface Waves from Pointlike Obstacles," accepted for publication, Journal Acoustical Society of America, Oct. 1997.

14. Lim, R., Lopes, J., Hackman, R., Todoroff, D., "Scattering by Objects Buried in Underwater Sediments: Theory and Experiment," Journal Acoustical Society of America, vol. 93 (4), Apr. 1993.
15. Lim, R., "Scattering by an Obstacle in a Plane-Stratified Poroelastic Medium: Application to an Obstacle in Ocean Sediments," Journal Acoustical Society of America, vol. 95 (3), Mar. 1994.
16. Damark International, Inc., Catalog No. B-40070, pp. 29.

INITIAL DISTRIBUTION LIST

1. Defense Technical Information Center 2
8725 John J. Kingman Rd., STE 0944
Ft. Belvoir, Virginia 22060-6218
2. Dudley Knox Library 2
Naval Postgraduate School
411 Dyer Rd.
Monterey, California 93943-5101
3. Dr. Jeffrey Simmen 1
Office of Naval Research, Code 321OA
800 N. Quincy St.
Arlington, Virginia 22217-5660
4. Dr. Douglas Todoroff 1
Office of Naval Research, Code 321
800 N. Quincy St.
Arlington, Virginia 22217-5660
5. Professor Steven R. Baker, Code PH/Ba 2
Department of Physics
Naval Postgraduate School
Monterey, California 93943-5000
6. Professor Thomas G. Muir, Code PH/Mt..... 2
Department of Physics
Naval Postgraduate School
Monterey, California 93943-5000
7. Dr. Raymond Lim 1
Coastal Systems Station, Code R22
6703 W. Highway 98
Panama City, Florida 32407-7001
8. Library, Coastal Systems Station 1
6703 W. Highway 98
Panama City, Florida 32407-7001
9. Dr. Richard Gramann 1
Applied Research Laboratories
University of Texas at Austin
P.O. Box 8029
Austin, Texas 78713

10. LT Frederick E. Gaghan 1
846 Central Ave.
New Providence, New Jersey 07974
11. Don Patton, Assistant Vice President, Public Services..... 1
California State Automobile Association
150 Van Ness Ave.
San Francisco, California 94102-5279

DUDLEY KNOX LIBRARY
NAVAL POSTGRADUATE SCHOOL
MONTEREY CA 93943-5101

15 483NPG TH 3485 C
10/99 22527-200 NLLC

DUDLEY KNOX LIBRARY



3 2768 00367913 5